**STATISTICAL PERFORMANCE EVALUATION,
SYSTEM MODELING, DISTRIBUTED COMPUTATION AND
SIGNAL PATTERN MATCHING FOR
A COMPTON MEDICAL IMAGING SYSTEM**

by

Li Han

A dissertation submitted in partial fulfillment
of the requirements for the degree of
Doctor of Philosophy
(Biomedical Engineering)
in The University of Michigan
2008

Doctoral Committee:

    Professor Neal H. Clinthorne, Co-Chair
    Emeritus Professor W. Leslie Rogers, Co-Chair
    Professor Jeffrey A. Fessler
    Professor Zhong He

DEDICATED TO MY PARENTS AND BROTHER.

ACKNOWLEDGMENTS

TABLE OF CONTENTS

LIST OF TABLES

Tables

LIST OF FIGURES

Figures

xiii

LIST OF ABBREVIATIONS

ART	Algebra Reconstruction Technique
ASIC	Application-Specific Integrated Circuit
CBC	Circulant-Block-Circulant
CT	Computed Tomography
CPDF	Cumulative Probability Distribution Function
CRLB	Cramer-Rao Lower Bound
CIRVS	Compton Imaging Random Variables Sampling System
CDDCS	Compton Double Differential Cross Section
D-PPE	Digital Pileup Prevention Energy
EM	Expectation Maximization
ET	Exeecution Time
FBP	Filtered Back-Projection
FPGA	Field-Programmable Gate Array
FIM	Fisher Information Matrix
FFT	Fast Fourier Transform
f-MRI	Functional Magnetic Resonance Imaging
FWHM	Full Width Half Maximum
GATE	Geant4 Application for Tomographic Emission
HE	High-Energy
HEGP	High Energy General Purpose
LEGP	Low Energy General Purpose
LIR	Local Impulse Response
LUT	Look Up Table
LECS	Low Energy Compton Scattering
M-UCRB	Modified Uniform Cramer-Rao Bound.
MCI	Monte Carlo Integration

MEGP	Medium Energy General Purpose
MLEM	Maximum Likelihood Maximization Expectation
MRI	Magnetic Resonance Imaging
MSE	Mean Square Error
MLE	Maximum Likelihood Estimation
MPI	Message Passing Interface
MPT	Message Passing Time
NaI	Sodium iodide
PDF	Probability Density Function
PET	Positron Emission Tomography
PSF	Point Spread Response Function
PMT	Photomultiplier Tubes
PDF	Probability Density Function
SPECT	Single Photon Emission Computed Tomography
UCRB	Uniform Cramer-Rao Bound
UHE	Ultra-High-Energy
VLSI	Very Large Scale Integration

CHAPTER 1

Introduction and background

The object of this research is to study a dual-planar silicon-based Compton imaging system and compare it to a conventional parallel-hole collimated Anger camera for tumor detection and treatment planning by statistical analysis of imaging performance. For this particular medical application, we are interested in tracers and therapeutic agents labeled with ^{131}I that emits predominately 364.4keV energy photons.

1.1 Motivation

The Compton imaging system is a potentially effective medical imaging device that can obtain greatly improved performance in both detection efficiency and spatial resolution for detecting higher energy photons. In a Compton imaging system, the incident photon impinges on the first detector and Compton scatters from an electron in the detector. The scattered photon is then absorbed in the second detector. A Compton imaging system, therefore, decouples the tradeoff between spatial resolution and detection efficiency that characterizes a conventional collimated Anger camera. Furthermore, higher energy photons can be imaged at higher spatial resolution in Compton imaging system than mechanically collimated systems.

Compared to the Compton imaging system, a conventional Anger camera system with parallel-hole high energy general purpose lead collimator imposes a tradeoff between resolution and sensitivity because of the physical constraints resulting from the mechanical collimation. As the imaged γ-ray photons exceed ~250keV, the collimator septal thickness must be increased to reduce the penetration and scattering of higher energy photons in the collimator material. Since collimator sensitivity for a fixed hole size is reduced as the square of septal thickness, resolution must be sacrificed by increasing hole size if sensitivity is to be maintained.

This dissertation describes practical methods for evaluating and comparing limiting system performance, speeding image reconstruction by distributed computation, and reducing problems caused by high count rates in the Compton imaging system. The modified uniform Cramer-Rao bound (M-UCRB)[1] is employed to evaluate and compare the imaging performance between the proposed Compton imaging system and a conventional collimated Anger camera for imaging 364.4keV photons emitted from ^{131}I. To obtain the M-UCRB within reasonable time limits, the Fisher information matrix (FIM) is evaluated by Monte Carlo integration, and simulation based on the statistical models of both imaging systems. Next, the distributed and parallel Maximum Likelihood Maximization Expectation (MLEM) algorithm with chessboard data partition is evaluated for reconstructing images from the Compton imaging system in an acceptable time. A real time signal processing system employing state-of-the-art digital electronics is described for solving problems raised by high photon count rate in the second detector.

1.2 Introduction to Nuclear Medical Imaging

The general purpose of nuclear medical diagnostic imaging is to obtain the in vivo picture of the spatial and temporal distribution of radioactive tracers, i.e. radio nuclides or radioactively labeled pharmaceuticals, within the patient's body after these substances have been taken orally or administered by intravenous injection[2]. The basic principle of radiotracers is that the radioactive compounds participate in the biochemical or physiologic processes in the body in the same way as the non-radioactive material. Because the emitted γ-rays from the radioactive material can be detected by an external camera, radiotracers may be used to track the flow or distribution of analogs of natural substances in the body. There are two major types of radioactive labels used: single photon emitters and positron emitters. Single photon emitters may emit one principal gamma ray or a sequence of gamma-rays that are directionally uncorrelated. In the case of positron emitters the emitted positron travels a short distance and annihilates with an electron. This annihilation generates two 511keV gamma rays, which travel in opposite directions. The 3-dimensional imaging modes for these two types of radionuclides are

Single Photon Emission Computed Tomography (SPECT) and Positron Emission Tomography (PET).

Figure 1.1 A planar collimated Anger gamma camera for detecting γ-ray photons from the radiotracer in whole body imaging.

Figure 1.2 A commercial SPECT system with triple imaging heads at 60 degrees to each other. (Picker PRISM 3000). This system can have three times the sensitivity as the single head system in Figure 1.1 and also rotates around the patient to obtain full angular sampling.

Currently, the planar collimated Anger gamma camera (Figure 1.1), the SPECT (Figure 1.2) is used to detect and image the γ rays emitted by the radiotracer concentrated in the organs or tissues. The PET (Figure 1.3) is used to image radio-nuclides that decay by positron emission.

The positron combines with an electron resulting in emission of a pair of gamma-rays traveling in opposite directions. For PET and SPECT, three dimensional images can be reconstructed that depict the relative or estimated absolute concentrations of these

3

tracers in various organs or tumors. In comparison, other medical imaging systems, such as X-ray computed tomography (CT), conventional ultrasound and Magnetic resonance imaging (MRI), with some exceptions, primarily provide high spatial resolution for anatomical imaging and detecting anatomic alterations.

Figure 1.3 A PET system. (Philips Allegro). The detector forms a ring around the patient to obtain full angular sampling and detects the annihilation gamma ray pairs in coincidence.

Because nuclear medicine imaging systems have the ability to provide information on the physiological or biochemical properties or function of organs non-invasively, some malignant tumors or lesions can be identified before they exhibit detectable anatomic change. Depending upon the specific tracer used, tumors may have increased uptake or decreased uptake compared to normal tissue. This may also distinguish between malignant and nonmalignant tumor types even though the tumors may have abnormal anatomic structure detected by other imaging systems. Functional magnetic resonance imaging (f-MRI) can also provide functional brain maps by measuring increased blood flow to different regions of brain by being able to distinguish oxygenated blood from deoxygenated blood by their different paramagnetic properties. There are efforts to develop paramagnetic tracer compounds for MRI and also functional contrast agents for ultrasound. Nuclear medicine imaging techniques can be much more sensitive and the radiotracers can be detected with 3-4 orders of magnitude lower concentration since the signal is directly emitted by the tracer rather than as merely a fraction of the input signal in MRI or ultrasound. There are numerous radiotracers that

have been developed for many different applications. However, the disadvantage of conventional nuclear medicine images is that spatial resolution must be sacrificed to obtain reasonable photon detection sensitivity.

1.3 Applications of γ-ray Radioactive Tracers in Medical Imaging

In this dissertation we will be mainly concerned with imaging higher energy photons. Efficient high resolution imaging for higher energy γ rays above 250keV such as emitted by ^{131}I, ^{113m}In, ^{137}Cs or ^{22}Na could well become clinically useful for diagnosing cancer, studying physiological and chemical processes of various tumors, monitoring tumor therapy, and tracking metabolic activity of essential trace elements. These radionuclides and corresponding radiopharmaceuticals cannot be replaced by low energy radiotracers because they have unique chemical properties that make them organ and/or tumor specific, but also because their longer physical half-lives make it possible to image patients several days after the compound is administered. This permits clearance of non-specific uptake from the human body and results in better organ or tumor contrast compared with background tissues.

1.3.1   Typical Applications of Low Energy γ-ray Radiotracers

Radio nuclides that emit low energy gamma-rays and corresponding radiopharmaceuticals are widely employed in the field of nuclear medical diagnostic imaging. This is because imaging gamma photons with energies less than 200keV by collimated Anger Cameras can achieve an acceptable tradeoff between spatial resolution and system sensitivity.

The most widely used radioisotope for clinical single photon imaging is ^{99m}Tc. It is obtained from a ^{99}Mo-^{99m}Tc generation system and has many favorable properties[3]. The 6 hour half-life (T1/2) is well suited for most of nuclear medicine diagnosis, and insignificant particulate emission during decay permits large activities to be injected into patients to obtain better quality images without exceeding radiation dose limits for the patient. The most important reason is the 140keV gamma-ray energy of ^{99m}Tc provides a good tradeoff between detection efficiency and spatial resolution for collimated Anger

gamma cameras. Currently, about 60% of radiopharmaceuticals and 90% of nuclear medicine imaging procedures use ^{99m}Tc. For example, the "blood-brain barrier" agent Tc^{99m}-glucoheptonate is used for the diagnosis of brain tumors and lung tumors[4], and ^{99m}Tc labeled pyrophosphate adheres to calcium deposits in damaged heart muscle and can help evaluate damage after a heart attack[5]. Another low energy radioisotope is ^{111}In (Indium) that emits both low energy 171keV (90% branch ratio) and high energy 245keV (94%) gamma-rays. It has a 2.8 day half life and is substituted for ^{99m}Tc in some nuclear medicine applications in cases of slow biological uptake. For instance, ^{111}In labeled anti-myosin, a substitute for ^{99m}Tc labeled Pyrophosphate, is also an infarct localizing agent to evaluate heart kinetics, ^{111}In labeled Satumomab Pendetide is used to detect colorectal cancer since it targets the tumor-associated glycoprotein-72, and ^{111}In labeled Pentetate can map the impaired flow of cerebrospinal fluid in brain [6].

1.3.2 Typical Applications of ^{131}I, a Higher Energy γ-ray Radiotracer

Although a number of high energy gamma-ray radiotracers are being used or developed, currently, in the fields of radionuclide diagnostic imaging, ^{131}I, or radiotracers labeled with it, can be used for both diagnostic imaging and internal radiotherapy. ^{131}I primarily emits detectable gamma-rays at 284keV (6.05%), 364.4keV (81.2%), 636keV (7.26%) and 723keV (1.8%), and it also emits Beta particles for radio-therapy that have short range and lose their energy locally in the tissue or tumor. This isotope is generated from fission in nuclear reactors and decays by beta emission and associated gamma emission with a physical half-life of 8.04 days.

Sodium iodide ^{131}I was used originally to treat an overactive thyroid gland and certain kinds of thyroid cancer, because it is taken up mainly by the thyroid gland or thyroid tumor and has a biologic T1/2 of about 24 days. Larger doses of radioiodine are usually used after thyroid cancer surgery to destroy remaining diseased thyroid tissue or thyroid cancer that has spread to other tissues [7, 8]. Small doses, below 10mCi, of ^{131}I are swallowed or injected to image and diagnose tumors in the thyroid gland.

In addition to detecting thyroid tumors, ^{131}I labeled radiopharmaceuticals are also used to treat and diagnose other cancers. ^{131}I-MIBG with affinity for catecholamine-secreting tissues and ^{131}I-6β iodomethylnorcholesterol that concentrates in the adrenal

cortex are tracers for imaging the adrenal gland to detect adrenal tumors, adrenal medullary cancer, and diseases in adrenocortical tissue, respectively [9]. Currently, clinical trials of ^{131}I radio-labeled tositumomab (an Anti-B1 antibody that produces significant anti-cancer activity), shows promise for the treatment of low grade, B-cell non-Hodgkin's-lymphoma and chronic lymphocytic leukemia [10]. Because tositumomab, a monoclonal antibody, is a protein that can bind to antigens on the surface of cancerous B-cells and ^{131}I emits high energy beta particles and gamma rays that it can image and destroy these cells.

Therefore, it is highly desirable to be able to perform quantitative in-vivo imaging of the radioisotope distribution during radiotherapy. The real-time information allows the doctor to accurately quantify the therapeutic dose and normal/abnormal tissue uptake, to assess changes in tumor size resulting from radiotherapy, and to make modifications to the treatment plan as necessary. However, accurate quantitative imaging of the high energy radio-nuclides maybe beyond the capability of conventional collimated gamma-ray cameras. A new imaging tool is highly desirable.

1.3.3 Additional Higher Energy Radiotracers and Gamma-Ray Emitters in Nuclear Medicine

In addition to ^{131}I, there are also a number of other higher energy single-photon emitters used in both diagnostic and therapeutic applications, which require good imaging performance with high resolution and high sensitivity.

1.3.3.1 Applications in the field of Clinical Diagnosis and Study of Physiology

Even though ^{99m}Tc is the most popular radioisotope for single photon imaging since it is readily available and easily collimated, there are several high energy single photon radiotracers listed in Table 1.1 with gamma-ray energies from 200keV to 511keV, that are employed to detect pathological change, diagnose the number and location of tumors, monitor the distribution of radiation dose during radionuclide therapy, and evaluate tumor response after therapeutic treatment [11, 12].

Because of the high energy of the emitted photons, attenuation and scatter in the patient are reduced and the un-scattered flux increases about 70% compared to the lower

energy photons of [99m]Tc. Moreover, the longer half lives of high energy isotopes, such as ^{131}I and [111]In(Indium) with 2.8 day half-life[13-15], are widely used for labeling tracers, such as, monoclonal antibodies, that may require up to several days to achieve high specific localization and maximum target-to-background contrast. In the clinic, [113m]In with photon emission at 392keV and a 1.7 hour half-life is generator produced from [113]Sn (tin) with 119day half life [16-19]. It has similar properties to ^{99m}Tc and could replace ^{99m}Tc in some clinical applications. Therefore, a nuclear medicine imaging system with both high resolution and high sensitivity for high energy gamma-rays is highly desirable.

Table 1.1 Higher energy radio nuclides for diagnostic imaging

Nuclide	Physical Half-life	Photon Energy(KeV)	Application Example
[131]I	8.04 days	β-69.4(2.12%) 96.6(7.36%) 191.4(89.3%) γ-284(6.05%) 364.4(81.2%) 636(7.26%) 723(1.8%)	^{131}I-sodium iodide: thyroid image, uptake, therapy ^{131}I-metaiodobenzyl-guanidine: imaging of pheochromocytomas and neuroblastomas ^{131}I labeled tositumomab: imaging and treatment of Non-Hodgkins Lymphoma
[111]In	2.8 days	171(90%) 245(94%)	^{111}In-oxyquinoline: labeling of leukocytes and platelets;for prostate imaging ^{111}In-satumomab pendetide: colorectal and ovarian tumor imaging
67Ga	3.261 days	93(38%) 184(24%) 300(16%)	^{67}Ga-gallium citrate: imaging of inflammatory processes and soft tissue tumors
[113m]In	1.66 hrs	391.7(65%)	Scan Lesions in Brain, Kidney, Liver, Lung
[11]C [18]F [13]N [15]O	20.3min 110min 10.0min 2.07min	511 keV positron Annihilation photon	In the field of PET imaging, such as ^{11}C-thymidine : brain tumor ^{18}F-deoxyglucose: Lymphoma, neuroblastoma ^{18}F-FDG: abnormal glucose metabolism of tumor

Another potential application for efficient imaging of high energy gamma-emitters, besides detection of disease, is to understand normal physiology and metabolism by measuring the bio-distribution of essential trace elements as a function of time using long-lived beta/gamma emitters such as listed in Table 1.2. For instance, ^{59}Fe would be a very useful element to determine the distribution of functional bone marrow, the imaging of ^{28}Mg is associated with the research of Mg distribution in the heart and changes in ^{24}Na distribution is relative to the anti-hypertensive therapy [20, 21]. Efficiency for detecting gamma particles is particularly important since many of these isotopes emit a large number of beta particles, and the number of gamma particles is relatively small.

Table 1.2 Isotopes of interest in the study of human metabolism[20, 21]

Element	Half-life	Gamma Energy (MeV) (Abundance %)		Beta Energy (MeV) (Abundance %)	
^{22}Na	2.6 y	1.27	(99.9)	0.2	(90)
^{24}Na	15 h	2.75	(99.9)	0.55	(99.9)
^{42}K	12.36 h	1.5	(18)	1.56	(82)
^{28}Mg	20.9 h	1.34	(53)	0.16	(94)
^{59}Fe	44.5 d	1.29	(43)	0.15	(53)
^{58}Co	70.9 d	0.81	(99.5)	0.20	(15)
^{65}Zn	244 d	1.1	(51)	0.14	(1.4)
^{47}Ca	4.5 d	1.30	(74)	0.24	(81)

1.3.3.2 Applications in the Field of Clinical Treatment and Therapy

Radiotherapy involves the exposure of parts of the body to substantial doses of radiation in the form of beams of high-energy X-rays, gamma rays, α or β particles [22, 23]. Because rapidly dividing cells, such as abnormal lesions and malignant tumors are particularly sensitive to damage by radiation, the growth of various forms of cancer can be controlled or eliminated by irradiating the area containing the growth. In contrast to

external X-ray beam based radiation therapy (EBRT), internal radiotherapy uses implanted radioactive sources or systemically administered tumor-specific radioactive compounds to irradiate tumors.

Systemic or metabolic radionuclide therapy [8] relies on the metabolic function of various tumors to concentrate the administered radioactive compound. Each year about 400,000 patients are treated with radiopharmaceuticals when the cancer is disseminated, mainly thyroid disorders (Grave's disease: 250,000; thyroid cancer: 95,000), bone metastases: 13,000, synovitis: 13,000, and polycytemia vera: 7000[24]. As in the case of diagnostic procedures, the unsealed radioactive source is given either orally or by injection. The radionuclide used must be an α or β emitters because their mean free path is limited to a few millimeters and the energy is selectively deposited in the tumors.

1.4 Anger Camera with Mechanical Collimators

1.4.1 Basic Principle of Anger Cameras with Mechanical Collimators

The Anger camera [25] with a mechanical collimator is the standard device used for imaging the distribution of radiotracers and is also the primary component of the SPECT head [26, 27]. The Anger camera (Figure 1.4) is a two dimensional position sensitive detector, which consists of a scintillating material such as a sodium iodide (NaI) crystal coupled to an array of photomultiplier tubes (PMT). A mechanical multi-hole collimator constructed of high Z materials, such as lead, tungsten, or gold, is placed in front of the scintillation crystal to determine the direction of the incoming γ-ray photons. Thus, each region of the scintillation crystal views only a small source area via the hole that defines the spatial resolution for the collimator. Most other photons not traveling in the proper direction are absorbed by collimator septa although some may penetrate the lead or be scattered by the lead and enter the scintillator. These undesirable events increase with increasing gamma-ray energy and reduce image resolution and contrast.

The scintillation crystal hit by a gamma-ray emits a flash of light that is proportional to the deposited energy at the position of the interaction. The light is collected and converted to an amplified electric signal by an array of PMT. The

interaction position and energy of each incoming gamma-ray photon is estimated and calculated by the associated electronic position logic and summing matrix circuit. Finally a pattern of scintillation interactions for many gamma-ray photons is obtained and displayed to form the image of radioactivity distribution in the body projected onto the plane of the scintillation crystal.
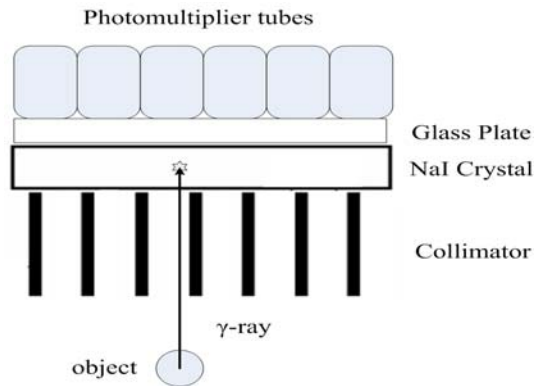
Figure 1.4 An Anger camera consists of a NaI scintillation crystal, an array of PMT, and a parallel hole lead collimator to limit the geometric acceptance angle of incident γ-ray photons.

The scintillation crystal is a dense material with a high atomic number (Z) to increase the probability of photoelectric absorption. The thickness of NaI scintillation crystal is typically ¼″ to ½″ to achieve reasonable detection efficiency and try to completely absorb the incoming photons while minimizing the spread of light in the crystal in order to preserve spatial resolution. For example, the detection efficiency is about 90% for 10mm think NaI crystals for 140keV photons [28]. A thicker crystal is required for detecting higher energy photons to obtain no-changed mean number of photons $\overline{N}$ in scintillation.

$$\sigma_{overall}^2 = \frac{\sigma_{LSF}^2}{\overline{N}} .$$ (1-1)

According to equation (1-1), however, since the width of the light spread function σ_{LSF}^2 become wider for the thicker crystal, the overall spatial resolution $\sigma_{overall}^2$ will be worse. Even though different types of collimators such as pinhole, converging, and diverging collimators are employed for different applications, parallel-hole collimators

with different hole diameters and thickness are specifically designed for γ-ray photons with different energies.

Gamma ray emission is a Poisson process that introduces noise into the recorded image and detection sensitivity is crucial in order to obtain low noise images in a reasonable imaging time. However, because of the inversely coupled relationship of collimator resolution and collimator efficiency, increasing the hole size to achieve a two-fold improvement of the detection sensitivity will decrease the spatial resolution a factor of 1.4.

1.4.2 Resolution and Efficiency Tradeoff of Anger Camera for Imaging Higher Energy γ Rays

The imaging performance of conventional collimated Anger camera systems is primarily determined by properties of the collimator. For imaging low energy γ-rays, i.e. 140keV of ^{99m}Tc, with a low energy general purpose parallel hole lead collimator, the spatial resolution (FWHM) at 10cm from the surface of collimator is about 1.0cm and total detection efficiency is around $2x10^{-4}$.

To image high energy gamma photons, however, the impact of penetration and scattering of radiation in the collimator material needs to be considered [29]. Thicker septa or higher Z material have to be employed. For the same collimator material, the septa of a high energy collimator for 364.4keV are 10 times as thick as the septa for a low energy collimator for 140keV. This causes a dramatic decrease of detection efficiency since the spatial resolution and detection efficiency of collimator have an inverse relationship [30, 31]. For example, to decrease penetration and keep the hole diameter constant, the septal thickness need to be doubled, then, the number of holes per unit crystal area drops a factor of 4. Thus, to maintain the detection sensitivity, the hole diameter must increase a factor of 2, and spatial resolution is also degraded correspondingly. This also increases collimator weight and introduces hole pattern artifacts since the hole spacing approaches the intrinsic spatial resolution of the Anger camera.

Meanwhile, high energy gamma rays also add substantial background to collimated Anger camera images due to penetration of the collimator and shielding. For

example, the 364.4keV γ-rays are the primary photons emitted from ^{131}I to be imaged clinically, but approximately 9% of the total gamma-rays emitted lie above 364.4keV. When a low energy collimator is used, a considerable number of 364.4keV γ-rays penetrate the thin collimator septa and deposit their full energy in the detector crystal. This results in low spatial resolution and reduced image contrast. A typical high-Energy (HE) collimator designed for ^{131}I will have a sensitivity of 64.6 Counts/sec/megabecquerel(cps/MBq) or 0.0064% efficiency, and a point source resolution around 17mm FWHM when the point source is located 15cm from the surface of the collimator. 43% of the detected events result from penetration and 29% from scattering in collimator material[32]. Therefore, an ultra-high-energy (UHE) collimator is required to reduce the penetration and obtain reasonable image contrast by reducing the long tail of the point spread response function (PSF). Thus, the sensitivity degrades a factor of 4 to 15.1 cps/MBq (0.00004% to 0.00151% efficiency) compared to the HE collimator, with spatial resolution of only 15 mm FWHM at a distance of 15 cm from the collimator. Furthermore, the collimator hole pattern becomes visible and is a distracting artifact [33]. Consequently, it is impossible to design a high energy lead collimator that avoids both penetration effects and image artifacts [34], and it is difficult to design a collimator used for imaging gamma rays with energies greater than about 410kev without substantial penetration [31].

1.5 Compton Imaging System

1.5.1 Basic Principles and Potential Advantages for Imaging High Energy γ-Rays

As described above good imaging performance for high energy γ-ray photons is difficult to achieve using conventional collimated Anger camera systems. In contrast, an alternative imaging technique known as a Compton camera appears to be well suited for high energy gamma-ray imaging. This technique is based on measuring the interaction position and scattering angle of a Compton scattered photon in the Compton camera.

The basic principle of Compton scattering is illustrated in the Figure 1.5. An incident γ-ray photon with energy E_0 scatters from and transfers part of its energy E_1 to a

bound electron. If the transferred energy exceeds the electron's binding energy, the electron will be released from the atom. The photon with reduced energy E_2 is scattered at an angle θ with respect to its initial direction. Assuming the initial electron is free and at rest, according to the conservation laws of energy of momentum, the relationship between the scattered photon energy E_2 and the scattering angle θ is shown in equation 1-2. [35]:

$$\cos \theta = 1 + m_0 c^2 \left(\frac{1}{E_0} - \frac{1}{E_2}\right) = 1 + 511 \left(\frac{1}{E_0} - \frac{1}{E_0 - E_1}\right),$$ (1-2)

where $m_0 c^2$ is the rest energy of the electron and equals to 511keV.
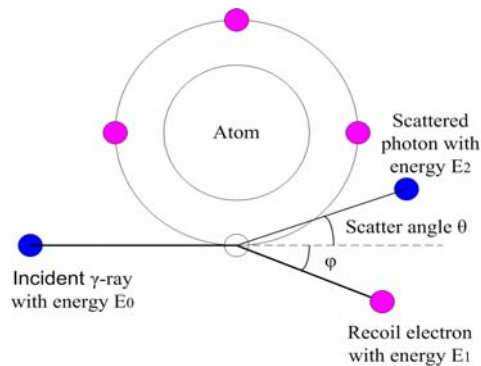
Figure 1.5 Illustration of a γ-ray photon Compton scattered by an electron.
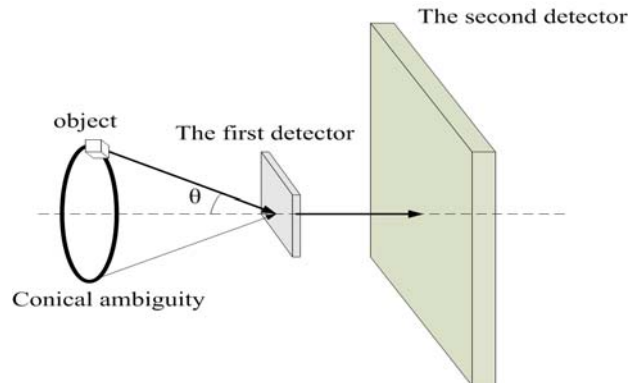
Figure 1.6 The principle of a Compton camera. The Compton camera consists of a scatter detector and an absorption detector. The incident gamma ray photon is Compton scattered and transfers parts of energy to the electron in the first detector; the scattered photon is absorbed in the second detector. The direction of incident gamma ray photon is restricted to lie on the surface of a cone. The half angle is equal to the scatter angle determined by the incident photon energy and the energy deposited in the first detector by the scattered photon. The cone vertex is located at the interaction position on the first detector and the cone axis is the vector connecting the interaction positions in first detector and second detector.

14

The Compton camera uses "electronic collimation" instead of mechanical collimation, and has the potential to improve detection efficiency and spatial resolution simultaneously by eliminating the efficiency-resolution tradeoff imposed by the mechanical collimator. To acquire the information about the incident γ-ray photon direction, the Compton camera detects a sequential interaction within a time coincidence window in two position and energy sensitive detectors. The first detector is referred to as the scatter detector, in which the Compton scattering takes place; and the second detector is denoted as the absorbing detector, In summary, an incident photon emitted from the radioisotope is Compton scattered and imparts part of its energy to a recoil electron in the first detector; and subsequently deposits the remaining energy in the second detector. Three quantities describing the interaction in the first detector are recorded: the time of the interaction, position of the interaction and energy of the recoil electron. Likewise, these three data elements for the scattered electron interaction in the second detector are also measured. A time coincidence window determines whether the interactions in the two detectors belong to one event.
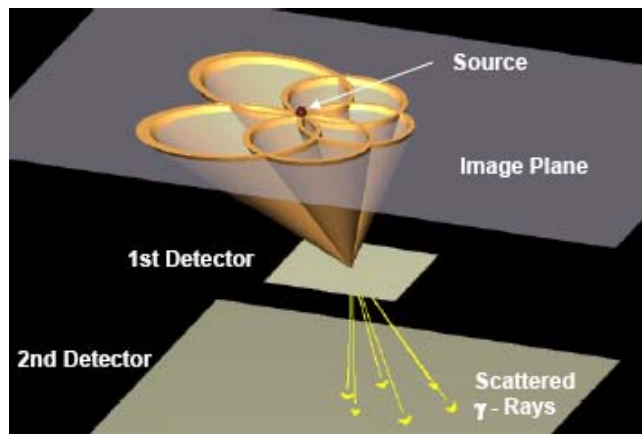
Figure 1.7 Reconstruction of a source distribution by the Compton camera. One coincidence event determines a unique hollow cone. The original γ-ray source position can be estimated from the intersection of multiple cones generated by several events. The thickness of the conical volume is related to uncertainty in the energy measurement in the first detector and spatial resolution in both first and second detectors.

On the basis of the acquired position and energy information from both detectors, the direction of the incoming γ-ray photon is determined within a conical ambiguity from Compton scatter equation (Eq.1-1) as illustrated in Figure 1.6 and 1.7, The cone axis is

15

determined by the vector connecting interaction positions in both first and second detectors. Cone vertex is on the interaction position on the first detector, and the open angle of the cone is equal to the scatter angle θ. Because one coincidence event determines a unique hollow cone, the original γ-ray source position can be estimated by the intersection of multiple cones generated by several events. Compared to a collimated Anger camera, the Compton camera overcomes the inverse tradeoff between spatial resolution and detection efficiency. However, the source location is only determined within a thin conical shell as opposed to small conical volume determined by the collimator hole dimensions, and a detailed analysis is required to quantify the net advantage of a Compton camera compared to a collimated Anger camera at the gamma-ray energies of interest.

In the real case, the electrons in the scattering detector are not free because they are bound to the atom in the first detector and have non-zero momentum. Therefore, the scattering angle is blurred for a given energy deposited in the first detector. This blurring is referred to as Doppler broadening. Therefore, due to the uncertainty in the recoil electron energy measurement and the effect of Doppler broadening in the first detector, combined with the intrinsic spatial resolution of the first and second detectors, the scattering angle is not precisely determined and the source location is known only within a conical surface with finite angular thickness. Thus, the spatial resolution is principally influenced by Doppler broadening and finite energy resolution of the scattering detector. A Compton camera also has problems as a result the reduced position information carried by each detected photon due to the conical ambiguity as illustrated in Figure 1.7. Because of this, the reduction in image noise will be less than that predicted just from the increased counting efficiency. Meanwhile, the advantage of Compton imaging system depends critically on the volume of the radioactive source distribution, as the source volume increases, the imaging performance degrades correspondingly.

Nevertheless a Compton camera still offers the potential for a joint improvement in image noise and spatial resolution compared to mechanically collimated cameras because the greatly increased count rate can overcome the reduced information carried per detected photon. Imaging high energy γ-ray photons, as we propose, substantially

reduces the influence of Doppler broadening and detector noise. This results in the potential to further improve the spatial resolution.

1.5.2 History of Compton Camera Development for Medical Imaging

The development of Compton scattering based coincidence imaging devices was started in 1973 by Schönfelder *et al.* for imaging in the relatively unexplored 1-10MeV energy range in the field of astrophysics [36]. The extension of this idea to the field of nuclear medical imaging was first proposed a year later by Todd *et al.* [37], in which a three dimensional structure of silicon cube arrays was suggested to track the first two events of a multiple Compton scatter of a γ-ray photon.

In 1983, Singh *et al.* described the first prototype Compton camera, ECC, in which the conventional collimator was replaced by a High Purity Germanium (HPGe) detector in front of an Anger Camera for nuclear medical imaging application[38, 39]. By imaging a point source of ^{99m}Tc and ^{137}Cs, this prototype Compton camera proved the photons could be electronically collimated. Later Singh reported an improved Compton camera using a 4×4 array of germanium detector elements backed by a scintillation camera as the second detector[40]. Images of a three-dimensional cylindrical phantom containing a γ-ray source were obtained. Compared to the image obtained using conventional SPECT for same phantom, the Compton camera displayed a higher sensitivity and slightly lower spatial resolution. Singh's research also demonstrated that the advantage of Compton scatter imaging would increase with higher energy sources. However, some difficulties and limitations were also reported: a) Since the sodium iodide second detector directly viewed the source, the high count rates saturated the detector electronics and only weak sources could be used with an unrealistically long acquisition time; b) An expensive cryogenically-cooled HPGe detector was required to achieve good noise characteristics.

After this first evaluation of the Compton camera for nuclear medicine, several groups experimented with different first detectors to improve performance. These included optical fibers[41], a gas scintillation proportional counter[42], high-pressure xenon detector[43], silicon strip detector and silicon pad detector[44-46], and cadmium zinc telluride (CZT) detector[47-49]. To decrease the impact of high second detector

count rate, a ring type NaI scintillation second detector was employed in the Ring Compton Camera (RCC) [50] and C-SPRINT [51] using an HPGe planar detector and silicon pad detector as the first scattering detector, respectively. The silicon detector became popular because it is relatively inexpensive, did not require cooling and the effect of Doppler broadening in silicon is smaller than for germanium because of its low atomic number. C-SPRINT is a prototype camera based on a 3cm × 3cm × 0.1 cm silicon pad detector as the first detector and the Michigan SPECT system (SPRINT) without its lead collimator as the second detector. As reported, for imaging a 140keV point source 10cm away from the silicon detector, C-SPRINT could achieve a sensitivity gain of about 20 over the mechanically collimated SPRINT if enough silicon was used, but its spatial resolution was around 1.5cm, which is not better than the conventional gamma camera [51]. However, it was estimated, that C-SPRINT would outperform a mechanically collimated camera at higher energy.

High energy gamma ray Compton imaging is currently used in astrophysics and industry and almost all prototype systems were evaluated for energies from 0.5MeV to 100MeV. In this energy range, the impact of Doppler broadening is small. Therefore, CZT detectors are a potential alternative for imaging higher energy gamma rays[48, 52] in the field of industry due to the higher intrinsic Compton scattering cross section and increased thickness. However, at present, the price of CZT detectors is quite high. For clinical imaging of ^{131}I 364.4keV photons, silicon is the best candidate for the scattering detector due to its small Doppler broadening, excellent energy and position resolution, room temperature operation, high Compton scattering to total cross section ratio, availability and price compared to germanium, neon and cadmium zinc telluride.

1.6 Contribution and Significance of This Research

The primary objective and contribution of this work is to evaluate and compare performance of the Compton scattering based gamma-ray camera with specific system geometry for higher energy γ-ray imaging to conventional mechanically collimated Anger camera using a modified uniform Cramer-Rao bound, system statistical model and Monte Carlo Simulation. The practical calculation studied uses approximations to

evaluate performance for 2D objects and any real system. In addition, theoretical analysis tools, image reconstruction software and improved system hardware were also developed during this research. For reconstruction of Compton camera images, a distributed and parallel MLEM algorithm was evaluated using a chessboard data partition to reduce computation time. Also, a real-time energy extraction and pileup prevention circuit for high count rate scintillation signals has been developed for an improved prototype Compton camera, in which the mechanical collimator of a commercial gamma ray camera will be replaced by a solid-state silicon pad detector as the "electronic collimator".

Imaging performance for 364.4keV γ-ray photons from ^{131}I has been selected for Compton camera evaluation because: (1) the nuclide ^{131}I is a commonly used high energy radioisotope for both nuclear imaging diagnosis and radionuclide therapy, (2) the 364.4keV gamma-ray emitted from ^{131}I is at the boundary between low energy and high energy in the field of nuclear medicine, and (3) the imaging performance of both Compton and mechanically collimated imaging systems can be compared at 364.4keV. Imaging of energies at 511keV and above is not practical for conventional gamma cameras with mechanical collimators.

This research confirms the hypothesis that a Compton scattering based gamma ray camera has potential to substantially outperform collimated Anger camera systems for quantitative, high resolution imaging of gamma-rays with the energy equal to or above 364.4keV. Further Compton imaging system development could then:

1. Result in improved cancer treatment planning, studying physiological and chemical processes of various tumors, and monitoring of the therapeutic response in patients. 2. Enable use of higher energy tracers such as ^{131}I or ^{111}In for diagnosis of cancers of thyroid, adrenals, prostate and other organs. 3. Make it possible to study normal and abnormal physiology by tracking long-lived high energy metabolically active tracers. 4. Enable coincidence imaging of positron emitters and single photon emitters with the same instrument. 5. Enable the development of new physiological tracers for different diagnostic applications based on radioactive elements that have not been considered suitable currently because of their high energy radiation.

1.7 Dissertation Overview

The basic background of radiotracers and introduction of the collimated Anger Camera and Compton imaging system have been introduced in the first chapter. The theoretical and qualitative analysis of the advantages and disadvantages of both imaging system are illustrated in Chapter 2. Next, in Chapter 3, the Monte Carlo Integration calculation of the Fisher information matrix and FFT based M-UCRB are introduced. The statistical system modeling and imaging performance analysis for both imaging systems are described in Chapters 4 and 5, respectively. In Chapter 6, a distributed parallel MLEM image reconstruction algorithm is evaluated; and, a real-time signal pattern match, energy extraction and pileup prevention circuit for high count rate scintillation signals is described and evaluated. Chapter 7 summarizes the results of this research and proposes topics for further research in this area.

CHAPTER 2

Qualitative Analysis of a Silicon Compton Imaging System and Anger Camera with HEGP collimator

This chapter illustrates the primary theoretical and qualitative analysis of both the Compton imaging system with silicon detector as scattering detector and the conventional Anger camera with high energy general purpose (HEGP) lead collimator for imaging the 364.4keV photons emitted from I^{131}. In the first section, a Compton imaging system now under development, and a commercial Anger Camera are described. Performance of the Anger Camera with HEGP collimator is analyzed by Monte Carlo simulation. Finally, the silicon based Compton imaging system is analyzed qualitatively.

2.1 Description of a collimated Anger Camera and a Silicon Compton Imaging System.

2.1.1 Anger Camera with Parallel Holes HEGP Lead Collimator

The conventional Anger Camera used in this study is an existing commercial Anger camera head with high energy general purpose lead collimator [53], as shown in figure 2.1. The camera is part of the ARGUS imaging system manufactured by ADAC laboratories.

Figure 2.2 illustrates a partial cross section view of the detector head and photomultiplier tube (PMT) location in the field of view. The detector consists of a thallium activated sodium iodide crystal, a glass optical window and 55 photomultiplier tubes. The NaI crystal is hermetically sealed in an aluminum housing with a glass

window. The PMT's are placed in a close-packed array over the glass window. The detector includes 49 3″ PMT's and 6 2″ PMT's, which are arranged in a 50.8cm by 36.8 cm field of view. The thin aluminum front layer is essentially transparent to γ-ray photons and blocks visible light. The glass window is employed as a light distribution element for mounting the PMTs through which the PMT's view the scintillations.   The mu metal shields the phototubes from the earth's magnetic field.

(A)   (B)
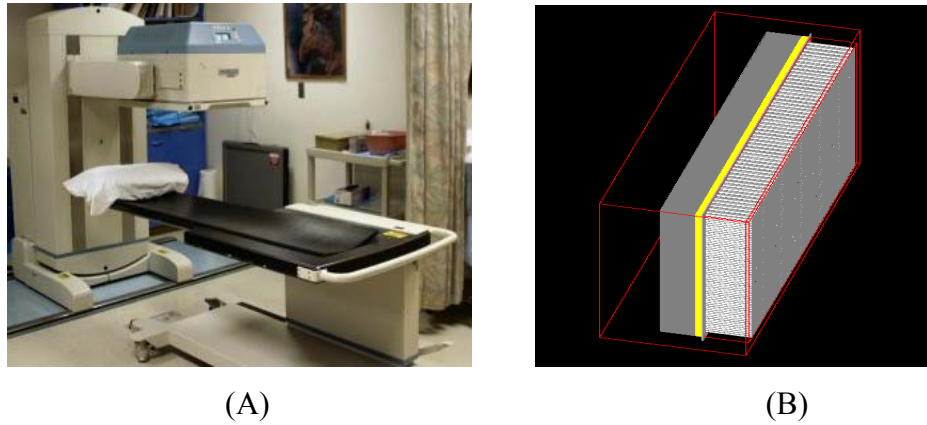
Figure 2.1 (A) The ADAC Lab ARGUS imaging system. (B) The simulated ARGUS camera head with parallel hole HEGP lead collimator.(white represents lead collimator, yellow represents NaI crystal, and gray represents phototube array)

(A)   (B)
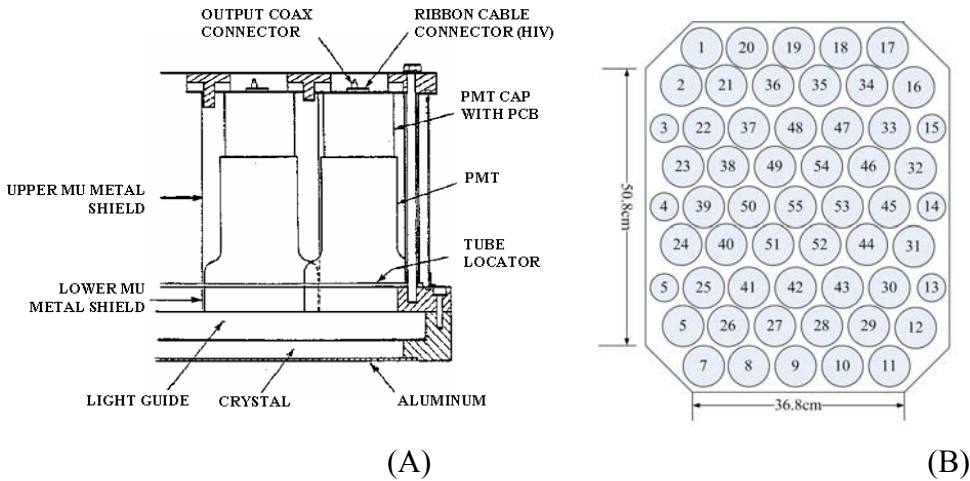
Figure 2.2 (A) Cross section of camera head-partial side view; (B) PMTs location and size of Field of View [53].

According to the ARGUS system specifications, the NaI crystal thickness is 9.5mm designed for a maximum energy of 400 keV, the intrinsic spatial resolution is

22

4mm (FWHM), and intrinsic energy resolution is 10.6% (FWHM) for 364.4keV. For detecting the photons with 364.4keV from ^{131}I, the hole size, septa and length of HEGP collimator is 3.81mm, 1.727mm and 60.0mm, respectively. The collimator spatial resolution is around 12.6mm as the 364.4keV point source at 10cm from the surface of the camera. As shown in figure 2.2 (B), the Anger Camera with collimator is simulated by GATE (Geant4 Application for Tomographic Emission) and GEANT4 Monte Carlo simulation system [54].

2.1.2 A Prototype "Silicon-NaI" Based Compton Imaging System

The scatter detector studied in this dissertation consists of 32x16x10 silicon pad detector elements and each silicon pad is 1.4mm by 1.4mm by 1mm, therefore, the total sensitivity area is 44.8x22.4x10mm^3. The absorption detector is a NaI Argus Anger camera imaging head, as described in the last section without a mechanical collimator. As demonstrated in Figure 2.3, the two planar detectors are parallel and centers of both detectors are aligned on axis. The distance between the two detectors can be adjusted to minimize angular uncertainty for a given photon energy. The geometry is symmetric, which simplifies performance simulation and image reconstruction. Silicon pad sensors can be stacked together to increase the scatter detector sensitivity. In this geometry, the NaI detector views the source directly. The resulting high count-rates make it necessary to design circuitry to reduce the effect of pulse pileup in the NaI detector.

2.1.2.1 Scatter Detector – Silicon Detector

Several scatter detectors designed specifically for Compton imaging systems, including the silicon pad sensors and associated hybrid readout electronics, were fabricated in the last decade by the Computer Imaging for Medical Applications collaboration between University of Michigan, Ohio State University, European Organization for Nuclear Research (CERN), Integrated Detector and Electronics (IDE), University of Ljubljana, and University of Valencia [55, 56]. Each generation of silicon detectors has improved energy resolution by reducing the leakage current using a superior fabrication process; constant spatial resolution by regulating the pad size; and improved

reliability and noise in the triggering by specially designed hybrid layout and power routing. The state-of-the-art silicon detector used in the current prototype Compton imaging system is shown in Figure 2.4. It is composed of a silicon pad sensor, and four VA/TAGP3 readout chips with signal readout lines.
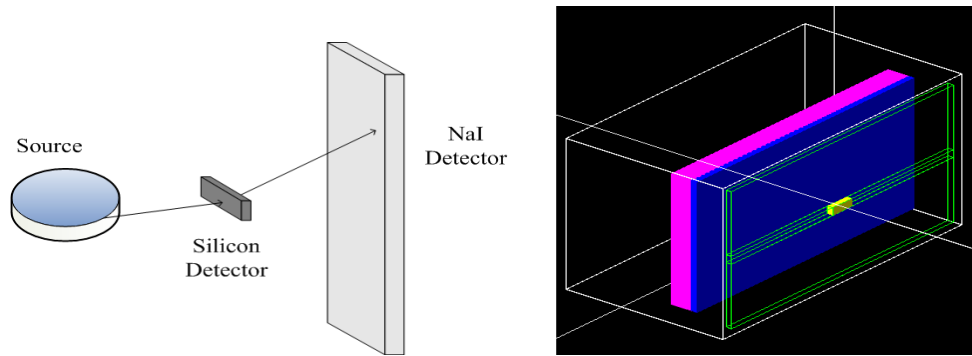
Figure 2.3 A parallel configured dual planar silicon-NaI Compton imaging system.
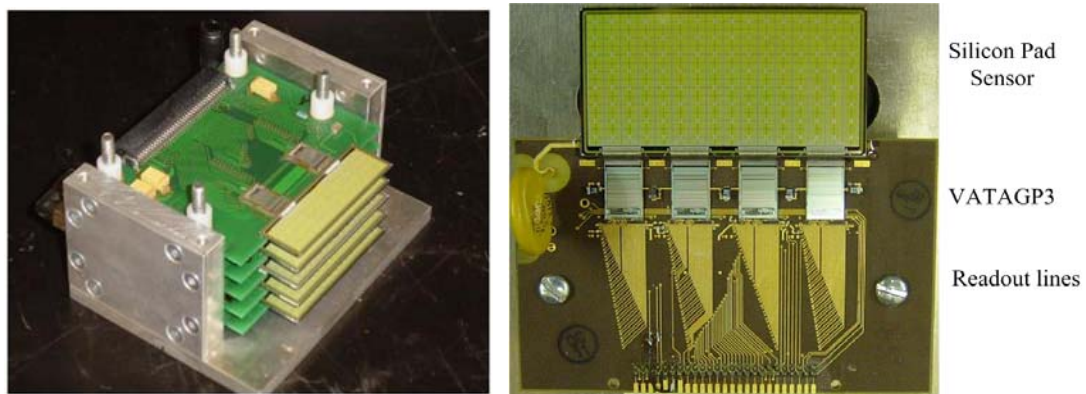
Figure 2.4 The scatter detector (left) and sub-modules(right), containing the silicon pad sensor, four VATAGP3 chips and readout signal lines on a PCB hybrid.

A cross section of the pad sensor, produced by SINTEF [57], is shown in Figure 2.5. Each pad is 1.39mm by 1.39mm p+ implants on high resistivity (5 kΩ/cm) n- silicon, and a 20μm wide non-implanted region forms a isolating layer between pads. Double metal technology is used here: Metal-1 directly covers the pad and Metal-2 routes the signal line from the pads to the 4 readout chips beside the sensor. Between the two metal layers is a polyimide insulating layer. Polyimide provides reduced preamplifier input capacitance compared to SiO_2. In order to reduce electric field at the edges, guard rings consisting of p implanted rings with aluminum metal separate the sensitive area from the

24

edges of the detector. An n+ implanted layer about 500nm thick covers the backplane of the whole sensor, to which a positive bias voltage is applied.

The silicon sensor is read out by fast self-triggering VATAGP3 chips. Each chip contains 128 channels providing the front-end electronics for 128 detector elements. The VATAGP3 is designed and fabricated by IDEAS[58] using low noise very-large-scale integration(VLSI) complementary metal oxide semiconductor (CMOS) ASIC technology and 0.8μm AMI process.
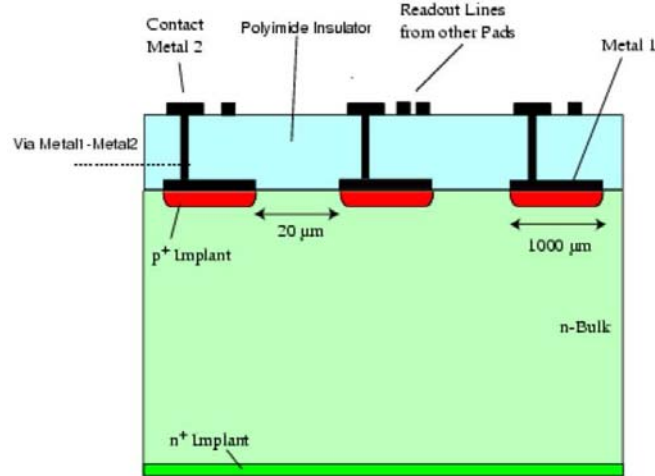
Figure 2.5 Schematic drawing of the cross section of p^+nn^+ doped silicon pad sensor with a double metal readout design [57].

In Figure 2.6, the functional blocks for one channel of the VATAGP3 are illustrated. In each channel, the output lead from one sensor pad is connected to a low noise, charge-sensitive preamplifier followed by VA and TA circuits. The VA module is for voltage readout and is composed of a slow semi-Gaussian shaper (3μs peaking time), sample and hold circuits and an analog multiplexer for outputing voltages of selected channels according to the controllable readout modes. The TA section consists of a fast semi-Gaussian shaper (200ns peaking time), a level discriminator and a monostable flip-flop that generates a trigger signal if the shaped signal exceeds the discriminator reference level. The reference level can be set to a common threshold for all channels or a 3 bit digital-to-analog converter (DAC) associated with each channel. The discriminator outputs of all 128 channels pass through an OR gate, and then generate a common signal to trigger the outside data acquisition unit to read the analog signals from the VA circuits.

The VATAGP3 can be disabled to prevent further triggering by another event until all analog signals are read out.
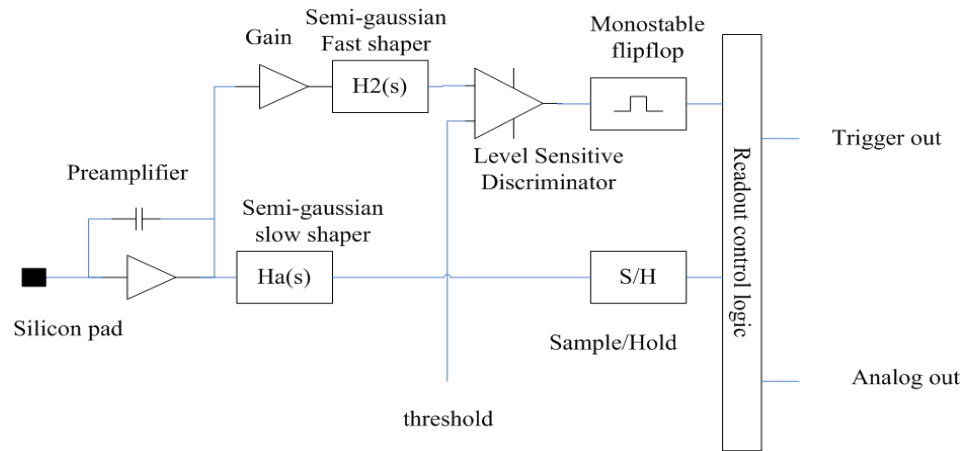
Figure 2.6 Block diagram of one channel of VATAGP3 readout chip.
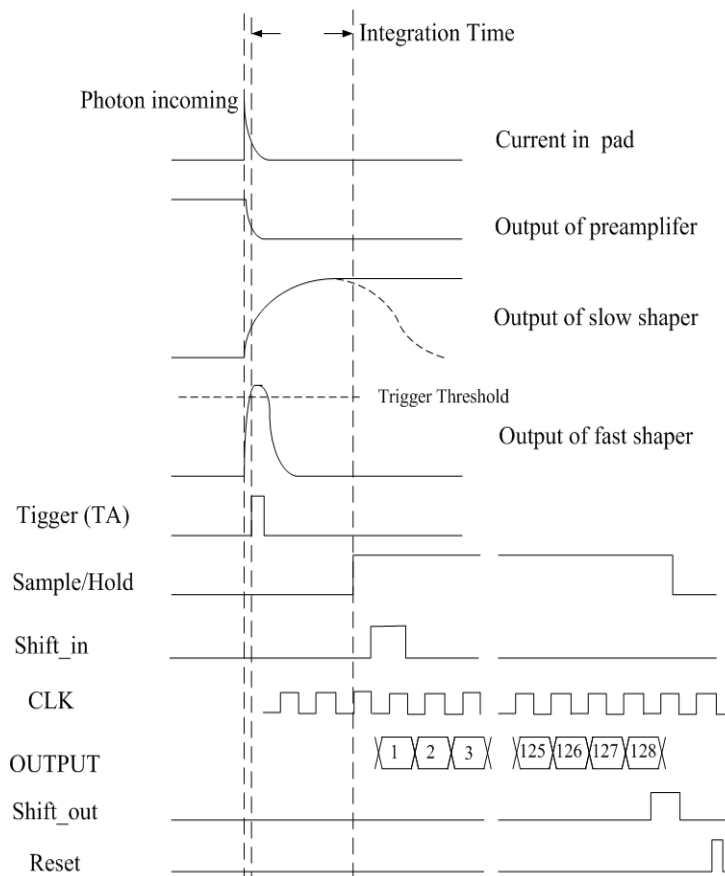
Figure 2.7 Signal and timing diagram for SERIAL readout mode of the VATAGP3 chip[58]

26

The VATAGP3 has three readout modes: SERIAL, SPARSE and SPARSE with adjacent channels. In the SPARSE mode, the chip only outputs the analog signals of the triggered channels for which the address is obtained from the data output. The readout speed of SPARSE is increased significantly. Another mode is SPARSE with adjacent channels. In addition to the SPARSE mode, this mode also outputs the analog signals of the channels around the triggered channels.

The most general mode is SERIAL mode, in which all channels of the chip are read out in sequence following a common trigger. The overall readout time for 128 channels of one chip is about 120μs. In figure 2.7, the primary signals to initiate SERIAL mode readout are illustrated. When a γ-ray photon interacts with one silicon pad sensor, the preamplifier integrates the incoming charge. Output of preamplifier is sent to both slow shaper of VA part and fast shaper of TA part. When the semi-Gaussian signal from the fast shaper exceeds a pre-set threshold, a trigger signal is sent from the monostable flip-flop circuit. Then, the common trigger signal from OR logic starts the process of serial readout. After approximately a 3μs integration time, the sample/hold signal reaches high logic and the output of slow shaper reaches a maximum value which is held in the sample-and-hold (S/H) circuit. The shift bit (shift_in) accompanied by a clock signal are pushed to the shift register, which indicates analog value output for corresponding channel held in S/H circuit and A/D converter. When the readout of the channel is finished in the period of one clock, the shift bit is clocked to the next channel. After completing readout from all 128 channels, the shift_out trigger is sent to the next VATAGP3 as a shift_in signal to continue reading channels for all silicon pads. Finally, a reset signal is sent out to finish the readout process.

Control and readout of the silicon sensor and VATAGP3 is controlled by the external data acquisition (DAQ) system, which is composed of four parts: the distribution board, the intermediate board, the VME ADC board and the computer. The distribution board is located functionally between the silicon detector and intermediate board, which reads out the multiple silicon sensor modules serially and distributes the control signal from the intermediate board to all silicon sensor modules. The intermediate board serves as the intermediate channel between the silicon detector modules and VME ADC board, and the intermediate board generates the necessary input voltages and currents for the

sensor and amplifies the acquired signals from detector to satisfy the VME requirement. The VME board controls the data acquisition. A 12 bit 10MHz analog-to-digital converter (ADC) is embedded in the VME board and control and readout sequence logic is pre-programmed in the FPGA on the board. The computer is employed as the master control and storage center, in which the developed DAQ software allows the user to change readout mode, threshold value and readout sequence. The digitized readout values are finally stored in the computer for off-line data analysis. The energy resolution of this silicon detector evaluated at the photo-peak energy 140.5 keV of ^{99m}Tc is about 1.3keV FWHM [59].

2.1.2.2 Absorption Detector – NaI Anger Detector Head

The second detector used in the prototype Compton camera is an existing commercial Anger camera head without its mechanical collimator [53]. The planar Anger camera head is part of an ARGUS imaging system manufactured by ADAC Lab., which was introduced in section 2.1.1.
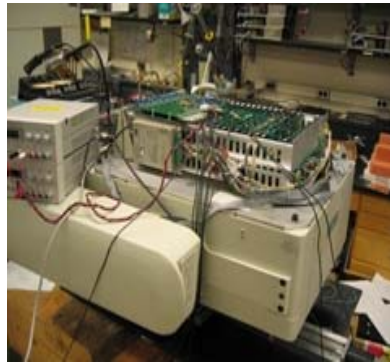
Figure 2.8 Photos of the ARGUS Anger camera head.

A state-of-the-art electronic circuit shown in Figure 2.8 has been designed for the specific requirements of the Compton imaging system. Each PMT is assigned to an independent acquisition system that includes a fast pre-amplifier and front-end board, a constant fraction discriminator board, and a SIS3300 VME ADC board. Each analog PMT output is digitized to 12 bits by a 100MHz ADC. The sum of PMTs is fed into the constant fraction discriminator. If the voltage exceeds the pre-set threshold a readout trigger is sent out and a snapshot of the digital PME waveforms is taken. The final digital

28

values are stored in the computer for off-line photon energy and interaction position calculation.

2.2 Properties and Limitations of Anger Camera with Parallel Hole HEGP Lead Collimator

2.2.1 Inverse Tradeoff between the Efficiency and Resolution

In Chapter 1, we introduced the collimator as an important component and performance factor of the conventional Anger camera system. As described in Chapter 1, the parallel hole collimator forms a projection image of the radioactive source distribution on the face of the Anger camera. The acceptance angle for incident gamma-rays (and thereby sensitivity and resolution) is determined by hole length and diameter. The thickness of the septa between holes affects sensitivity and also penetration and scatter of incident gamma rays that degrade resolution. That is: if greater efficiency is required, then the hole size needs to be increased or the hole length must be shortened. Either of these choices results in degrading the spatial resolution of images since if only photons with directions near to the ideal are selected by reducing the size of hole or increasing the length, then the efficiency is reduced and the counting statistics will be poor[29].
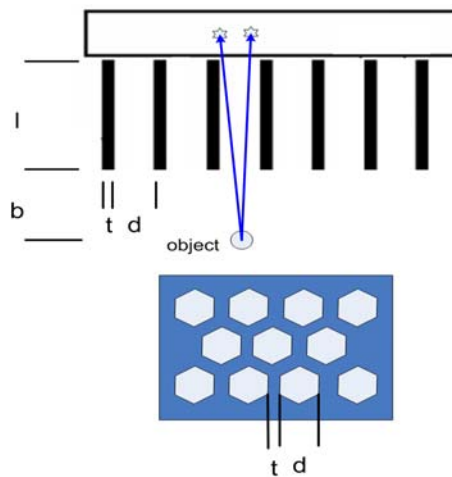
Figure 2.9 The parallel hole collimator with hexagonal hole pattern. l is the length of hole or thickness of collimator. d is the width of the hexagonal collimator holes. t is the septal thickness. b is the distance between a typical source and the front of the collimator.

A parallel hole collimator with hexagonal holes is displayed in Figure 2.9, in which l is the length of hole or thickness of collimator; d is the width of the hexagonal hole; t is the septal thickness; b is the distance between the source and the front of the collimator.

Therefore, the collimator efficiency g, which is the fraction of γ-rays emitted by the no attenuation source in air that pass though the holes of the collimator, is given by[60],

$$g \approx K^2 (d/l)^2 [\frac{d^2}{(d+t)^2}]$$
(2-1)

Where K is a constant that depends on the hole shape equal to ~0.26 for hexagonal holes in a hexagonal array. The collimator resolution R_c is the Full Width at Half Maximum (FWHM) of the PSF, which is the radiation profile of a point source of radiation projected through the collimator onto the detector. It is defined as

$$R_c \approx \frac{d}{l}(l+b)$$
(2-2)

From the equation (2-1) and (2-2), the collimator efficiency approximately equals to the square of the ratio of hole diameter to length. The thinner collimator with larger size hole could achieve higher collimator efficiency. Whereas, the collimator resolution decreases, i.e. FWHM increases, approximately as the ratio of hole diameter to length. Long, narrow holes provide better image resolution. Thus, for a given septal thickness, there is an approximately inverse relationship between the collimator efficiency and square of the FWHM resolution.

$$g \propto R_c^{2}$$
(2-3)

The overall system resolution R_s is determined by both collimator resolution R_c and intrinsic resolution R_i, which is the spatial resolution of the detector and the electronics, and R_s is given approximately by

$$R_s = \sqrt{R_c^2 + R_i^2}$$
(2-4)

The intrinsic resolution R_i is primarily limited by two factors. The first is the multiple scattering of photons within the detector, and another is statistical fluctuation in the distribution of light photons from the scintillation events between photo multiplier tubes [60]. According to equation (1-1), the intrinsic resolution R_i becomes worse as the

30

crystal is thicker, and it also approximately constant for detecting a given energy γ-ray for a given detector design with unchanged crystal. Thus, optimization of overall system resolution is dominated by the selection of collimator.

According to Eq. (2-2), for an Anger camera with a specified collimator, the overall system resolution strongly depends on the source-to-collimator distance b, and collimator resolution degrades by a factor of 2 as the source-to-collimator distance changes from 0cm to 5cm. Therefore, the best image quality is achieved when the radiation source is closest to the front surface of the collimator.

2.2.2 Collimator Scatter and Septal Penetration for Higher Energy γ-rays

As previously mentioned for the ideal situation, the incident γ-ray photons with undesired direction are all absorbed or rejected by the collimator septa. As illustrated in the Figure 2.10, however, the detected γ-ray photons not only include the photons with desired direction, (geometric photons), but also include the photons scattered in the collimator septa and the septal penetration photons, which pass through the collimator septa directly without interaction. Even though the last two types of photons will increase the overall collimator sensitivity, those photons contribute a foggy background image onto the desired image giving rise to long tails on the point spread function and consequently a degradation of image contract.
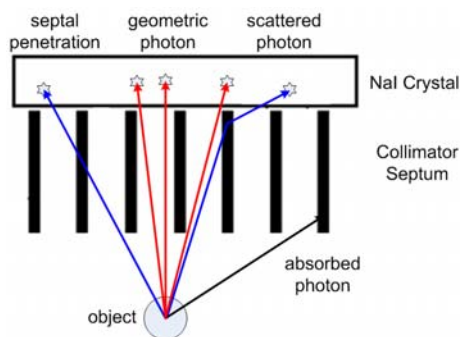
Figure 2.10 Illustration of types of detected photons. Detected photons include the desired geometric photon, the undesired photon scattered in the collimator, and the undesired septal penetration photons.

According to the Eq. (2-1), the collimator sensitivity is maximized by the thinnest possible septa. Unfortunately, the collimator with thin septa increases septal penetration.

Increasing the thickness of septa is necessary to control penetration. However, no thickness of collimator septa for a given material can entirely to stop all γ-ray photons based on the law of attenuation. Following common criteria, a small fraction of photons, i.e. ~5%, is allowed to penetrate to the septa[61].
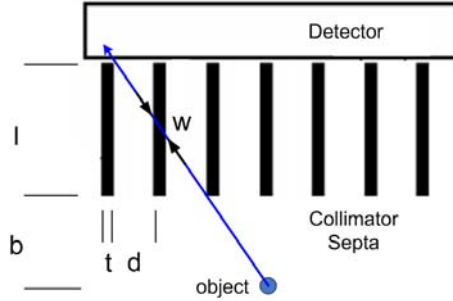
Figure 2.11 Calculation of the minimum path length w allows one to estimate the maximum probability of a γ-ray photon penetrating through the collimator septa between the holes. l is the length of septa, t is the thickness of septa and d is the diameter of the collimator holes.

Therefore, as illustrated in Figure 2.11, the minimum path length w for a γ-ray photon to pass through the septa between holes can be expressed as

$$w = \frac{tl}{2d + t}.$$ (2-5)

If the fraction of acceptable penetration photons is 5%, based on the attenuation law, the percentage of photon transmission for the path w is approximately

$$e^{-\mu w} \leq 0.05$$ (2-6)

Where μ is the linear attenuation coefficient of the septal material for the energy of the incident photons, and thus the minimum thickness of septa for 5% penetration is

$$t \geq \frac{6d/\mu}{l - (3/\mu)}$$ (2-7)

To obtain the maximum collimator efficiency, materials of high atomic number Z, high density ρ, with large value μ are selected to minimize septal thickness. Lead with Z=82 and ρ=11.34 g/cm^3 is the common choice, but both tungsten (Z=74 and ρ=19.25 g/cm^3) and gold (Z=79 and ρ=19.3 g/cm^3) have been used in special applications.

The energy of γ-ray photon strongly determines the value of the linear attenuation coefficient μ of the collimator martial, which becomes much smaller for higher energy γ-

32

rays. Compared to a collimator designed for 140keV γ-ray photons, the collimator septa for 364.4keV γ-ray photons is thicker to reduce the septal penetration. Therefore, the hole diameter must be enlarged to preserve reasonable collimator efficiency, with a corresponding degradation in collimator resolution. The specifications for collimators designed for different γ-ray energies are given in Table 2.1, in which the LEGP is a low energy general purpose collimator for 140keV photons; the MEGP is a medium energy general purpose collimator designed for photon energies from 200keV to 400keV; and the HEGP is a high energy general purpose collimator for photons with energy between 300keV to 511keV. Comparing LEGP and MEGP collimators, the septa thickness increases about 6 fold and the hole diameter also increases about factor of 2 to maintain acceptable sensitivity. For the high energy γ-rays, the thicker septa reduces penetration, but also results in increased photon scattering in the collimator's material[62-64].

Table 2.1 Collimator Specifications for Argus System

Collimator Type	Hole size diameter (mm)	Septa Thickness (mm)	Length (mm)	Sensitivity	Resolution @10cm
LEGP	1.4	0.178	25.4	1.729E-4	8.8 mm
MEGP	2.95	1.143	48.0	1.420E-4	11.4mm
HEGP	3.81	1.727	60.0	1.382E-4	12.6mm

For the case of imaging the γ-ray photons emitted by ^{131}I, the effects of collimator scattering and septal penetration become worse and more complicated. Unlike ^{99m}Tc that emits single γ-ray energy at 140keV, ^{131}I not only emits a γ-ray with the photo peak at 364.4keV (82%), it also emits other two higher energy γ-ray photons at 637keV (7.2%) and 723keV (1.8%). Even though the photo-peak energy window is usually centered at 364keV and γ-ray photons with 637keV and 723keV have low intensity, the scattering effect of these two γ-rays is significant since they have higher probability of scattering in the lead collimator septa rather than being absorbed. Increased collimator scattering and penetration of 637keV and 723keV photons will degrade image contrast and spatial resolution in the final image.

To illustrate the effects of collimator scattering and septal penetration of multiple energy photons emitted from ^{131}I, Monte Carlo simulation is used to track the un-

scattered and scattered photons with different energies separately. In this work, GATE is employed, which is a Monte Carlo simulation platform designed for simulating SPECT and PET systems[65-67] based on the CERN Geant4 Code. Compared to other Monte Carlo simulation programs, GATE accounts for all kinds of interactions, including scattering and penetration in the collimator.

To determine the significance of collimator interaction, a point source of ^{131}I in air is located 1 mm from the front face of the collimator. The GATE platform simulates a point source in air detected by Argus Anger Camera Head with HEGP collimator and records the geometric, penetration and scatter photons for the three ^{131}I photon energies, separately
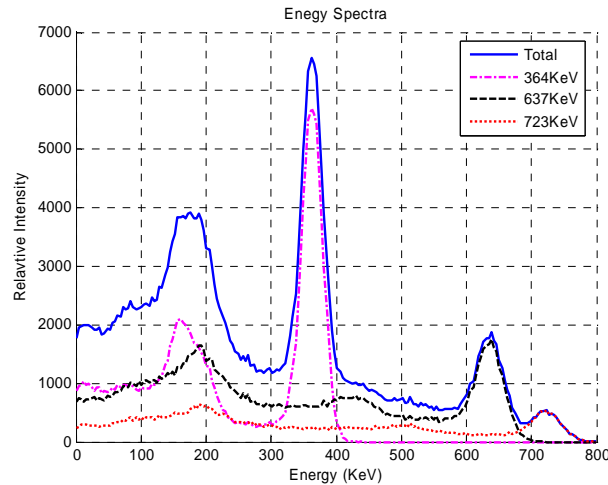
Figure 2.12 Energy spectra of detected photons separated according to the emission energy by 364keV, 637keV and 723keV.

Without any energy windows, the simulated energy spectra of detected photons for each of the three photon energies are shown in Figure 2.12. The 364keV photons that undergo scattering in the collimator and deposit partial energy in the detector are the primary component of the low energy parts. Within the 30% photo-peak energy windows at 364keV, the scatter and penetration spectra corresponding to 637keV and 723keV photons are relatively flat.
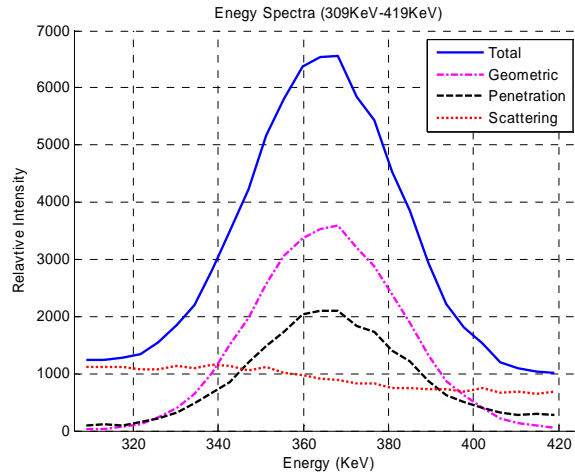
Figure 2.13 Energy spectra of detected geometric, penetration and scattered photons within the 30% photo-peak window at 364keV.

The separated geometric, scatter and penetration energy spectra of detected photons are shown in Figure 2.13. Even within the 30% photo-peak window at 364keV, a large fraction of detected photons have undergone collimator scattering and septal penetration. The scattering spectrum is relatively flat and is primarily contributed by the 637keV and 723keV γ-ray photons after losing energy due to Compton scattering within the collimator. The penetration spectrum shows a photo-peak the same the geometric spectrum which is primarily contributed by photons with 364keV energy passing through the septa without losing any energy.

In summary, the percentage of geometric, septal penetration and scattered photons detected within a 30% energy window at 364keV for a point source of ^{131}I in air are shown in Table 2.2. Only 42% of the detected photons are the desired geometric photons. The contribution of the 637keV and 723keV photons represents more than 28% of total detected photons within 30% windows.

Table 2.2 Contribution of geometric, septal penetration and scattered photons within 30% window at 364 keV for a point source of ^{131}I in air

Energy (Kev)	Geometric (%)	Penetration (%)	Scattering(%)	Total Acq. Events
364.4	**42.38**	22.84	6.16	71.38%
637	0.35	4.17	16.48	21.0%
723	0.02	0.75	6.85	7.62%
Total	42.75	27.76	29.49	
Sensitivity	44753/369858096=1.21e-4 (All events in energy windows)			

As shown in Figure 2.14, therefore, the final image for a point source of ^{131}I consists of the components from geometric, scattering and penetration photons. For the hexagonal hole pattern, the penetration photons forms a star-pattern in the direction in which the septa are thinnest. The scattered photons impose a foggy background on the desired image contributed by the geometric photons. Both star-pattern and foggy background degrade the image resolution and contrast since they introduce a long tail on the point source function and add a structured background.

A) Geometric photons   B) Septal penetration photons

C) Scattering photons   D) Image of a point source
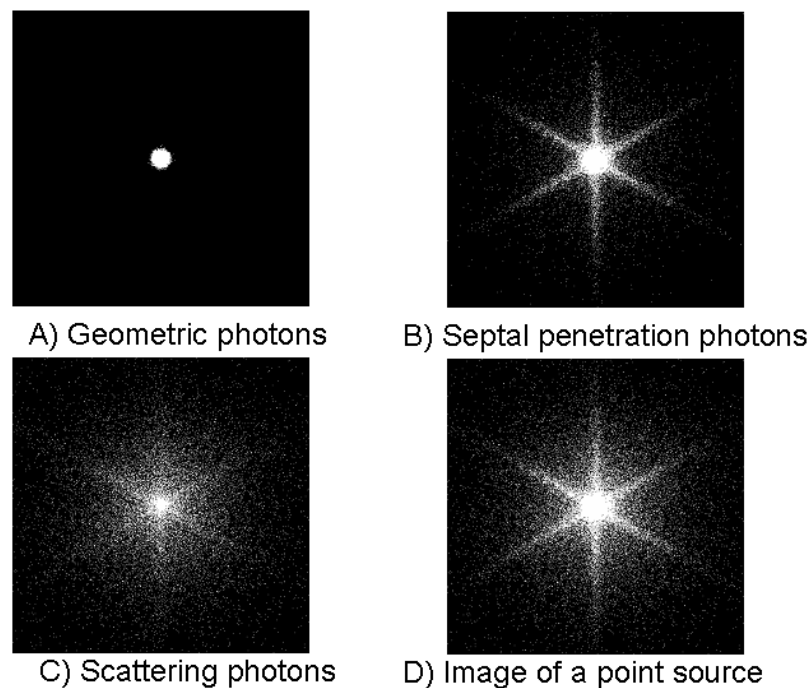
Figure 2.14 An image (D) of a point source of ^{131}I placed at 1mm from the front face of collimator in a 30% energy window, and image components contributed by Geometric photons(A), Septal penetration photons (B) and Scattered photons(C).

2.2.3 Sampling and Limited-Angle Problem for Tomography

To obtain a correct reconstruction of emission or transmission images, the collection of projections over a full angular range from 0 to 180 degree is required. The projections must satisfy the requirements of appropriate linear and angular sampling intervals to avoid aliasing due to under-sampling.

According to the sampling theorem[68], if the maximum spatial frequency response of the system (that is half of Nyquist frequency) is V_{max}, which depends on the detector resolution and on the cutoff frequency used for the reconstruction filter, required a linear sampling distance Δx is,

$$\Delta x \leq \frac{1}{2 \times V_{max}} \qquad (2\text{-}8)$$

<table>
<tr><td>(A) 180 degree</td><td>(B) 135 degree</td></tr>
<tr><td>(C) 90 degree</td><td>(D) 45 degree</td></tr>
</table>
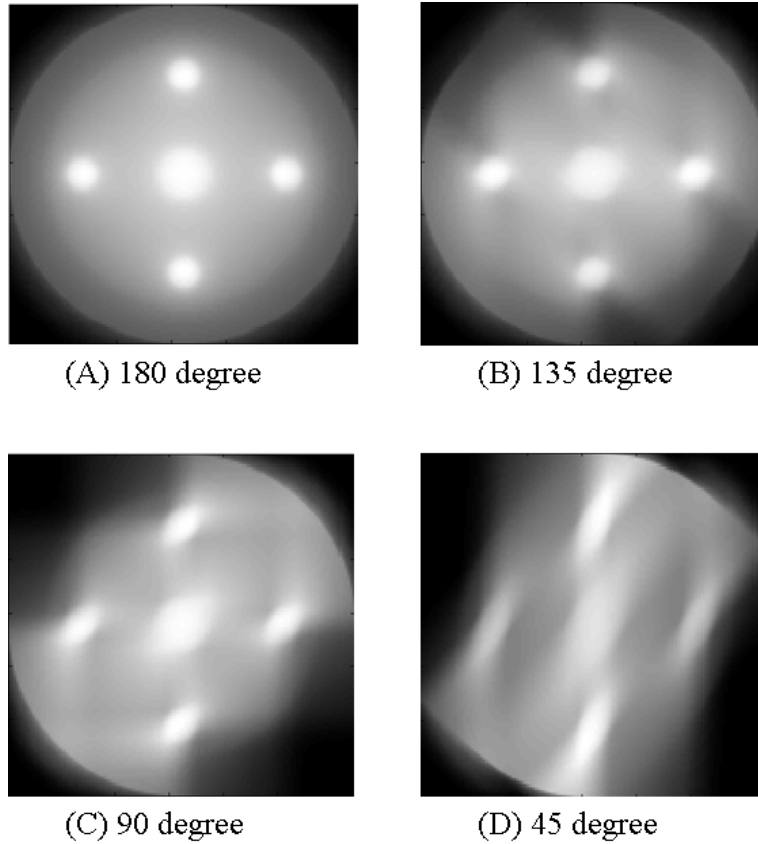
Figure 2.15 Examples of effects of angular sampling range in tomographic transmission images obtained by sampling over A) 180 degrees B) 135 degrees C) 90 degrees C) 45 degrees.

Because sampling in angle is a sampling in the Fourier domain of the object and under-sampling in this domain will result in the aliasing of spatial information in the final image. Thus the angular sampling interval (angle between projections) should be

$$\Delta\theta \leq \frac{1}{2\Delta x \times FOV}, \qquad (2\text{-}9)$$

where, the FOV is desired field of view. if the diameter of field of view is D, then number of angular views for an full range of angles from 0 to 180 degree is given as

$$N_{projections} = \frac{\pi D}{2\Delta x} = \frac{\pi}{\Delta\theta_{max}} .$$
(2-10)

However, in some practical cases shown in Figure 2.15, the complete tomographic projection data collected over a full 180 degree cannot be achieved. In these cases, limited-angle views of the projection data are insufficient to correctly reconstruct the tomographic distribution of activity. Limited-angle tomography induces image artifacts and produce geometric distortions perpendicular to the direction of the missing projections.

2.3 Theoretical Analysis for a Prototype Silicon based Compton Imaging System for Detecting 364.4keV

In this section, the detailed principles and qualitative analysis for a dual planar Silicon-NaI Compton camera imaging system are investigated. As described in the previous section, this Compton camera consists of two types of detectors: the first detector is the scatter detector, which consists of several silicon pad detector; the second detector is the absorption detector, which is a commercial Anger camera head without a mechanical collimator and composed of a NaI scintillation crystal. Both detectors are planar detectors and parallel to each other. The theoretical analysis that predicts the Compton camera performance for higher energy γ-ray imaging includes the Compton scattering efficiency of the silicon detector, and its energy resolution, the effect of Doppler broadening for silicon and overall system geometry as well as the imaging characteristics of the Anger camera used for the absorption detector.

2.3.1 Compton Scattering of Silicon Detector

As introduced in Chapter 1 and illustrated in Figure 2.16, Compton scattering takes place between the incident γ-ray photons and an electron in the scatter detector material. During Compton scattering, the incoming γ-ray photon with energy E_0 is

deflected at a scatter angle θ with respect to its original direction and transfers a fraction of its energy to a recoil electron.
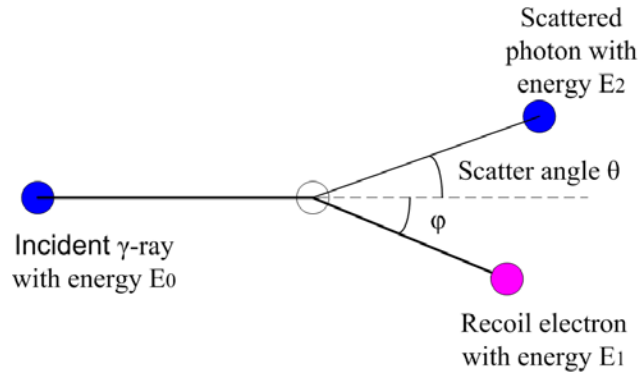
Figure 2.16 The basic principle of Compton scattering.

After a Compton scattering and detection of the scattered photon by the second detector, the direction of the incident γ-ray photon can ideally be localized on the surface of a cone. The cone apex is the interaction position in the first detector and the half angle of the cone is equals to the scatter angle θ, which can be determined as:

$$\cos\theta = 1 - \frac{m_0 c^2}{E_0}\left(\frac{E_1}{E_0 - E_1}\right) = 1 + m_0 c^2 \left(\frac{1}{E_0} - \frac{1}{E_0 - E_1}\right), \qquad (2\text{-}11)$$

where $m_0 c^2$ is the rest-mass energy of the electron (511 keV), E_0 is the energy of the incident γ-ray photon, E_2 is the energy of the scattered γ-ray photon and θ is the scattering angle. The difference between E_0 and E_2 is the energy deposited in the recoil electron in the scatter detector and denoted as E_1. The location of incident γ-ray photons from a source point can be identified by intersection of multiple cones after a collection of many Compton scattering events as illustrated in Figure 1.7.

Therefore, the image quality depends on large numbers of γ-ray photons undergoing Compton scattering interactions in the scatter detector and subsequent detection in the second detector. The probability of Compton scattering per atom depends on the number of electrons available for scattering and the energy of incoming γ-ray photons. The probability for various types of interaction between a γ-ray photon and a specific material can be evaluated from the various interaction coefficients, which depends on the material atomic number Z and energy of incoming γ-ray photons E. The total linear attenuation coefficient μ is the probability of an interaction per unit distance in

a given material[69, 70]. It can be broken down into components due to the photoelectric effect, Compton scattering, Rayleigh scattering and pair production. The linear attenuation coefficient as a function of γ-ray energy for silicon is shown in Figure 2.17. Compton scattering is the dominant interaction type from 57keV to several MeV. When the γ-ray energy is below 57keV, photoelectric absorption is the most dominant interaction. When the γ-ray energy is above 15MeV, pair production is the principal interaction. The curve of linear attenuation for Compton scattering is fairly constant over the energy range for medical imaging. For the 364keV γ-ray, the linear attenuation coefficient for Compton scattering is about 0.22904 cm^{-1}, and for photoelectric absorption is 0.00104 cm^{-1}.
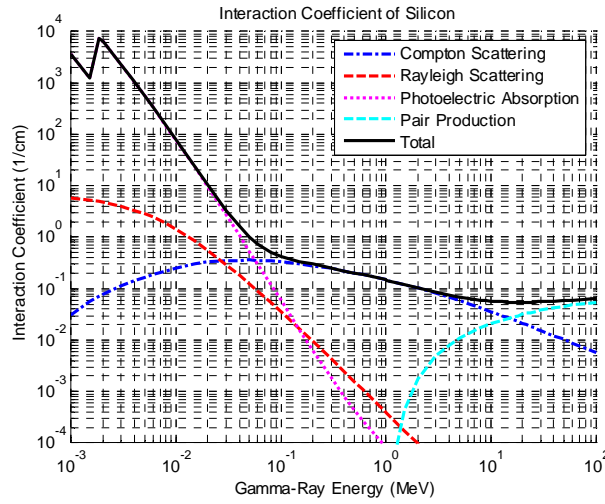
Figure2.17 Interaction coefficients for Gamma energy from 0.001MeV to 100MeV in Silicon.

After Compton scattering, the scattered γ-ray photon will be deflected an angle θ with respect to its original direction. Under the assumption that the interacting electron is free and at rest, the scattered photon angular distribution is predicted by the Klein-Nishina (KN) Differential Cross Section (DCS) formula[71]:

$$f_{KN}(\theta) = \frac{d\sigma}{d\Omega} = Zr_0^2 \left(\frac{1}{1+\alpha(1-\cos\theta)}\right)^2 \left(\frac{1+\cos^2\theta}{2}\right)\left(1+\frac{\alpha^2(1-\cos\theta)^2}{(1+\cos^2\theta)[1+\alpha(1-\cos\theta)]}\right), \quad (2\text{-}12)$$

where Z is the atomic number of the target atom, r_0 is the classical electron radius and

$\alpha = \dfrac{E_0}{m_0 c^2}$ [26]. The DCS formula for the differential of the in-plane scattering angle

could expressed as

40

$$f_{KN}(\theta) = \frac{d\sigma}{d\theta} = 2\pi \sin\theta \frac{d\sigma}{d\Omega},$$
(2-13)
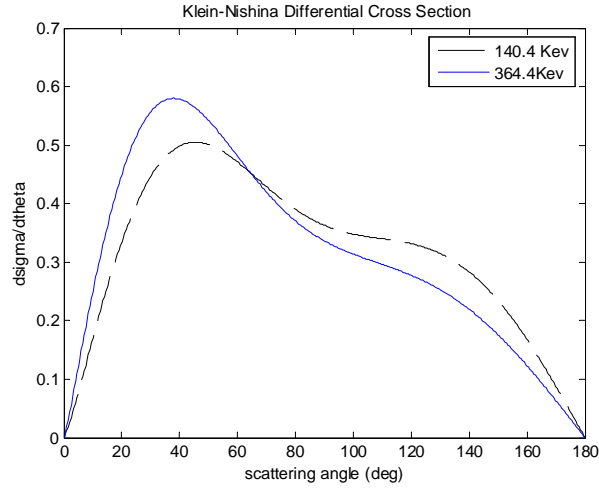
Figure 2.18 Klein-Nishina differential Cross Sections for Silicon as a function of scattering angle for incident γ-ray photons with energies of 140.4keV and 364.4keV.

According to Eq. (2-13), the normalized Klein-Nishina differential cross section as a function of scattering angle for incident γ-ray energies of 364.4keV and 140.4keV is illustrated in Figure 2.18. The angular distribution exhibits preferred forward scattering. Compared to the angular distribution at 140.4keV, the Compton scattering at 364.4keV has higher probability from 0 to 64 degrees.

2.3.2 Doppler Broadening for Silicon

The classic Klein-Nishina cross section formula for Compton scattering is based on the assumption that the target electron is free and at rest. However, in the actual scatter detector, especially for material with higher atomic number or incoming γ-ray photons with lower energy, atomic electron binding decreases the Compton scattering cross section given by the classic Klein-Nishina DCS formula. Furthermore, the kinetic energy and randomly directed momentum of the bound electrons cause the scattered γ-ray photons with a given scattering angle to have a narrow distribution of energies around the predicted energy defined by the scattering angle. This effect is denoted as Doppler broadening, which is governed by the momentum distribution of the target electrons in

the scatter detector. Doppler broadening increases with both increasing atomic number of the scatter material and with the scattering angle[72].

A more accurate description of Compton scattering cross section taking account of both atomic binding effects and Doppler broadening is based on the relativistic impulse approximation(IA), in which it is assumed that the energy transfer is large enough that binding effects for the electrons may be neglected and that the final state of the excited electron may be approximated by a plane-wave state[73]. According to the above assumption, Ribberfors derived a double differential Compton scattering cross section for un-polarized photons colliding with bound atomic electrons[74].

The Compton Double Differential Cross Section (DDCS) model can be expressed as

$$f_{IA}(\theta) = \frac{d\sigma_n}{d\Omega dE_2} = \frac{r_0^2}{2}(\frac{E_c E_2}{E_0^2})\frac{dp_z}{dE_2}(\frac{E_c}{E_0} + \frac{E_0}{E_c} - \sin^2\theta)J_n(p_z), \tag{2-14}$$

where

$$p_z = -137\frac{E_0 - E_2 - E_0 E_2(1 - \cos\theta)m_0 c^2}{qc}, \tag{2-15}$$

$$\frac{dp_z}{dE_2} = \frac{137 E_0}{(qc)E_c} - \frac{p_z(E_0 - E_2\cos\theta)}{(qc)^2}, \tag{2-16}$$

$$E_c = \frac{E_0}{1 + \frac{E_0}{m_0 c^2}(1 - \cos\theta)}, \tag{2-17}$$

and

$$qc = \sqrt{E_0^2 + E_2^2 - 2E_0 E_2 \cos\theta}, \tag{2-18}$$

where σ_n represents the Compton scattering cross section at sub-shell n; r_0 is the classical electron radius; E_0 and E_2 are energies of the incident and scattered γ-ray photons, respectively, and E_c is the Compton scattered photon energy for an electron at rest; m_0c^2 is the electron rest mass and is equal to 511 keV; θ is the in-plane scattering angle; p_z is normalized projection of the electron pre-collision momentum onto the photon scattering vector; $J_n(p_z)$ is the Compton profile of the n-th sub-shell. The electron momentum distribution is represented by the Compton profile, which depends on the element type, i.e. the atomic number, the sub-shell of the specified electron, and binding effects of neighboring atoms. The Compton profile of the n-th sub-shell electron is a function of p_z

and may be calculated from Hartree-Fock Compton profiles[75], in which a sub-shell based Compton profile is tabulated for all atomic elements. To take account of the additional momentum due to the atomic binding in the crystalline lattice, the measured Compton profile for silicon, germanium and diamond crystals is tabulated by Reed and Eisenberger[76].

The Compton Double Differential Cross Section formula expressed in Eq. (2-14) is just for an individual sub-shell electron. The overall Double Differential Cross Section is obtained taking account of the overall Compton profile, which is calculated from a weighted summation of all individual profiles of the sub-shell and number of electrons in the sub-shell. For crystalline Silicon, the Compton profile is obtained from measurement, which includes the total contribution from outer-shell valence electrons and inner-shell core electrons. The DDCS formula in Eq. 2-14 is differential for the solid angle Ω, in terms of in-plane scatter angle θ, the double differential cross section, which is also referred to as the joint-pdf, can be expressed as

$$f_{IA}(\theta) = \frac{d\sigma_n}{d\theta dE_2} = 2\pi \sin\theta \frac{d\sigma_n}{d\Omega dE_2} \cdot \qquad (2\text{-}19)$$

According to the Eq. 2-19, the Compton Double Differential Cross Section for a particular material for a given energy γ-ray photon can be discretized into a two-dimensional matrix, which is indexed by both scattering angle and energy of the scattered γ-ray photon or deposited energy in the recoil electron. From this two-dimensional matrix, in which each item depicts the probability of Compton Scattering at a specified scattering angle and specified energy deposited in the recoil electron, the uncertainty of scattering angle around an expected angle θ due Doppler broadening can be illustrated by a profile along the specified energy row in the two-dimensional matrix and this one-dimensional profile is indexed by angles.

The two-dimensional discretized double-differential cross sections, i.e. joint pdf, for crystalline silicon indexed by the scattering angle (vertical axis) and deposited energy (horizontal axis) are illustrated in Figure 2.19(a) and (b), in which the intensity is related to probability of Compton scattering at the specified recoil energy and scattering angle. The bright spots in the image represent high probability and central trace of those spots is corresponds to the Compton scattering cross section without the effect of Doppler

Broadening, whereas the darker spots bordering the central trace describe the degree of Doppler Broadening. Figure 2.19(a) is the joint PDF map for incident γ-ray photons with energy of 140.4keV, and (b) is for the 364.4keV γ-ray. Comparing these two images, the blurring at 140.4keV is much wider than at 364.4keV. This demonstrates that Doppler Broadening is more significant for the lower energy incident γ-ray photons for the same scatter material.

(A)   (B)
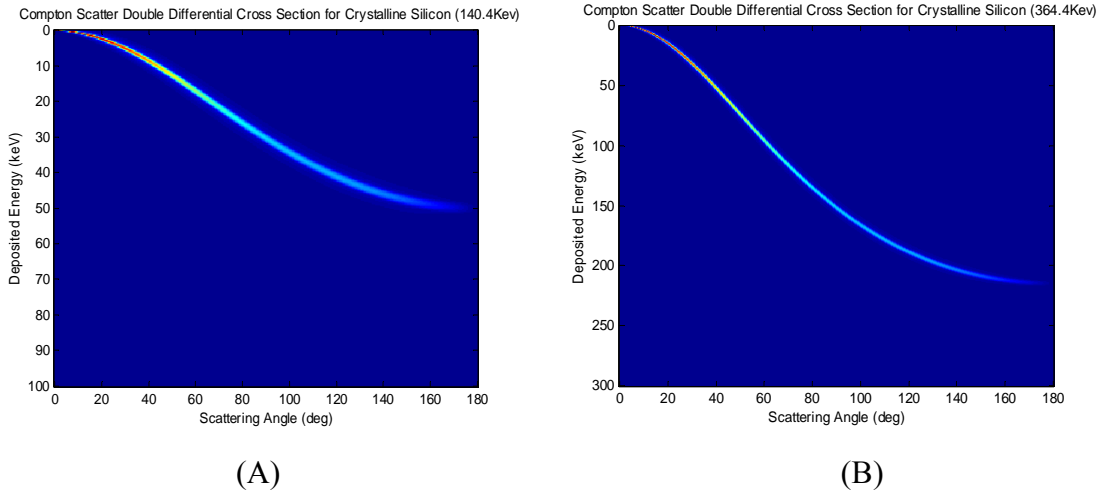
Figure 2.19 (A) The discretized Double-differential cross section for incident γ-ray photons with energy of 140.4keV for crystalline silicon. (B) The discretized Double-differential cross section for incident γ-ray photons with energy of 364.4keV for crystalline silicon.

(A)   (B)
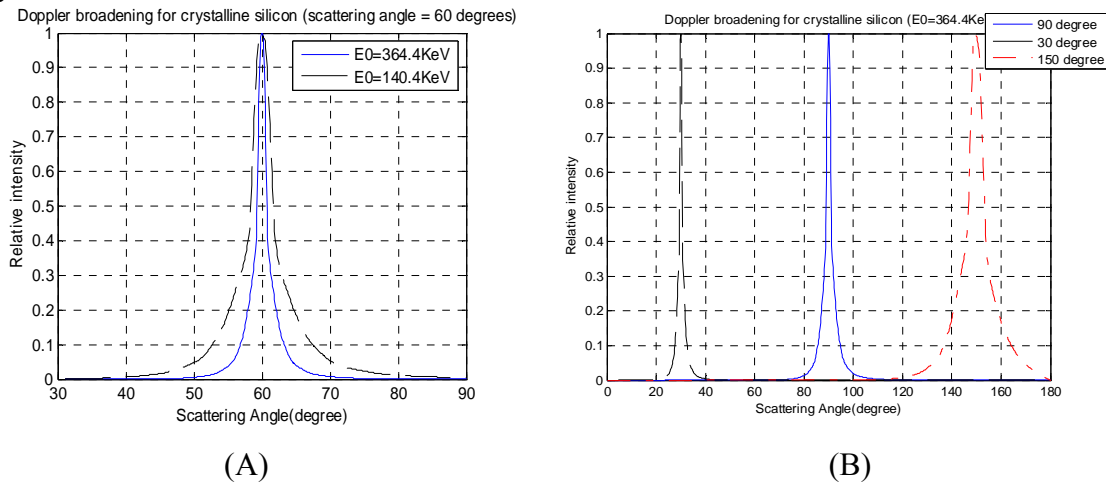
Figure 2.20 (A) Comparison of the normalized Doppler profiles of the joint pdf matrix for a deposited energy corresponding to the nominal scattering angle of 60° for 140.4keV and 364.4keV photons. (B) Comparison of the normalized Doppler profiles corresponding to nominal scattering angles at 30°, 90° and 150° for 364.4keV incident photons.

To further illustrate the angular uncertainty due to the effect of Doppler broadening for the 364.4keV and 140.4keV incident γ-ray photons, the normalized Doppler-broadening profiles corresponding to 60° scattering are displayed in Figure 2.20(a). A horizontal cross section of the joint PDF map for a given scattering material and incident gamma-ray energy gives the distribution of scattering angles for the corresponding deposited energy. A vertical cross section displays the probability distribution of deposited energy for the corresponding scattering angle. For the 60° scattering angle, the deposited recoil energies for 140.4keV and 364.4keV incident photons are 16.9keV and 95.8keV, respectively. For a silicon detector with perfect energy resolution, the angular uncertainty for 140.4keV incident photons is broader than for 364.4keV energy photons. The reason for this difference is that the binding energy of the electrons in Silicon is comparatively smaller and the momentum distribution is comparatively smaller for the higher energy photons and the Doppler broadening is reduced compared to that for low energy gamma rays. From Figure 2.20(b), which displays the Doppler profile of 364.4keV for different scattering angles, the effect of Doppler broadening is substantially reduced at small scattering angles.

2.3.3 Energy Resolution for Silicon Detector

In addition to Doppler broadening, another important factor impacting the energy uncertainty is the energy resolution of the scatter detector. According to the principle of Compton camera imaging, from the known incident γ-ray energy E_0 and measured deposited energy E_1, the scattering angle can be evaluated by Eq. 2-11. Thus, increasing energy uncertainty, due to both Doppler broadening and energy resolution, further increases uncertainty of scattering angle.

In general, the detector response to a mono-energetic radiation source is a Gaussian-shaped pulse height distribution, referred to as the detector energy resolution function. The energy resolution is defined as the FWHM of the full energy peak divided by the energy of the central peak. Small values of FWHM correspond to good resolution[26].

To illustrate the angular uncertainty due to the intrinsic energy resolution of the semiconductor silicon detector, a simple model is deduced to describe the Gaussian shape

energy spectrum and associated energy resolution. Two kinds of noise are considered in the model: one is the statistical noise, which results from the uncertainty in the number of electron-hole pairs generated by the recoil electron after a γ-ray photon interaction with this electron in the silicon detector, the other is the electronic noise, which is dependent on the series resistance, that includes electrical contact resistance, capacitance of the detector and leakage currents.

Assuming the actual deposited energy to the recoil electron is E_1 (keV) and a silicon detector needs a average ionization energy 3.62eV to generates an electron-hole pair, the mean number of generated electrons is

$$N = 1000 \times E_1 / 3.62 .$$ (2-20)

To derive the variance in N, the Fano factor, f, for silicon must be known. The Fano factor quantifies the departure of the observed statistical fluctuations in the number of charge carriers from pure Poisson statistics[26] and the Fano factor for silicon is 0.14. Therefore, statistical noise is given by,

$$\sigma^2_{statistical} = fN = \frac{1000 \times 0.14 \times E_1}{3.62} .$$ (2-21)

The electronic noise of the silicon detector is typically modeled as a zero-mean Gaussian distribution with variance $\sigma^2_{electronic}$. If the detector energy resolution (FWHM) due to the electronic noise is ΔE, then $\sigma^2_{electronic}$ is given by

$$\sigma^2_{electronic} = (\frac{1000 \times \Delta E}{3.62 \times 2.35})^2 ,$$ (2-22)

Assuming that electronic noise and statistical noise are independent, the total variance in units of (electrons)^2 is given as

$$\sigma^2_{total} = \sigma^2_{statistical} + \sigma^2_{electronic} .$$ (2-23)

Finally, the total variance with the units of (keV)^2 is given by

$$\sigma^2_{total} = \frac{3.62^2}{1000^2}(\sigma^2_{statistical} + \sigma^2_{electronic})$$

$$= \frac{3.62}{1000} \times 0.14 \times E_1 + (\frac{\Delta E}{2.35})^2$$ (2-24)

Therefore, the measured energy E_m for the case of deposited energy E_1 to the recoil electron is a Gaussian distribution, which is expressed as conditional probability density function $p(E_m|E_1)$ with mean at E_1 and variance is σ^2_{total}

$$p(E_m \mid E_1) = \frac{1}{\sqrt{2\pi\sigma^2_{total}}} e^{-\frac{1}{2}\frac{(E_m - E_1)^2}{\sigma^2_{total}}}, \qquad\qquad (2\text{-}25)$$

Therefore, the total energy uncertainty due to both Doppler broadening and energy resolution can be obtained by convolution of the energy resolution blur function Eq. (2-25) and the Doppler broadening uncertainty. A two-dimensional matrix describing the relationship between the scattering angle and measured recoil energy is also obtained by multiplying the two-dimensional double-differential cross sections with the energy resolution matrix indexed by the actual deposited energy E_1 and measured energy E_m, in which the value of each element is defined by Eq. (2-25).

Thus, the blurred joint-pdf considering both the detector energy resolution and Doppler broadening for the incident 364.4keV γ-ray photon is displayed in Figure 2.21, which is indexed by the scattering angle and measured recoil energy. The energy resolution of the crystalline silicon detector is 2keV (FWHM) for electronic noise.
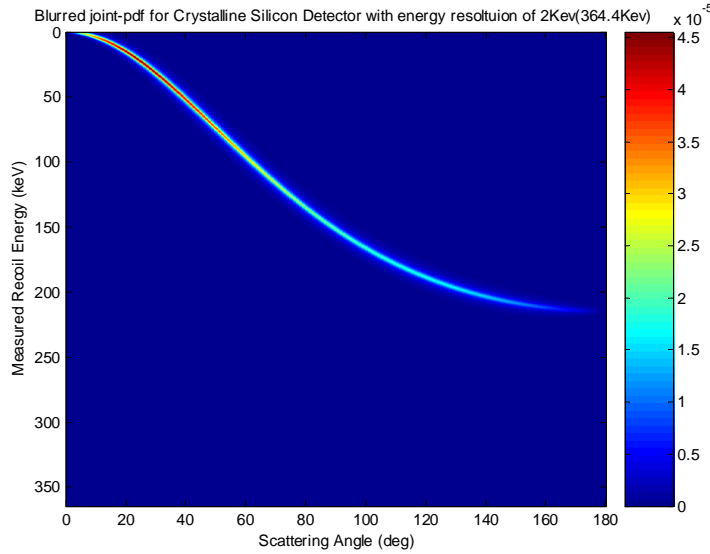
Figure 2.21 Blurred joint-pdf describing the relationship between the scattering angle and measured recoil energy for an incident photon with 364.4keV energy detected by a crystalline silicon detector with energy resolution of 2keV (FWHM).

A horizontal profile along a given measured energy from the blurred joint-pdf illustrates the angular uncertainty around that energy. For the incident photon with energy of 364.4keV, the angular uncertainty around a nominal scattering angle of 60° for the

crystalline silicon detector with energy resolution of 0keV, 1keV and 2keV (FWHM) for electronic noise is compared in Figure 2.22 (a). At this scattering angle, the angular uncertainty becomes worse with decreased energy resolution. In comparison to the angular uncertainty resulting from Doppler broadening, however, as the energy resolution is less than 1keV (FWHM), the angular uncertainty due to the energy resolution is not very significant. From Figure 2.23(b), which compares the angular uncertainties for the incident photons with energy of 364.4keV and 140.4keV around the scattering angle of 60°, the angular distribution for detecting lower energy photon becomes broader for the crystalline silicon detector with the same energy resolution of 1keV (FWHM).
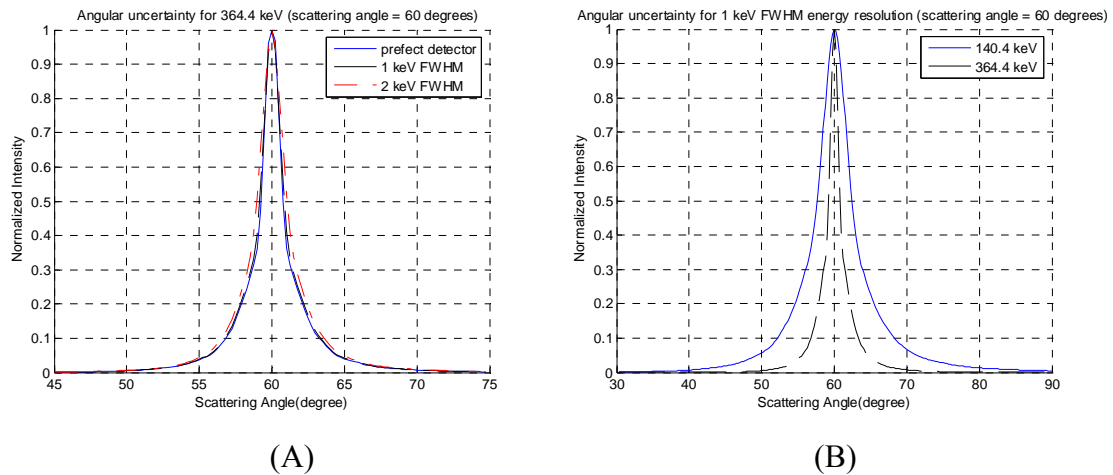
Figure 2.22 Comparison of Angular uncertainty around the nominal scattering angle of 60° for a crystalline silicon detector (A) For a perfect detector and detectors with energy resolution of 1keV and 2keV for incident photon with energy of 364.4keV (B) For the same detector with 1keV (FWHM) energy resolution and incident photons with energy of 140.4keV and 364.4keV.

In Figure 2.23, the angular resolution is illustrated in terms of degrees FWHM for 140keV (^{99m}Tc) and 364keV (^{131}I) incident γ-ray photons over a range of scattering angle from 0° to 180°, The combined effect of finite detector noise and Doppler broadening of a crystalline silicon detector with energy resolution from 0keV to 1keV. For the perfect detector with energy resolution of 0keV (FWHM) for both low and higher energy photons, the angular uncertainty is primarily affected by the Doppler broadening, which is smaller at small scattering angles. Compared to the angular resolution for low energy γ-rays, the scattered higher energy γ-ray photon has smaller angular uncertainty for a

detector with identical energy resolution. In the range of forward scattering from 20° to 90°, the effect of detector noise for detecting the higher energy photon (364.4keV) is small, and in this range, angular resolution is less than 2°.

ANGULAR RESOLUTION
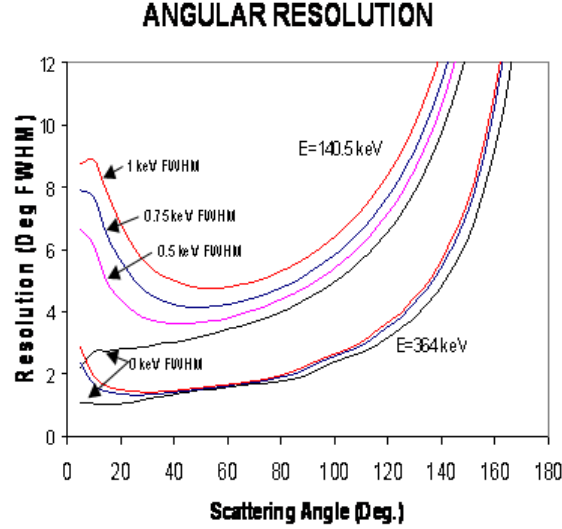
Figure 2.23 Angular resolutions (degrees FWHM) for 140keV (top) and 364keV (bottom) γ-ray photons scattered from crystalline silicon detector due to both Doppler broadening and energy uncertainty. The detector energy resolution is 0keV, 0.75keV and 1keV (FWHM).

2.3.4 System Geometry and Spatial Resolution for Compton Imaging System with Dual Planar Detectors.

For the Compton image reconstruction, the open angle of the backprojection cone can be calculated from the measured deposited energy in the scatter detector, and the axis of the cone is determined by the interaction positions in both detectors. Therefore, the angular uncertainty not only results from the energy resolution and Doppler broadening of the scatter detector, evaluated in the previous section, but also depends on system geometry and spatial resolution of both detectors. As studied by Ordonez[77], the angular resolution $\Delta\theta_g$ due to system geometry and spatial resolution of detectors depends upon the lateral and depth of interaction resolution of the scattering detector, expressed as [Δx_s, Δy_s, Δz_s]; the lateral and depth of interaction resolution of the absorption detector, denoted as [Δx_a, Δy_a, Δz_a]; the distance of the source from the interaction position in the

scatter detector R_1; and, the distance between two interaction positions in the scatter and absorption detector R_2.

Therefore, the overall angular uncertainty $\Delta\theta_g$ for the Compton imaging system is given as

$$(\Delta\theta_g)^2 = (\Delta\theta_{scatter})^2 + (\Delta\theta_{absorb})^2$$
$$= [(\Delta\theta_{scatter}^{\Delta x})^2 + (\Delta\theta_{scatter}^{\Delta y})^2 + (\Delta\theta_{scatter}^{\Delta y})^2] + [(\Delta\theta_{absorb}^{\Delta x})^2 + (\Delta\theta_{absorb}^{\Delta y})^2 + (\Delta\theta_{absorb}^{\Delta y})^2] \tag{2-26}$$

$$(\Delta\theta_{scatter})^2 = \frac{1}{R_1^2}\{[(\Delta x_s \cos\phi)^2(1+\frac{R_1}{R_2}\cos\theta)^2] + [(\Delta y_s \sin\phi)^2(1+\frac{R_1}{R_2}\cos\theta)^2] + [(\Delta z_s \frac{R_1}{R_2}\sin\theta)^2]\}, \tag{2-27}$$

$$(\Delta\theta_{absorb})^2 = \frac{1}{R_2^2}\{[(\Delta x_a \cos\phi\cos\theta)^2] + [(\Delta y_a \sin\phi\cos\theta)^2] + [(\Delta z_a \sin\theta)^2]\}, \tag{2-28}$$

where θ is the polar scatter angle and ϕ is the azimuthal scatter angle in spherical coordinates.

For the proposed Compton camera system, the first detector consists of one or more silicon pad detectors with a pixel size of 1.4mm×1.4mm×1mm. The second detector is an un-collimated NaI Anger camera head which has intrinsic lateral spatial resolution $\Delta a=\Delta x_a=\Delta y_a=4$mm. Depth of interaction in the crystal is unknown so depth spatial resolution Δz_a is assumed as 10mm, the thickness of NaI crystal. The two detectors are parallel to each other with an adjustable separation distance, and their centers are aligned on axis. If the distance between the centers of two detector is R_c, then $R_2=R_c/\cos\theta$. For this system, the formula of $\Delta\theta_g$ in Eq. 2-26,2-27 and 2-28 can be simplified as,

$$(\Delta\theta_{scatter})^2 = \frac{1}{R_2^2}\Delta^2 s[(\frac{R_2}{R_1}+\cos\theta)^2 + \sin^2\theta], \tag{2-29}$$

$$(\Delta\theta_{absorb})^2 = \frac{1}{R_2^2}[(\Delta a\cos\theta)^2 + (\Delta z_a\sin\theta)^2], \tag{2-30}$$

$$(\Delta\theta_g)^2 = (\Delta\theta_{scatter})^2 + (\Delta\theta_{absorb})^2$$
$$= \frac{1}{R_2^2}\{\Delta^2 s[(\frac{R_2}{R_1}+\cos\theta)^2 + \sin^2\theta] + [(\Delta a\cos\theta)^2 + (\Delta z_a\sin\theta)^2]\} \tag{2-31}$$
$$= \frac{\cos^2\theta}{R_c^2}\{\Delta^2 s[(\frac{R_c}{R_1\cos\theta}+\cos\theta)^2 + \sin^2\theta] + (\Delta a\cos\theta)^2 + (\Delta z_a\sin\theta)^2\}$$

Therefore, from Eq. 2-31, the angular resolution $\Delta\theta_g$ due to the system geometric and spatial resolution has an inverse relationship with the distance between the scatter

detector and the absorption detector. As this distance increases the angular uncertainty, $\Delta\theta_g$, decreases at the expense of sensitivity.

Figure 2.24 illustrates the geometric angular uncertainty $\Delta\theta_g$ for the prototype Compton camera as a function of distance R_c between the two detectors. Described in Figure 5-10, the point source is 10cm from the pixel first detector, the centers of source and two detectors lie along the same axis. As can be seen, the peak of the angular uncertainties for all R_c is around a scattering angle of 40°. With decreasing R_c, the angular uncertainties become worse. For R_c greater than 200mm, geometric angular uncertainties become fairly uniform over scattering angles from 0° to 180° and are less than 0.3 degree FWHM. Comparing the angular uncertainties due to the energy resolution and effect of Doppler broadening in Figure 2.26, the angular uncertainty $\Delta\theta_g$ could be neglected for detector separation above 50cm.
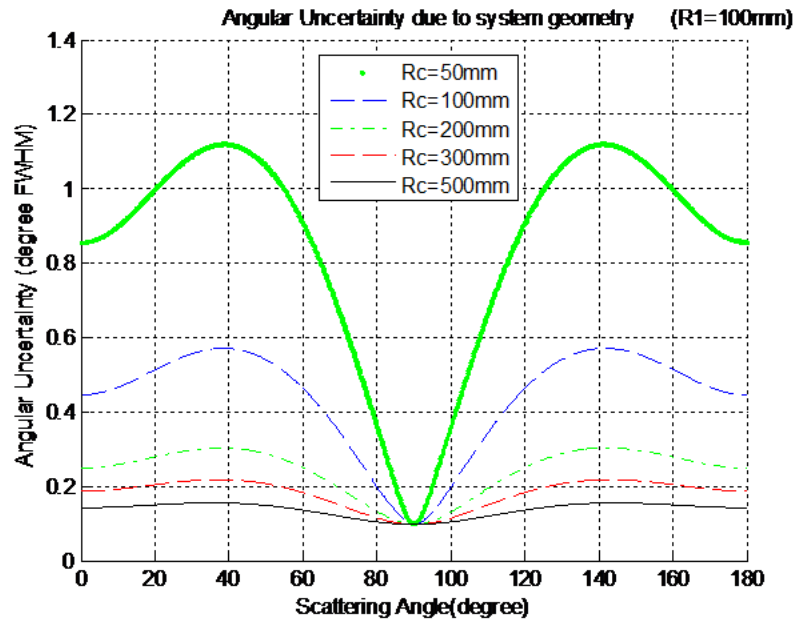
Figure 2.24 Angular uncertainty $\Delta\theta_g$ of the back-projected cone due to the system geometry of Compton system with parallel dual planar detectors. The distance between the sources to the scatter detector is 100mm and the separation between two detectors is 50mm, 100mm, 200mm, 300mm and 500mm, respectively.

Because the position uncertainty due to system geometry and detector spatial resolution may be expressed by

$$\Delta x_g = R \Delta \theta_g,$$ (2-32)

for a fixed distance between two detectors, the position uncertainty is primarily determined by the distance R from the image plane to the first detector. From Figure 2.25, which displays the position uncertainty for various R_1 and R_c equal to 150mm, as the distance of R_1 is deceased, the position uncertainty Δx_g become smaller.
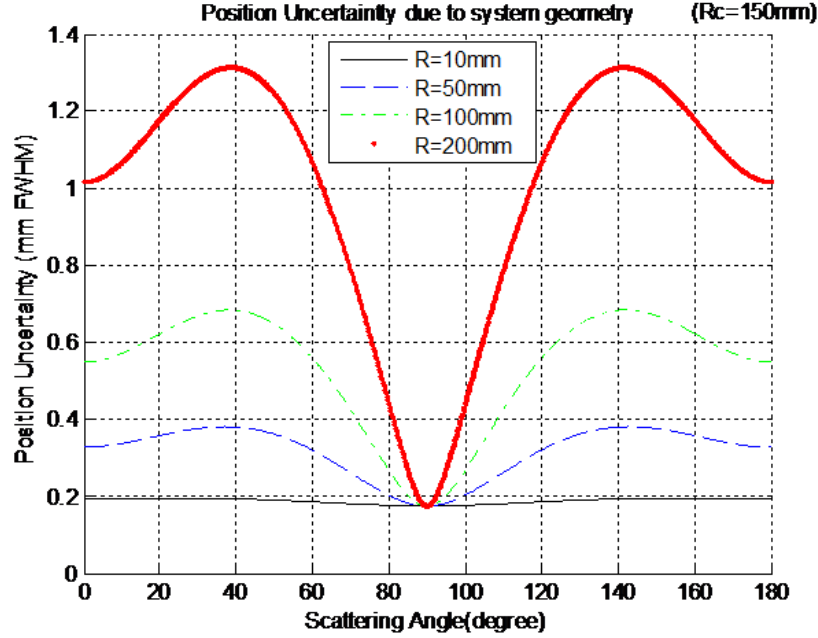
Figure 2.25 Position uncertainty of the back-projected cone due to the system geometry of the Compton system with parallel dual planar detectors. The distance between the scatter detector and absorption detector is 150 mm. the distance for the source or the real image plane to the scatter detector varies from 10mm to 200mm.

Theoretically, therefore, the image resolution due the system geometry and spatial resolution of both detectors can be improved. For the proposed Compton camera design, in which the spatial resolutions are fixed, when the object plane is close to the surface of the scatter detector and the absorption detector is located far away from the second detector, the uncertainty Δx_g can be ignored at the cost of reduced detection sensitivity. In this case, the overall position uncertainty is primary determined by the energy uncertainty of the scatter detector due to the energy resolution and Doppler Broadening.

2.3.5 Detection Sensitivity

The detection efficiency or sensitivity is defined as the ratio of the number of accepted detected events to the total number of emitted gamma-rays from the source. The sensitivity is determined by the energy of the photons, system geometry and detector martial. Interaction probabilities, energy measurements, intervals between emitted photons etc are random events, thus, it is very difficult to estimate by a simple calculation. Therefore, the estimated detection sensitivity is evaluated by the Geant4 Monte Carlo Simulation. For the conventional Anger camera with HEGP collimator, the effective events are the detected events in the energy window from 320keV to 400keV. The effective Compton events are the detected coincidence events with only one scatter in the first detector. As displayed in Figure 5.17, the size of first detector is 22.4x44.8x10mm and the size of second detector is 508x380x10mm. The point source is located 10cm from the surface of the detector, and for the Compton camera, the distance of two detectors is 10cm. As listed in Table 2.3, the Compton camera has higher sensitivity by a factor of ~28 for detecting 364.4.keV photons emitted from I^{131}.

Table 2.3   Sensitivity Comparison for ^{131}I Detection

	Anger camera with HEGP collimator	
Efficiency	**Total Emitted Particles**	**Accepted Event**
1.02E-4	355229093	42374
	Compton Imaging System with Si-NaI Dual Planar detectors	
3.4E-3	58235338	196226
Efficiency Ratio	**3.4E-3/1.22E-4=27**	

Unlike the Anger camera with parallel hole collimation, for a given distance from source to detector, the sensitivity of Compton imaging system is not uniform. Using the system model of Compton imaging system presented in Section 2.2 and Chapter 4, the histogram of calculated sensitivities is displayed in Figure 2.26 for a 65x0.31cm by 65x0.31cm object located at 10cm from the surface of the silicon detector. The maximum sensitivity for the center point is around 3.45E-3, and the average sensitivity is around 2.34E-3.
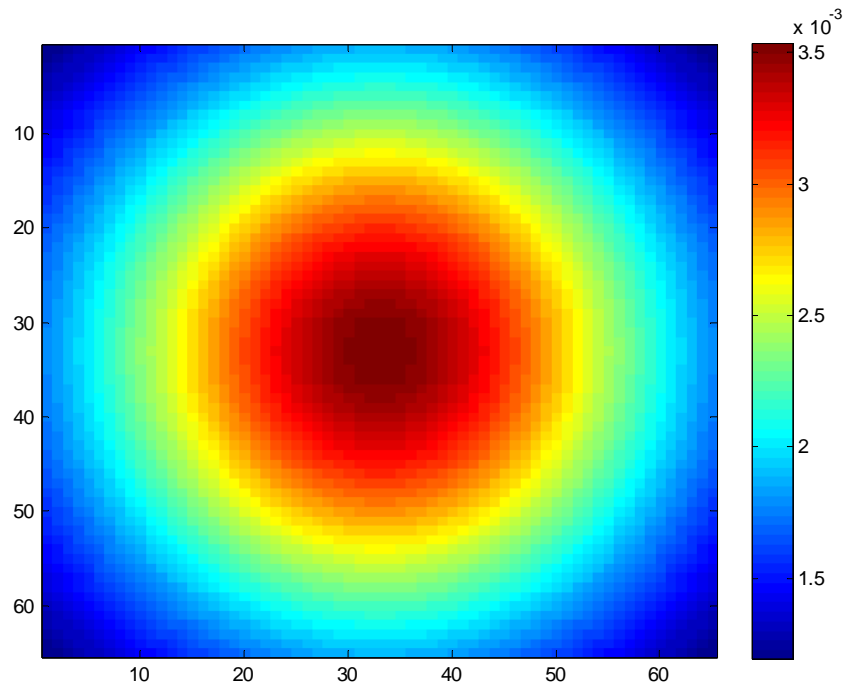
Figure 2.26 Calculated detection sensitivity for the proposed Compton imaging system. The source plane is located at 10cm from the surface of the first detector. The object plane is divided into 65 by 65 pixels, and each pixel is 0.31 by 0.31 cm.

CHAPTER 3

Practical Methods to Calculate Fisher Information and Estimate Modified Uniform Cramer-Rao Bound

This chapter illustrates a statistical method, the modified uniform Cramer-Rao bound (M-UCRB), to evaluate and analyze the imaging performance of a Compton imaging system and an Anger Camera with HEGP collimator. To realize this method practically, algorithms are introduced for calculating the Fisher information matrix (FIM) by Monte Carlo Integration (MCI), and for estimating M-UCRB using the fast Fourier transform (FFT). Finally, Monte Carlo simulation system of a Compton imaging system and conventionally collimated Anger camera are studied.

3.1 Introduction

Beyond a qualitative analysis of an imaging system, powerful mathematical methods are required to quantitatively compare task-specific performance of different imaging systems. Tasks may include tumor detection, volume estimation of an organ or tumor, or quantification of tracer uptake in an organ or tumor. All these task-based evaluations can finally be related to physical characteristics of the images and imaging systems, such as achievable spatial resolution, signal to noise ratio or detection sensitivity and intrinsic spatial resolution. Thus, quantitative methods are required to determine whether and how much a new imaging system outperforms the existing system for which kinds of imaging tasks.

Historically, several methods have been developed for performance evaluation of the lesion detection task. The structure accuracy measure[78] estimates image performance by calculating the differences of intensity between the reconstructed image and the imaged phantom. The mathematical human observer[79] evaluates the imaging

performance. However, most methods based on lesion detection tasks ineluctably depend on the image reconstruction algorithm.

Another evaluation method is based on performance in a parameter estimation task in the absence of a well characterized clinical task. The precision of parameter estimation can be measured by the mean square error (MSE) which is the sum of the estimation variance and square of bias. Variance is fluctuation of estimated parameter due to noise, which depends on both imaging system and image reconstruction. Image bias is the error between the mean estimated image and the original object. Bias is strongly related to image resolution. To decrease the value of MSE, one can either reduce the variance or bias. A regularized image estimator enforces a tradeoff between the bias and variance. Decreasing noise will also reduce image spatial resolution. To separate the influence of a particular reconstruction algorithm from the limitations imposed by the imaging system on image resolution and variance, the family of Cramer-Rao lower bounds provide useful figure of merit for comparing performance among different imaging systems, in terms of a reconstruction-algorithm-independent theoretical limit on the variance and resolution tradeoff in reconstructed images.

The classical Cramer-Rao lower bound (CRLB)[80, 81] shows that the total variance of any unbiased estimator is bounded by the inverse of the Fisher information. This bound is independent of the estimation or reconstruction method, and only relies on the likelihood function relating the measurements to the unknown parameters. As the measurements are independent identically distributed, the maximum likelihood estimator can asymptotically approach the CRLB. Since estimators with regularization methods are normally biased, the variance is bounded by the biased CRLB, which depends on the bias gradient vector, i.e., the derivative of bias, instead of bias. The drawback of this biased form of the bound is that it is only a lower-bound among estimators having the same bias-gradient.

Therefore, to evaluate biased estimation performance of an imaging system and quantify the tradeoff between bias and variance, the uniform Cramer-Rao bound (UCRB) proposed by Hero, Fessler and Usman[82] has been used. The UCRB defines the lowest achievable variance for a bias gradient whose length is less than a pre-specified constant tolerance δ. An important aspect is that the limiting performance defined by the bound

can be asymptotically achieved by an appropriate image reconstruction estimator with the selected bias-gradient length. According to the UCRB, the limiting standard deviation (σ) is plotted as a function of δ, on the "sigma-delta" plane to evaluate the tradeoff of noise and the "potential for bias". The curve divides the plane into achievable and unachievable performance regions which bound the resolution-noise performance of any estimator. The performance evaluated is based on the intrinsic quality of the imaging system itself and not the reconstruction algorithm. To compare two different imaging systems using the "sigma-delta" plane, the system with the lower curve will have the better imaging performance with lower variance at a given bias gradient norm.

Since the bias is the difference between the local impulse response function (LIR) and an ideal impulse response, a problem with the UCRB is that different shaped point response function with the same FWHM can have the same bias gradient norm. Therefore, the bias-gradient norm used in UCRB makes it difficult to compare performance of different imaging systems effectively by a measure of reconstructed image spatial resolution [83]. To rectify this issue, the M-UCRB was proposed to compare the minimum achievable variance in reconstructed images for a given target point spread function[1]. Compared with the original UCRB, which is based on the constraint on the bias gradient length, the modified UCRB is determined by pre-specifying a desired shape response function and allows that response to be achieved within a specified tolerance rather than exactly. If the Euclidean norm is used to quantify this difference, the mean-estimator gradient is the same as the local impulse response in the reconstructed image. Therefore, it is more meaningful to use the M-UCRB to evaluate imaging performance of different imaging systems, such as the Compton camera and the conventional Anger Camera with collimator, by comparing the image variance at the same target spatial resolution.

Calculation of M-UCRB by conventional algorithms is computationally expensive as it requires inversion of an n×n FIM, where n is the total number of image pixels. Direct inversion for bound calculation require $O(n^3)$ flops. Although an inversion algorithm based on conjugate gradient approaches may be exploited[84], but for a 65×65×65 three dimensional image, the computation speed and memory requirements are

still intractable. Under the assumption of spatial shift-invariance, a one column FIM can be generated by MCI and the bound calculation speeded up by FFT.

3.2 Modified Uniform Cramer-Rao Bound and Fisher Information Matrix

3.2.1 Mean Square Error

The image reconstruction for both a Compton scattering camera and conventional Anger camera with collimator are considered as a parameter estimation problem. The continuous object to be imaged is represented by discrete pixels. The pixel intensities are treated as unknown and non-random parameters and expressed by a column vector, $\underline{\theta} = [\theta_1, \theta_2, \ldots, \theta_p]^T$. The noisy measurement data $\underline{Y}$ is a vector of random variables and depends on a probability relationship with $\underline{\theta}$ expressed as a conditional density function $p_{\underline{Y}}(\underline{y}|\underline{\theta})$. The scalar estimate of the j$^{\text{th}}$ pixel intensity from $\underline{Y}$ is represented as $\hat{\theta}_j$.

One of the criteria for evaluating the precision of a given estimator is MSE, and is given by

$$
\begin{aligned}
MSE_{\underline{\theta}}(\hat{\theta}_j) &= E_{\underline{\theta}}\left[\left(\hat{\theta}_j - \theta_j\right)^2\right] \\
&= \left(E_{\underline{\theta}}\left[\hat{\theta}_j^{\,2}\right] - E_{\underline{\theta}}^2\left[\theta_j\right]\right) + \left(E_{\underline{\theta}}\left[\hat{\theta}_j\right] - \theta_j\right)^2, \\
&= \sigma_{\underline{\theta}}^2\left(\hat{\theta}_j\right) + b_{\underline{\theta}}^2\left(\hat{\theta}_j\right)
\end{aligned}
\tag{3-1}
$$

where $E_{\underline{\theta}}(\hat{\theta}_j)$ represents a mean value or an expectation value of the estimated parameter; $b_{\underline{\theta}}(\hat{\theta}_j)$ is the bias in the estimation, which measures the error or mismatch between the mean of the estimated and true values; and, $\sigma_{\underline{\theta}}^2(\hat{\theta}_j)$ represents the variance of the estimated value which reflects the degree of statistical fluctuation due to noise in the measured data $\underline{Y}$.

A parameter estimation algorithm attempts to minimize the value of MSE by decreasing the variance and bias simultaneously. However, since image reconstruction is an ill-posed inverse problem; there is a trade-off between the variance and bias. For example, a low variance estimator or high spatial frequency filter will increase the overall

bias, i.e., degrades the reconstructed spatial resolution. The trade-off relationship is plotted as a curve in the variance-bias plane to evaluate the performance of each estimator. Given an object to be imaged and a defined imaging system, therefore, the best possible performance, independent of reconstruction algorithm, may be calculated by the various CRB techniques. The best algorithm is the one that has a bias-variance curve closest to the bound.

3.2.2 The Classical and Biased Cramer-Rao Bound

The classical Cramer-Rao Bound[85], or Cramer-Rao inequality is a method to determine the minimum achievable variance of an unbiased estimator $\hat{\theta}_j$ of a deterministic parameter. Given the n×n positive definite FIM of the $F_Y(\underline{\theta})$ of measurement $\underline{Y}$, the variance of an unbiased estimator $\hat{\theta}_j$ is bounded below by the jth diagonal element of $F_Y^{-1}(\underline{\theta})$, and given by,

$$Var\left(\hat{\theta}_j\right) = \sigma_{\underline{\theta}}^2\left(\hat{\theta}_j\right) \geq \underline{e}_j^T F_Y^{-1}(\underline{\theta})\underline{e}_j, \tag{3-2}$$

where, $F_Y^{-1}(\underline{\theta})$ is the inverse of the Fisher information matrix and

$$\begin{aligned}
F_{\underline{Y}} &= F_{\underline{Y}}(\underline{\theta}) \\
&= -E_{\underline{\theta}}\left\{\nabla_{\underline{\theta}} \log p_{\underline{Y}}\left(\underline{Y}|\underline{\theta}\right)\right][\nabla_{\underline{\theta}} \log p_{\underline{Y}}\left(\underline{Y}|\underline{\theta}\right)]^T\right\}, \\
&= -E\left\{\frac{\partial^2}{\partial \theta^2} \log p_{\underline{Y}}\left(\underline{Y}|\underline{\theta}\right)\right\}
\end{aligned} \tag{3-3}$$

and $\underline{e}_j$ is a p-element zero vector except for the one at jth position $[0,\ldots,0,1_j,0,\ldots0]^T$.

However, since most image reconstruction estimation algorithms are biased, the classic Cramer-Rao bound is not applicable. For the biased estimator $\hat{\theta}_j$, the biased Cramer-Rao bound[80] is given as,

$$Var\left(\hat{\theta}_j\right) \geq [\nabla_{\underline{\theta}} m_{\underline{\theta}}\left(\hat{\theta}_j\right)]^T F_{\underline{Y}}^{-1}[\nabla_{\underline{\theta}} m_{\underline{\theta}}\left(\hat{\theta}_j\right)], \tag{3-4}$$

where the $\nabla_{\underline{\theta}} m_{\underline{\theta}}\left(\hat{\theta}_j\right)$ is the gradient of the estimator mean-response function, also named as "mean-gradient". Because the gradient of the estimator bias-response function $\nabla_{\underline{\theta}} b_{\underline{\theta}}\left(\hat{\theta}_j\right)$ can be expressed as $\nabla_{\underline{\theta}} m_{\underline{\theta}}\left(\hat{\theta}_j\right) = \underline{e}_j + \nabla_{\underline{\theta}} b_{\underline{\theta}}\left(\hat{\theta}_j\right)$, the biased Cramer-Rao bound in terms of "bias-gradient" $\nabla_{\underline{\theta}} b_{\underline{\theta}}\left(\hat{\theta}_j\right)$ is

$$Var\left(\hat{\theta}_j\right) \ge [\underline{e}_j + \nabla_{\underline{\theta}} b_{\underline{\theta}}\left(\hat{\theta}_j\right)]^T F_{\underline{Y}}^{-1} [\underline{e}_j + \nabla_{\underline{\theta}} b_{\underline{\theta}}\left(\hat{\theta}_j\right)] . \qquad (3\text{-}5)$$

The above classic Cramer-Rao bound for a biased estimator only applies to estimators with a given bias-gradient. It cannot be used for different estimators unless they exhibit the same bias-gradient. Therefore, the norm or length of bias-gradient or mean-gradient, which is a measure of the overall bias or mean respectively, is introduced to the Cramer-Rao bound calculation.

3.2.3 Uniform Cramer-Rao Bound

The bias gradient vector $\nabla_{\underline{\theta}} b_{\underline{\theta}}\left(\hat{\theta}_j\right)$ describes sensitivity or fluctuant potential of the bias in the jth pixel estimate to perturbations in the true parameter values, which is defined by a vector of partial derivatives of overall bias:

$$\nabla_{\underline{\theta}} b_{\underline{\theta}}\left(\hat{\theta}_j\right) = \left[\frac{\partial b_{\underline{\theta}}\left(\hat{\theta}_j\right)}{\partial \theta_1}, \frac{\partial b_{\underline{\theta}}\left(\hat{\theta}_j\right)}{\partial \theta_2}, \cdots , \frac{\partial b_{\underline{\theta}}\left(\hat{\theta}_j\right)}{\partial \theta_p} \right], \qquad (3\text{-}6)$$

$$= \nabla_{\underline{\theta}} E_{\underline{\theta}}\left(\hat{\theta}_j\right) - \underline{e}_j$$

Therefore, the bias gradient is the mean gradient, which is same as the local impulse response function under certain conditions[82], minus one at the jth position. A large value at the specific position m in the bias gradient vector indicates the estimator strongly coupled with perturbation of θ_m. Thus, the norm or length of the bias gradient $\left\| \nabla_{\underline{\theta}} b_{\underline{\theta}}\left(\hat{\theta}_j\right) \right\|$ is a measure of the sensitivity of the estimator $\hat{\theta}_j$ to the perturbation of all the remaining pixels.

Hero[82] introduces a UCRB on the variance of a given signal parameter estimator for a non-singular FIM $F_Y(\underline{\theta})$, by which the restriction of a lower bound requiring a fixed bias gradient is removed and a lower bound on variance is calculated as a function of bias gradient norm, and this bias gradient norm is equal to or less than pre-specified thresholds. Therefore, the uniform Cramer-Rao bound can compare performance of different imaging systems in terms of variance-bias gradient norm curves for all biased estimators whose norm of the bias gradient is less than a small pre-specified maximal tolerable constant δ :

$$\left\| \nabla_{\underline{\theta}} b_{\underline{\theta}}\left(\hat{\theta}_j\right) \right\|^2 \le \delta^2 < 1 , \qquad (3\text{-}7)$$

According to [86], the UCRB defined as: when an estimator $\hat{\theta}_j$ with bias $b_{\underline{\theta}}(\hat{\theta}_j)$ and norm of its bias gradient vector is less than or equal to $\delta \in [0,1)$, then the variance of $\hat{\theta}_j$ satisfies the lower bound:

$$\text{var}_{\underline{\theta}}(\hat{\theta}_j) \geq B(\underline{\theta}, \delta), \tag{3-8}$$

where $B(\underline{\theta}, \delta)$ is equal to

$$B(\underline{\theta}, \delta) = [\underline{d}_{\min} + \underline{e}_j]^T F_Y^{-1} [\underline{d}_{\min} + \underline{e}_j], \tag{3-9}$$

where $\underline{d}_{\min}$ is optimal bias-gradient vector that minimizes the biased Cramer-Rao bound on overall bias gradient vector and given as,

$$\underline{d}_{\min} = -[I + \lambda F_Y]^{-1} \underline{e}_j. \tag{3-10}$$

In the above equation, F_Y is Fisher information matrix and λ is the Lagrange multiplier given by the unique positive solution determined by the following equation involving the monotonically decreasing and convex function:

$$g(\lambda) = \underline{d}_{\min}^T \underline{d}_{\min} = \delta^2 \qquad g(\lambda) \in [0,1] \text{ and } \lambda \geq 0. \tag{3-11}$$

Therefore, bias-variance tradeoff curves are located in "sigma-delta" plane. Each curve divides the plane into achievable and unachievable performance regions which bounds the resolution-noise performance of any estimation algorithms. The bound curve is based on the intrinsic quality of the imaging system itself and not on the specific estimation algorithms. The imaging system with lower curve has better performance than the system with the upper curve. However, the variance-bias tradeoff curve only describes the trend that the limiting variance decreases with the increase norm of bias gradient. The UCRB does not reflect the direct relationship between the limiting variance with the specific local impulse response. Systems with identical bias-gradient norm can have very different impulse response shapes, and different type of local impulse response shapes can have the same bound.

3.2.4   Modified Uniform Cramer-Rao Bound

The M-UCRB is proposed in [87] and was used to evaluate the multiple pinhole small animal SPECT by Meng and Clinthorne [1] by a list of desired or target point

response functions. The M-UCRB impose a constraint on the mean gradient of the estimator $\nabla_{\underline{\theta}} m_{\underline{\theta}}(\hat{\theta}_j)$, is given as:

$$\nabla_{\underline{\theta}} m_{\underline{\theta}}(\hat{\theta}_j) = \nabla_{\underline{\theta}} b_{\underline{\theta}}(\hat{\theta}_j) + \underline{e}_j$$
$$= \left[\frac{\partial E_{\underline{\theta}}(\hat{\theta}_j)}{\partial \theta_1}, \frac{\partial E_{\underline{\theta}}(\hat{\theta}_j)}{\partial \theta_2}, \cdots, \frac{\partial E_{\underline{\theta}}(\hat{\theta}_j)}{\partial \theta_p} \right], \tag{3-12}$$

The mean gradient describes the sensitivity of a single reconstructed pixel to the perturbations in true parameter values. Under the conditions[88], that the mean of the estimator is $E_{\underline{\theta}}[\hat{\underline{\theta}}] = L\hat{\underline{\theta}}$ and the matrix L is approximately symmetric, the mean gradient of the jth estimator is close or equal to the local impulse response of the jth pixel. This specifies the influence of a perturbation of a single source pixel on all other true parameter values.

By using the M-UCRB, the Euclidean norm of error vector between the desired mean gradient vector *f*, i.e. the target local impulse response and the actual mean gradient *g* is less than a small pre-specified small tolerance *δ*, is given as:

$$\| g - f \|_c \leq \delta \quad \text{and} \quad \delta = \| \lambda [F_Y + \lambda I]^{-1} \cdot f \|, \tag{3-13}$$

From the biased Cramer-Rao bound, that is

$$Var(\hat{\theta}_j) \geq [\nabla_{\underline{\theta}} E_{\underline{\theta}}(\hat{\theta}_j)]^T F_Y^{-1} [\nabla_{\underline{\theta}} E_{\underline{\theta}}(\hat{\theta}_j)],$$
$$= g^T \cdot F_Y^{-1} \cdot g \tag{3-14}$$

The optimal actual mean gradient is equal to

$$g_{optimal} = \arg \min_{\|g - f\| \leq \delta} \{ g^T \cdot F_Y^{-1} \cdot g \},$$
$$= [F + \lambda I]^{-1} \cdot F \cdot f \tag{3-15}$$

Thus, the M-UCRB can be derived as

$$Var(\hat{\theta}_j) = \sigma^2 \geq f^T \cdot [F_Y + \lambda I]^{-1} \cdot F_Y \cdot [F_Y + \lambda I]^{-1} f, \tag{3-16}$$

where F_Y is the Fisher information Matrix, λ is a small positive scalar and I is the identity matrix with same size as F_Y

Therefore, the lower bound of variance imposed by the target response function with desired spatial resolution can be calculated. It is meaningful to use the M-UCRB to evaluate imaging performance of different imaging systems, such as the Compton scattering based gamma-ray camera and the conventional Anger Camera with HEGP collimator, by comparing the difference of variance in the image at the same LIR.

3.3 Monte Carlo Calculation of FIM and FFT estimation of M-UCRB

Application of the M-UCRB suffers from the computation and memory requirements for calculating the Cramer-Rao bound and for calculating the FIM for high dimensional images. For both the Compton imaging system and the Anger Camera with collimator, the detection process is described by Poisson statistics.

$$\underline{Y} \sim Possion(\ \Lambda A \underline{\theta})\ , \tag{3-17}$$

where A is the D×P system response matrix, the element is denoted as a_{ij} or $p_{\underline{Y}}(\underline{y}|\underline{\theta})$, D is the total number of detector elements, P is the total number of image pixels, Λ is the mean total number of events in the measurement interval, Y =[Y1, … ,YD] is a vector of the projection measurements, and $\underline{\theta}$ =[θ_1, … , θ_P]^T is the parameterized image space vector, and normalized as

$$\sum_{i=1}^{D} \sum_{j=1}^{P} a_{ij} \theta_j = 1\ , \tag{3-18}$$

Therefore, the Fisher information matrix has the following form[82]:

$$F_{\underline{Y}}(\underline{\theta}) = \Lambda A^{T}[\ diag\ (A \underline{\theta})]^{-1} A\ , \tag{3-19}$$

Obviously, for a high dimensional or complex medical imaging system with a huge system response matrix, directly calculating and inverting the non-sparse FIM by the above equations is impracticable in terms of both computation time and memory requirements. Therefore, an alternative method is required to reduce the computation complexity and size of memory required to calculate the FIM.

The size of the system matrix for a conventional Anger camera does not present a problem. However, for the Compton camera, the total required memory space is around 100 gigabytes if each element requires one byte of memory and this system matrix is not sparse in our application. Although, a symmetric system geometry, in which the center of the first and second detectors lie on the same axis, and diagonal interpolation is used will help to decrease the system matrix size by a factor of 20.[89] However, memory space requirement is also a serious issue for high dimensional images when attempting to calculate the Fisher information matrix using a non-parallel computation system.

Furthermore, calculating the M-UCRB requires calculation of the inverse of the matrix $[F_Y + \lambda I]$. For a n^2 pixel image, the size of the Fisher information matrix has n^4

elements and the direct inversion of the above matrix would require about n^6 floating point operations. Generally, a conjugate gradient algorithm [84] is employed to calculate inversion recursively. In the limit, it requires n^2 ops to completely solve problem and obtain acceptable convergence. To further improve the computational efficiency, Monte Carlo integration and fast Fourier transform-based inversion have been used for these calculations.

3.3.1   Monte Carlo Integration for Calculation of the Fisher Information Matrix

According to the definition of the Fisher Information Matrix, given the observed random variable $\underline{Y}$ and the conditional probability density function $p_{\underline{Y}}(\underline{Y}|\underline{\theta})$, which is dependent on a column vector of unknown, nonrandom parameters $\underline{\theta}$ with p elements, the p×p standard Fisher information matrix $F_{\underline{Y}}$ is defined in (3-3)

To reduce the computational complexity and size of required memory to calculate the Fisher information matrix, an alternative method to evaluate every element in the Fisher information matrix is introduced [90]. Given Λ independent identical distributed list-mode measured samples of $\underline{Y}$, the expectation of the observed Fisher information matrix   is defined as:

$$
\begin{aligned}
F_{\Lambda}(\underline{\theta})_{ij} &= \Lambda \cdot F_{1}(\underline{\theta})_{ij} \\
&= \Lambda \cdot \left\langle \frac{\partial^2 \log p(Y|\underline{\theta})}{\partial \theta_i \partial \theta_j} \right\rangle_{Y|\underline{\theta}} ,
\end{aligned}
\tag{3-20}
$$

where $\left\langle \dfrac{\partial^2 \log p(Y|\underline{\theta})}{\partial \theta_i \partial \theta_j} \right\rangle_{Y|\underline{\theta}}$ is the mean of the function of $\dfrac{\partial^2 \log p(Y|\underline{\theta})}{\partial \theta_i \partial \theta_j}$ (3-21)

According to the properties of the observed Fisher information matrix,

$$
F_{\Lambda}(\underline{\theta})_{ij} = \Lambda \cdot F_{1}(\underline{\theta})_{ij} ,
\tag{3-22}
$$

which means the value of the element in the Fisher information matrix for a sample of Λ independent identical distributed observations is equivalent to Λ times the value of this element in the Fisher information matrix for a single observation.

Therefore, the average value of one element in the observed Fisher information matrix may be calculated by a Monte Carlo Integration instead of using the multidimensional integration. This method has the considerable advantage that the exact

imaging geometries are straightforward to evaluate as long as (1) an appropriate Monte Carlo model exists, and (2) given an event in the measurement space, corresponding transition probabilities are available for "back-projection". According to the basic theorem of Monte Carlo Integration[91], the mean value of a function f can be approximated by discrete integration and given as,

$$\langle f \rangle \approx \frac{1}{N} \sum_{i=1}^{N} f(y_i) \, , \qquad (3\text{-}23)$$

where $y_i\,(i = 1 \ldots N)$ are actual measured or simulated sampled events for Monte Carlo calculation.

Benefiting from the Monte Carlo integration, therefore, if the FIM corresponds to a desired mean number of detected events Λ, the estimated value of the one element in the observed FIM from N detected or simulated events is defined as,

$$F_\Lambda(\underline{\theta})_{ij} = \Lambda \cdot F_1(\underline{\theta})_{ij}$$

$$\approx \frac{\Lambda}{N} \cdot \sum_{l=1}^{N} \frac{p(Y_l / i)\, p(Y_l / j)}{\left(\sum_{n=1}^{M} p(Y_l / n) \cdot \theta_n \right)^2} \, , \qquad (3\text{-}24)$$

In the above equation, the conditional probability density $p(Y_l / i)$ is the probability that an event generated in source bin *i* leads to a measurement Y_l by the imaging system; where θ_n is the relative intensity for the nth source bin; M is the number of source bins; N is the number of sampled events for Monte Carlo integration; and, Λ is the number of actual events in the period of evaluation for the specific task.

Clearly, the calculation of the observed Fisher information Matrix by Monte Carlo Integration not only decreases the computational complexity, since only $M \times N$ floating point calculations are required for computing the value of one element, but also reduces the memory space required to storage the entire system matrix and Fisher information matrix. Since Monte Carlo method also introduces noise, however, the number of samples determines the accuracy of estimated Fisher information; insufficient samples will induce large error and noise.

3.3.2 M-UCRB Calculation by Fast Fourier Transform.

Another primary computational issue of the M-UCRB is the inversion of the matrix $[F_Y + \lambda I]$, and multiplication of several matrices which have the same size as the FIM F_Y. Fortunately, according to the Equation 3-19, as employing a source with uniform activities, the FIM can be expressed approximately as,

$$F_Y \approx \alpha A^T A , \qquad (3\text{-}25)$$

which is close to a locally spatial invariance, under this assumption, the matrices of both F_Y and $[F_Y + \lambda I]$ are approximately a circulant-block-circulant (CBC) matrices[92].

The matrix C, shown below, is called circulant or one dimensional shift invariant with wrap-around. It belongs to a special case of the Toeplitz matrix and the rows are circular right shifts of the elements of the preceding row. A block circulant matrix, such as the Fisher information matrix, is special block Toeplitz, the block rows are circular right shifts of the block elements of the preceding block row, and each block is a circulant matrix.

$$C = \begin{bmatrix} c_0 & c_{N-1} & \cdots & c_2 & c_1 \\ c_1 & c_0 & c_{N-1} & \ddots & c_2 \\ \vdots & \ddots & \ddots & \ddots & \vdots \\ c_{N-2} & \ddots & c_1 & c_0 & c_{N-1} \\ c_{N-1} & c_{N-2} & \cdots & c_1 & c_0 \end{bmatrix} , \qquad (3\text{-}26)$$

with a block circulant matrix, the inversion and multiplication of these matrices with a vector can be achieved quickly using the discrete Fourier transform (DFT) and it's inverse (IDFT) [93], by which the computation complexity reduces from $O(N^3)$ to $O(NlogN)$.

According to the Fourier transform, the DFT of an N-dimensional complex vector can be defined as matrix W, in which $W_{kn} = \left(e^{-\left(i \frac{2\pi}{N} \right)} \right)^{kn}$. Thus, with unitary normalization constants $1/\sqrt{N}$, the above DFT matrix is further defined by a unitary matrix: $Q = W/\sqrt{N}$. A corresponding IDFT unitary matrix is its Hermitian transpose matrix Q^* and $Q \cdot Q^* = 1$. And, the circulant matrix C can be separated as $C = Q^* diag (QC_{1c})Q$, where Cc is the first column of C.

Therefore, the calculation of modified uniform Cramer-Rao bound is given as,

$$\sigma^2 \geq f^T [F + \lambda I]^{-1} \cdot F \cdot [F + \lambda I]^{-1} f$$
$$= f^T Q^* ((Qf) \cdot / (Q[F + \lambda I]_{1c}). * (QF_{1c}) \cdot / (Q[F + \lambda I]_{1c})) \quad , \quad \text{(3-27)}$$

Where ".*" and "./" are element-wise multiplication and division, respectively.

3.4 The principle and development of Monte Carlo Simulation.

As described in the last section, to solve the computation and memory issues required to directly calculate the M-UCRB, the MCI method is employed to calculate the FIM instead of a direct matrix multiplication. This method has the potential to evaluate very complex imaging systems and large three dimensional source objects with small size of image pixels, such as the Compton camera imaging system.

To satisfy the requirements of the Monte Carlo method, a list of random variables or sampled events must be generated from a probability distribution function. For more complex imaging systems, for which a statistical relationship between the emitted photons from a source object and their detection is not a simple function or a simple random variable, a Monte Carlo or stochastic simulation system is required to generate the random variables or set of sampled events according to the statistical model of the specific imaging system [94].

3.4.1   Introduction to Monte Carlo Simulation

Monte Carlo numerical simulation methods have been widely used in radiation therapy as well as for research related to medical imaging system design. In radiation therapy, Monte Carlo simulation can estimate the radiation dose to tumors and normal tissue and help design the therapy plan before the actual treatment. For the design of a complex imaging system, Monte Carlo modeling of system performance can be predicted by generating random variables based on known system or physical process probability models. In this way, the designer can optimize the system design before actually manufacturing it.

Historically, several Monte Carlo simulation systems have been tested and employed to simulate SPECT and PET imaging systems. Some of them are specially designed to make simulations quick using variance reduction techniques or simple

assumptions, such as SIMSET, SIMSPECT, and SIMIND simulation systems[95]. Others are coded and applied to an the all-purpose particle simulation system, such as Electron Gamma Shower code (EGS3), Monte Carlo N-Particle code (MCNP) and Geometry and Tracking code (GEANT4), which simulate the detailed physical processes of particle motion and interactions in the object and detector components. Three fundamental elements are required in every Monte Carlo simulation system; a random number generator, sampling techniques and a probability model for each physical process involved in the imaging system and the object to be imaged.

3.4.1.1 The Random Number Generation

The random number generator is a fundamental part of the Monte Carlo calculation, by which a sequence of numbers are generated such that each number has no relation with the previous numbers. One approach to obtain a true random number is by sampling a noisy process in nature, such as the electrical noise or thermal noise in the electronic components. However, acquisition of this kind of true random number is typically time consuming and impractical. Alternative methods use various computer programs to generated pseudo random number sequences[96], in which the generated number is approximately a true independent random number.

Therefore, there are two criteria to evaluate the quality of a sequence of pseudo random numbers by computer calculation. One is a high randomness of random number lists, another is the pseudo random number sequence has a sufficiently long cycle period to avoid sequence repeat during the simulation.

The basic pseudo random number generator is a linear congruent algorithm that generates uniformly distributed random numbers between zero and one[91, 97]. By this algorithm, one random number I_{i+1} is calculated from its previous number I_i based on the following formula,

$$I_{i+1} = (aI_i + b) \bmod(m),$$ (3-28)

Here a and b are positive integers called multiplier and the increment respectively, and $m=2^k$ is called the modulus, in which k is the bit length of the computer. The first number I_0 is the pre-specified SEED in the random number sequence. Even though this fundamental algorithm can generate a 2^k length random number sequence using little

memory and computing time, the risk of this algorithm is that the initial seed value can be re-generated in the calculation. To avoid this problem, a portable random number generator algorithm based on a shuffling procedure is employed. This generator uses three linear congruent generators [97], in which the first generator generates random numbers as the SEED of the second and third generator, the second generator calculates a vector of 97 random numbers, and the third generator calculates a random number pointing to a number in the list generated by first generator, which is the final random number generated Using this method, the period of the sequence of random number is almost infinite for general practical applications.

3.4.1.2 Introduction of Sampling Techniques for Random Variable Generation and Variance Reduction

According to the a-priori determined probability distribution function, which describes the statistical properties of the physics processes involved, three different sampling or random number generation methods are used in various Monte Carlo algorithms to generate random numbers which satisfy the a-priori distribution from a sequence of uniformly distributed random numbers. The three methods are: the distribution function or direct inverse transform method, the acceptance-rejection method and mixed method.

1. *The direct inverse transforms method.*

If the probability density function is *pdf(x)* on the range $[-\infty, \infty]$, its cumulative distribution function CPDF(x) is found by integrating *pdf(x)* in the interval [a,x]

$$CPDF\ (x) = \int_a^x pdf\ (x')dx',\tag{3-29}$$

If *b* is an upper bound of *pdf(x)*, then the cumulative probability distribution function CPDF(b) is the integrated *pdf(x)* from *a* to *b*, and, the uniform CPDF(x) is distributed from 0 to 1. Assume the number from the uniform random number generator is *u* and is substituted into the inverse CPDF(x) function, then sampled random number *y* with distribution *pdf(x)* is $y = CPDF^{-1}(u)$.

In a simple case, CPDF(x) and its inverse function could be calculated by hand. However, for the case with a complex *pdf(x)* function, the integration of *pdf(x)* may be

obtained by numerical methods to generate a uniform CPDF histogram with values ranging from 0 to 1. This is known as discrete invertible cumulative distribution sampling. As shown in Figure. 3.1, by interpolated method, the required random number *y* with distribution *pdf(x)* is sampled from CPDF histogram, which satisfies $CPDF(y_k) < u \leq CPDF(y_{k+1})$ and $0 < u \leq 1$.
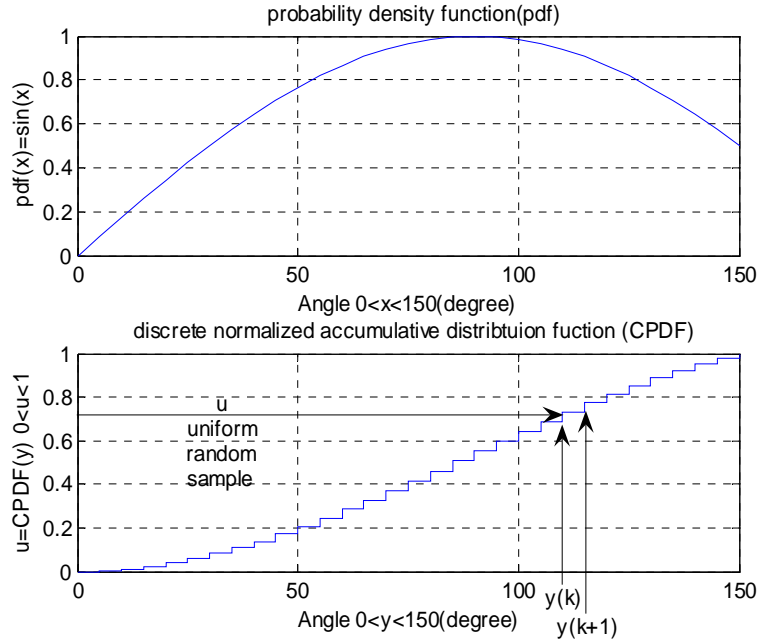
Figure 3.1, The probability density function (pdf) curve (top) and its discrete normalized CPDF curve (bottom). A random number **u** generated from a uniform distribution (0,1) to sample a random number **y** from a CPDF distribution function.

2. *The Acceptance-Rejection Method.*

The direct inverse transform method is often hard to realize due to an unknown analytic form of CPDF(x) or it's inversion is impractical. The acceptance-rejection method is an alternative method, in which a uniform distribution function *updf(x)* is generated from pdf(x), as given by

$$updf\ (x) = \frac{pdf\ (x)}{\max[\ pdf\ (x)]} \ . \tag{3-30}$$

Therefore, the acceptance-rejection method includes two other steps:

Step 1. Generate two random number **r1** and **r2** uniformly distributed over [0,1]. From **r1**, a uniform distributed value **x** within the range [a,b] is sampled according to the equation

$$x = a + r_1(b-a),\qquad\qquad\qquad\qquad\qquad\qquad\qquad (3\text{-}31)$$

Step 2. Compare with **r2** and updf(x), if $r_2 < updf(x)$, the **x** is accepted as the sampled random number. Otherwise, new **x** value needs to be re-sampled and step1 is repeated.

Compared with the direct inverse transform method, this method will work for any kind of complex distribution at a price of very long computation time for the case of a probability distribution function with small range.

3. *The Mixed Method.*

To overcome potential problems and benefit from advantages of the direct inverse transform and acceptance-rejection methods, the mixed method combines both methods. The complex distribution function *pdf(x)* is separated as the product of two probability distribution functions *pdf1(x), pdf2(x).*

4. *Variance Reduction and Forced Detection.*

The purpose of Monte Carlo simulation is to obtain an accurate model of a real physical or statistical process. However, for the medical imaging system studied, a process such as Compton scattering, has very low probability, and most sampled events are wasted and discarded in the simulation history path. To avoid time consuming simulation, therefore, variance reduction techniques have been developed to increase the probabilities of sampling these unlikely but critical physical processes[95]. Therefore, to recover the original and true probability of the whole process, the *weight* (WHT) must be attached to each photon history. In our research, the forced detection [98] technique is employed to increase the probability of Compton scattering in the first detector, the probability of absorption in the second detector, and the probability of the emitted photon impinging on the first detector.

3.4.2 Development of the Compton Imaging Random Variable Sampling System

3.4.2.1 Introduction

The Compton imaging system is difficult to simulate using the Monte Carlo system designed specifically for a conventional nuclear medical imaging system. This is

because some important physical interactions, such as Compton scattering, are not contained in the software package. Even for some general purpose Monte Carlo systems used to simulate particle transmission, such as GEANT4, the separate low energy Compton scattering (LECS) package[99] is required to correctly simulate Compton scattering with Doppler broadening. There are two remaining issues pertinent to our application. The first problem is that the package only provides Doppler broadening data for atomic elements, whereas the effect of Doppler broadening in crystalline silicon is required for our research. Another issue is the simulation time required. Since GEANT4 simulates all of the physical processes involved and Compton scattering has low probability compared to other processes, the time needed to acquire enough sampled data for the Compton imaging system can be impractical. For these reasons, the Compton imaging random variables sampling system (CIRVS) has been designed for a special geometric configuration.
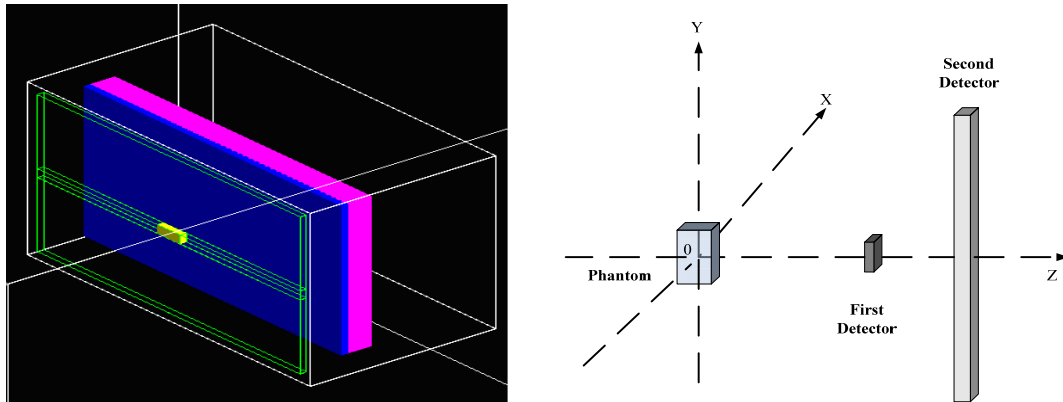
Figure 3.2. Geometric configuration of the simulated Compton Camera with two planar detectors. The yellow rectangle is the silicon first detector, the green hollow rectangle surrounding the first detector is shielding, and the blue and pink rectangles represent the NaI crystal layer and PMT layer in the second detector, respectively.

As shown in figure 3.2, the imaging system has two planar detectors which are placed parallel to each other. Except for the sides facing the source and the second detector, the first detector is surrounded by lead shielding to decrease the number of photons impinging on the second detector. CIRVS is written in the C++ language and consists of the following six subroutines shown in Figure 3.3.
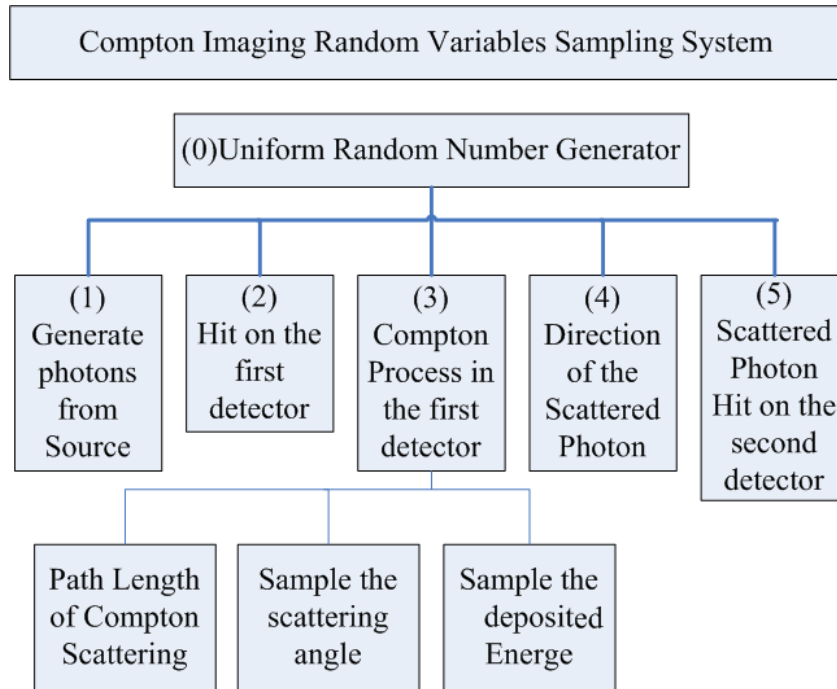
Figure 3.3 The Subroutine structure of the Compton Scattering Random Number Sampling System.

3.4.2.2 Overview of CIRVS system

CIRVS was developed primarily to study the performance of a Compton scattering camera with two planar detectors using the M-UCRB. For this specific, the CIRVS did not consider the Rayleigh scattering and multiple Compton scattering. To resolve the long computation time issue, some assumptions and techniques of force detection[98] and variance reduction can be used. Therefore, in order to maintain the original probability of a sampled random number along the simulated sequence, theoretically, a WHT is required to be associated with each step of the photon history path.

1. *Generate the photons from the source*

In the subroutine for generating the photons from the source, the phantom used is defined as a volume matrix of cubic pixels. A attenuation, scatter and decay of the photons in the phantom are ignored under the assumption of the material of the phantom is in the air, i.e. a constant emission rate of gamma rays. The dimension of the matrix may be adjusted according to specific application. To improve the position resolution of

the emitted photon, one bin may be subdivided into a matrix of sub-bins. The minimum sub-bins size may be as small as 0.001mm. Consideration of simulation speed, limits the sub-bin size to around 1/20 of the bin. The origin of an emitted photon in each sub-bin is taken as the center of the sub-bin. For a phantom with non-uniform distribution of radioactivity, the number of emitted photons from one sub-bin is determined by the relative activity concentration of the source in the sub-bin.

To generate a random variable sample of the photon from a sub-bin, the sub-bin matrix is tabulated as a one dimensional array A_{source}. The overall length of the array l_{max} is the sum of the sub-bins weighted by the relative activity concentration of the sub-bins. The entry of the array is the index of the sub-bins and the total number entries with the index of a specific sub-bin is the relative activity concentration. As an example shown in figure 3.4, the 2 by 2 sub-bins matrix, in which relative activity concentration of sub-bin A, B, C, D, is 1,2,3,4, respectively. Therefore, the non-uniform source becomes the uniformly sampled entries of the array A_{source}. This technique is clearly a variation of the discrete invertible cumulative distribution sampling method.

A(1)	B(2)
C(3)	D(4)

The sub-bins matrix
Index(relative activity concentration)

1	2	3	4	5	6	7	8	9	10
A	B	B	C	C	C	D	D	D	D

The array A_{souce}
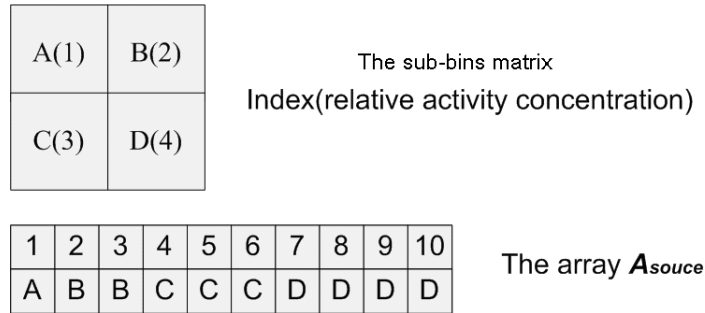
Figure 3.4. An example of a sub-bin matrix and its sampling table A_{source}, in which each entry is the index of a sub-bin and number of entries for a sub-bin is the relative activity concentration in the simulated phantom.

2. The photon direction and intersection point on the first detector.

Given the position from which a single photon is emitted, the sampled direction of the photon is defined by the polar or elevation angle, $\theta \in [0, \pi)$, which is the angle between the direction vector of the photon and z axis. The azimuthal angle, $\Phi \in [0, 2\pi)$, is the angle between the x axis and the projection of the direction vector on the x-y plane. In

spherical coordinates, the direction of the emitted photon is defined in terms of solid angle $\Omega \in [0, 4\pi)$. The relationship among the Ω, θ, Φ is given as,

$$d\Omega = \sin \theta\, d\theta\, d\Phi \ . \tag{3-32}$$

Because the direction vector is uniformly distributed in the unit sphere, the probability of the one direction vector is equal to,

$$d\Omega = \frac{1}{4\pi} \ . \tag{3-33}$$

Therefore, given a uniform random number $R \in [0,1]$, the azimuthal angle Φ is uniformly sampled by

$$\Phi = 2\pi \bullet R \ , \tag{3-34}$$

and the polar angle θ can be obtained from

$$\cos \theta = 1 - R \ . \tag{3-35}$$

Since the solid angle subtended by the first detector is relatively small compared with the phantom size and distance from phantom to the first detector, conventional sampling methods would require a long time to generate the required number of photon interactions with the first detector. Therefore, variance reduction[100] and forced detection techniques [98]are employed here to reduce the time. To speed sampling for an emitted photon, the location of the corner of the front face of the first detector, and the maximum and minimum of the azimuthal angle Φ_{max}, Φ_{min} and polar angle $\theta_{max}, \theta_{min}$ subtended by the first detector are calculated. Therefore, the probability of the direction of a sampled photon emitted at the angle θ within the range of $\theta_{max}, \theta_{min}$ is given by,

$$P(\theta) = \frac{\int_{\theta_{min}}^{\theta} \sin x\, dx}{\int_{\theta_{min}}^{\theta_{max}} \sin x\, dx} \ . \tag{3-36}$$

Thus, by sampling the above probability, the polar angle θ is determined by

$$\cos \theta = \cos \theta_{min} - R[\cos \theta_{min} - \cos \theta_{max}] \ . \tag{3-37}$$

And, since the azimuthal angle Φ is uniformly distributed in the range of Φ_{max}, Φ_{min}

$$\Phi = \Phi_{min} + R[\Phi_{max} - \Phi_{min}] \ . \tag{3-38}$$

Therefore, the photon history weight, WHT_1 is the probability of the emission within $\theta_{max}, \theta_{min}$ and Φ_{max}, Φ_{min}. That is the solid angle subtended by the first detector over 4π,

$$WHT_1 = \frac{\cos\theta_{max} - \cos\theta_{min}}{2}.$$
(3-39)

3. Compton Process in the first detector

When the photon reaches the front the surface of the first detector, it will continue into the first detector and interact with the detector material with a probability determined by the detector martial and photon energy. In the simulated Compton Imaging system, the Compton scattering process is the only process simulated in the first detector. However, since the probability of a Compton scattering event is quite small and the absorption probability at the energies of interest are even smaller, most photons pass though the first detector without any interaction. Therefore, a forced detection technique is used as described above so that every incoming photon undergoes Compton scattering. Three sub-routines generate the position of Compton scattering, the scattering angle and the energy deposited in the first detector.

A. Photon path length in the first detector.

Given the direction vector of the incoming photon and the geometric parameters describing the planar first detector, the maximum distance that the photon can travel in the first detector is given by,

$$d_{max} = \frac{l_{Thickness}}{\cos\theta},$$
(3-40)

The probability of the photon traveling a path length d, is given by,

$$P(d) = \frac{\int_0^d \frac{\mu_{compton}}{\mu_{total}} e^{-\mu_{total} x} dx}{\int_0^{d_{max}} \frac{\mu_{compton}}{\mu_{total}} e^{-\mu_{total} x} dx},$$
(3-41)

where $\mu_{compton}$ is the linear attenuation coefficient for the Compton process and μ_{total} is the linear attenuation coefficient for all processes including photoelectric interaction, pair production, Compton scattering and coherent scattering, respectively. Both of these coefficients are a function of the photon energy and the detector material atomic number.

Therefore, with a uniformly distributed random number R, the sampled photon path-length d is given as

$$d = -\frac{1}{\mu_{total}} \cdot \ln[\, 1 - R \cdot [1 - e^{-\mu_{total} \cdot d_{max}}\,]]\;, \qquad\qquad\text{(3-42)}$$

The spatial coordinates $(X_1{}',Y_1{}',Z_1{}')$ relative to the original coordinates in the first detector are

$$\begin{aligned}
X_1{}' &= d \cdot \sin\,\theta \cdot \cos\,\Phi \\
Y_1{}' &= d \cdot \sin\,\theta \cdot \sin\,\Phi \\
Z_1{}' &= d \cdot \cos\,\theta
\end{aligned} \qquad\qquad\text{(3-43)}$$

Due to the forced detection process for Compton Scattering used here, the WHT_2 of this step is equal to the true probability of Compton scattering, and given as,

$$WHT_2 = \frac{\mu_{compt}}{\mu_{total}} \cdot [\, 1 - e^{-\mu_{total} \cdot d_{max}}\,] \cdot \qquad\qquad\text{(3-44)}$$
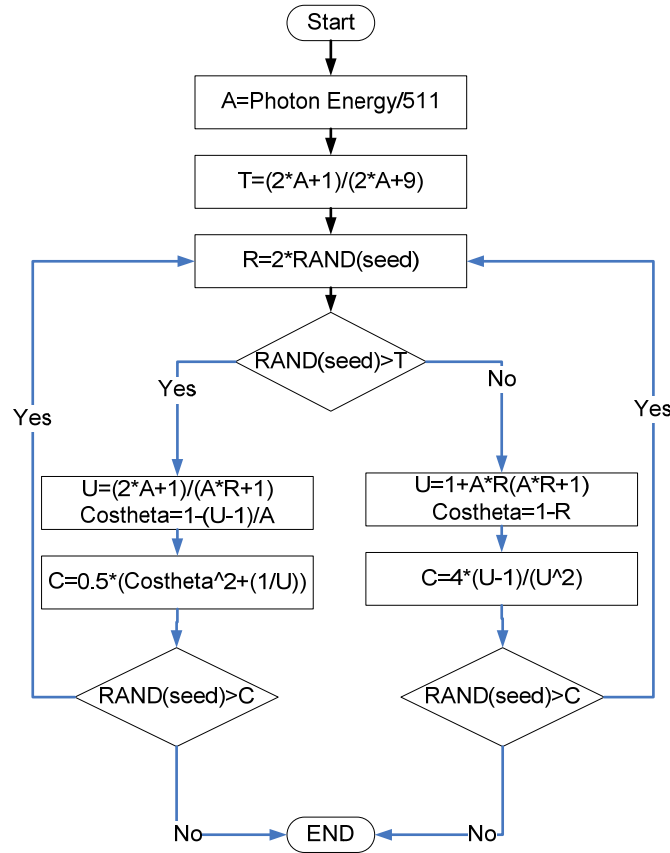
Figure 3.5 Flow chart of the Scattering Angle Sampling Program. $\cos\theta_1 = \text{CosTheta}$.

A. Scattering angle of the scattered photon.

The scattering angle θ_1 is sampled by the Klein-Nishina cross-section equation and Mixed Kahn's sampling method[101]. The flow chart of scattering angle sampling is

shown in Figure 3.5. The scattering angle Φ_1 is a random sample for the uniform distribution with the range from 0 to 2π.

(A) (B)
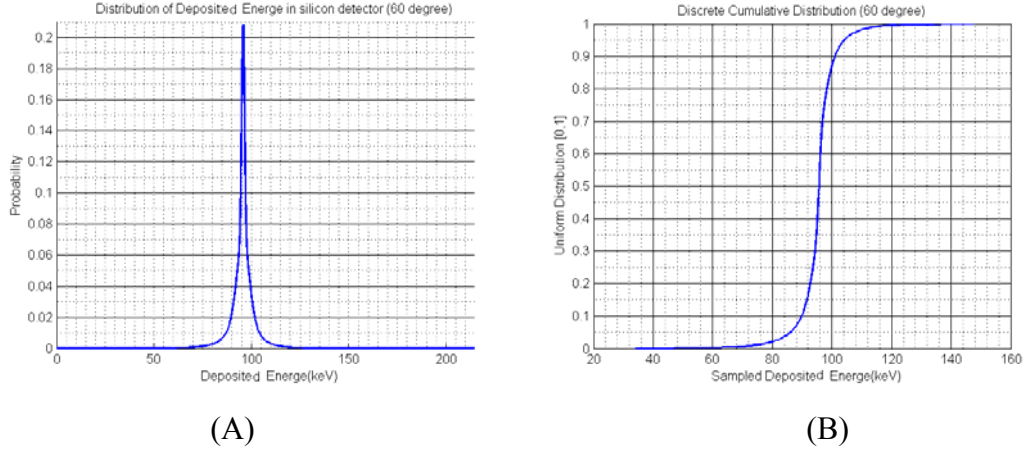
Figure 3.6 (A) The normalized probability profile for 364.4keV photon Compton scattering at 60° scattering angle in silicon detector. (B) The discrete cumulative distribution curve for energy sampling at 60° scattering angle.

B. The energy deposited in the first detector.

To determine the deposited energy in the first detector for a Compton scattering that includes the effect of the Doppler broadening, the Compton Double Differential Cross Section equation introduced in Chapter 2 combined with the discrete invertible cumulative distribution sampling technique is employed. For example, the normalized probability distribution as a function of absorbed energy for detecting a 364.4 keV photon in a silicon detector, given the scattering angle is 60 degree or $\pi/3$ is shown in Figure 3.6(A). Its discrete normalized cumulative distribution function curve is shown in Figure 3.6(B), in which the x axis is the uniform distribution ranging from 0 to 1, and y axis is the deposited energy. Therefore, for a random number R with uniform distribution [0,1] and given scattering angle, the curve gives the deposited energy sample. In the real calculation, a two dimensional table with entries of possible deposited energy is used as shown in figure 3.7, which is indexed by the [0, 1] uniform distribution and possible scattering angle in the range of [0,180] along the x axes and y axes, respectively. The final sampled deposited energy is calculated by a linear interpolation algorithm according to the given scattering angle and the generated random number.
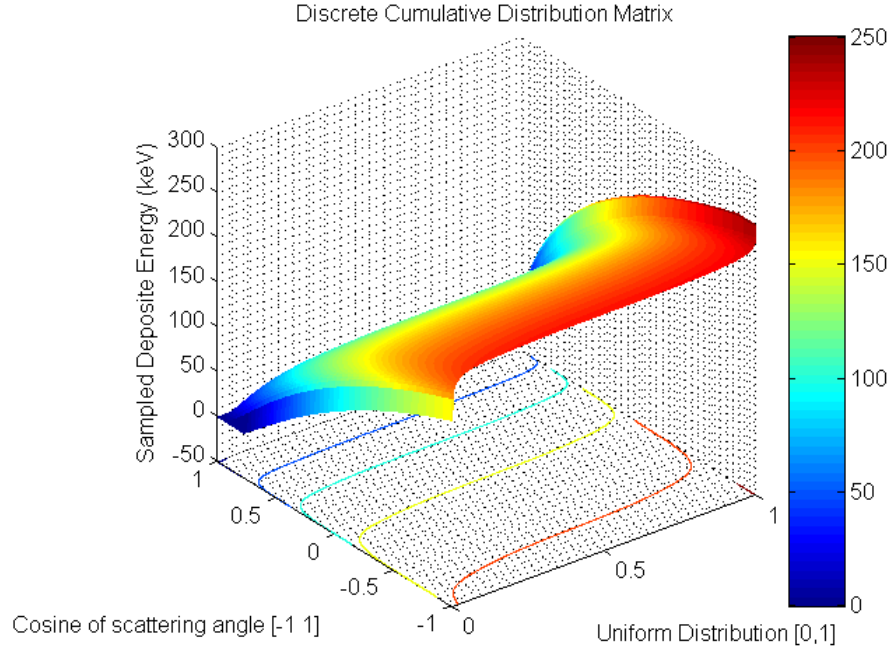
Figure 3.7 The discrete cumulative distribution matrix of deposited energy after Compton scattering in the silicon detector for an incoming 364.4keV photon. The matrix indexed by the range of uniform random numbers from 0 to 1 and the range of cosine value of scattering angle from -1 to 1.

4. *Direction of the scattered photon*

The scattering polar angle θ_1 and azimuthal angle Φ_1 are both relative to the direction of incoming photon, thus, the direction vector of the scattered photon in the same Cartesian coordinates as the incoming photon needs to be calculated. Given the unit direction vector of an incoming photon $[x,y,z]'$, the unit direction vector of scattered photons $[uxx,uyy,uzz]'$ can be obtained by a compound rotation around z and x axes, which is given as

$$
\begin{bmatrix} uxx \\ uyy \\ uzz \end{bmatrix} = \begin{bmatrix} \cos\Phi_1\cos\theta_1 & -\sin\Phi_1 & \cos\Phi_1\sin\theta_1 \\ \sin\Phi_1\cos\theta_1 & \cos\Phi_1 & \sin\Phi_1\sin\theta_1 \\ -\sin\theta_1 & 1 & \cos\theta_1 \end{bmatrix} \begin{bmatrix} ux \\ uy \\ uz \end{bmatrix},
$$
(3-45)

5. *The interaction position on the second detector*

The scattered photon may then interact with the second detector. To increase the simulation speed, the CIRVS system assumes all of the scattered photons impinging on

the second detector are absorbed by the second detector by a forced detection technique and the depth position z of interaction location z is unknown since the current ARGUS Anger camera simulation does not provide any depth information. Therefore, the relative x and y position of interaction in the second detector can be calculated from the unit direction vector [uxx,uyy,uzz]' and the distance d_{12} along the z axis between the second detector and Compton scattering location in the first detector.

$$X_2' = uxx \cdot d_{12} / uzz ,$$
$$Y_2' = uyy \cdot d_{12} / uzz$$

(3-46)

The WHT3 of the step for a NaI detector with thickness of t_{max} can be estimated as

$$WHT_3 = [1 - e^{-\mu_{total}(naI) \cdot t_{max} / uzz}] ,$$

(3-47)

6. ***Blurring the deposited energy and position.***

The simulated positions on the first and second detector and the deposited energy in the first detector are finally blurred by normal distributions with variances defined by the energy resolution and spatial resolution for different evaluation tasks.

CHAPTER 4

System Modeling of Compton Imaging System and Collimated Anger Camera

The statistical system models for both the Compton imaging system with parallel dual planar detectors and conventional Anger camera with parallel hole HEGP lead collimator for detecting photons emitted from ^{131}I are described and evaluated in this chapter. The computational system models and derived detection sensitivity and list-mode or bin-mode transition probabilities are required for calculating Fisher information by Monte Carlo integration or reconstructing images by MLEM algorithms.

4.1 Introduction

For the collimated Anger camera, assuming local shift invariance for source bins with identical distance to the surface of the detector, the system model can be obtained by measuring or simulating a series of point source response functions at different distance. However, for the relatively complex Compton imaging system, it is very difficult to obtain the transition probabilities by simulation or measurement due to the very large number of measurement elements. Instead, the system model must be derived by mathematical approximation for each physical process involved.

Ideally, a rigorous statistical model should be used to describe all of the physical processes in the Compton imaging system including the estimation of position resolution, energy resolution and the effect of Doppler broadening. However, this model is impractical to calculate by straight-forward computation. This is because the sensitivities and transition probabilities require multi-dimensional numerical integration of the probabilities of deposited or scattering energy for multiple interaction positions over the areas of each pixel on the first detector and second detector.

Several simplified mathematical models based on several assumptions, therefore, have been developed by many researchers to calculate detection sensitivity and transition probability. The key requirements for a practical model are reducing the computational complexity and reasonably approximating the physical processes, especially, calculation of the Compton Differential Cross Section and evaluation of the Doppler broadening effect for our application.

In [102], authors presented a method to calculate the transition matrix considering the Poisson nature of a prototype Compton camera. This method requires a very large memory to store the pre-computed transition probabilities and does not take account of Doppler broadening. Wilderman developed two efficient methods to calculate system matrix coefficients and relative sensitivities for a Compton camera with planar scattering detector. The first method[103, 104] cuts the number of matrix elements to be computed in half by assuming uniform sensitivity and perfect energy and spatial resolution on both detectors. Since Doppler broadening of the energy spectrum is also ignored and transition probabilities are estimated using a uniform sensitivity times the line integral of the conic intersection with each pixel, the computation is rapid. The updated method[105] takes into account the relative spatial variation of the sensitivity, which depends approximately on solid angle subtended by the scatter detector and interaction probability in this detector. The transition probabilities or measured probabilities are approximated by relative escape probabilities of the scattered photons in the first detector, Klein-Nishina differential Compton cross section, finite energy resolution and representing Doppler broadening by a sum of two Gaussian functions assuming the cone spread function is uniform for all energies. To evaluate the Doppler broadening, a Fisher Von-Mises Model is implemented instead of a Gaussian model in [106]. However, the parameters of the Von-Mises Width need to be pre-computed by fitting results of Monte Carlo simulation. Furthermore, the whole model is developed for specified hemispherical detector geometry and exploits the assumed symmetries. To consider the effect of the Doppler broadening and finite energy resolution, Kragh alternatively proposed the method[87] to calculate the probability of scattering at a particular angle and energy by interpolating a two dimensional matrix pre-calculated by jpdf, which is calculated by convolving the energy measurement error with the Compton scattering double differential cross section.

To get an approximate model, however, a thin planar first detector is assumed and the probability of transmission of a scattered photon is set equal to 1.

In our application, we proposed a more accurate and reasonable Compton camera statistical model employing an interpolatable jpdf matrix, calculated using double differential cross section, blurred by both energy and spatial resolution to satisfy the requirements of our proposed Compton imaging system.

4.2 System Modeling of Anger Camera with HEGP Collimator by Monte Carlo Simulation

In order to analyze the performance of a conventional Anger camera equipped with an HEGP lead collimator for imaging the high energy gamma rays from ^{131}I. A system model of an Anger Camera with HEGP collimator for ^{131}I gamma rays that includes photon penetration and scattering in the collimator is required. The goal of this model is to find a relatively simple function to correctly describe the point-spread function at different distances from the image plane to the surface of the lead collimator. The model primarily considers the resolution properties of a parallel hole HEGP lead collimator and sodium iodide Anger camera.

For this propose, An ADAC Argus Anger Camera with HEGP parallel-hole collimator as described in Chapter 2 is simulated by GATE to determine the PSF for ^{131}I. As shown in Fig. 4.1, based on published system specifications[107] for the Argus system, five layers of material in the camera head are included in the simulation, the lead collimator, aluminum sheet, NaI(Tl) scintillation crystal, PMT compartment, and lead shielding.
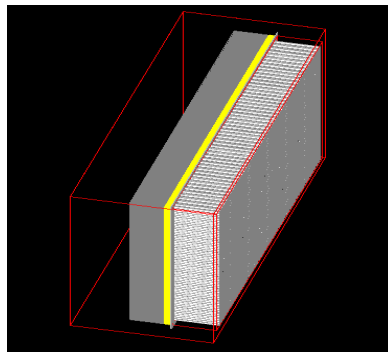
Figure 4.1 The simulated ARGUS Anger camera head with HEGP collimator.

Using the GATE simulation system, the point spread function images at source distances from 0cm to 50cm from the front face of the collimator are generated for a point ^{131}I source in air, which emits photons at 364.4keV(82%),637keV(7.2%) and 723keV (1.8%). The energy window is 20% around 364.4keV. The simulated ^{131}I point spread function images and their profiles at distances of 10 and 35cm are shown in Fig. 4.2. The simulated PSF is fit with a Gaussian combined with an exponential function that arises from collimator penetration and scattering using a non-linear least squares method. At a given distance x, this function is given as,

$$PSF \ (x) = A_{Gauss} \ e^{(\frac{-x^2}{2\sigma^2})} + A_{exp} \ e^{(-\lambda x)} , \tag{4-1}$$
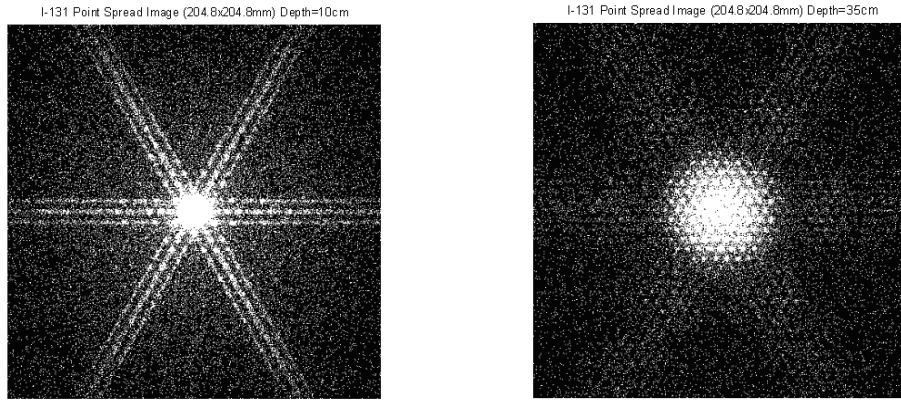
(a)   (b)
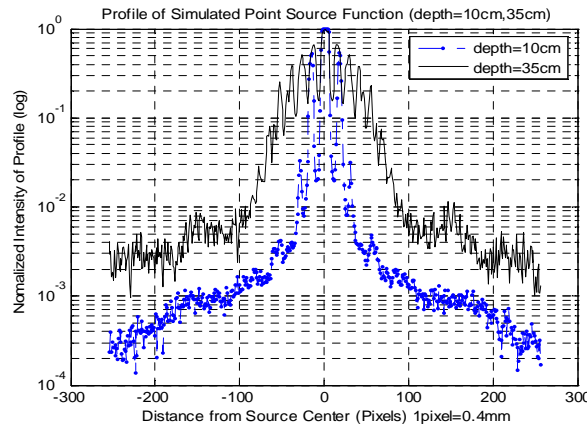
(c)

Figure 4.2 The two-dimensional point spread images from an I^{131} point source at a distance of 10cm and 35cm shown in (a), (b), respectively. The bottom image (c) shows the horizontal profiles of point spread functions at different distances. One pixel=0.4mm.

In Fig. 4.3, the right half profiles of the simulated normalized point spread function and the fitted point spread function form equation 4.1 are displayed for the ^{131}I point source at 10cm and 35 cm, respectively. There is a good match between the original simulated PSF and parameterized PSF. However, the smooth fit reduces the hole-pattern artifacts seen in Fig. 4.2 and 4.3, but Jaszczak has shown that the pattern can be removed and some improvement in resolution can be observed if the collimator is moved and the images shifted by the same amount as the collimator motion and superimposed.
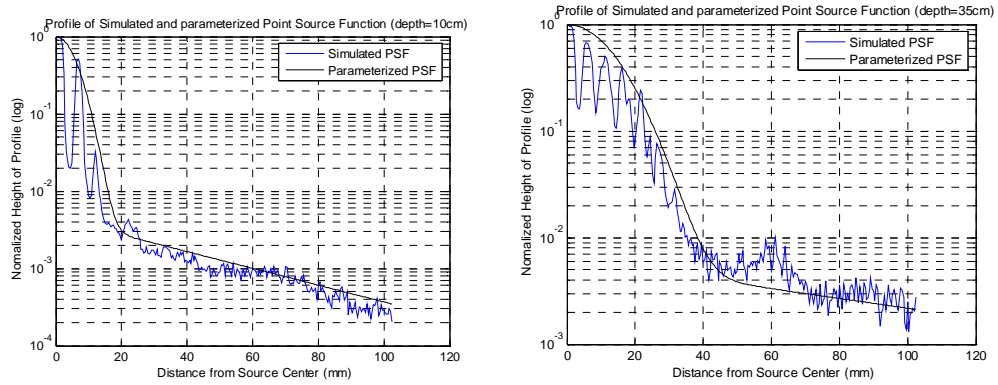
Figure 4.3 Right half of simulated and parameterized point spread function from I[131] at a distance of 10cm and 35cm on the left and right, respectively.

To derive the relationship of coefficients in the parameterized point spread function with point source to collimator distance, the simulated point spread images were obtained at 0cm, 1cm, 2cm, 3cm, 5cm, 7cm, 10cm, 15cm, 20cm, 25cm, 30cm, 35cm and 40cm, respectively. The value of coefficients A_{Gauss}, A_{exp}, σ and λ at different source to collimator distances and the curve obtained by non-linear curve fitting are displayed in Fig. 4.4. The final fitted functions for the four coefficients as a function of source to collimator distance **d** are:

$$A_{Gauss} = 0.03645 \times 10^{(-0.05967 \times d)} + 0.007193 \quad , \tag{4-2}$$

$$\sigma_{Gauss} = 0.2768 \times d + 2.454 \quad , \tag{4-3}$$

$$A_{exp} = 0.002876 \times e^{(-0.07266 \times d)} + 0.0007339 \quad , \tag{4-4}$$

$$\lambda_{exp} = 0.03877 \times 10^{(-0.04374 \times d)} + 0.009312 \quad , \tag{4-5}$$

(a)

(b)

(c)

(d)
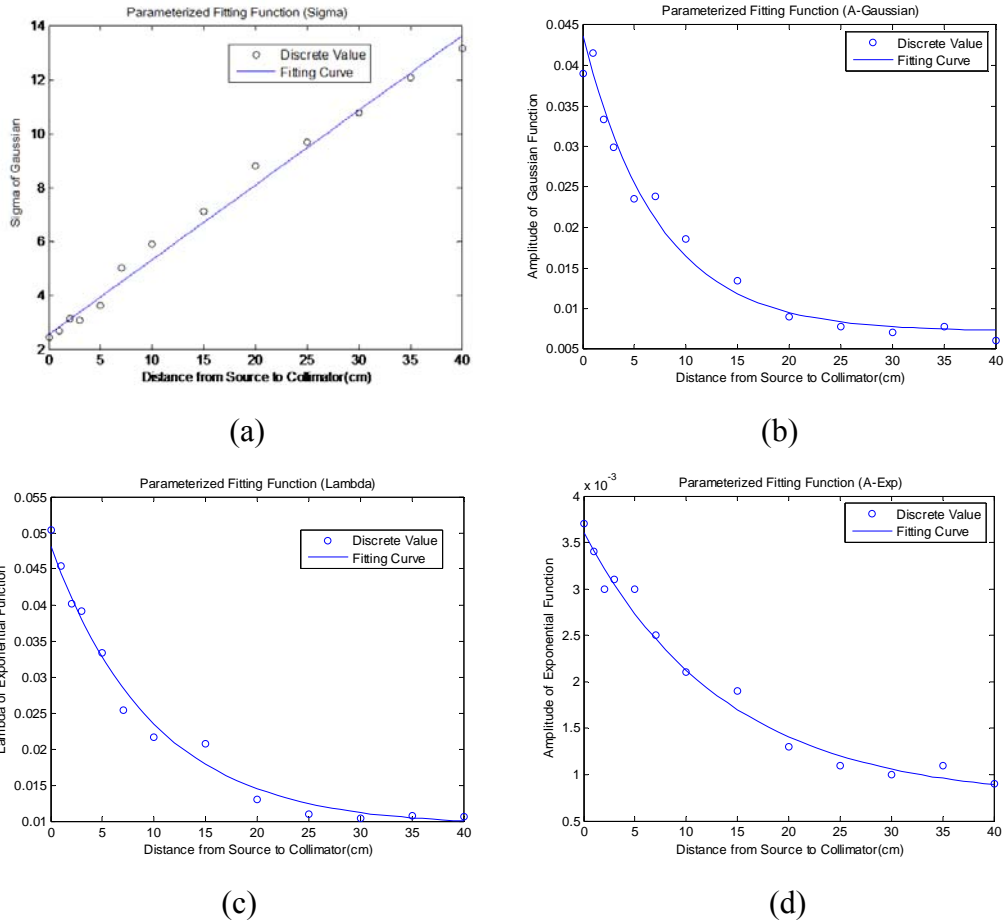
Figure 4.4 The discrete value and fitted curve for coefficients of the parameterized point spread function.(a)σ, (b)$A_{Gaussian}$, (c)λ and (d) $A_{exp.}$
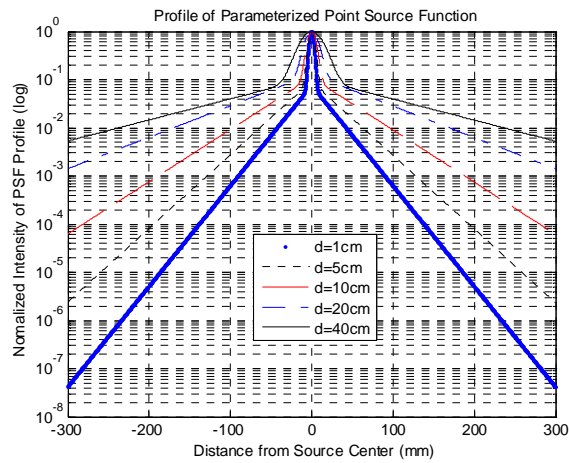
Figure 4.5 Profiles of the parameterized point spread function of the simulated Anger Camera with HEGP collimator for detecting I^{131} point source at 1cm, 5cm, 10cm, 20cm and 40cm distance from the surface of the collimator.
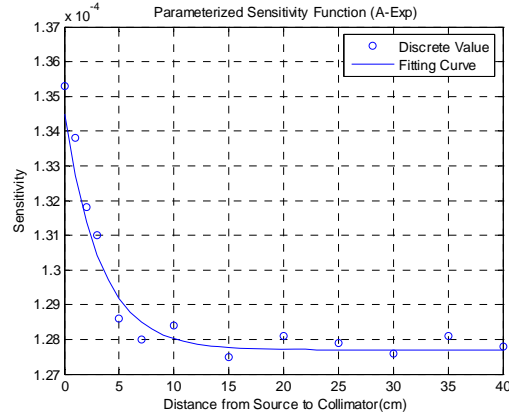
Figure 4.6 The discrete simulated sensitivity value compared to a parameterized sensitivity curve for detecting a I^{131} point source by ARGUS Anger Camera with HEGP collimator. The overall sensitivity is less than 1.35×10^{-4} and almost a constant as the source to collimator distance exceeds 15 cm. The penetration induces the higher sensitivity as the source is moved closer to the collimator.

The normalized curves of the parameterized point spread function for different source to collimator distances are shown in Figure 4.5. For the same maximum intensity, as the point source is positioned further from the collimator, the central Gaussian profile becomes wider and flatter, and the exponential tails that represent the collimator penetration and scattering also spread and flatten. The FWHMs of the PSF parameter at distances of 5cm and 10cm are 9.48mm and 12.74mm, and these values are pretty close to the system spatial resolution published in the specifications for the simulated ARGUS Anger camera, which are 9.2mm and 12.6mm, respectively.

The parameterized point spread functions are finally normalized, so that the integral under the PSF is equal to one. To determine the correct detection efficiency or sensitivity for detecting a ^{131}I point source by an ARGUS Anger Camera with HEGP lead collimator, a parameterized sensitivity function was generated by fitting the simulated discrete detection efficiency at different source to collimator distance. The function is given as,

$$Sensitivity = 0.0000068 \times 10^{(-0.1326 \times d)} + 0.0001277,$$
(4-6)

As shown in Figure 4.6, the sensitivity curve is almost a flat line and less than 1.35×10^{-4}, for the source to collimator distance larger than 10cm with sensitivity of 1.277×10^{-4} since septal penetration becomes much smaller and essentially constant as the angle of incidence to the camera face approaches 90 degrees.

4.3 System Modeling of Silicon based Compton Camera by Theoretical Analysis

Accurate modeling of the Compton Camera System is necessary to correctly calculate the detection sensitivity s_j and transition probabilities a_{ij}, which determine the estimated quality of image reconstruction and the accuracy of performance evaluation by the M-UCRB. A single valid Compton camera event consists of the following sequence: 1. A scattering interaction in the first detector in which the interaction point x1, y1 and z1, and deposited energy are determined. 2. An absorption (or interaction) in the second detector that is essentially coincident with the first interaction and for which the position and deposited energy are determined. However, calculating the s_j and a_{ij} from a rigorous statistical model suffers from the computational complexity of the multi-dimensional integration involved. The trade-off between a practical calculation and accurate estimation needs to be taken into account. In this section, we investigate an approximate statistical model for the configuration of the proposed Compton camera that accurately describes the sequence of physical processes.

4.3.1 Detection Process of Compton Imaging System

The sequence of physical processes involved in one detected event in a Compton imaging system is:

1. A γ-ray photon is emitted from $\underline{x}_0$ in the object with initial energy e_0 and direction Ω_1.

2. The emitted photon escapes from the object.

3. The escaped photon is directed toward the first (scatter) detector.

4. At location $\underline{z}_1$ of the first detector, the photon Compton scatters from an electron and energy e_1 is deposited in the first detector and the scattered photon escapes from the first detector in direction of solid angle Ω_2. If the energy e_1 is larger than the detection threshold, the location $\underline{z}_1$ and energy e_1 are recorded.

5. If the second detector lies within Ω_2, the scattered photon passes through an attenuating medium or air between the first detector and second detector.

88

6. The scattered photon with energy $(e_0 - e_1)$ strikes the second detector and may be absorbed in the second detector. The energy e_2 and position z_2 are measured by the second detector. The energy e_2 may or may not equal to $(e_0 - e_1)$. This depends on whether the scattered photon is fully absorbed by the second detector or perhaps scatters and escapes.

From the system illustrated in Figure 4.7, the position $z_1(x1, y1, z1)$ and energy measurement e_1 of the Compton scattering interaction in the first detector, the position $z_2(x2, y2, z2)$ and energy measurement e_2 deposited by the scattered photon in the second detector are recorded as $\{z_1, e_1, z_2, e_2\}$. According to this measurement, the γ-ray incident direction, $|z_1 - x_0|$, may be determined to lie on the surface of cone. The apex of the cone is located at $z_1(x1, y1, z1)$, the cone axis is defined by the vector $|z_2 - z_1|$ and the scatter angle can be calculated from the known energy of the incident γ-ray and measured energy deposited in the first detector. However, the apex of the cone and scattering angle are not precisely known due to the uncertainty of Doppler broadening, detector energy resolution, and position resolution. The location of a source point can only be estimated by the intersections of multiple cones from a collection of measurements $\{z_1, e_1, z_2, e_2\}$ of Compton scattered photons.
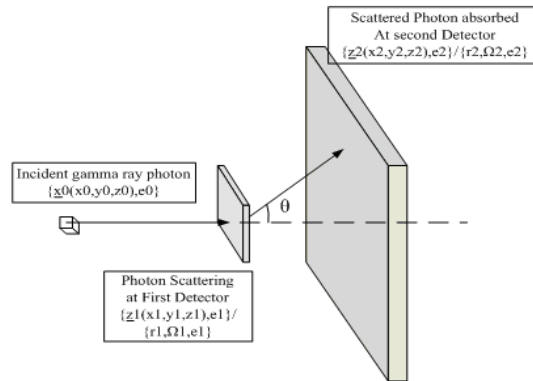
Figure 4.7 Detection and physical process involved for an ideal Compton camera. The incident γ-ray emits from x_0 with energy e0, scatters in the first detector at point z_1 and the scattered photon is absorbed by second detector at location z_2.

The above measurement vector $\underline{A}$ represents actual coordinates of a detected event under the assumption of a perfect detector. However, due to finite energy and spatial resolution of both detectors, the noisy measurement vector is $\underline{A}'$, a probability density function $p(\underline{A}'|\underline{A})$, that describes the relation of the noisy measurement $\underline{A}'$ to the actual attribution $\underline{A}$. $p(\underline{A}'|\underline{A})$ is the product of the distribution of all the uncertainties mentioned above. Therefore,

$$p(\underline{A}'|\underline{A}) = p(\underline{z}'_1|\underline{z}_1)p(e'_1|\underline{e}_1)p(\underline{z}'_2|\underline{z}_2)p(e'_2|\underline{e}_2) \tag{4-7}$$

4.3.2 Physical Events and Probabilities Involved in Photon Detection in the Compton Imaging System

As exampled in Figure 2.26, the *survival probability*, $P(D|\underline{x}_0)$, is the detection probability of a single photon emitted from the point $\underline{x}_0$. It is also referred to *detection sensitivity* s_i [108], i.e. the probability of a gamma ray emitted from source pixel i being detected anywhere can be evaluated by integrating over all detectable measurements, S. If we assume the source pixel is a point-like pixel where pixel i is centered at $\underline{x}_0$, then

$$s_i = P(D|\underline{x}_0) = \int_S \int P(D|\underline{A}, \underline{x}_0) p(\underline{A}|\underline{x}_0) p(\underline{A}'|\underline{A}) d\,\underline{A}' d\,\underline{A} \tag{4-8}$$

For analytical purposes, we convert the reference frame from Cartesian coordinates to spherical coordinates. Thus, the measurement $\underline{A}$ emitted from $\underline{x}_0$ is described as $\{r_1, \Omega_1, e_1, r_2, \Omega_2, e_2\}$, where r_1, r_2 are the vectors from $\underline{x}_0$ to $\underline{z}_1$ and from $\underline{z}_1$ to $\underline{z}_2$, respectively, and unit vectors Ω_1, Ω_2 are the directions of the incident and scattered photon, respectively. Then,

$$r_1 = |\underline{z}_1 - \underline{x}_0| \quad , \tag{4-9}$$

$$r_2 = |\underline{z}_2 - \underline{x}_1| \quad , \tag{4-10}$$

$$\Omega_1 = \frac{\underline{z}_1 - \underline{x}_0}{|\underline{z}_1 - \underline{x}_0|} \quad , \tag{4-11}$$

$$\Omega_2 = \frac{\underline{z}_2 - \underline{z}_1}{|\underline{z}_2 - \underline{z}_1|} \quad , \tag{4-12}$$

To conveniently analyze probabilities involved in the detection sequence of a Compton camera, we assume a perfect detector at first, i.e. $\underline{A} = \underline{A'}$ and $p(\underline{A}|\underline{A'}) = \delta(\underline{A} - \underline{A'})$, then Equation (4-8) reduces to

$$s_i = P(D|\underline{x}_0) = \int_S P(D|\underline{A},\underline{x}_0)\, p(\underline{A}|\underline{x}_0)\, d\underline{A}\, , \tag{4-13}$$

where S is the set including all the possible measurements. Hereby, $P(D|\underline{x}_0)$ may be derived from integrating all of the following probabilities associated with physical events in the process for all possible measurement elements.

4.3.2.1 γ-ray Emission from $\underline{x}_0$ toward First Detector in the Direction Ω_1.

Photons emitted from a point $\underline{x}_0$ in the objects are isotropically distributed. A photon emitted in direction of Ω_1 to the first detector will passes through the surface of an imaginary unit sphere with surface area 4π. Therefore, the probability density of a photon emission from $\underline{x}_0$ in the direction of Ω_1 is,

$$p(\Omega_1|\underline{x}_0) = \frac{1}{4\pi} \tag{4-14}$$

4.3.2.2 Following the Direction Ω_1, γ-ray Transits the Attenuation Medium a Distance r$_{01}$ in Direction Ω_1 between $\underline{x}_0$ and the First Detector.

Figure 4.8, illustrates a parallel beam of γ-ray photons with energy e and initial intensity I_0 (photons/cm^2/sec) passing through a 3D attenuating medium following a path r. The total path may include different materials with different linear attenuation coefficients μ_i (1/cm). The value of linear attenuation coefficient $\mu(l,e)$ is dependent on the absorbing material at location l and the incident photon energy. The cumulative total attenuation coefficient is an integral of all attenuation process along the path r.

The residual intensity $I(r)$ is described by Beer's Law[109],

$$I(r) = I_0 e^{-\int_0^r \mu(l,e)\, dl} \tag{4-15}$$

and the intensity decrease, (I_a), due to interaction in the material is,

$$I_a = I_0 - I(r) = I_0 - I_0 e^{-\int_0^r \mu(l,e)\, dl} \tag{4-16}$$

Therefore, for a given event, where the γ-ray passes through the attenuating medium between $\underline{x}_0$ and the first detector for a distance of r_{01} along the direction Ω_1, the transition probability is,

$$P_t\,(\,r\,|\Omega_1\,,\,\underline{x}_0\,)\;=\;\frac{I\,(\,r\,)}{I_0}\;=\;e^{\,-\int_0^{r_{01}}\,u\,(\,l\,(\,\Omega_1\,),\,e_0\,)\,dl\,(\,\Omega_1\,)} \qquad (4\text{-}17)$$

And the probability of a γ-ray photon absorbed in the material is,

$$P_a\,(\,r\,|\Omega_1\,,\,\underline{x}_0\,)\;=\;\frac{I_a}{I_0}\;=\;1\;-\;e^{\,-\int_0^{r_{01}}\,u\,(\,l\,(\,\Omega_1\,),\,e_0\,)\,dl\,(\,\Omega_1\,)} \qquad (4\text{-}18)$$
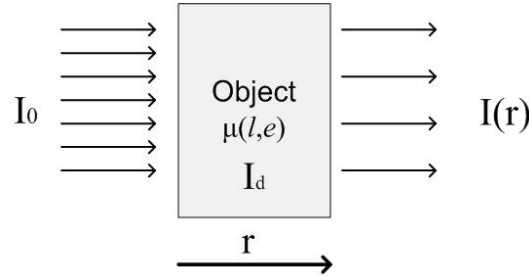
Figure 4.8 Transmission of a beam of photons with energy e through attenuating media with attenuation coefficients $\mu(l,e)$. The flux of photons with initial intensity I_0 transmits through the object with thickness r and attenuation coefficients of $\mu(l,e)$ and exits with reduced intensity I(r).

4.3.2.3 In the First Detector, the γ-ray Emitted from $\underline{x}_0$ in the Direction $\underline{\Omega}_1$ Interacts with Electron via Compton Scattering

To evaluate the probability of a Compton scattering event at the point r_1 in the silicon detector after traversing a distance s in the first detector and assuming no attenuation between the source and first detector we require the total attenuation coefficient for silicon μ_t. μ_t is the sum of the attenuation coefficients for the different types of γ-ray interactions in silicon[60], namely, Compton Scattering μ_{sc}, Rayleigh-Thompson Scattering μ_{rt} and Photoelectric Absorption μ_{pa}. Therefore, the total attenuation coefficient (1/cm) is expressed as,

$$\mu_t(e) = \mu_{rt}(e) + \mu_{pa}(e) + \mu_{sc}(e) \qquad (4\text{-}19)$$

As illustrated in Figure 4.9, the total incident number of incident photons is N_0. At depth x, the number of residual photons after absorption or scatter is N_x. The number of Compton scattered photons in the infinitesimal interval dx should be

$$N_{cs}(x)\,dx \;=\; \mu_{cs}\,N_x\,dx \tag{4-20}$$

Where $\;N_x \;=\; N_0\,e^{-\mu_t x}$

The total number of Compton scattered photons that have occurred in the object at the depth of l is the integral of $N_{cs}(x)$.

$$
\begin{aligned}
N_{cs}(l) &= \int_0^l N_{cs}(x)\,dx \\
&= \int_0^l \mu_{cs}\,N_x\,dx \\
&= \int_0^l \mu_{cs}\,N_0\,e^{-\mu_t x}\,dx \\
&= \frac{\mu_{cs}}{\mu_t}\,N_0\,(1 - e^{-\mu_t l})
\end{aligned}
\tag{4-21}
$$

For a single photon, the probability of Compton scattering is,

$$P(C\,|l) \;=\; \frac{Ncs}{N_0} \;=\; \frac{\mu_{cs}}{\mu_t}(1 - e^{-\mu_t l}) \cdot \tag{4-22}$$

Therefore, the probability of Compton scattering of an incident photon at position of r_1 in the first detector, conditioned on this photon being emitted from $\underline{x_0}$ in the direction Ω_1 where the distance traveled by the photon in the first detector is $r_{1in}=r_1-r_{01}$ and given by

$$
\begin{aligned}
&P(C\,|r_1,\Omega_1,\underline{x}_0)\,P_a(r_1\,|\,r_{01},\Omega_1,\underline{x}_0) \\
&= \frac{\mu_{cs-1}(e)}{\mu_{t-1}(e)}(1 - e^{-\mu_{t-1}(e)r_{1in}})
\end{aligned}
\tag{4-23}
$$
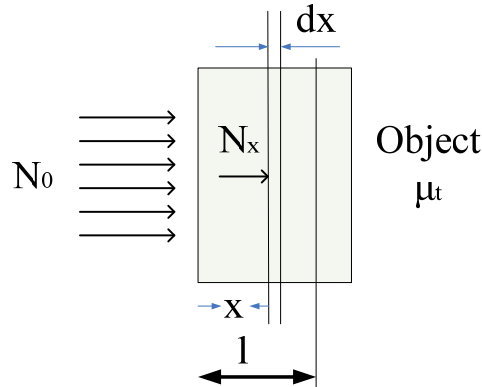
Figure 4.9 The number of N_0 photons that are transmitted through the object consisting of a single material with attenuation coefficient μ_t. N_x is the number of remaining photons without any interaction at depth x.

4.3.2.4 After a Compton Scattering, the Incident Photon Deposits Energy E_1 in the First Detector and Scatters in the Direction Of Ω_2.

As shown in Figure 4.10, the direction of scattered photon can be specified by the two scattering angles θ and φ. The angle φ is called out-of-plane scatter angle, which is uniformly distributed over $[-\pi, \pi)$, and is independent of scattering angle θ and the energy deposited in the first detector. The angle $\theta \in [0, \pi]$ is referred as in-plane scatter angle or Compton scatter angle, which may be represented by the scalar product of incoming photon and scattered photon direction vectors Ω_1 and Ω_2 as,

$$\cos \theta = \Omega_1 \bullet \Omega_2, \tag{4-24}$$
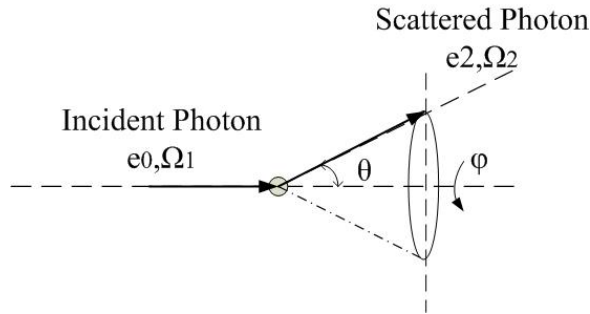
Figure 4.10 Definition of Compton scatter angle $\theta \in [0, \pi]$ and azimuthal scatter angle φ distributing uniformly over $[-\pi, \pi)$. $\cos(\theta)$ is the vector product of the unit vectors Ω_1 and Ω_2.

Therefore, the differential probability involved in this step of the detection process is $p(\Omega_2, e_1 | C, r_1, \Omega_1, \underline{x}_0) d\Omega_2 de_1$, that is the probability of a γ-ray depositing energy e_1 and scattering in the direction of Ω_2 in the first detector given that the γ-ray is emitted from point x_0 and Compton scatters at r_1. Because the out-of-plane scatter angle or azimuthal scatter angle φ is distributed uniformly over $[-\pi, \pi)$, the differential probability may be expressed in term of Compton scatter angle θ and deposited energy e_1. That is

$$
\begin{aligned}
p(\Omega_2, e_1 | C, r_1, \Omega_1, \underline{x}_0) d\Omega_2 de_1 &= p(\varphi, \theta, e_1 | C, r_1, \Omega_1, \underline{x}_0) d\varphi d\theta de_1 \\
&= p(\varphi | C, r_1, \Omega_1, \underline{x}_0) d\varphi p(\theta, e_1 | C, r_1, \Omega_1, \underline{x}_0) d\theta de_1 \\
&= \frac{1}{2\pi} p(\theta, e_1 | C, r_1, \Omega_1, \underline{x}_0) d\theta de_1
\end{aligned}
\tag{4-25}
$$

The Compton scattering joint probability density of the scattering angle and energy of scattered photon, $p(\theta, e_1)$ is proportional to the Compton Double Differential Cross Section function[73, 110], i.e. $f(\theta, e_0 - e_1)$.

$$p(\theta, e_1) = Kf(\theta, e_0 - e_1)\sin\theta \tag{4-26}$$

Where K is a proportionality constant, that is $K = \dfrac{1}{\int_0^\infty \int_0^\pi f(\theta, e)\sin\theta \, d\theta \, de}$. Through the adjustment of K, the integral of $p(\theta, e_1)$ over $e \in [0, \infty]$ and $\theta \in [0, \pi]$ is equal to 1, which implies that the probability that a Compton scatter event occurred is 1.

4.3.2.5 The Scattered Photon Tranvels from the First Detector to the Second Detector

The scattered photon with energy e_2 escapes from the first detector from the point of Compton scattering passes through any attenuating material between the first and second detector and is absorbed by the second detector at location r_2 in the direction of Ω_2. We must compute the probability that the Compton scattered photon at point r_1 with energy e_2 in the direction of Ω_2 will escape from the first detector and pass through any attenuation medium before being absorbed by the second detector at a certain location r_2. Along the direction of Ω_2, the path from r_1 to r_2 consists of three parts, those are r_{1out}, the transmission path in the first detector, r_{12}, the transmission path from the back face of the first detector to the front face of the second detector, and r_{2in} is absorption path in the second detector.

As first, we assume the photon travels from point 0 to a, and $a \in [0, \infty]$, and passes through point a_0. Similarly to step 2, the transmission probability is,

$$P_t(a) = e^{-\int_0^a u_t(l)\,dl} \tag{4-27}$$

The absorption probability of a scattered photon in this path is,

$$
\begin{aligned}
P_a(a) &= 1 - P_t(a) \\
&= 1 - e^{-\int_0^a u_t(l)\,dl}
\end{aligned} \tag{4-28}
$$

The absorption density function of the interaction at position a is the derivative of the above probability P_a

$$
\begin{aligned}
p_a(a) &= u_t \, e^{-\int_0^a u_t(l)\,dl} \\
&= u_t \, e^{-\int_0^{a_0} u_t(l)\,dl} \, e^{-\int_{a_0}^a u_t(l)\,dl} \\
&= P_t(a_0) u_t \, e^{-\int_{a_0}^a u_t(l)\,dl}
\end{aligned}
\tag{4-29}
$$

Thus, the absorption probability of the photon being absorbed between a_0 and a, after transmission between 0 and a_0 is,

$$
\int_{a_0}^a p_a(l)\,dl = P_t(a_0)(1 - e^{-\int_{a_0}^a u_t(l)\,dl})
\tag{4-30}
$$

To determine the probability of photon absorption in the second detector after traveling a distance of r_{2in} after the photon was scattered in the first detector, the total attenuation probability of considering both the first detector and second detector attenuation is u_{t-1}, u_{t-m} and u_{t-2}, respectively.

$$
\begin{aligned}
&P(r_2 | \Omega_2, e_1, C, r_1, \Omega_1, \underline{x}_0) \\
&= \int_{r_2 - r_{2in}}^{r_2} p_a(l | \Omega_2, e_1, C, r_1, \Omega_1, \underline{x}_0)\,dl \\
&= \int_{r_2 - r_{2in}}^{r_2} u_{t-2}\, e^{-\int_0^l u(l')\,dl'}\,dl \\
&= \int_{r_2 - r_{2in}}^{r_2} u_{t-2}\,(e^{-u_{t-1} r_{1out}}\, e^{-u_{t-m} r_{12}})\, e^{-u_{t-2}(l - r_{2in})}\,dl \\
&= (e^{-u_{t-1} r_{1out}}\, e^{-u_{t-m} r_{12}})(1 - e^{-u_{t-2} r_{2in}})
\end{aligned}
\tag{4-31}
$$

4.3.2.6 Absorbed photon deposits its energy in the second detector.

Under the assumption of a planar second detector and photon absorption at location r_2 without further scattering, the probability of depositng energy e_2 at location r_2 is

$$
p(e_2 | r_2, \Omega_2, C, r_1, \Omega_1, \underline{x}_0)\,de_2 = \delta(e_2 - (e_0 - e_1))
\tag{4-32}
$$

4.3.3 Detection Sensitivity and Simplification

As mentioned in the last section, in order to acquire a single valid Compton camera event and calculate detection sensitivity, the whole process is broken down into a sequence of events and the detection sensitivity is the product of all the individual

probabilities. Therefore, according to the chain rule of the probability, equation (4-13) can be written as

$$
\begin{aligned}
s_i = P(D|\underline{x}_0) &= \int_S P(D|\underline{A}, \underline{x}_0) p(\underline{A}|\underline{x}_0) d\underline{A} \\
&= \int_S p(e_2 \mid r_2, \Omega_2, e1, C, r_1, \Omega_1, \underline{x}_0) p(r2 \mid \Omega_2, e1, C, r_1, \Omega_1, \underline{x}_0) \\
&\quad p(\Omega_2, e1 \mid C, r_1, \Omega_1, \underline{x}_0) P(C \mid r_1, \Omega_1, \underline{x}_0) \\
&\quad p(r_1 \mid r_{01}, \Omega_1, \underline{x}_0) P_t(r_{01} \mid \Omega_1, \underline{x}_0) p(\Omega_1|\underline{x}_0) de_2 d\Omega_2 dr_2 de_1 d\Omega_1 dr_1
\end{aligned}
\tag{4-33}
$$

The above formula assumes a perfect detector. Considering the measurement uncertainty, equation (4-7) should be combined with (4-33) to obtain the final detection sensitivity. This multiple integral is very computationally complex. It is essential to simplify the calculation to make it practical for system simulation. The following assumptions are made to simplify the calculation.

1. The object, attenuation medium and detectors are uniform. Therefore, the linear attenuation coefficients depend only on the photon energy. As a result, $u_{t-o}(e)$ is the total attenuation coefficient of the source object in front of the first detector, $u_{t-m}(e)$ is the total attenuation coefficient of the medium between the first detector and the second detector, $u_{t-1}(e)$ is the total attenuation coefficient of the first detector, $u_{cs-1}(e)$ is the Compton attenuation coefficient for the material of the first detector, and, $u_{t-2}(e)$ is the linear attenuation coefficient of the second detector.

2. The deposited energy of scattered photons is completely detected by the second detector. Since energy of incident photon is known, the deposited energy in the second detector is not required for image reconstruction or the uniform Cramer-Rao bound calculation. Therefore,

$$
\int_{S_{e2}} \int p(e_2|r_2, \Omega_2, C, r_1, \Omega_1, \underline{x}_0) p(e_2^{'} \mid e_2) de_2 de_2^{'} = 1
\tag{4-34}
$$

where $e2 \in S_{e2}$ is the set of all possible detected energy.

3. The spatial uncertainty is negligible since: 1) The pixel size of silicon detector can be very small compared to the spatial resolution of the second detector. For example the pixel size of silicon chip is $1.4mm \times 1.4mm \times 1.0mm$,while the intrinsic spatial resolution of the second detector, which is an Anger camera is about 4.1mm (FWHM) [107]. 2) The second detector can be placed

97

further from the first detector such that the effect of spatial resolution of the second detector is trivial. This is at the expense of detection sensitivity if detector size remains constant. Therefore, the conditional probability $p(\underline{z}'_1 | \underline{z}_1)$ and $p(\underline{z}'_2 | \underline{z}_2)$ is approximately a delta function, i.e. $\delta(\underline{z}_1 - \underline{z}'_1)$.

4. The energy measurement error of the first detector is a Gaussian distribution.

5. The photons from $\underline{x}_0$ are emitted uniformly over 4π steradians.

According to the assumptions described above, the distribution of measurement uncertainty is simplified to just one term. This term illustrates the conditional probability density function (pdf) of the energy measurement error for the first detector and may be modeled as a zero-mean Gaussian-distribution. The variance, σ^2, of this distribution is determined by the energy resolution (FWHM) of the silicon detector, which includes two noise sources of silicon detector, ionization noise and electronics noise. Therefore,

$$p(\underline{A}' | \underline{A}) = p(\underline{e}'_1 | \underline{e}_1) \sim N(0, \sigma^2) \tag{4-35}$$

The Compton scattering joint probability density function $p(\theta, e_1 | C, r_1, \Omega_1, \underline{x}_0)$ just depends on the scattering angle θ and deposited energy e_1 in the first detector. Hence, the noisy measurement based on the joint pdf $p(\theta, e'_1)$ is the convolution of the $p(\theta, e_1)$ with $p(e'_1 | e_1)$. That is,

$$p(\theta, e'_1) = \int p(\theta, e_1) p(e'_1 | e_1) de_1 \tag{4-36}$$

Meanwhile, the integral of the noise based joint pdf $p(\theta, e'_1)$ over all energy measurements within the energy measurement threshold $S_{e'_1}$ is the marginal density of θ, i.e. $p_m(\theta)$

$$p_m(\theta) = \int_{e'_1 \in Se'_1} \int p(\theta, e'_1) p(e'_1 | e_1) de_1 de'_1 \tag{4-37}$$

Therefore, both the noise based joint pdf $p(\theta, e'_1)$ and un-normalized marginal density of $p_m(\theta)$ can be calculated in advance to form a discrete table indexed by scatter angle θ and measurement energy e'_1 using numerical integration and convolution and then evaluated by interpolation[87].

According to these assumptions, and combining with (4-37), the detection sensitivity (4-33) may be simplified as,

$$s_i = P(D|\underline{x}_0)$$

$$= \frac{1}{8\pi^2} \frac{u_{cs-1}(e_0)}{u_{t-1}(e_0)} \int_{\Omega 1 \in S_{\Omega 1}} \int_{\Omega 2 \in S_{\Omega 2}} e^{-u_{t-o}(e_0)r_{01}} (1 - e^{-u_{t-1}(e_0)r_{1in}}) e^{-u_{t-1}(e_2)r_{1out}} e^{-u_{t-m}(e_2)r_{12}} (1 - e^{-u_{t-2}(e_2)r_{2in}}) p_m(\theta) d\Omega_1 d\Omega_2 \qquad (4\text{-}38)$$

The detection sensitivity and corresponding individual probabilities are represented in a spherical coordinates. However, it is desirable that the final detection sensitivity be expressed in the Cartesian coordinates because the acquired experimental measurements are based on the block detectors composed of pixels arrays or voxels in the Cartesian coordinates.

As illustrated in Figure 4.11, the differential area dA at an angle φ away from the z point, the distance from the z to the dA is r. The $dA(proj)$ is differential projection area dA on the surface of sphere with radius is r. Therefore, the differential solid angle $d\Omega$ subtended by a differential area dA is equal to the projection of the area $dA(proj)$ divided by the square of the distance r from the point z to the differential area dA. That is,

$$\frac{d\Omega}{4\pi} = \frac{dA(proj)}{4\pi r^2} = \frac{dA \cdot \cos\varphi}{4\pi r^2} \Rightarrow d\Omega = \frac{dA \cdot \cos\varphi}{r^2} \qquad (4\text{-}39)$$

Combining equation (4-39) with (4-38), the detection sensitivity (4-40) is described in the Cartesian coordinates and integrated over all detectable area of the first detector and second detector.

$$s_i = P(D|\underline{x}_0)$$

$$= \frac{1}{8\pi^2} \frac{u_{cs-1}(e_0)}{u_{t-1}(e_0)} \int_{A1 \in S_{A1}} \int_{A2 \in S_{A2}} e^{-u_{t-o}(e_0)r_{01}} (1 - e^{-u_{t-1}(e_0)r_{1in}}) e^{-u_{t-1}(e_2)r_{1out}} e^{-u_{t-m}(e_2)r_{12}} (1 - e^{-u_{t-2}(e_2)r_{2in}}) p_m(\theta) \frac{\cos\Phi_1}{r_1^2} \frac{\cos\Phi_2}{r_2^2} dA_1 dA_2 \qquad (4\text{-}40)$$
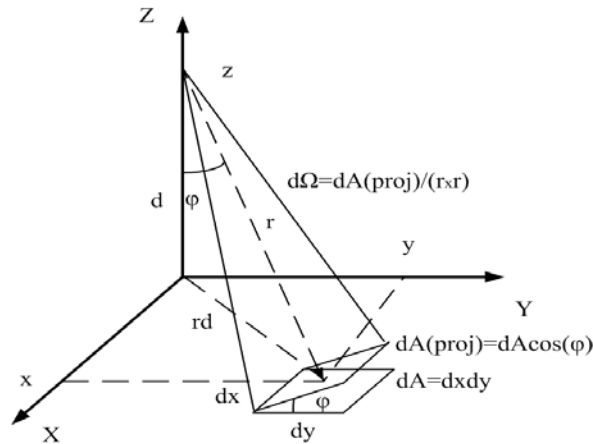
Figure 4.11 The relationship of $d\Omega$ in the spherical coordinates and dA in Cartesian coordinates. $d\Omega$ represents the differential solid angle subtended by dA. $dA(proj)$ is the projected area of dA onto the surface of a sphere with radius r.

4.3.4 Transition Probabilities

The definition of transition probabilities or measurement probabilities a_{ij} are illustrated by Parra [108] and Wilderman[111] for the PET system and Compton system, respectively. As described in equation (4-41), The term a_{ij} is the combination of the probability that an emitted photon from bin i is detected, i.e. the detection sensitivity s_j, and the probability density of a detected event generated in bin i leads to a measurement $\underline{A}'_j$. Detection sensitivity, s_j, is equal to the integral of a_{ij} over all the possible measurements.

$$a_{ij} = p(\underline{A}'_j | \underline{x}_i, D) s_i \qquad (4\text{-}41)$$

$$s_i = \int_{S_{\underline{A}'}} a_{ij} d\underline{A}' = \int_{S_{\underline{A}'}} p(\underline{A}'_j | \underline{x}_i, D) s_i d\underline{A}' \qquad (4\text{-}42)$$

Therefore, combining of (4-42),(4-40) and (4-36), the transition probabilities can be evaluated as.

$$a_{ij} = p(\underline{A}'_j | \underline{x}_i, D) P(D | \underline{x}_i)$$

$$= K \frac{1}{8\pi^2} \frac{u_{cs-1}(e_0)}{u_{t-1}(e_0)} e^{-u_{t-o}(e_0)r_{01}} (1 - e^{-u_{t-1}(e_0)r_{1in}}) e^{-u_{t-1}(e_2)r_{1out}} e^{-u_{t-m}(e_2)r_{12}} (1 - e^{-u_{t-2}(e_2)r_{2in}}) p(\theta, e_1') \frac{\cos\Phi_1}{r_1^2} \frac{\cos\Phi_2}{r_2^2} \qquad (4\text{-}43)$$

$$K = \Delta A_1 \Delta A_2 \Delta e'$$

where $p(\theta, e_1')$ is the Compton scattering based joint probability density function combined with energy and position measurement noise The density is evaluated by interpolation from the pre-calculated 2-D table indexed by Compton scatter angle θ and measured deposited energy e_1' in the first detector. K is the product of pixel area of both detectors and the energy interval, which is constant under the assumption of fixed pixel size and fixed energy interval. The definition of some parameters in (4-43) is described in Figure 4.12.

4.3.5 Interpolating joint probability density matrix blurred with energy and spatial resolution

As illustrated in the equation (4-43), the kernel of derived transition probability function is a pre-calculated matrix, which is the joint probability density function including the effect of Doppler broadening convolved with probability due to energy

resolution and spatial resolution. The matrix indexed by the Compton scatters angle θ and deposited energy in the first detector, e_1.
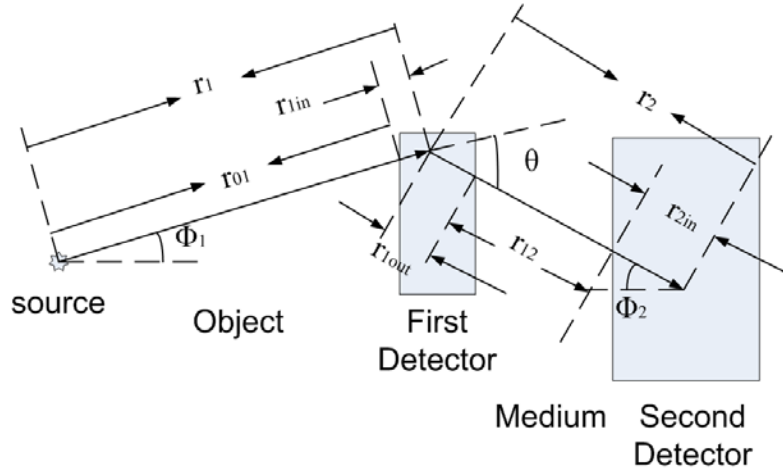
Figure 4.12 Geometry of Compton Camera with two parallel block detectors. Φ_1 is the zenith angle of source photon; Φ_2 is the zenith angle of scattered photon; θ is the Compton scatter angle; $r_1 = r_{01} + r_{in}$; $r_2 = r_{1out} + r_{12} + r_{2in}$

(a)   (b)
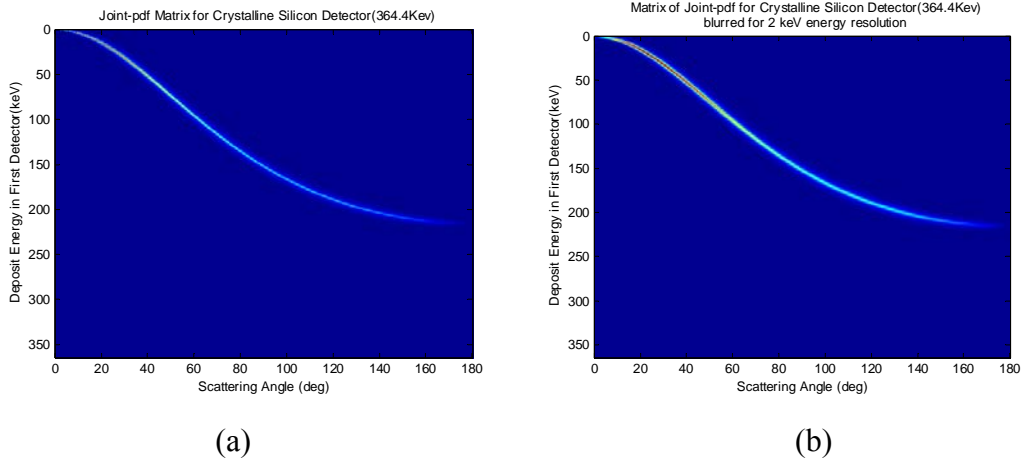
Figure 4.13 The interpolation matrix for a crystalline silicon detector for 364.4keV incoming photons. (a) Joint probability density function. (b) blurred due to 2keV detector energy resolution.

The joint probability density function matrix is calculated by equation (2-14), i.e. the DDCS model for the double-differential cross section. The matrix for crystalline silicon detecting 364.4keV photons is displayed in figure 4.13a, which is indexed by the scattering angle (horizontal axis) and deposited energy (vertical axis). The matrix is

further blurred by a Gaussian distribution function, i.e. equation (2-14) that describes the energy resolution, is displayed in figure 4.13b.

To obtain the blurred interpolating matrix due to the spatial resolution of the first detector and second detector, the uncertainty due to spatial resolution is mapped to energy uncertainty by using the calculated Angular resolution $\Delta\theta$. According to the Compton scattering equation (4-44),

$$\cos\ \theta = 1 - \frac{m_0 c^2}{E_0}\left(\frac{E_1}{E_0 - E_1}\right) = 1 + m_0 c^2 \frac{1}{E_0} - m_0 c^2 \frac{1}{E_0 - E_1} \cdot \tag{4-44}$$

The energy uncertainty ΔE_1 of the first detector contributing to the angular uncertainty $\Delta\theta_{energy}$ is given by

$$\Delta\theta = \frac{d\theta}{dE_1}\Delta E_1 = \frac{m_0 c^2}{\sin\ \theta}\frac{1}{(E_0 - E_1)^2}\Delta E_1 \tag{4-45}$$

Therefore, from equation (4-44) and (4-45), the relationship between the ΔE_1 and $\Delta\theta$ can be expressed as,

$$\Delta\theta = \frac{m_0 c^2}{\sin\ \theta}\left(\frac{1 + m_0 c^2 / E_0 - \cos\ \theta}{m_0 c^2}\right)^2\Delta E_1 \tag{4-46}$$

According to the model expressed by Ordonez[77], the angular uncertainty depends upon the spatial resolution and geometry configuration of the two detectors. For our proposed Compton imaging system with 2 parallel planar detectors, the effects of first detector lateral position resolution, depth position resolution, and the second detector lateral position resolution are illustrated in Figure 4.14. The central distance between two planer detectors is d.

The angular uncertainty introduced by the first detector lateral position resolution is displayed in Figure 4.14(a). For one pixel of the first detector, the lateral length of elements is W. For estimating the maximum error, the photon from the source interacts at the edge of the pixel of the first detector with Compton scatter angle θ. The scattered photon strikes the second detector at O_2. In the back projection, the center position, O_1, of the pixel in the first detector is used for calculation. Therefore, the pixel size introduces angular error, $\Delta\theta_1$, between the true source direction and back projected direction. From illustrated figure,

$$d \cdot \frac{\sin(\ \theta + \Delta\theta_1)}{\cos(\ \theta + \Delta\theta_1)} = \frac{W}{2} + d\ \tan(\ \theta + \Phi) \tag{4-47}$$

Since the distance from source point to the first detector is much larger than the pixel width, W_1, then, Φ is may be ignored, i.e. $\theta + \Phi \approx \theta$. And, $\sin(\theta + \Delta\theta_1)$ and $\cos(\theta + \Delta\theta_1)$ can also be approximated as

$$\sin(\theta + \Delta\theta_1) = \sin(\theta) + \cos(\theta)\Delta\theta_1 \qquad (4\text{-}48)$$

$$\cos(\theta + \Delta\theta_1) = \cos(\theta) - \sin(\theta)\Delta\theta_1 \qquad (4\text{-}49)$$

From equation (4-47), therefore, the angular uncertainty introduced by the first detector lateral position resolution is given as,

$$\Delta\theta_1 = \frac{W/2 \cdot \cos\theta}{W/2 \cdot \sin\theta + d\cos\theta + d\tan\theta\sin\theta}$$
$$= \frac{W/2 \cdot \cos\theta}{W/2 \cdot \sin\theta + d/\cos\theta} \qquad (4\text{-}50)$$

From figure 4.14(b), the depth Z of the pixel in the first detector also contributes to the final angular uncertainty and can be expressed as,

$$d \cdot \frac{\sin(\theta + \Delta\theta_2)}{\cos(\theta + \Delta\theta_2)} = (d + \frac{Z}{2})\tan(\theta) \qquad (4\text{-}51)$$

And,

$$\Delta\theta_2 = \frac{Z/2 \cdot \sin\theta}{(d + Z/2)\tan\theta \cdot \sin\theta + d\cos\theta} \qquad (4\text{-}52)$$

From figure 4.14(c), the second detector lateral position resolution R also contributes to final angular uncertainty, and can be approximated as

$$\Delta\theta_3 = \frac{R/2}{d/\cos\theta} \qquad (4\text{-}53)$$

Therefore, combining equation (4-45) with (4-51),(4-52) and (4-53), the relationship between the position resolution of the two detectors and mapped energy resolution is derived. The interpolation matrix is finally blurred by the above mapped energy resolution by convolving the relative Gaussian function at each corresponding scatter angle θ.

For the Compton imaging system in this example, the pixel size of the silicon detector is 1.4mm by 1.4mm by 1.4mm, the lateral position resolution of the second detector is 4mm, the energy resolution of the first detector is 2keV and the distance between the two detectors is 100mm. The matrix and profile of 30° scatter angle for the crystalline silicon detecting 364.4keV incoming photon blurred by the energy resolution

and the position resolution of the first detector and the position resolution of the second detector are displayed in Figure 4.15(a) and (b), respectively.

In a real application, given the measured energy deposition in the first detector and the calculated Compton scatter angle, the relative probability can be determined by interpolation from the pre-calculated table. This method tremendously decreases the computation time required in image reconstruction or Fisher information evaluation, and the memory for storing the matrix depends on the required calculation resolution.
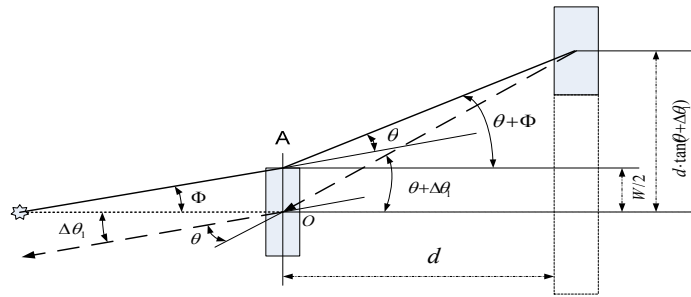
(a) Angular uncertainly due to the first detector lateral position resolution

(b) Angular uncertainty due to the first detector depth position resolution
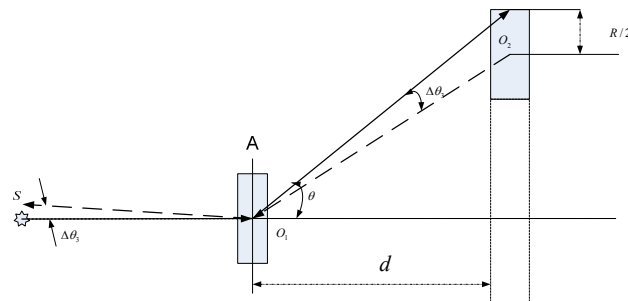
(c) Angular uncertainty due to the second detector lateral position resolution

Figure 4.14 Angular uncertainties introduced by the position resolution. The solid lines represent the true interaction path; the dashed lines show the back-projected path involving the uncertainties.
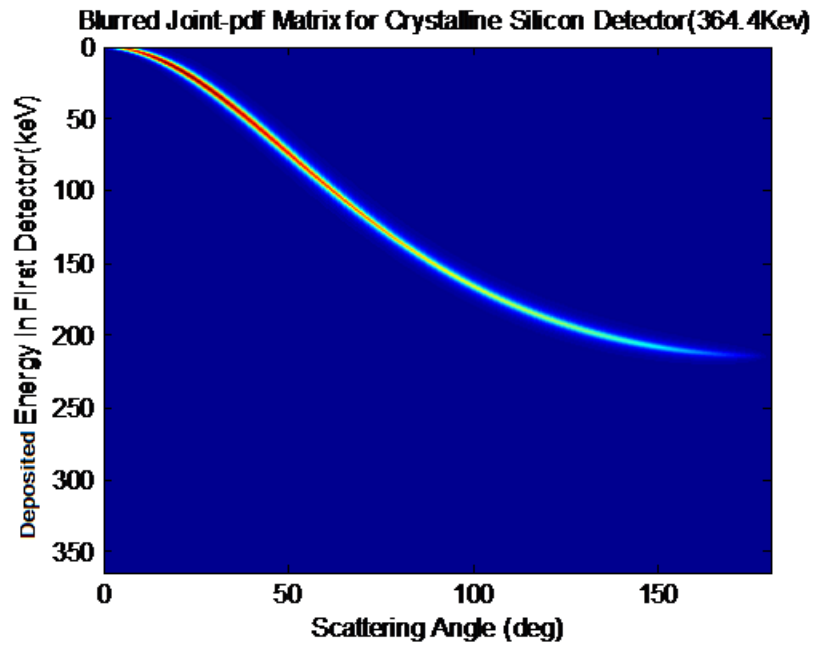
(a)
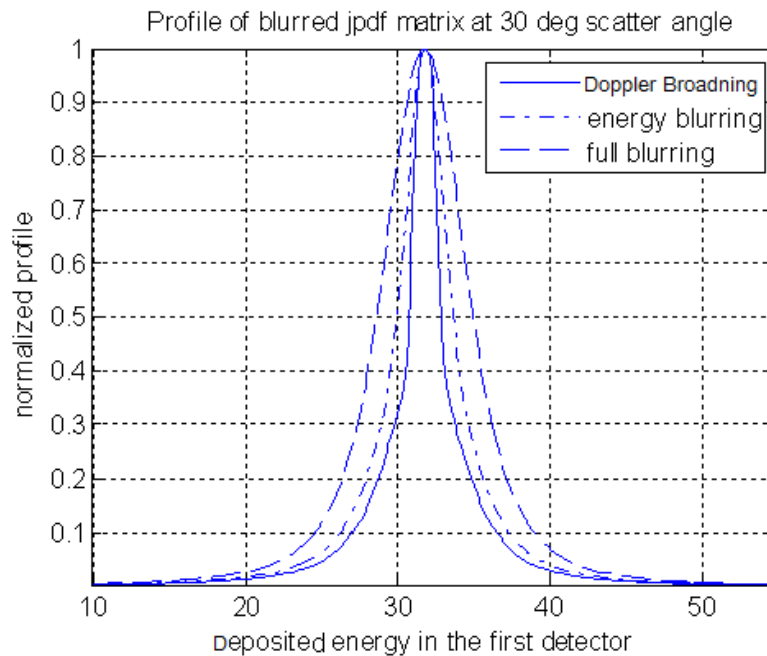
(b)

Figure 4.15 (a) The blurred joint pdf matrix for a crystalline silicon sensor detecting 364.4keV incoming photons. The position resolution of the silicon detector is 1.4mm, energy resolution of silicon detector is 2keV. The position resolution of the second detector is 4mm, and the distance between the two detectors is 100mm.(b) normalized profile at 30° scatter angle for three cases of no blurring, energy blurring, energy and position blurring.

CHAPTER 5

Error Evaluation, Algorithms Validation and Imaging Performance Analysis Using the Modified Uniform Cramer-Rao Bound

Using the algorithms introduced in Chapter 3 and system modeling derived in Chapter 4, in this chapter we will analyze the errors of the FIM and M-UCRB introduced by MCI and the limited numbers of sampled events in the Monte Carlo simulation. We also evaluate the validity and correctness of the system model for both proposed imaging systems and the Monte Carlo simulation. Finally, we discuss and compare system performance of both imaging systems.

5.1 Analysis of Error Introduced by MCI for estimated FIM and M-UCRB

As described in Chapter 3, the M-UCRB, obtained by inverting the FIM, provides a lower bound on the covariance matrix as a function of spatial resolution described by the FWHM of a Gaussian point spread function. The primary obstacles to practical application of the M-UCRB are excessive computer memory requirements and the computational complexity involved in inversion and multiplication of very large matrices for a high-dimensional measurement space. MCI and FFT are feasible mathematical methods to estimate the FIM and M-UCRB. The accuracy of M-UCRB is determined by errors in the calculated FIM that are introduced by the finite number of samples used for MCI. The validity of these feasible mathematical methods and the problem of error propagation due to the limited number of samples will be evaluated below.

5.1.1 Methods and Algorithms for Analysis

5.1.1.1 The Issue of Errors and Error Propagation Introduced by MCI

According to the basic theorem of MCI[91], if the N random independent identical distributed samples x_i are uniformly distributed in a multidimensional volume V, the estimated integral of a function g over the multidimensional volume is,

$$\int g dV = \int dV \times \left\{ \langle g \rangle \pm \sqrt{\frac{\langle g^2 \rangle - \langle g \rangle^2}{N}} \right\},$$
(5-1)

where the denotation of $\langle \; \rangle$ is the arithmetic mean of the N sample points, and

$$\langle g \rangle \equiv \frac{1}{N} \sum_{i=1}^{N} g(x_i) \quad \text{and}$$
(5-2)
$$\langle g^2 \rangle \equiv \frac{1}{N} \sum_{i=1}^{N} g^2(x_i)$$

Therefore, the absolute error involved in MCI is

$$\varepsilon = \sqrt{\mathrm{var}(\langle g \rangle)} = \sqrt{\frac{\langle g^2 \rangle - \langle g \rangle^2}{N}},$$
(5-3)

and the relative error is

$$e = \frac{\varepsilon}{\langle g \rangle}.$$
(5-4)

In the case of the MCI calculated FIM, the absolute error ε involved for each entry of FIM can expressed as,

$$\varepsilon_{ij}^2 = \frac{1}{N^2} \sum_{l=1}^{N} \frac{(p(Y_l / i) \cdot p(Y_l / j))^2}{\left(\sum_{n=1}^{M} p(Y_l / n) \cdot f_n \right)^4} - \frac{1}{N^3} \left\{ \sum_{l=1}^{N} \frac{(p(Y_l / i) \cdot p(Y_l / j))}{\left(\sum_{n=1}^{M} p(Y_l / n) \cdot f_n \right)^2} \right\}^2 .$$
(5-5)

Therefore the error introduced by the MCI is decreases with the square root of the number of sampled events. The error due to the limited number of sampled events is further propagated to the results of M-UCRB illustrated in (3-27), in which the most critical part is the inversion of $[F_Y + \lambda I]$. Therefore, the absolute value of propagated error for this inversion can expressed as,

$$[\varepsilon_{inv}] = \frac{1}{[< F_Y > + \varepsilon_{mcifim} + \lambda I]} - \frac{1}{[< F_Y > + \lambda I]}$$
$$= \frac{[\varepsilon_{mcifim}]}{[< F_Y > + \lambda I]^2 + [\varepsilon_{mcifim}][< F_Y > + \lambda I]}$$
$$\approx [< F_Y > + \lambda I]^{-1} [\varepsilon_{mcifim}][< F_Y > + \lambda I]^{-1}$$
(5-6)

Combining equation (5-6) and (3-27), the values of absolute errors of the estimated M-UCRB are controlled by the target PSF, the value of λ, source object, the

whole FIM and transition probabilities of the evaluated medical imaging system and specified imaging task. To estimate the range of errors, a special case may be evaluated, in which the FIM and error matrix is assumed to be a diagonal matrix that is $F_{ij} = 0$ and $\varepsilon_{ij} = 0$ if $i \neq j$. Therefore, the relative errors e of each element in estimated FIM and elements of the inverse $[F_Y + \lambda I]$ can be expressed by (5-7) and (5-8), respectively.

$$e_{(FIM)ii} = \varepsilon_{ii} / \langle F_{ii} \rangle \quad , \tag{5-7}$$

$$e_{(FIMinv)ii} \approx \frac{\varepsilon_{ii} / (\lambda + \langle F_{ii} \rangle)^2}{1 / (\lambda + \langle F_{ii} \rangle)} \quad . \tag{5-8}$$

$$\approx \frac{\varepsilon_{ii}}{(\lambda + \langle F_{ii} \rangle)}$$

For the case where λ is far less than the value of F_{ii}, the $e_{(FIM)ii} \approx e_{(FIMinv)ii}$.

Therefore, even though the error in M-UCRB introduced by the MCI is decreased by increasing the number of sampled events for MCI, it is difficult to derive a final formula to express the relationship between error and the number of samples. Empirically, confidence interval methods are used to find the number of sampled event for MCI to obtain an acceptable relative error in the calculation of FIM and M-UCRB.

5.1.1.2 Method to Analyze Error and the Number of Samples in Real Applications

In a real application, the relative error confidence interval methods from financial modeling [112, 113] are used here to analyze the error propagation introduced by MCI for FIM and M-UCRB calculation and determine the number of sampled events required for the desired accuracy. Because the MCI calculation of FIM or value of M-UCRB should approach a steady value asymptotically as the number of simulated events increases, for a given number of events, N, the error in the calculated FIM should be less than a desired small value in the pre-specified confidence value.

According to the randomly sampled events x_i with an identical independent distribution with a total number of events, N, the calculated entries of FIM or the value of the bound of variance is f_i and $f_i = f(x_i)$. According to the strong law of large numbers, the estimated value of the elements of the FIM $\hat{y}_N$ evaluated by $\frac{1}{N} \sum_{i=1}^{N} f(x_i)$, will approach the mean value y_t as the number of samples approaches infinity.

From the definition of the Chebyshev inequality for the finite mean and variance, the probability of the accurate estimation of y_t is defined as,

$$P(|\hat{y}_N - y_t| \geq k) \leq \frac{\text{var}(\hat{y}_N)}{k^2}. \tag{5-9}$$

where the estimation of $\hat{y}_N$ is a Gaussian distribution with mean of y_t and with variance of $\frac{\sigma^2}{N}$, and σ^2 is given as

$$\sigma^2 = \frac{\sum_{i=1}^{N}(f_i - \hat{y}_N)^2}{N-1}. \tag{5-10}$$

According to the central limit theorem,

$$\frac{\hat{y}_N - y_t}{\sqrt{\sigma^2/N}} \Rightarrow N(0,1) \text{ as } N \rightarrow \infty, \tag{5-11}$$

and the relative error $e = \left|\frac{\hat{y}_N - y_t}{y_t}\right|$, therefore, the $100(1-\alpha)\%$ confidence interval for the relative error is defined as,

$$P\left(\frac{|\hat{y}_N - y_t|}{\sqrt{\sigma^2/N}} \leq z^{(1-\frac{\alpha}{2})}\right) \approx 1-\alpha, \tag{5-12}$$

$$P\left(e \leq \frac{z^{(1-\frac{\alpha}{2})}}{|y_t|}\sqrt{\sigma^2/N}\right) \approx 1-\alpha. \tag{5-13}$$

Therefore, for a given confidence interval $(1-\alpha)$ and maximum desired relative error $e_d \geq 0$, and $P(e \leq e_d) \approx 1-\alpha$, the number of sampled events N required to achieve the desired relative error using MCI is

$$N = \frac{\sigma_N^2\left[z^{(1-\alpha/2)}\right]^2}{y_t^2 e_d^2}. \tag{5-14}$$

For example, for a 95% confidence interval, z-score associated with the probability of 0.025 is $z^{(1-\alpha/2)} = 1.96$.

In the real application, the sample mean $\hat{y}_N$ and variance var(f_N) can be evaluated on the fly by

$$\hat{y}_N = \hat{y}_{N-1} + \frac{f_i - \hat{y}_{N-1}}{N}, \tag{5-15}$$

$$\sigma_N^2 = \left(\frac{N-2}{N-1}\right)\sigma_{N-1}^2 + N(\hat{y}_N - \hat{y}_{N-1})^2. \tag{5-16}$$

Therefore, in the calculation of elements in FIM, we specified $z^{(1-\alpha/2)} = 1.96$ and relative error $e_d \leq 0.005$ to find the suitable number of Monte Carlo events N.

5.1.2 Analysis and Results

In this section, the correctness and validity of the FIM computed using MCI and the M-UCRB obtained by FFT is compared with the original direct calculation method for a low dimensional image space. The propagated errors introduced by MCI were further evaluated and analyzed. The medical imaging system illustrated here is the Argus NaI Anger Camera with HEGP parallel-hole lead collimator for imaging 364.4keV photons. The system spatial resolution at 10cm is 12.6mm, and then, point source response function is described as a two dimensional Gaussian function with the standard deviation of 5.3508mm. In this study, a thin disk source of I^{131} with given diameter is located 10cm from the surface of the collimator. The activity is uniformly distributed in the disk. The image pixel size is 0.4mm by 0.4mm, and the total number of pixels depends upon the diameter of the disk.

5.1.2.1 Evaluation of Validity of MCI Calculated FIM

A disk with diameter of 13.2cm is simulated and the corresponding image space is 33×33 pixels. Thus, the full size of the Fisher information matrix is 1089×1089.

(A)   (B)
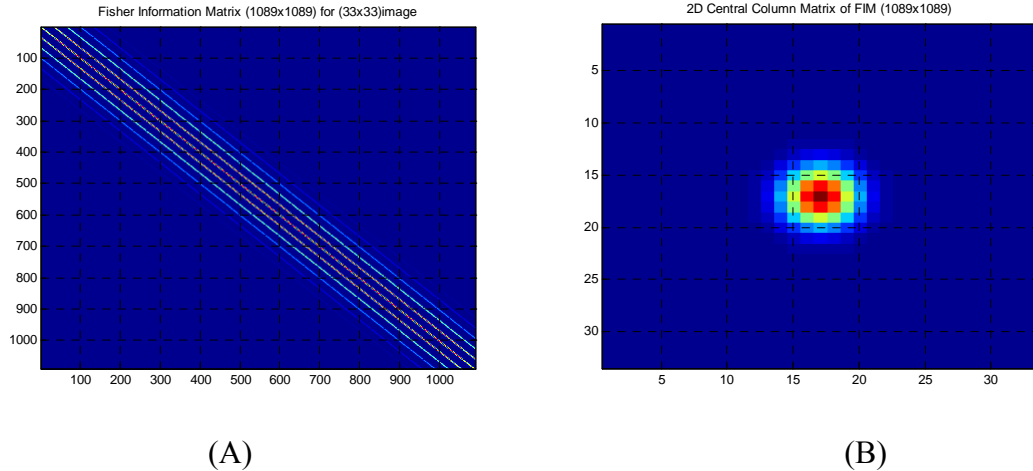
Figure 5.1 (A) Full Fisher information matrix for 33×33 image. Size of FIM is 1089×1089. (B) Center column of the Fisher information matrix reshaped as 2D matrix for the uniform source 13.2cm diameter disk imaged by the conventional Anger Camera with HEGP collimator. (12.6mm FWHM at 10cm)

In figure 5.1A, the normalized full Fisher information matrix calculated by equation (3-19) is displayed, and is clearly a block Toeplitz matrix or block diagonal-constant matrix. The central column of the FIM is re-shaped as a two dimensional matrix and shown in figure 5.1B, which is denoted as 2D central column matrix. The central profiles of the 2D column matrices calculated by conventional methods (3-19) and Monte Carlo integration (3-24) with 2 million independent sampled events are displayed and compared in figure 5.2A. The relative error of two profiles is less than 0.5% illustrated in figure 5.2B, the maximum error is about 5×10^{-3}.

(A)   (B)
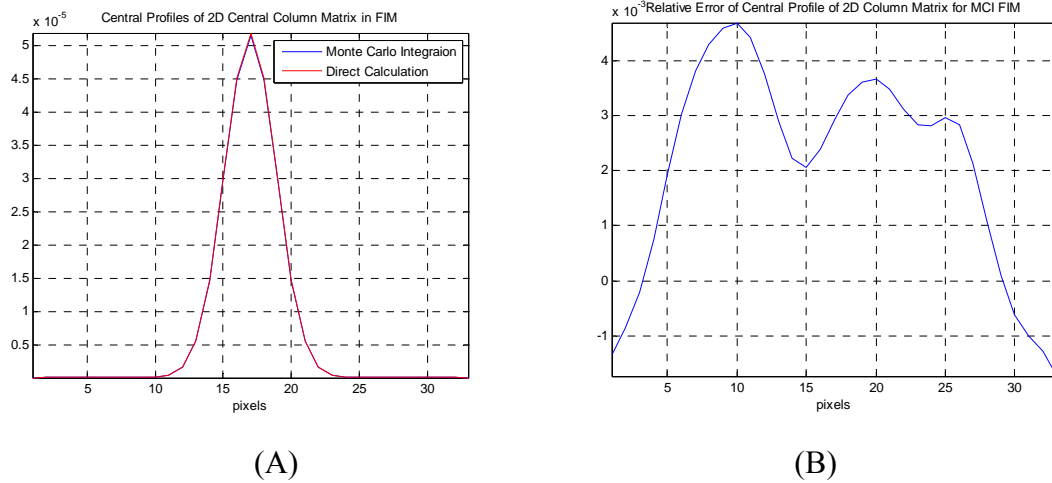
Figure 5.2 (A) Central profiles of 2D central column matrix in the FIM calculated by direct method and Monte Carlo Integration, respectively. (disk with 13.2cm diameter). (B) The relative error of Monte Carlo calculated central profile of 2D column matrix in FIM with 2 million events.

5.1.2.2 Evaluation of FFT Calculated M-UCRB

To avoid the computational complexity of inverting the Fisher information matrix, the FFT method is used to calculate the M-UCRB. The FFT method is based on the assumption of local shift invariance. In this case, the full FIM is a block circulant matrix, as shown in figure 5.1A, whereas, the true FIM is a block Toeplitz matrix or block diagonal-constant matrix.

It is necessary, therefore, to compare the calculated error of M-UCRB by FFT with the original direct method. For calculating the M-UCRB, the control parameter λ is pre-specified as $1e^{-20}$, which guarantees that the actual point spread function is close to

the target point spread function in our presented studies. The desired PSFs are two-dimensional Gaussian functions with FWHM ranging from 0.5cm to 3cm.

(A)   (B)
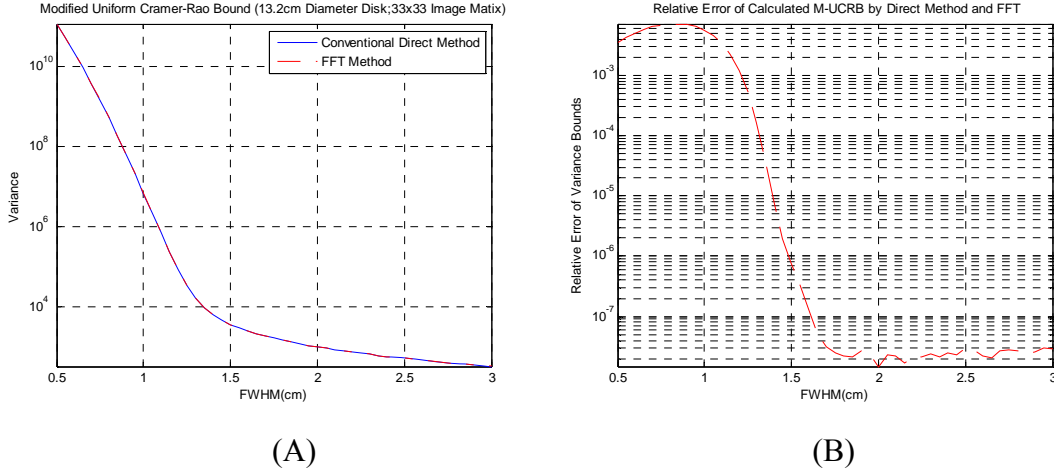
Figure 5.3 (A)M-UCRB curves calculated by conventional direct matrix multiplication and FFT. The source is a thin uniform with diameter of 13.2cm and image matrix of 33×33. (B) Relative error of M-UCRB curves calculated by conventional direct matrix multiplication and FFT.

In Figure 5.3, the M-UCRB curves calculated by conventional direct matrix methods and FFT are compared. The max relative error is less than 0.5% as the FWHM of target PSF ranges from 0.5cm to 3cm. When the FWHM of target PSF is close to or larger than the system spatial resolution of 12.6mm, the two curves essentially overlap, and the relative errors decrease rapidly to about 0.005%.

5.1.2.3 Estimated Errors Involved from Monte Carlo Simulation for a Diagonal FIM

According to equations (5-7) and (5-8), the relative error can be estimated by assuming a diagonal FIM. The elements do not equal to zero is the diagonal elements in the FIM. The FIM and corresponding M-UCRB are estimated using 20000 samples. The central profile of this diagonal FIM for 500 independent trials and the variance of FIM are displayed in the figure 5.4A, 5.4B, respectively. The calculated relative error is about 0.0026.

The corresponding curves for the M-UCRB are displayed in Figure 5.5, which is calculated with $\lambda = 1e^{-20}$. From this evaluation, the relative errors are almost identical for estimated FIM and M-UCRB.
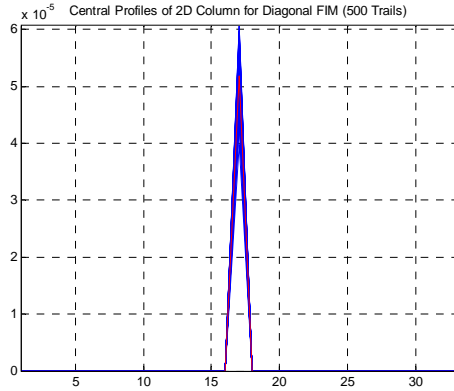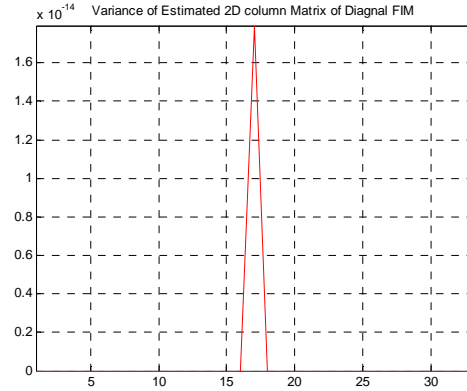
(A)   (B)

Figure 5.4 (A) Central profiles of 2D central column matrices of estimated diagonal FIM by MCI for 500 trials, each trial has 20000 samples. (B) Variance of estimated diagonal FIM for 500 trials. The relative error is 0.0026.
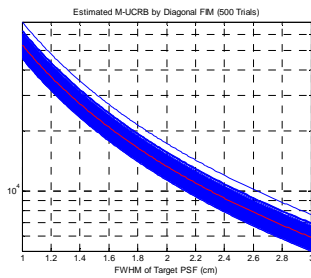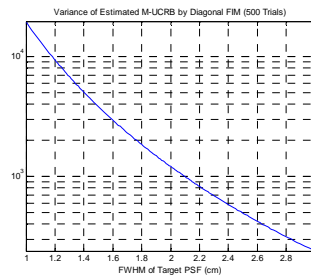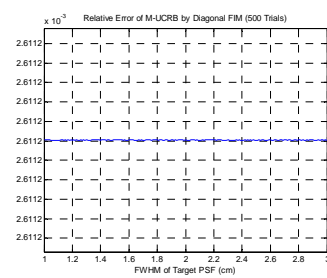
(A)   (B)   (C)

Figure 5.5 (A) Estimated M-UCRB by diagonal FIM with $\lambda = 1e^{-20}$ for 500 trials, each trial has 20000 samples. (B) Variance of estimated M-UCRB for 500 trials. (C) The mean relative errors for estimated FM-UCRB for 500 trials.

5.1.2.4 Error Propagation for FIM and M-UCRB due to Monte Carlo Calculation

The central column of FIM and corresponding M-UCRB calculated using 20000 samples were estimated. The central profile of 2D central column matrix of FIM for 500 independent trials and the variance curve are displayed in Figure 5.6A and 5.6B, respectively. Figure 5.6C, shows that the mean relative errors are around 0.00275.

The estimated M-UCRBs with $\lambda = 1e^{-20}$ for 500 independent trials are displayed in figure 5.7A. As shown in figure 5.7B and 5.7C, values of both variance and relative error are determined by the FWHM target PSF and the relative errors. For large FWHM of the target PSF the errors are small, whereas these propagated errors are amplified about a

113

factor of 4 when the FWHM of the target PSF is small, that is when the target PSF is less than the system response function. The minimum relative errors are around 0.008.

(A)   (B)   (C)
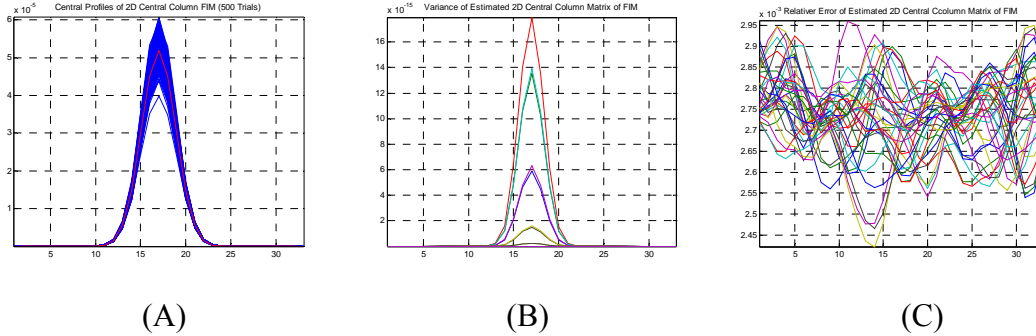
Figure 5.6 (A) Central profiles of 2D central column matrices of estimated central column FIM by MCI for 500 trials, each trial has 20000 samples. (B) Variance of the 2D central column Matrix of estimated diagonal FIM for 500 trials. (C) Relative Error of Estimated 2D central column Matrix of FIM, the relative error is less than 0.0026.

(A)   (B)   (C)
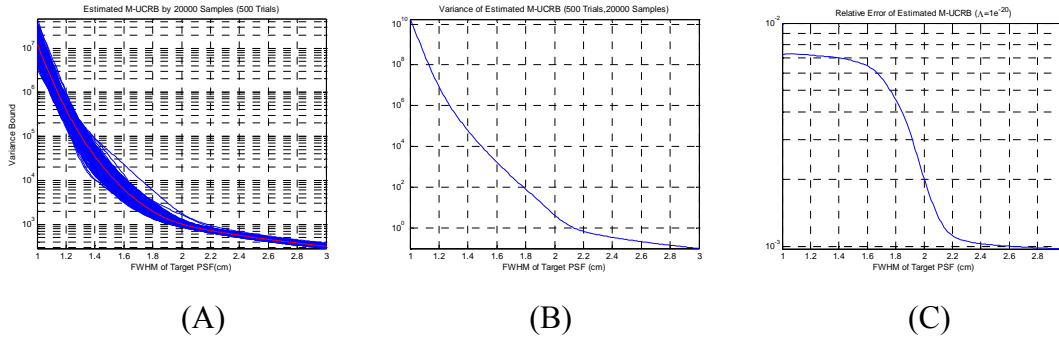
Figure 5.7 (A) Curves of Estimated M-UCRB with $\lambda = 1e^{-20}$ for 500 trials, each trial has 20000 samples; red curve is the mean value (B) Variance of estimated M-UCRB for 500 trials. (C) The mean relative errors for estimated FM-UCRB for 500 trials.

5.1.2.5 Estimated Number of Samples for a Relative Error in the 95% Confidence Interval

As illustrated above, the FIM estimated by MCI and the M-UCRB calculated by FFT under the spatially invariant approximation are close to the true FIM and M-UCRB calculated by conventional direct methods as the number of random sampled events becomes large enough. The estimated values and relative errors of the central pixel in the 2D central column matrix of FIM changes with the number of the sampled events as shown in Figure 5.8A and 5.8B, respectively. In Figure 5.8C, the upper bound of relative error in the 95% confidence interval for this entry of FIM is displayed. This is calculated

by equation (5-13) and $z^{(1-\alpha/2)} = 1.96$. For the case, in which for $e_d \leq 0.005$, the minimum number of samples required is 2.5 million.

The calculated M-UCRBs based on the estimated FIMs with increasing number of sampled events are shown in Figure 5.9A. The FWHM of target PSF is 1.5cm and the λ is equal to 1e^{-20}. The calculated value of M-UCRB approaches the true value gradually and the relative error can achieve 0.001 as shown in Figure 5.9B. From Figure 5.9C, for $e_d \leq 0.005$ in the 95% confidence interval for M-UCRB, the minimum number of samples required is 4 million. Therefore, M-UCRB calculation increases the error and requires more samples than FIM estimation to obtain an acceptable relative error.

(A)   (B)   (C)
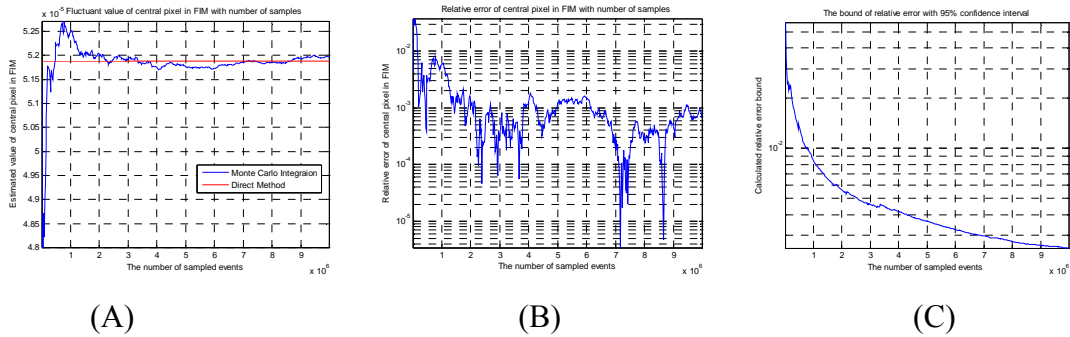
Figure 5.8 (A) Calculated values of central entry of FIM stabilize gradually with increasing number of sampled events for Monte Carlo integration. (B)The relative error decreases with the number of samples. (C) The bound of relative error for 95% confidence interval decreases with the number of samples.

(A)   (B)   (C)
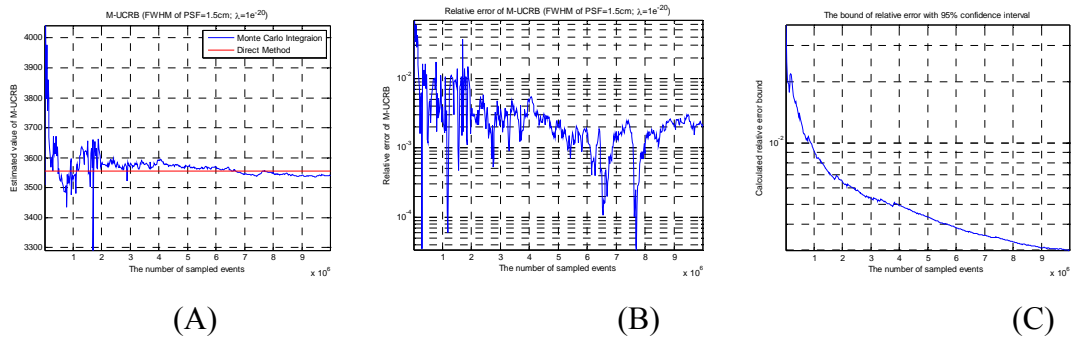
Figure 5.9. (A)Calculated values of M-UCRB stabilize gradually with increasing number of sampled events for FIM obtained by MCI. (FWHM of target PSF is 1.5cm and λ is 1e^{-20}. (B)The relative error decreases with the number of samples. (C) The bound of relative error for 95% confidence interval varies with the number of samples.

5.1.3 Conclusion

As presented above, use of Monte Carlo Integration to estimate the Fisher information matrix and employing a fast Fourier transform to calculate the modified uniform Cramer-Rao bound are shown to be efficient and useful tools to evaluate imaging system performance. Using MCI can calculate the FIM for a medical imaging system with a more complex or higher dimensional system matrix, such as a Compton Imaging system. Under the spatially invariant approximation and the properties of block circulant FIM, calculating M-UCRB using FFT requires only one column of the full FIM and obtains the similar results calculated by the original matrix algorithm. This decreases the computational complexity, and also requires much less memory compared to memory requirements for direct full FIM multiplication and inversion. For example, in the above study, the full FIM is 1089×1089, whereas, the required 2D central column matrix is just 33×33. The calculated errors introduced by Monte Carlo Integration for FIM are propagated to the estimated M-UCRB. The final relative error of M-UCRB is controlled by many factors, such as the number of samples, the target PSF, source object, the size of reconstructed image, and the imaging system being evaluated. The relative error will decrease with increasing the number of samples for MCI, and the propagated errors are amplified when the FWHM of target PSF is small. In this case, more sample events for MCI will be required to achieve acceptable relative error. But the error become negligible as the FWHM of the target PSF increases, especially as the FWHM of target PSF become larger than the system point source response function. For specific applications, the suitable number of sampled events may be found using the confidence interval method for pre-specified and desired relative error.

5.2 Validation and Verification for Monte Carlo Simulation and M-UCRB for Compton Imaging System

5.2.1 Validation of Compton Imaging Random Variables Sampling System

The proposed Compton Scattering random number sampling system is an independent Monte Carlo simulation system that focuses on the Compton scattering process of the photon interacting with the material in the first detector. To speed up the

116

random number sampling, most parts of the simulation are based on the technique of discrete cumulative distribution. Therefore, the CIRVS system described in Chapter 3 needs to be validated before using it for calculating the Cramer-Rao bound. Since it is difficult to experimentally determine the various effects of the many different physical processes that affect detector system performance, the general purpose Monte Carlo simulation system Geant4 with LECS package (Low energy Compton Scattering), which embeds the codes to simulate the effect of Doppler broadening on Compton scattering, is selected to validate the CIRVS system under similar simulation conditions. Because of the limitations of Geant4 with the LECS package, the material of the simulated first detector is atomic silicon while the actual detectors are crystalline and the values of position and energy uncertainty will be different from the actual detector. The validation primarily focuses on the following three parts, the distribution of absorbed energy with the effect of Doppler Broadening, the conic intersection of the interaction of the scattered photon on the second detector, and the distribution of scattering angle.
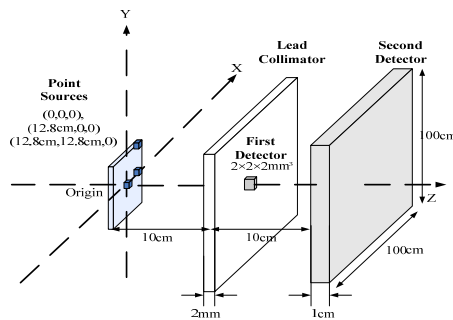
Figure 5.10 Illustration of geometrical configurations used to validate the Compton imaging random variables sampling system.

The simulation setup and geometric configuration for validation is shown in figure 5.10. The first detector is 2mm by 2 mm by 2mm and constructed of atomic silicon. Its 4 edges are surrounded by lead shielding to prevent emitted photons from impinging directly on the second detector. The center position of the silicon detector is located 10cm from the source, and is located at the zero point in the x-y plane. The material of the second detector is NaI and it is 100cm by 100cm by 1cm thick and is parallel to the first detector. The coordinates of the center of the front face of the first detector are 0cm, 0cm, 20cm along the x,y,z axis, respectively. Three 364.4kkeV sources

are located on the x-y plane at z = 0. The sources are .002 mm square located at (0,0),(12.8cm,0), and (12.8cm,12.8cm).

5.2.1.1 Validation of the Effect of Doppler Broadening

To validate the effect of Doppler broadening, a total of 0.2 million scattering event distributed over scattering angles of 30°, 60° and 90° acquired from the CIRVS and GEANT4 (LECS) Monte Carlo simulations. The energy probability distributions of CIRVS are compared with distribution obtained from the theoretical calculation by the Compton Double Differential Cross Section formula (CDDCS) and GEANT4 (LECS) Monte Carlo simulation, respectively. According to the Compton scattering formula for 364.4keV incident photons, the ideal value of energy absorbed by the silicon detector or the central energy of the distribution, for 30°, 60° and 90°, are 31.7keV, 95.6keV and 115.4keV, respectively.

(a)

(b)
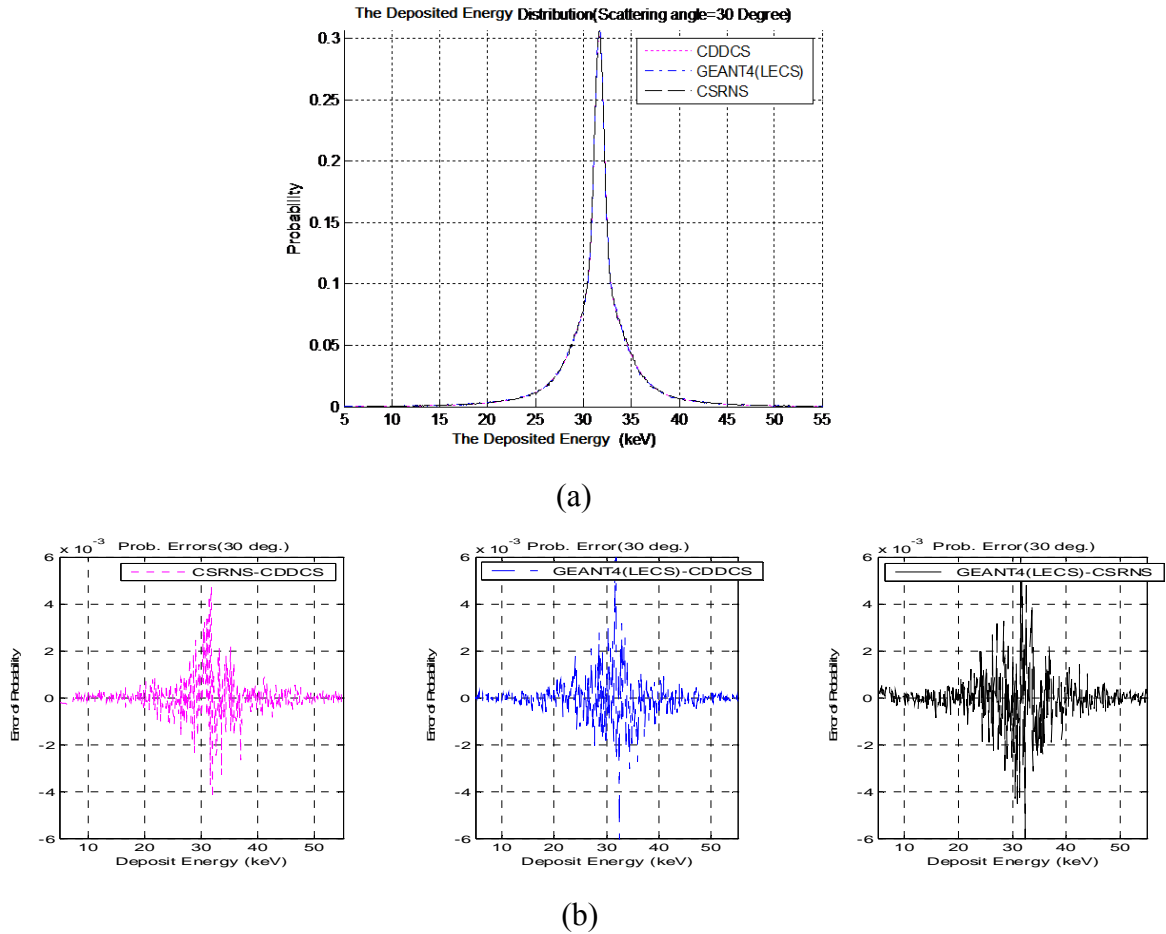
Figure 5.11 Comparison of the probability distribution profiles (a) and errors(b) at 30° scattering angle for Geant4(LECS), CIRVS, and CDDCS calculation.

The validation and comparison results for 30°, 60° and 90° are illustrated in Figures 5.11, 5.12 and 5.13, repetitively. In each group of figures, the subplot (a) is a comparison of the deposited energy probability distributions at the given scattering angle obtained using CIRVS, GEANT4 (LECS) and CDDCS calculations. The area under each curve is normalized to one. Subplot (b) illustrates the differences between the probabilities of three datasets. The probability distributions, which illustrate the effect of Doppler Broadening, from CIRVS, GEANT4 (LECS) and CDDCS calculations at different scattering angles, are similar. The maximum error is around 6×10^{-3} at the center of the profile. Because the values of the CDDCS calculation are the mean value at each energy, the total mean square error (MSE) for GEANT4 (LECS) and CIRVS are $1.09e^{-6}$ and $8.4e^{-7}$.

(a)

(b)
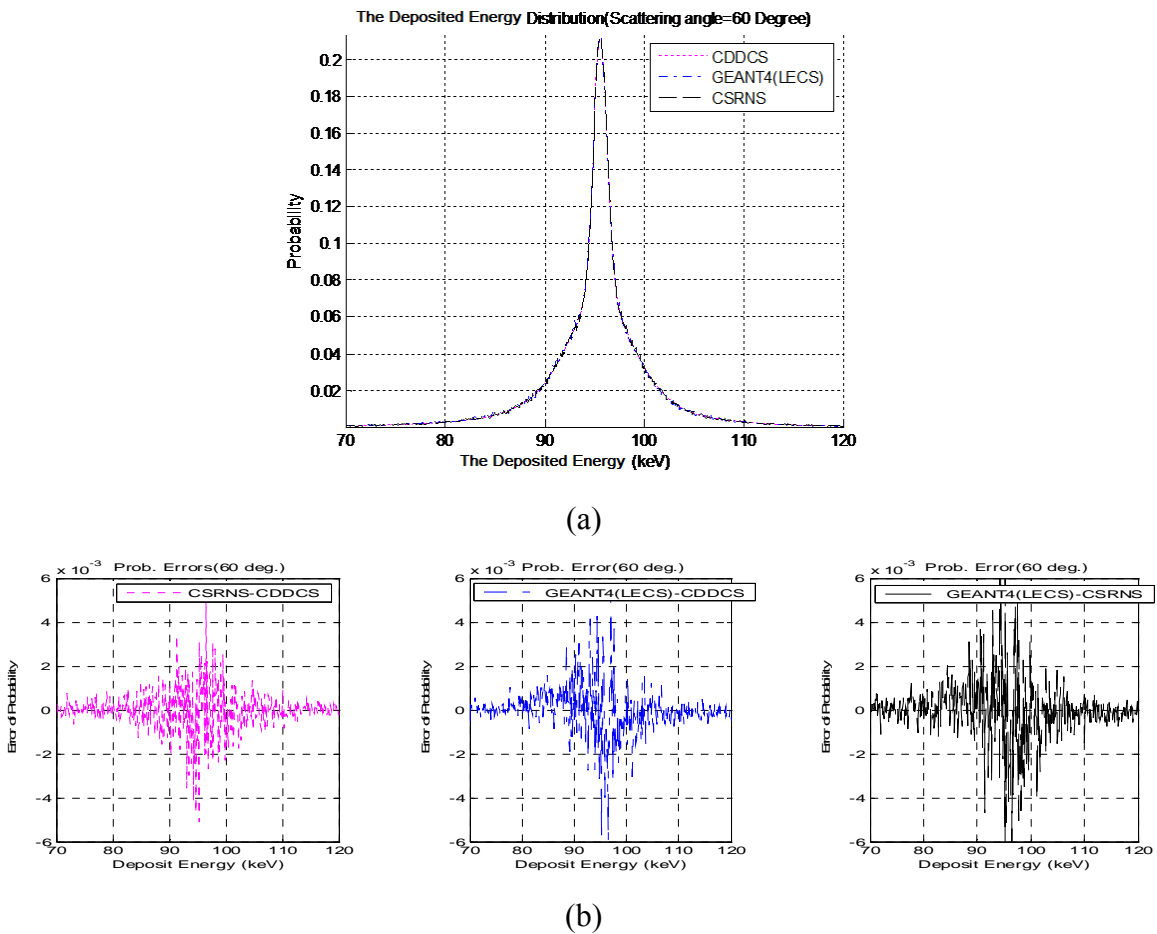
Figure 5.12 The probability distribution profiles(a) and errors(b) at 60° scattering angle comparisons for Geant4(LECS), CIRVS, and CDDCS calculation.

119

The Deposited Energy Distribution(Scattering angle=90 Degree)
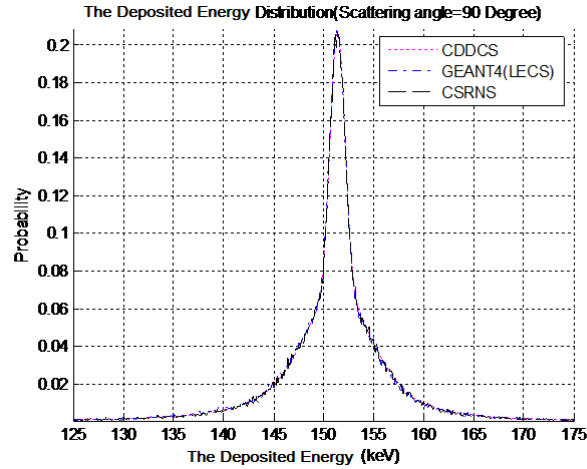
(a)
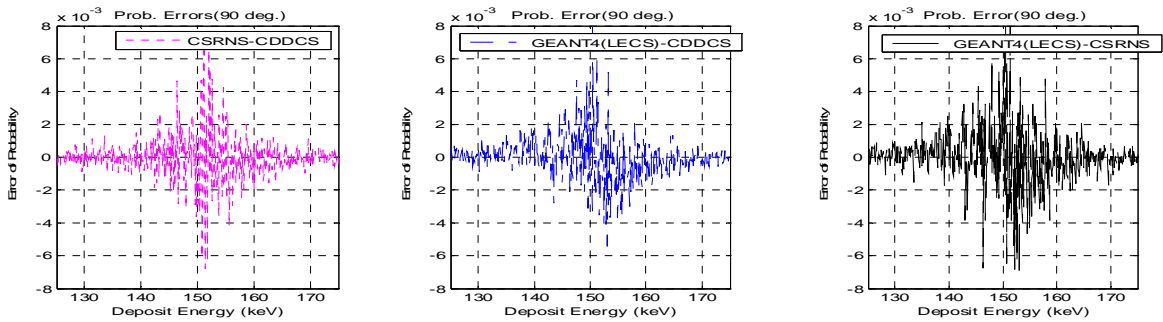
(b)

Figure 5.13 Comparisons of the probability distribution profiles (a) and errors(b) at 90° scattering angle for Geant4(LECS), CIRVS, and CDDCS calculation.

5.2.1.2 Validation of the Distribution of Scattering Angle

Theoretically, the scattering angle distribution could be obtained from the Klein-Nishina Differential Cross Section (KNDCS). The 0.2M scattering angles values were sampled from Geant4 (LECS) and CIRVS system. The three curves of scattering angle probability distribution scattering angle were displayed on Figure 5.14(a), meanwhile, the square errors between Geant4 (LECS) and KNDCS, CIRVS and KNDCS; and errors between Geant4(LECS) and CIRVS are shown in Figure 5.14(b). Considering that calculated results from KNDCS is the mean value of the probability, the mean square errors of Geant4(LECS) and KNDCS are $5.81e^{-8}$ and $6.15e^{-8}$,respecitively. CIRVS is validated with Geant4(LECS) with a maximum error is 2.0e-3.
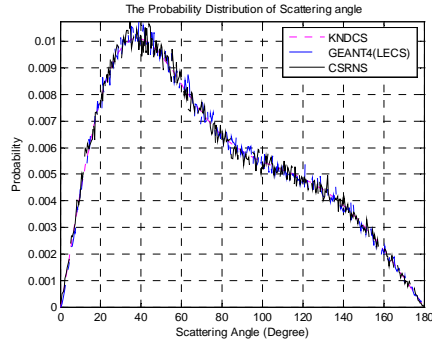
(a)
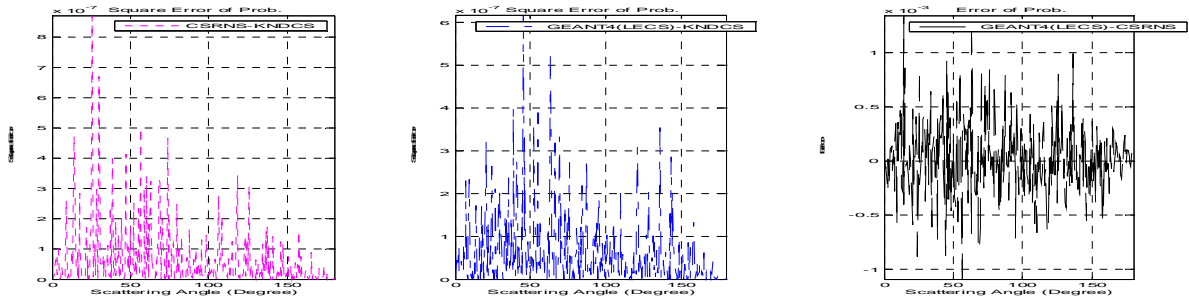
(b)

Figure 5.14 (a)The silicon scattering angle probability profile for 364.4keV photons (b)left: square errors between CSRNS and Klein-Nishina DCS calculation; middle: square errors between Geant4(LECS) and Klein-Nishina DCS calculation; right: Error between Geant4(LECS) and (CIRVS) system.

5.2.1.3 Validation of Location that Scattered Photons Impinge on the Second Detector

In the Monte Carlo simulation, photons from a point source impinge on the second detector after scattering from the silicon detector. Ignoring the interaction depth in the second detector and assuming that the photons are scattered from a single small pixel in the silicon detector, the scattered photons will form a conic section on the second detector for a specific scattering angle. Doppler broadening only affects the energy distribution for a given scattering angle in the simulation. The thickness of the conic intersection is determined by the pixel size on the first detector, the distance between the source plane and the first detector and distance between the first detector and the second detector. The goal of this part of the validation is to prove the accuracy of the three

121

dimensional graphic rotations and intersection of the cone of scattered photons and the plane of the second detector. In both the GEANT4(LECS) and CIRVS simulation, the original photons are emitted from three different point source locations and scattering angle is fixed as 30°, 60° and 90°. In each of the nine groups of data, 1 millions scattered photons are detected by the second detector.

(a)   (b)
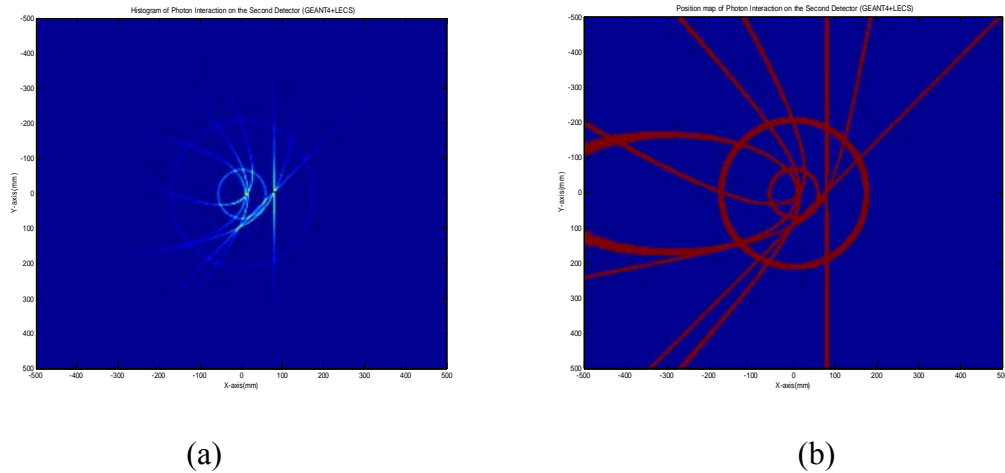
Figure 5.15 The two dimensional histogram (a) and position map(b) of the scattered photons intercepting the second detector as simulated by GEANT4 (LECS). The point sources are located at (0,0),(128mm,0) and (128mm,128mm); and the scattering angles are 30°,60° and 90°.

(a)   (b)
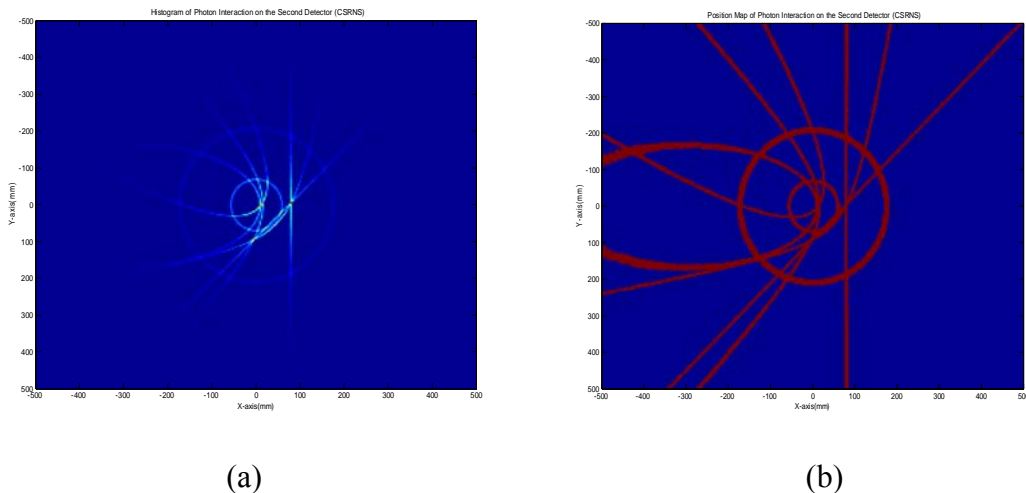
Figure 5.16 The two dimensional histogram (a) and position map (b) of the scattered photons on the second detector simulated by CIRVS System. The point sources are located at (0,0),(128mm,0) and (128mm,128mm) and scattering angles are given as 30°,60° and 90°.

As illustrated in Figure 5.10, the size of the second detector is 100cm by 100cm. In both the GEANT4 (LECS) and CIRVS simulation, the photons interacting in the second detector are mapped into a two dimensional histogram in which each pixel size is 4mm by 4mm. The two-dimensional intensity histogram and interaction position map, in which pixel equals to one if the value of relative pixel in the histogram is larger than one, are shown in figure 5.15 (a),(b) and 5.16 (a),(b) for the dataset obtained from GEANT4(LECS) and CIRVS. From the comparison, the positions and shapes of the different conic sections from both systems match. The relative mean square error of the two histograms, which is the detection sensitivity error between two simulation systems, is around $3.2e^{-5}$.

5.2.2 Analysis of the MCI Calculated FIM and FFT Based M-UCRB for the Compton Imaging System

As described earlier, in order to solve the problems of computational complexity and very large memory requirements, the FIM is calculated by MCI; and the M-UCRB may be computed by FFT assuming that the Fisher information matrix is shift invariant and a block circulant matrix. Along with the statistical models of the imaging systems and random number sampling techniques, the accuracy of the MUCRB calculation depends on the number of simulated measurement events. An insufficient number of simulated events will introduce unacceptable error in final results while over sampling will increase computation time and storage requirements.

In the next section we discuss the use of confidence intervals methods to determine the appropriate compromise between accuracy and computation time for these estimates.

5.2.2.1 Output Analysis for Monte Carlo Integration based FIM

Using the Chebyshev Inequality and confidence interval method as illustrated in section 5.1, the well suitable number of simulated measurement events was found. This number of random variable guarantees the probability of relative error of calculated FIM item is less than a given trivial value equals to the pre-specified confidence value.

(a)   (b)
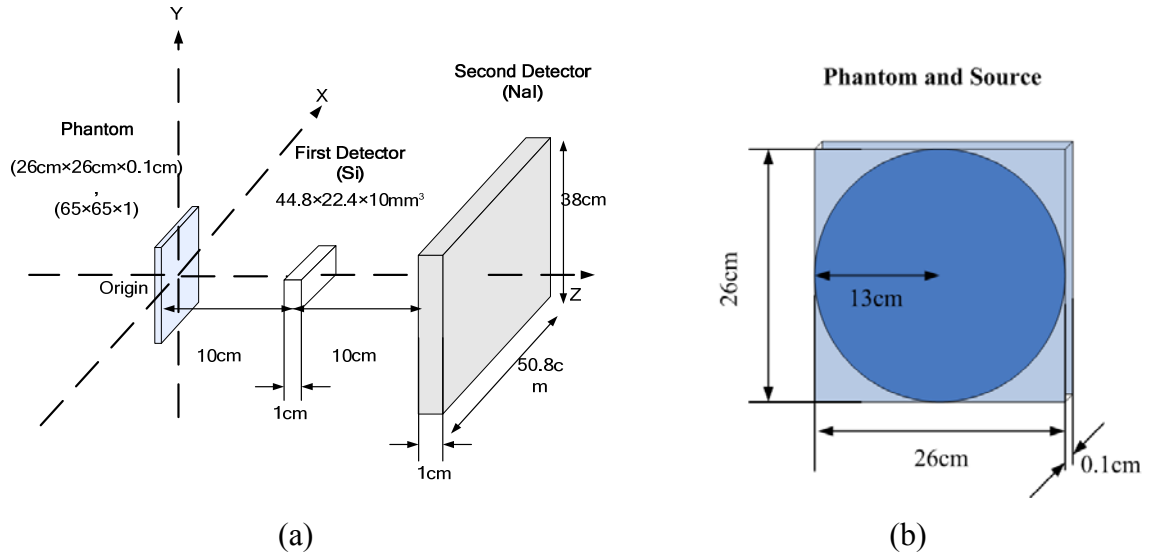
Figure 5.17 (a) Geometrical configuration of the Compton scatter camera simulation. (b) The thin disk source emitting 364.4keV photons.

As shown in the figure 5.17(a), the simulated Compton camera system has a similar geometrical configuration as Figure 5.10. The primary difference is that the simulated phantom, shown in figure 5.17(b), is a 13.2 cm diameter disk in a 65×65×1 pixel field of view. The size of each pixel is 4mm×4mm×1mm. The source emits 364.4keV photons, and there is no radioactivity outside of the disk.

(a)   (b)
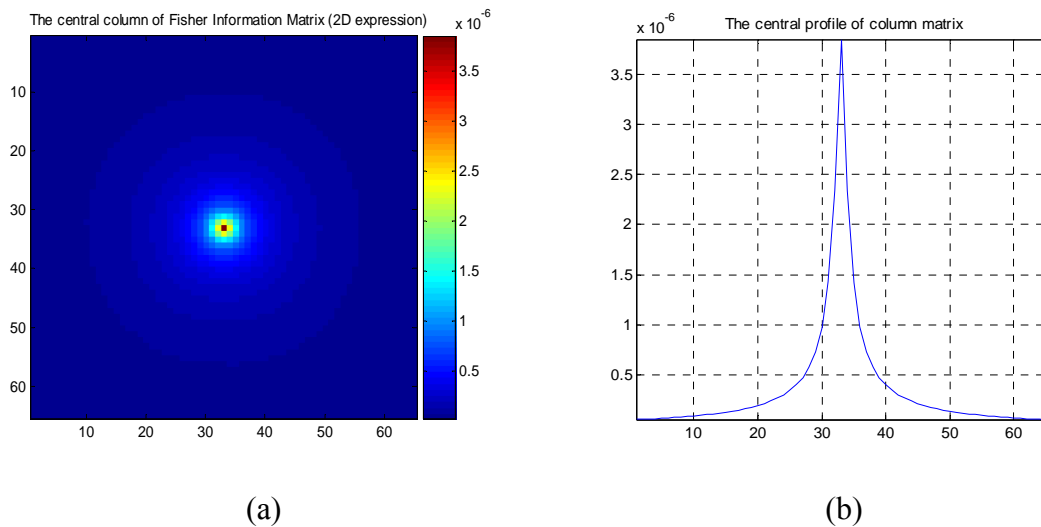
Figure 5.18 (a) Central column of Fisher information matrix expressed a two dimensional matrix/image (b) The central profile of the column matrix.
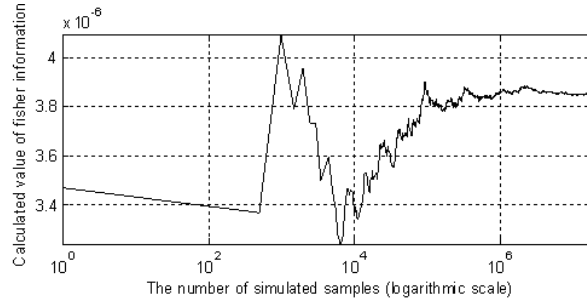
(a)
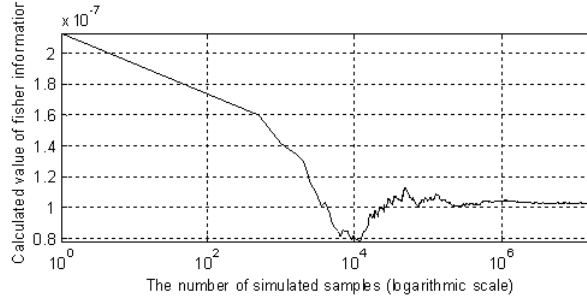
(b)
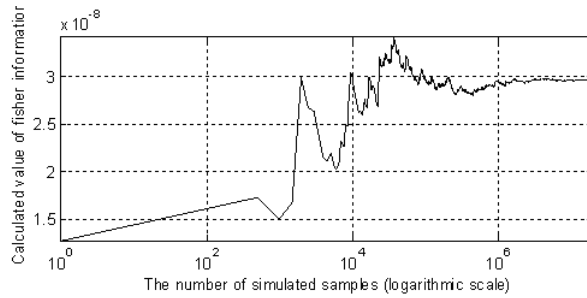
(c)

Figure 5.19 Calculated values of Fisher information matrix as a function of the number of the sampled events used for Monte Carlo integration.(a),(b) and (c) illustrates the curve for matrix elements (33,33),(49,49) and (65,65), respectively.

According to the number of pixels in the phantom or reconstructed image, the FIM is a two dimensional positive definite symmetric matrix with 4225×4225 elements. Under the assumption of shift invariance, the center column is selected for the M-UCRB calculation. In fact, each entry of this column of the Fisher information matrix can be expressed as,

$$F_{i,2113} = E\left\{ [\frac{\partial}{\partial \theta_i} \log p_{\underline{Y}}(\underline{Y}|\underline{\theta})][\frac{\partial}{\partial \theta_{2113}} \log p_{\underline{Y}}(\underline{Y}|\underline{\theta})] \right\},$$ (5-17)

125

in which pixel number 2113 corresponds to the central pixel of the reconstructed image. The center column of the Fisher information matrix can also be expressed as a two dimensional matrix with 65 by 65 entries, referred to as 'a column matrix' and shown in Figure 5.18 (a), the central row profile of the column matrix is shown in Figure 5.18(b).

The Fisher information matrix displayed in figure 5.18 was obtained using Monte Carlo integration with 20 million independent samples, which is an adequate number of events to provide acceptable statistical error. To illustrate the effect of the number of sampled events on the value of an entry in the Fisher information matrix, calculated values of entry (33, 33),(49,49) and (65,65) corresponding to the number of sampled events are plotted in the Figure 5.19 (a), (b) and (c), respectively. Values fluctuate substantially when the number of events less than 2 million, but gradually stabilize as the number of samples increase.
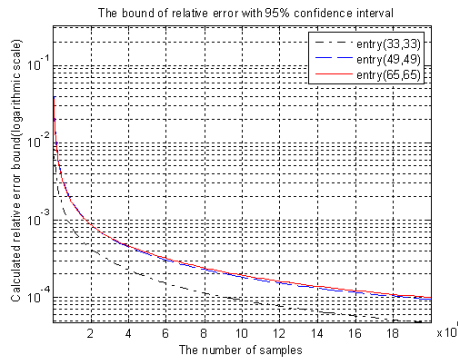
Figure 5.20 The values of $\hat{\sigma}_n\left[z^{(1-\alpha/2)}\right]\Big/\left(\hat{\theta}_n\sqrt{n}\right)$ for entries (33,33),(49,49) and (65,65) in the calculated Fisher information column matrix corresponding to the number of the sampled events for which the confidence interval is 95%.

To obtain the sufficiently good estimates of all entries of the Fisher information matrix, the minimum number of events could be evaluated with approximately 95% confidence intervals with a relative error less than 0.001. $z^{(1-\alpha/2)} = 1.96$ and $\varepsilon = 0.001$. The values of $\hat{\sigma}_n\left[z^{(1-\alpha/2)}\right]\Big/\left(\hat{\theta}_n\sqrt{n}\right)$, i.e the upper bound of the relative error with a confidence interval of 95%, for the entries of (33,33),(49,49) and (65,65) in the Fisher information column matrix are plotted in Figure 5.20. As shown, the relative error decreases as the number of sampled events increases, and the minimum number of sampled events required for the worst case is 2 million.

126

5.2.2.2 Analysis of the value of parameter λ

The variable λ in the M-UCRB must be positive in order for matrix inversion to be possible. According to the formula (3-15), which describes the relationship between the optimal actual PSF with the desired PSF, a relatively large value of λ will induce mismatch between the desired PSF and actual PSF. Figure 5.21 illustrate 4 examples of the relation between the actual PSF and the target PSF with different values of λ. Very small values of λ, such as $1e^{-18}$ are required to obtain a close match between target PSF and actual PSF. As the value of λ increases, the actual PSFs become broader than the desired one. To compare curves of error between the target PSF and actual PSF for different of FWHM target PSFs, curves of mean square error between the target PSF and actual PSF corresponding to the target PSF FWHM with range from 0.05cm to 20cm are displayed in the figure 5.22. From comparison, as the value of λ less than $1e^{-15}$, the mean square error between the target PSF and actual PSF is less than $1e^{-20}$. Therefore, in the following research, the value of λ is set to $1e^{-20}$, the error between the target PSF and actual PSF is negligible, and the two point source functions are essentially identical.
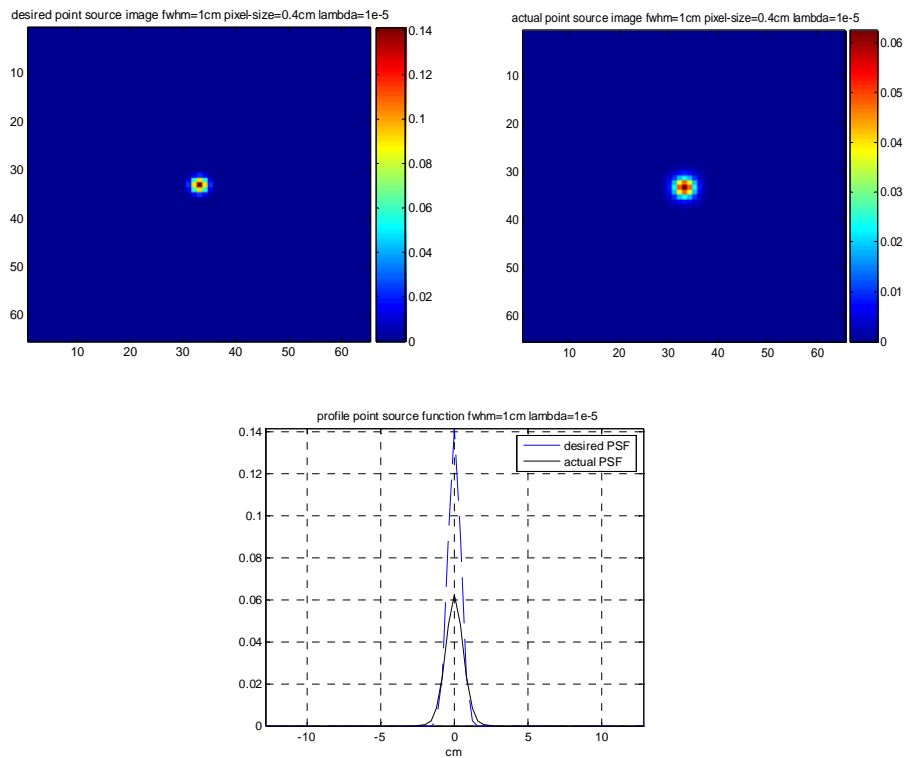
(a)
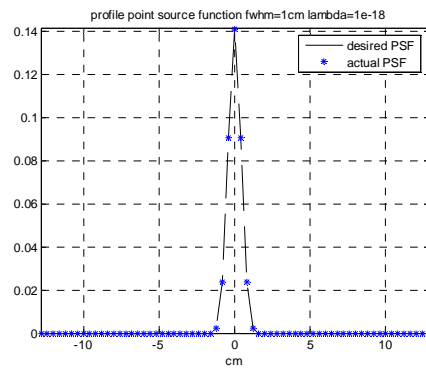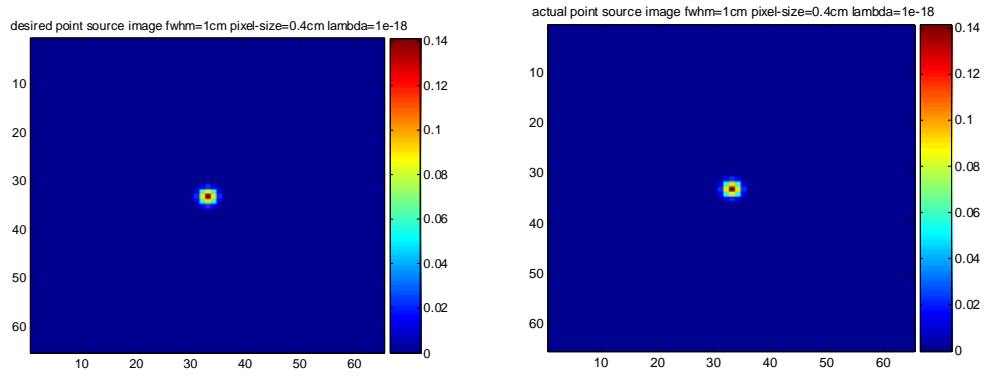
(b)
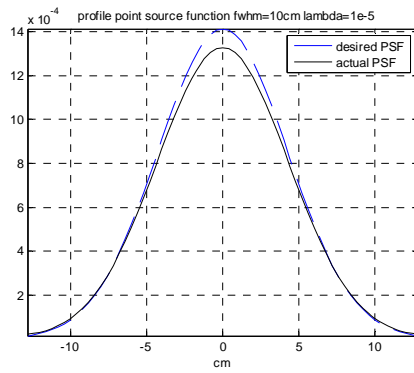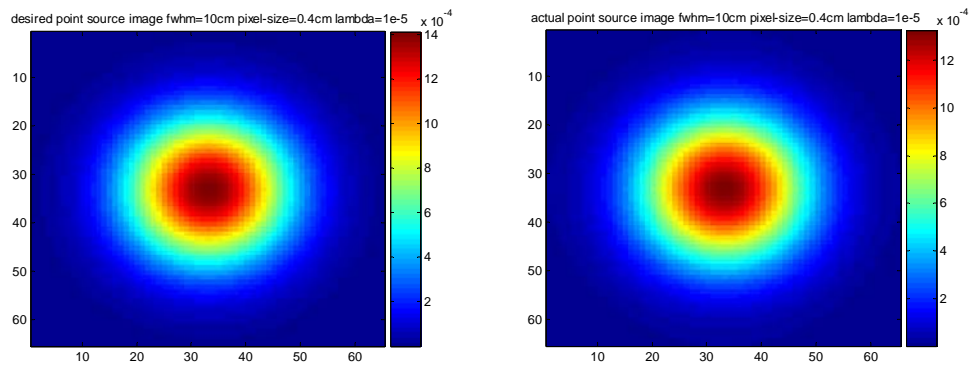
(c)
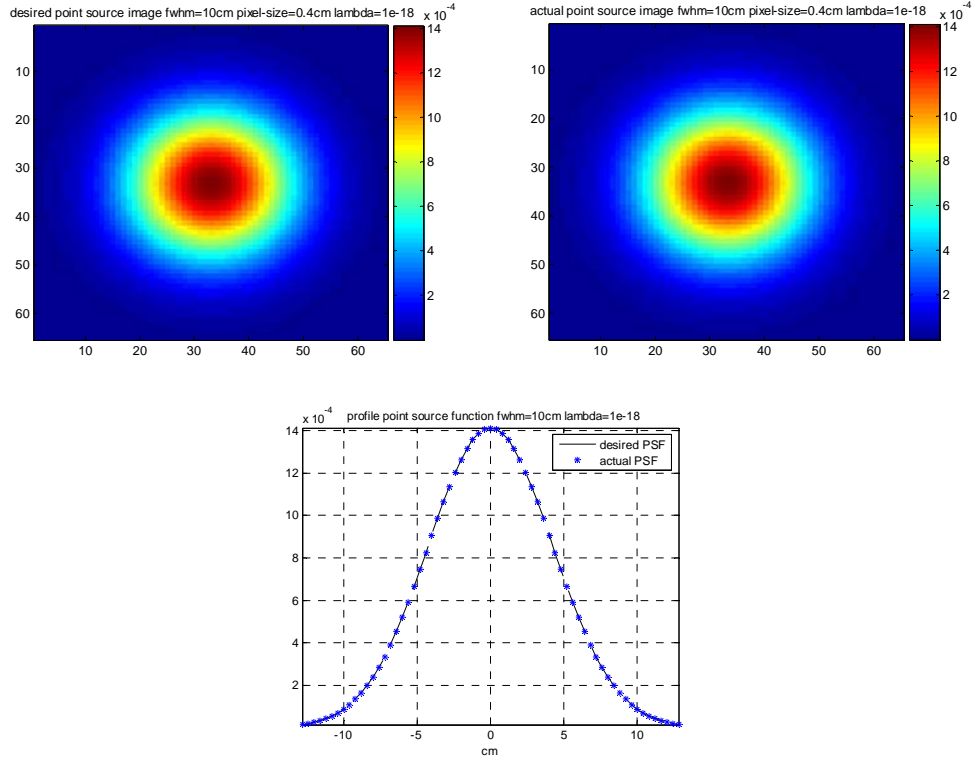
(d)

Figure 5.21 Comparison of target and actual point source image and their profiles for different target FWHM and λ.(a) fwhm=1cm, λ=1e^{-5}; (b) fwhm=1cm, λ=1e^{-18}; (c) fwhm=10cm, λ=1e^{-5}; (d) fwhm=10cm, λ=1e^{-18}.
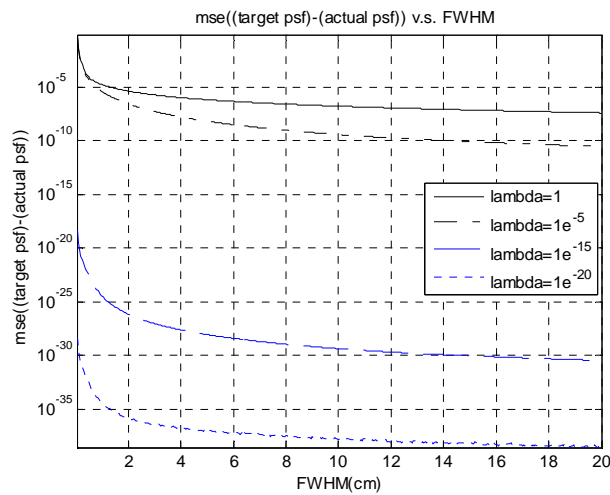
Figure 5.22 Comparison curves of mean square error between target PSF and actual PSF corresponding to the FHWM of target PSF from 0.05cm to 20cm with different value of λ. (i.e. 1, 1e^{-5}, 1e^{-15}, 1e^{-20}).

5.3 Performance Analysis by Modified Uniform Cramer-Rao Bound

In this section we use the performance evaluation and system modeling tools described in Chapters 3 and 4 to compare imaging performance of a Compton camera and a collimated Anger camera for imaging the 364.6keV gamma-rays from [131]I. The computational methods include the various techniques employed to reduce computation time and memory requirements. Performance is quantified in terms of the M-UCRB for 2 and 3-dimensional objects of varying size. The bound was calculated for the central pixel to ensure that the assumption of shift invariance for the bound calculation was justified.

5.3.1 Effects of Performance due to Objects Size

The imaging performance of Compton imaging systems is highly objects dependent. Because of the multiplexing of information, larger objects will have noisier reconstructed images even though they have the same number of detected photons per unit object volume for a planar object. This will also be manifested by higher bounds on variance for a given desired FWHM. For evaluating the effects of object size, the simulated Compton camera is the same as that described in Chapter 2. The Silicon detector has perfect resolution, that is, electronic noise and position blur are not considered. Therefore, detected energy is only blurred by the Doppler broadening. The NaI detector is also modeled with perfect spatial resolution and is located 10cm away from the first detector. The objects are uniform disks 26cm, 13.2cm and 6.8 cm diameter. The distance from the object to the first detector is 10cm. The center of object, first detector and second detector are aligned on the same axis. The calculated M-UCRB for three disk objects with identical FOV and image space are displayed in Figure 5.23. The pixel size in all three cases is 0.4cm×0.4cm, so the reconstructed image sizes are 65×65, 33×33 and 17×17 pixels.

As mentioned before, the M-UCRB shown in the figure 5.24 is calculated on a per-detected-photon basis. However, considering a real application, the count rate will increase approximately as the square of the disk diameter for the same tracer concentration. Using the 26cm disk as a reference, the relative number of detected events for the 13.2cm and 6.8cm diameter disks are 0.2578, 0.0684. Therefore, the M-UCRB for

the three discs normalized to the same detection period are shown in Figure 5.24. As demonstrated in Figures 5.23 and 5.24, for the same number of detected events and the same imaging time, the bigger object has the higher variance bound and worse performance comparing with the smaller object.
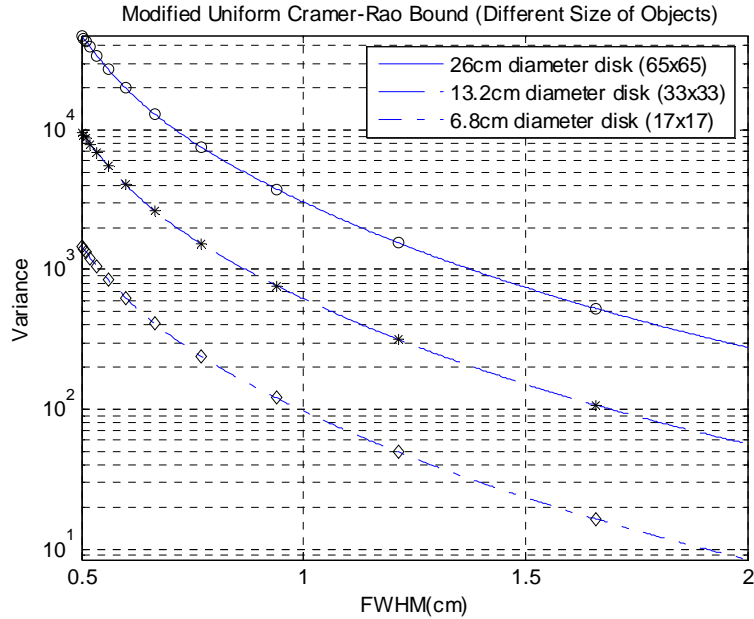
Figure 5.23 Mean MUCRB per detected photon for the three disk objects with diameters of 26cm, 13.2cm and 6.8cm and the matched FOV with sizes of 65×65, 33×33 and 17×17 pixels, respectively. (Pixel size is 0.4×0.4cm^2).
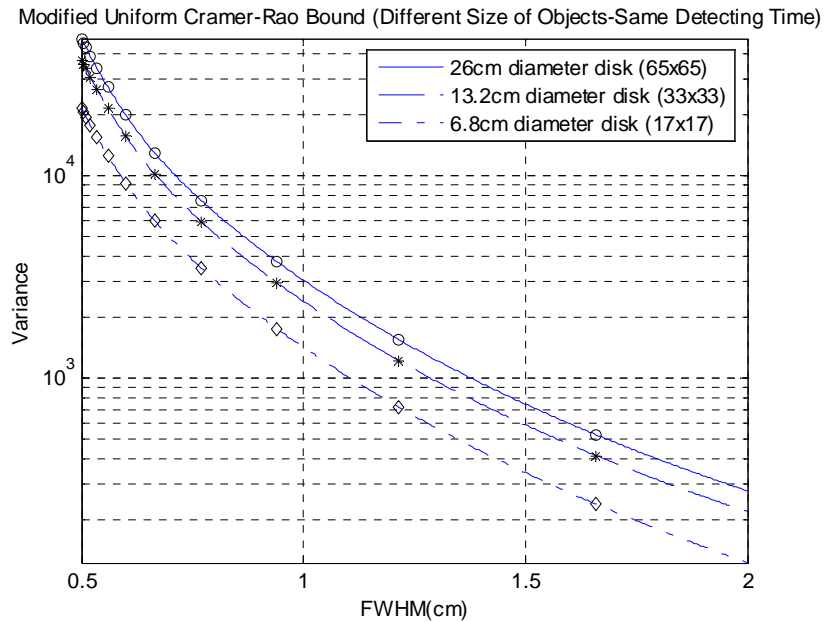
Figure 5.24 MUCRB for 26cm, 13.2cm and 6.8cm diameter disks normalized to the same imaging time for ideal detectors.

5.3.2 Effects of Silicon Detector Energy Resolution on Performance

The MUCRB curves for different energy resolution of the crystalline silicon detector for the incident photon energy of 364.4keV are displayed in Figure 5.25. The silicon detector energy resolution is an important factor in determining performance of a Compton imaging system. Low energy resolution, i.e. larger FWHM, severely degrades the quality of reconstructed images. This is especially true for low energy photons. As reported in [114], for an incident photon with 140.5keV energy, a silicon detector with perfect energy resolution and considering only the effect of Doppler broadening, a detector with 1keV FWHM energy resolution and perfect spatial resolution will further increase bound on variance of the reconstruct image about 240%. For the higher energy of 364.4keV incident photons, however, mean relative variance degradation in energy resolution of 1keV and 2kev FWHM are about 4.7%, 16%, respectively, compared to a perfect detector.
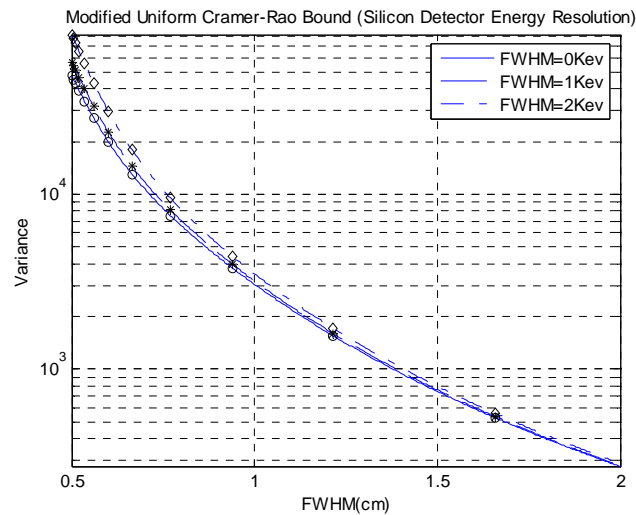
Figure 5.25 M-UCRB curve for the center pixel of the 26cm diameter uniform disk with different energy resolutions of crystalline silicon detectors. The incident photon energy is 364.4keV. The bound curve with 0keV FWHM is the effect of Doppler broadening.

5.3.3 Effects of Silicon Detector Spatial Resolution on Performance.

The spatial resolution of the silicon detector is an important parameter that can contribute to the uncertainty in the scattering angle and further influence the reconstructed image quality. Since the silicon detector studied is a pixel-pad based silicon

sensor, the spatial resolution is determined by the pixel size. Even though small pixel size can improve spatial resolution significantly, a moderate size pixel is desired in this application to decrease the complexity of fabrication and probability of scattered electrons being detected in multiple pixels. For this research, the pixel sizes under consideration are 1.4mm, 2mm, and 3mm. thus the relative variance of spatial resolution are 0.1633mm, 0.333mm and 0.75mm, respectively. From Figure 5.26, the variance bound curves increase, i.e. imaging performance decreases, as silicon detector spatial resolution worsens. However, for the 1.4mm FWHM resolution of the silicon detector currently used, the variance bound is almost equal to the variance bound for a silicon detector with perfect spatial resolution, and the mean relative error is about 2.15%.
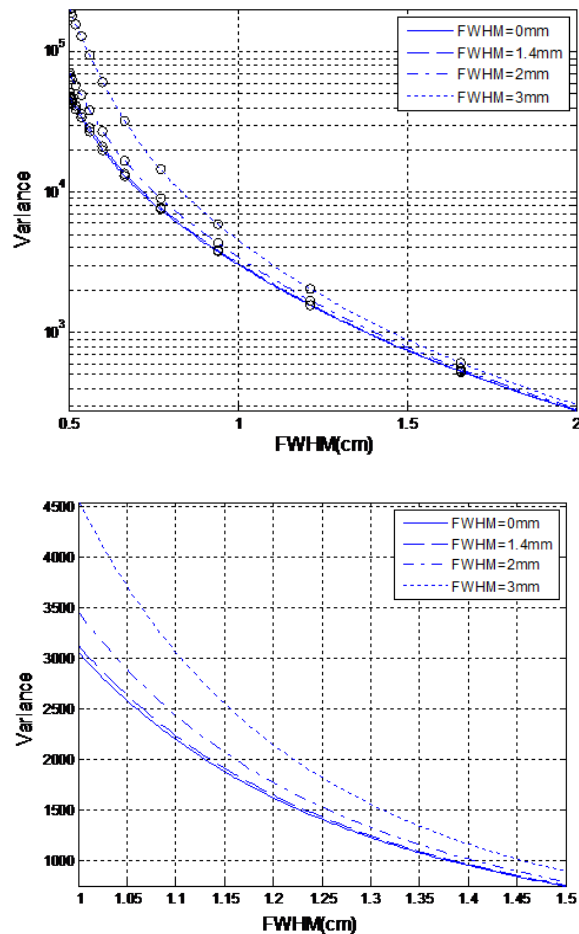
Figure 5.26 M-UCRB curve for the center pixel of the 26cm diameter uniform disk with different spatial resolutions of crystalline silicon detectors. The incident photon energy is 364.4keV. The bound curve with 0mm FWHM shows the effect of Doppler broadening only. Lower figure is expanded linear representation of upper curves from 1 to 1.5cm FWHM.

133

5.3.4 Performance Comparisons of Compton Imaging system and the Anger Camera with HEGP Collimator

In this section, the performance of the Compton imaging system and the Anger Camera with HEGP collimator for imaging 364.4keV photons are analyzed and compared using the M-UCRB. The simulated systems and system models of both imaging systems were introduced in chapter 2 and chapter 4, respectively. As given in Chapter 2, the average sensitivity of the studied Compton imaging system is around 23 times that of the Anger Camera with HEGP collimator for imaging the ^{131}I photons.

5.3.4.1 Two Dimensional Thin Disk Object

The object simulated is the 26cm diameter disk with uniform activity shown in Figure 5.17. The reconstruct image is 65×65 pixels with a pixel size of 0.4cm by 0.4cm. The disk faces the imaging system and the center of disk is aligned with center of the detector. It is located 10 cm from the collimator of the Anger camera and 10 cm from the first detector of the Compton imager as same as illustrated in Chapter 2. The center pixels of the disk are selected for evaluation.

Three MUCRB curves and MUCRB ratio of one event for the Compton imaging system and Anger camera are displayed in figure 5.27 and figure 5.28, respectively, in which the Anger cameras with HEGP collimator is illustrated by two mathematical models. The Anger camera modeled with a pure Gaussian response according to the specification of Angus Anger Camera, its FWHM is 12.6mm[114], has better performance when the FWHM of the desired PSF is larger than 1cm, and the ratio of MUCRB on variance is around 9. This indicates that the sensitivity of the Compton Imaging system must be about 9 times greater than the Anger Camera to obtain similar performance. However, as previously mentioned, a pure Gaussian response cannot be achieved for higher energy photons that penetrate the septa and scatter in the collimator. Following the Equation 4-2,3,4 and 5, the coefficients $A_{Gauss}, \sigma_{Gauss}, A_{exp}$ and λ_{exp} of PSF function are 0.0164,5.22, 0.0021 and 0.0235, respectively. Therefore, as these figures illustrate, when the FWHM of the desired PSF is less than 1.3cm, the Compton imaging system significantly outperforms the collimated Anger camera. At the lowest reconstructed resolution, the MUCRB curves for the two systems with identical

sensitivity are close with a ratio are around 1.1. Therefore, considering the higher sensitivity, of the Compton Imaging system, its performance is about 20 times over the Anger Camera for detecting 364.4keV photons for the same imaging time.
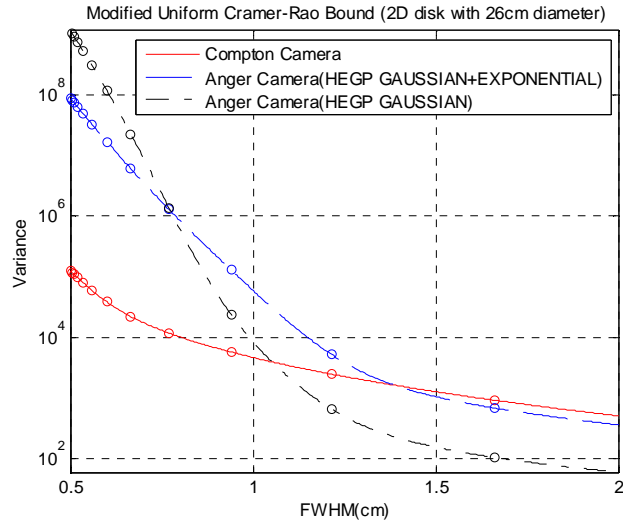
Figure 5.27 M-UCRB curves of one event for a Compton imaging system and an Anger camera with HEGP for imaging 364.4keV photons. The variance in center pixel intensity of the 26cm diameter uniform source disk is evaluated. The Anger Camera with HEGP response is modeled as a pure Gaussian function (FWHM=12.6mm) and as a Gaussian plus exponential tails (A_{Gauss}=0.0164,σ_{Gauss}=5.22,A_{exp}=0.0021,and λ_{exp}=0.0235) that more accurately represents the collimator response for 360keV photons.
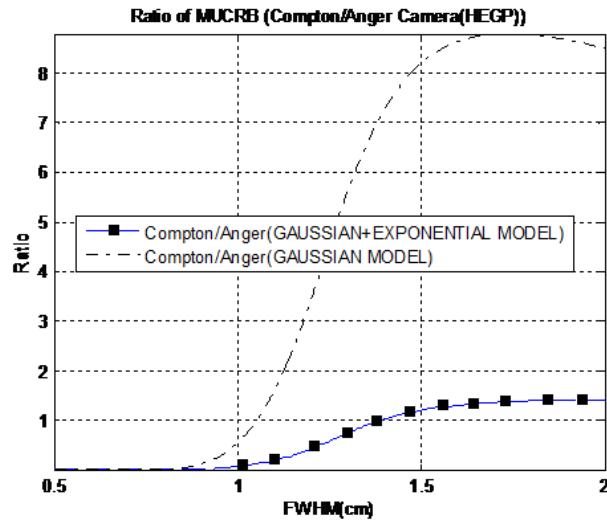
Figure 5.28 The variance ratio of M-UCRB of one event for a Compton imaging system over Anger Camera with 2 HEGP collimator models.

5.3.4.2 The Three Dimensional Cylindrical Object

The reconstruction domain for a 3D object study was 20cm×20cm×20cm segmented into 65×65×65 pixels. Each pixel is a 0.31cm cube. The simulated object was a uniform cylinder with diameter of 20cm. The central axis of the cylinder is parallel to the surface of the detector, and the distance between the axis and detector surface is 14cm. The Object was rotated in steps of 1deg increments for calculating the 3D Fisher information matrix for a total of 360 degrees.

The central element in image is selected to calculate M-UCRB, and the number of event for calculating FIM is averaged to one. As shown in figure 5.29, for the 3D tomography case, the Compton imaging system achieves a substantially lower bound on variance than the collimated Anger camera with HEGP per detected photon. Compared with Anger camera with HEGP from curves, the minimum ratio between two bound curves is about 1.9 and around 1.4 cm (FWHM). Also benefiting from the higher sensitivity of Compton imaging system, Compton imaging system absolutely outperforms the Anger Camera. For the 3D case, linear integral and conic integral are employed to reconstructing image and calculating FIM for Anger camera and Compton imaging system, respectively. Comparing with the M-UCRB in 2D case, the effects of these integrals induce more degradation on the performance of Anger Camera than that of Compton imaging system.
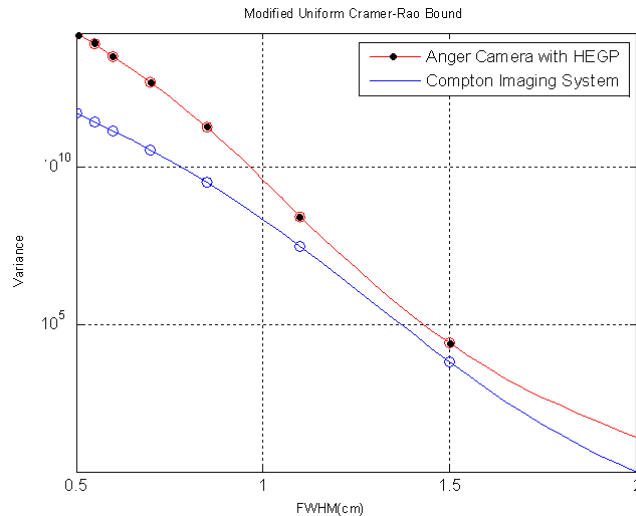
Figure 5.29 M-UCRB curves of one event and central element for Compton imaging system and Anger camera with HEGP for detecting 364.4keV photons. The source object is 3D cylinder with diameter of 20cm and height of 20cm with same number of counts.

5.4 Performance Comparison Using Reconstructed Images

Figure 5.30 illustrates a simulated two dimensional thin sheet phantom with ^{131}I that was placed 10cm from the front surface of the two detectors. The diameters of hot spots on the phantom are 0.6cm, 0.8cm, 1cm, 1.5cm, 2.0cm and 2.4cm. The intensities of hot spots are uniform and the background activity is zero.
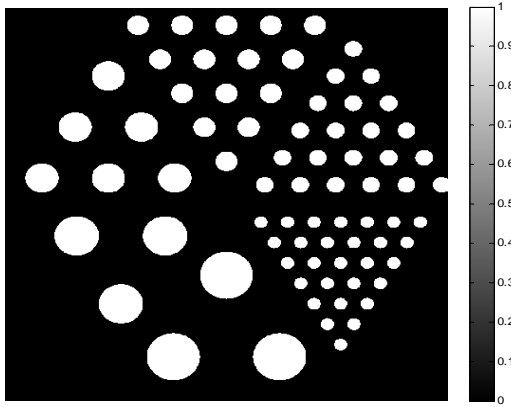
Figure 5.30 The simulated 2d thin sheet phantom. The diameters of hot spots are 0.6cm, 0.8cm, 1.0cm, 1.5cm, 2.0cm and 2.4cm. The intensities of hot spots are uniform and a background activity is 0.

The images with 65 by 65 0.308cm pixels were reconstructed using MLEM for both proposed Compton imaging system and the Anger camera with HEGP. The restored images by different number of iterations are compared in the appendix. The images restored using 100 iterations are analyzed in this section.As shown in Figure 5.31, the three million events were acquired for the Compton imaging system and its image was reconstructed by list-mode MLEM. Since the detection sensitivity of Compton imaging system is about 20 times of the Anger camera with HEGP, 200 thousand events were acquired and binned to a forward projection matrix of 520 by 520 for Anger Camera with HEGP and its reconstructed image was displayed in Figure 5.32. For comparison, the image for Anger Camera with HEGP with three million event was also shown in Figure 5.33. Comparing Figure 5.31 with Figure 5.32 and 5.33, the Compton image system performance is clear better than the conventional Anger camera, even using the same number of events. In particular, hot spots less than 1.0cm diameter cannot be reconstructed by Anger camera with HEGP, since information provided by this imaging

system is not sufficient to recover such small hot spots. However, smaller hot spots detected Compton image system can be reconstructed effectively.
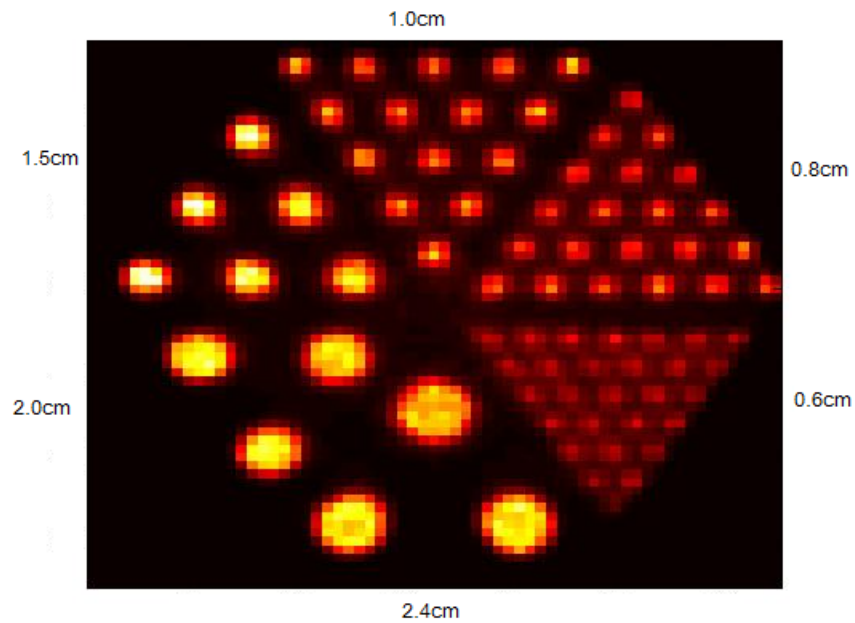
Figure 5.31 The reconstructed image for Compton imaging system for 100 iterations of the list-mode MLEM algorithm with 3 million events. The diameters of hot spots are 0.6cm, 0.8cm, 1.0cm, 1.5cm, 2.0cm and 2.4cm.
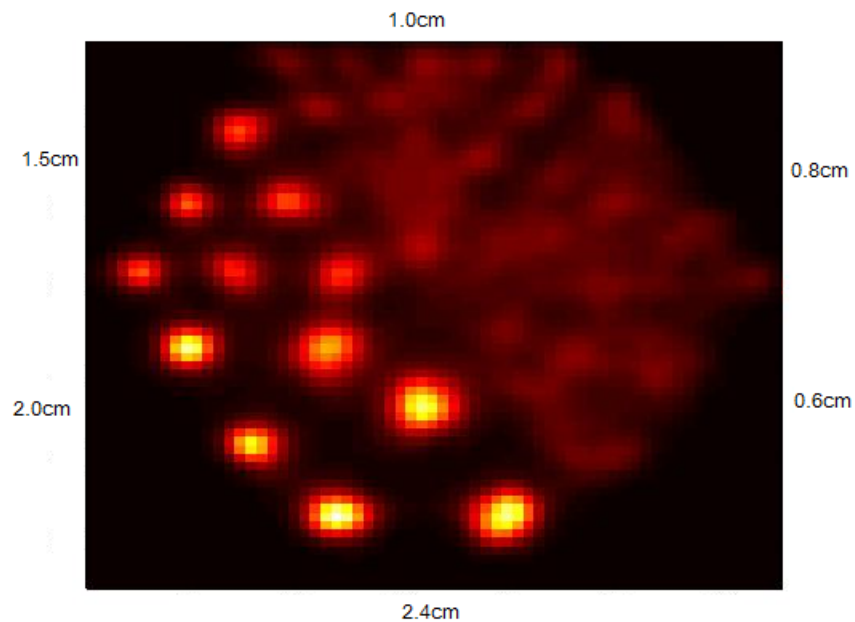
Figure 5.32 The reconstructed image for Anger Camera with HEGP for 100 iterations of the bin-mode MLEM algorithm with 200 thousand events. The diameters of hot spots are 0.6cm, 0.8cm, 1.0cm, 1.5cm, 2.0cm and 2.4cm.
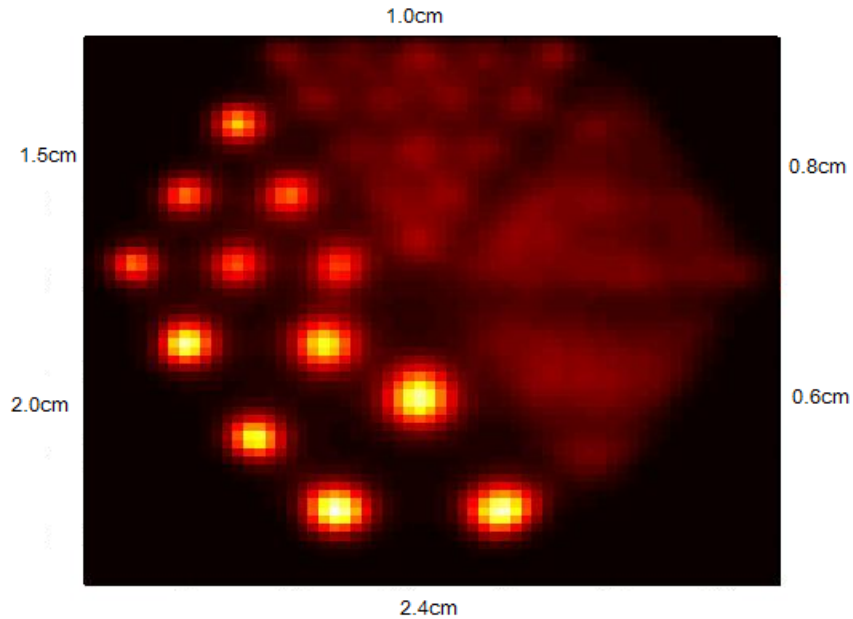
Figure 5.33 The reconstructed image for Anger Camera with HEGP for 100 iterations of the bin-mode MLEM algorithm with 3 million events. The diameters of hot spots are 0.6cm, 0.8cm, 1.0cm, 1.5cm, 2.0cm and 2.4cm.

5.4 Conclusion

For 364.4keV photon imaging, the performances of both systems were compared using M-UCRB for 2D disk, and also by reconstruction image for a disk object with different size of hotspots in this chapter. Given the same number of imaged events, both systems have similar performance as the FWHM of the desired PSFs is larger than 1.3cm. However, as the FWHM of desired PSFs or the diameter of hotpot is less than 1.3cm, the Compton imaging system has much better performance than conventional Anger Camera with HEGP collimator. From the M-UCRB comparison for the 3D cylinder object, the Compton imaging system has better performance than Anger Camera with HEGP even for desired PSF with larger FWHM. It is because that the linear integral for imaging on Anger Camera greatly degrades the overall performance than imaging 2D disk, even though the conic integral also degrades the performance of Compton imaging system.

CHAPTER 6

Distributed Image Reconstruction and Real time Signal Processing for Pileup Correction at High Count Rates

Previous chapters have demonstrated that a Compton camera medical imaging system can obtain improved performance compared to a conventional collimated Anger Camera for tumor imaging with radiotracers such as ^{131}I that emit high energy photons. However, for actual clinical applications, two additional problems must be addressed: First, image reconstruction time for the MLEM algorithm must be reduced, and second, pulse pileup resulting from high count rates in the second detector need to be avoided for correct position and energy estimation. In section 6.1, a parallel MLEM algorithm based on a chess-board data partition is introduced to speed up image reconstruction for a Compton medical imaging system using a multiple CPU cluster with a message passing interface (MPI). In section 6.2, a digital real time signal processing design for energy extraction and pileup reduction for the scintillation detector in the prototype Compton system is described and evaluated.

6.1 Parallel Image Reconstruction

6.1.1 Introduction

After the Compton scatter camera was first introduced by Todd [115], there were various image reconstruction methods developed for this imaging system.

The direct or analytical approach includes simple back-projection and filtered back-projection (FBP). For a Compton imaging system, each measurement only determines the source location to lie within a back-projection cone of finite thickness. Multiple back-projection cones from different measured events corresponding to the

same source point intersect at the source position on the image plane. To identify the image pixels that intersect the back-projected cone, the source space tree algorithm was proposed in [116] and another, faster approach to determine the intersection from list-mode measurements by solving a quadratic equation was presented by Wilderman [103]. Since a simple back-projection algorithm generates a very poor image, it is primarily used to estimate an initial image for an iterative image reconstruction.

Filtered back-projection algorithms have been investigated for 2D and 3D Compton image reconstruction. Compared with the parallel projection imaging of original parallel line SPECT, which back-projections into the image space are groups of straight lines and are shift invariant, the back-projection of Compton events onto the source plane is a conic section and is spatially variant. The principle method for implementing FBP for Compton imaging is: to convert the conical integrals from the measured data into spherical coordinates using spherical harmonics, then, using known FBP reconstruction techniques, to synthesize the 2D or 3D source distribution from these projections. As illustrated in [117], however, the proposed reconstruction algorithm requires a complete set of conic projections collected over an infinite plane and the scattering direction is restricted to be perpendicular to the second detector. Basko et al.[118] first presented a method to convert the conic surface to spherical coordinates using spherical harmonics, however, this did not account for the scatter angle distribution. Parra [119] improved the above algorithm by considering the Klein-Nishina distribution, but this method requires a complete data set of all possible scattering angles. Gunter[120] applied a fast FBP algorithm based on a specially defined absorption detectors that would be sensitive to scattering angles from 0 to 180 degrees. However, sampling a complete data set with a full range of scattering angle is unpractical since it would require an infinitely long cylindrical second detector[121]. All of the above mentioned direct or analytical approaches are based on the mathematical assumption of spatially invariant and complete sampling. Furthermore, when imaging gamma rays with energy lower than 511keV in medical imaging, the scattering angular uncertainty due to Doppler broadening and finite spatial and energy resolution on both detectors needs to be concsidered in the image reconstruction algorithms.

Since no straight-forward mathematical method has been found to simply express the relationship from the original object to conic projections, iterative algorithms have been investigated for this application. The principle of iterative reconstruction algorithms is to estimate the original source distribution by consecutively revising the estimate, in which the new estimate is generated by adjusting the current estimate according to the difference between the measurements and a set of projections based on the current estimate. Although the computational cost of iterative algorithms is a concern and errors in the reconstructed image are sensitive to the accuracy of the system model and system sensitivity[122], the quality of reconstructed images is superior to the results of the direct approach.

The Algebraic Reconstruction Technique (ART) and Simultaneous Iterative Reconstruction Technique (SIRT), which is a variation of the standard ART, were presented in [123, 124] to reconstruct images from Compton camera projection data. In[125], Shepp first applied Maximum Likelihood Estimation (MLE) and its corresponding iterative algorithms, i.e. expectation maximization (EM) algorithm to the field of emission tomography for estimating the incomplete data. The MLEM is an optimization method, by which the best solution is estimated by maximization of the likelihood of the reconstructed image. The maximum likelihood estimation (MLE) algorithm was first implemented for the Compton camera image reconstruction by Hebert, Leahy and Singh [102, 126], in which the physical and the Poisson nature of radioactive nuclear decay were taken into account. Because the number of measured events is far less than the total number of potential detector bins, List-mode Maximum Likelihood Reconstruction for Compton camera data was described by Wilderman [111] for C-SPRINT imaging. A Penalized MLEM algorithm[127] was also proposed to reduce the statistical noise as the number of iterations increased in the standard MLEM.

There are two computational problems that must be solved in order for MLEM or List-mode MLEM to be considered practical for Compton Camera image reconstruction. First, since the MLEM algorithms converge slowly, many iterations are required to reach a satisfactory solution, and each iteration involves multiplication of large matrices. Second, a very large numerical memory is required to store the system matrix, acquired data, and reconstructed images. This computational issue also depends on the number of

measured events, around $10^7 \sim 10^8$ events in a typical study. In [128], the authors investigated the space-alternating generalized EM algorithm to accelerate convergence by statistical considerations in which a sequence of small hidden data spaces are used instead of one large complete-data space which requires a much larger memory space.

Parallel computation for MLEM algorithms for PET or SPECT requires specially designed hardware architecture. A parallelized EM algorithm was investigated in [129], in which the forward projection and back projection are approximated by profile convolution and calculated on a very large scale integration (VLSI) based systolic structure. In [130] a combination of parallel rotations and parallel generation of Gaussian convolutions were employed and the parallelization was realized on a mesh-connected single-instruction and multiple data system. To implement 3-D PET image reconstruction on an interconnected shared memory system, Chen and Lee [131] investigated the parallelized MLEM algorithm using 3 different data partitions: "partition-by-box", in which all computation of one pixel is completed on one processing units (CPU) for both forward projection and back projection; "partition-by-tube", where computation of a pixel vector is completed by one CPU for both forward projection and back projection; and "partition-by-box and tube" where the first two data partition scheme are used by forward projection and back projection, respectively.

The above implementations are limited for practical application since they are based on special purpose parallel computation platforms. For this reason we have implemented parallel computation of MLEM on an MPI based, net-connected cluster. Forward and back projections inherent to all reconstruction methods can be easily partitioned among many processors. This type of parallel platform is easily implemented and widely used for many mathematical and engineering computations. Since message passing is slow relative to the CPU computation and the total running time is the sum of CPU execution time and message passing time, an efficient parallel algorithm depends on data partition to optimize the trade-off between execution time (ET) and message passing time (MPT). This implementation was based on one master node and multiple work nodes[132], which does not permit balancing execution and message passing time. Therefore, Parallel MLEM based on a chess-board data partition is presented for our application.

6.1.2 The List-mode Maximum Likelihood Expectation Maximization Algorithms

Image reconstruction can be intrinsically regarded as a parameter estimation problem. The problem is to estimate the unknown distribution of the radiotracer from the measured noisy data. As mentioned above, MLE has been widely employed in emission image reconstruction. The benefit of this statistical reconstruction is that the Poisson nature of photon counting noise and the physical model of the detection system are represented in the likelihood function. In practice, an iterative method, i.e. the EM algorithms, is used to find the maximum of likelihood solution. For the Compton camera, since the measured data are much more sparse than the number of detection bins, the list-mode MLEM algorithm exhibits a significant practical advantage over bin-mode MLEM algorithms. In this section, the MLEM algorithm is derived according to a statistical model that describes the photon noise characteristics involved in Compton camera detection. Then, the derivation of list-mode MLEM is described.

6.1.2.1 Linear model for Emission Imaging Systems

The goal of tomographic imaging is to estimate the 3-dimensional distribution of a radiotracer in a human subject by measuring the flux of gamma-rays reaching a detector that is generally external to the patient

The photon-emission and detection process is assumed to be a linear process. Therefore, the image reconstruction problem is essentially a linear inverse problem[133] of the following form:

$$y_i = \int_R a_i(\underline{x})\lambda(\underline{x})d\underline{x} , \qquad\qquad (6\text{-}1)$$

where y_i is the ith projection measurement, $a_i(\underline{x})$ is the PSF of the ith measurements for a source γ-ray emitted from $\underline{x}$ and $\lambda(\underline{x})$ is the radioactivity volume concentration at $\underline{x}$ in the object.

In practice, however, estimating a continuous distribution $\lambda(\underline{x})$ from a finite number of measurements y_i is an ill-posed problem. Furthermore, the reconstructed images are represented by a discrete-domain function. Therefore, the continuous quantity $\lambda(\underline{x})$ is represented by λ_j.

$$\lambda_j = \int_R \lambda(\underline{x}) b_j(\underline{x}) d\underline{x} \qquad (6\text{-}2)$$

In general, the pixel or voxel basis function $b_j(x)$ is selected as piece-wise constant within a small, non-overlapping square or cube, respectively. The estimated number of emissions from one pixel per unit time is represented as the intensity of the pixel in the reconstructed image. Therefore, the discretized linear model of photon emission imaging process can be illustrated as,

$$\underline{y} = \mathbf{A}\underline{\lambda} \qquad (6\text{-}3)$$

$\underline{y} = [y_1, y_2, \ldots, y_i, \ldots, y_M]^T$ is a vector of measurements and each element y_i is the number of counts accumulated in the ith detector bin and the total number of detector bins is M. $\underline{\lambda} = [\lambda_1, \lambda_2, \ldots, \lambda_j, \ldots, \lambda_N]^T$ is the vector of the parameterized object, each item λ_j stands for the intensity in the voxel j, and total number of pixels is N. $\mathbf{A}$ is an M×N matrix called the system response matrix. Each element a_{ij} in the matrix $\mathbf{A}$ is a weighting factor representing the mean contribution of voxel j in the object to the number of counts detected in detector bin j or the probability that a photon emitted from voxel j in the object is detected in bin j. To evaluate the source distribution directly requires inversion of $\mathbf{A}$, that is $\underline{\lambda} = \mathbf{A}^{-1}\underline{y}$. However, this direct method is not practical because $\mathbf{A}^{-1}$ may not exist or may have multiple solutions. Even though $\mathbf{A}^{-1}$ may have unique solution, the direct inversion will amplify the statistical noise mostly due to the low count rates in photon-emission imaging. Furthermore, a direct solution is hardly achieved that takes into account the correct physical model of the Compton camera or even the collimated camera with collimator penetration whereas the iterative likelihood solution can. Because of these disadvantages of direct inversion, the MLEM algorithm is used to find the best estimate of a much less noisy solution by fitting a given criterion that is the maximization of the likelihood of the reconstructed image.

6.1.2.2 The MLEM Algorithm for Emission Imaging Systems

1. Maximum Likelihood Estimation

The Maximum Likelihood Expectation Maximization algorithm with Poisson statistical model was first introduced to the field of photon-emission image reconstruction by Shepp and Vardi[134] and by Lange and Carson[135]. This algorithm consists of two components: one is the ML criterion, by which the best estimate $\hat{\underline{\lambda}}$ of the unknown object $\underline{\lambda}$ must have the greatest probability of producing the measurement $\underline{y}$. This strategy can be written as follows:

$$\hat{\underline{\lambda}} = \arg \max_{\underline{\lambda} \geq 0} \ p(\underline{y}|\underline{\lambda}) \tag{6-4}$$

The second component is using the EM algorithm[136] to find the solution that satisfies the ML criterion.

During a fixed observation time, the total number of photons emitted from radio-nuclei is a random variable with a Poisson distribution. Therefore, the total number of photons emitted from voxel j is also Poisson distributed with mean value of this random variable λ_j.

Because the detection process is also a Poisson process[109], in a fixed measurement time, the total number of measured photons in each detector bin i is also a Poisson random variable. Since $a_{ij}\lambda_j$ and λ_j are both independently Poisson distributed, the mean number of photons $\overline{y}_i$ detected in detector bin i is the sum of the mean number of photons emitted from all voxels times the transition probability a_{ij}, that is

$$\overline{y}_i = \sum_{j=1}^{N} a_{ij}\lambda_i \ , \tag{6-5}$$

where the N is the number of pixels and transition probabilities a_{ij} is an element in the system response matrix that describes the probability that a gamma ray emitted from voxel j is detected in the ith detector bin.

Since the number of detected photons in detector bin i results from the photons emitted from all voxels it is also a Poisson random variable, and the probability of observing y_i events in the ith bin is given by

$$y_i \sim Poisson \ (\overline{y}_i) \Rightarrow P(y_i|\underline{\lambda}) = \frac{\overline{y}_i^{\ y_i}}{y_i!}e^{-\overline{y}_i} ; i = 1 \dots M \tag{6-6}$$

Assuming the number of detected photons in all detector bins are independent variables, the conditional probability $P(\underline{y}|\underline{\lambda})$, the likelihood of observing measurement $\underline{y}$ given the source distribution $\underline{\lambda}$ is derived by multiplying all of the individual probabilities $P(y_i|\underline{\lambda})$. Therefore, the likelihood function is

$$P(\underline{y}|\underline{\lambda}) = \prod_{i=1}^{M} P(y_i|\underline{\lambda}) = \prod_{i=1}^{M} \frac{\overline{y}_i^{\,y_i}}{y_i!} e^{-\overline{y}_i} \, . \tag{6-7}$$

Maximizing the likelihood function is equivalent to finding the maximum of the log-likelihood function, the log-likelihood function is used to simplify the calculation of maximization. From above equations, the log-likelihood function is expressed as follows,

$$\begin{aligned} L(\underline{y}|\underline{\lambda}) &= \sum_{i=1}^{M} (y_i \ln(\overline{y}_i) - \overline{y}_i - \ln(y_i!)) \\ &= \sum_{i=1}^{M} (y_i \ln(\sum_{j=1}^{N} a_{ij}\lambda_j) - \sum_{j=1}^{N} a_{ij}\lambda_j - \ln(y_i!)) \end{aligned} \tag{6-8}$$

Therefore, according to the maximum likelihood criterion, the estimate of the object $\hat{\underline{\lambda}}$, which gives the highest probability of generating $\underline{y}$, is also the estimate for which $L(\underline{y}|\underline{\lambda})$ is a maximum.

The straightforward way to find the local maximum of $\underline{\lambda}$ is to set the derivative of $L(\underline{y}|\underline{\lambda})$ equal to zero.

$$\frac{\partial L(\underline{y}|\underline{\lambda})}{\partial \lambda_j} = -\sum_{i=1}^{M} a_{ij} + \sum_{i=1}^{M} \frac{y_i a_{ij}}{\sum_{j=1}^{N} a_{ij}\lambda_j} = 0 \, , \tag{6-9}$$

where $\sum_{i=1}^{M} a_{ij} = s_j$ is the detection sensitivity, which is the probability that a photon emitted from pixel j will be detected anywhere.

2. Expectation Maximization Algorithm

Finding the local maximum of positive $\underline{\lambda}$ by direct solution of Eq. (6-9) is a complicated and difficult process since Eq. (6-9) is a nonlinear equation. The current approach is the EM algorithm[134-136], by which the MLE of $\underline{\lambda}$ may be achieved asymptotically via an iterative method. In each iteration, the EM algorithm is decomposed into two-steps. The first step is the expectation step (E step). In this step, the

conditional expectation of the likelihood functions is obtained in terms of the complete data given the measurement $\underline{y}$ and the estimation $\underline{\hat{\lambda}}^n$ from the previous iteration. The second step is the maximization step (M step), in which the maximum estimation $\underline{\hat{\lambda}}^{n+1}$ of the current iteration can be obtained by solving the derivatives of the expectation function deduced from the E step.

To satisfy the requirement for a complete data set for the EM algorithm, the random variable x_{ij} is involved, and is defined as the number of photons emitted from j^{th} pixel in the object and detected in the ith detector bin. Each x_{ij} in the complete data set $\underline{x}$ remains an independent Poisson distribution. Clearly, the relationship of $\overline{x}_{ij}$ and $\overline{y}_i$ can be expressed as:

$$\overline{y}_i = \sum_{j=1}^{N} \overline{x}_{ij} = \sum_{j=1}^{N} a_{ij}\lambda_j \tag{6-10}$$

And, the log-likelihood in terms of $\underline{x}$ is written as follow,

$$L(\underline{x}|\underline{\lambda}) = \ln(P(\underline{x}|\underline{\lambda})) = \prod_i \prod_j P(x_{ij}|\underline{\lambda})$$
$$= \sum_{i=1}^{M} \sum_{j=1}^{N} (x_{ij}\ln(a_{ij}\lambda_j) - a_{ij}\lambda_j - \ln(x_{ij}!)) \tag{6-11}$$

In the E step, therefore, the conditional expectation of above log-likelihood with respect to the measured data and the estimation $\underline{\hat{\lambda}}^n$ from last iteration is,

$$E[L(\underline{x}|\underline{\lambda})|\underline{y},\underline{\hat{\lambda}}^n] = \sum_{i=1}^{M} \sum_{j=1}^{N} (N^n_{ij}\ln(a_{ij}\lambda_j) - a_{ij}\lambda_j) \tag{6-12}$$

where $N^n_{ij} = E(x_{ij}|y_i,\underline{\hat{\lambda}}^n) = y_iP(j|i) = y_i\dfrac{a_{ij}\hat{\lambda}^n_j}{\sum_{j=1}^{N} a_{ij}\hat{\lambda}^n_j}$ $\qquad$ (6-13)

In the M step, the maximum estimate $\hat{\lambda}^{n+1}$ can be calculated by solving the derivative of Eq.(3-12) and setting it to zero.

$$\dfrac{\partial E[L(\underline{x}|\underline{\lambda})|\underline{y},\underline{\hat{\lambda}}^n]}{\partial \lambda_j} = \dfrac{1}{\hat{\lambda}_j}\sum_i N^n_{ij} - \sum_i a_{ij}\bigg|_{\lambda_j=\underline{\hat{\lambda}}^{n+1}} = 0 \tag{6-14}$$

where $\sum_{i=1}^{M} a_{ij} = s_j$ is the detection sensitivity.

Consequently, combining Eq. (3-14) and (3-13), the final MLEM algorithm for one iteration is,

$$\widehat{\lambda}_j^{n+1} = \frac{\widehat{\lambda}_j^n}{s_j} \sum_{i=1}^{M} \frac{y_i a_{ij}}{\sum_{k=1}^{N} a_{ik} \widehat{\lambda}_k^n} \qquad (6\text{-}15)$$

3. Properties of the MLEM algorithm

When the number of observed data is large enough, the Maximum Likelihood estimator is asymptotically efficient as shown by H. V. Trees [137]. This means that ML estimators can achieve unbiased estimates with minimum variance in comparison to other unbiased estimators. However, in the real application of image reconstruction, this minimum variance is not acceptable since the image noise after reconstruction remains too high because the number of detected photons is too small. Several methods have been proposed to reduce image noise by introducing a certain amount of bias Methods, such as stopping the iterations in MLEM before convergence to the actual ML solution[138], adding a penalty term to the likelihood function[139], or post-smoothing the image[140].

Considering the properties of the MLEM algorithm described in Eq. (6-15), there are at least five advantages for the image reconstruction application: 1) This method is very simple to implement on a computer; 2) The total number of estimated photons in each iteration is not changed and remains equal to the total number of detected photons; 3) The MLEM algorithm automatically constraints the estimates in each iteration to be non-negative; 4) Because the log-likelihood function with Poisson distribution is concave, the MLEM algorithm is guaranteed to converge to a global maximum point if the total number of measurements is not less than the total number of pixels. However, the convergence rate of the MLEM algorithm is slow. Generally, an acceptable solution requires 30-100 iterations[135].

6.1.2.3 The List-mode MLEM Algorithm.

The MLEM algorithm illustrated in the last section is used for imaging systems with a bin-mode projection data set. For example, in a conventional Anger camera based SPECT, each measurement consists of a two dimensional matrix of projections of the

object distribution onto the detector plane at some angle, theta. Each element in the matrix is referred to as a detector bin. The intensity of a bin is the number of events recorded in this bin. In general, the number of measured events is substantially more than the number of detector bins. The memory size required to store the system response matrix, is equal to the product of number of detector bins and number of image pixels, is acceptable.

However, for PET imaging systems and especially Compton camera imaging systems, the number of detected events is far less than the total number of system elements or detector bins. Consequently the required memory is far beyond that of a general purpose computer. For a typical study, the number of detected event is around 10^7, significantly less than the total number of system elements. Therefore, instead of using an impractical and inefficient bin-mode MLEM algorithm for the Compton camera image reconstruction, the list-mode MLEM algorithm is an attractive alternative [108, 111, 126, 141]. In the list-mode MLEM algorithm for a Compton camera system, the acquired events are indexed by the first detector position, second detector position, and are energy deposited in the first detector, are stored in a list.

In the list-mode MLEM algorithm, the image reconstruction task is to find the best estimate, $\hat{\underline{\lambda}}$, of a discrete source distribution according to the finite measurement data set $\underline{A}'$. The total number of discrete source elements (pixels or voxels) is N, denoted as $\{x_1, x_2, \ldots, x_j, \ldots x_N\}$. The unknown discrete source distribution $\underline{\lambda}$ is denoted as $\{\lambda_1, \lambda_2, \ldots, \lambda_j, \ldots \lambda_N\}$. The source element x_j has source activity is λ_j. The survival probability or detection sensitivity, s_j, is the corresponding probability $P(D \mid x_j)$ that a photon emitted from source elements x_j is detected. The measurement data set consists of M measured events $\{A_1', A_2', \ldots, A_i', \ldots, A_M'\}$, and, each measurement has an independent identical distribution.

The likelihood function for the list measurements is

$$p(A_1', A_2', \ldots, A_M' \mid \underline{\lambda}) = \prod_{i=1}^{M} p(A_i' \mid \underline{\lambda}) \tag{6-16}$$

where $p(A_i' | \underline{\lambda})$ is the conditional probability density of measuring a single event A_i' given that this event is generated in the object $\underline{\lambda}$. And

$$p(A_i' | \underline{\lambda}) = \sum_{j=1}^{N} p(A_i' | x_j, D) P(x_j, D | \underline{\lambda}) \tag{6-17}$$

where, the probability density $p(A_i' | x_j, D)$ is a detected event generated from bin x_j and leads to a measurement A_i' in the detector. $P(x_j, D | \underline{\lambda})$ is the probability that the detected event originated in the source bin j given the source distribution $\underline{\lambda}$, and is equal to

$$P(x_j, D | \underline{\lambda}) = \frac{\lambda_j s_j}{\sum_{k=1}^{N} \lambda_n s_n} \tag{6-18}$$

Therefore, the log-likelihood based on the list of measurements A_i' is[142]:

$$\begin{aligned} L(\underline{A'} | \underline{\lambda}) &= \ln p(A_1', A_2', \ldots, A_M' | \underline{\lambda}) \\ &= \sum_{i=1}^{M} \ln p(A_i' | \underline{\lambda}) \\ &= \sum_{i=1}^{M} \ln\left(\sum_{j=1}^{N} p(A_i' | x_j, D) s_j \lambda_j \right) - \sum_{j=1}^{N} s_j \lambda_j \end{aligned} \tag{6-19}$$

Similar to the bin-mode ML estimation, estimating the unknown object distribution $\underline{\lambda}$ in list-mode requires finding the maximum of Eq. (6-19) with respect to $\underline{\lambda}$ with a non-negative constraint. That is,

$$\underline{\hat{\lambda}} = \arg \max v_{\hat{\lambda} \geq 0} L(A_1', A_2', \ldots, A_M' | \underline{\lambda}) \cdot \tag{6-20}$$

Consequently, the list-mode ML estimation can also be solved using the EM iterative algorithm. After combining the E step and M step, the estimate of $\hat{\lambda}_j^{n+1}$ is

$$\begin{aligned} \hat{\lambda}_j^{n+1} &= \frac{\hat{\lambda}_j^n}{s_j} \sum_{i=1}^{M} \frac{p(A_i' | x_J, D) s_j}{\sum_{k=1}^{N} p(A_i' | x_K, D) s_k \hat{\lambda}_k^n} \quad ; a_{ij} = p(A_i' | x_J, D) s_j \\ &= \frac{\hat{\lambda}_j^n}{s_j} \sum_{i=1}^{M} \frac{a_{ij}}{\sum_{k=1}^{N} a_{ik} \hat{\lambda}_k^n} \end{aligned} \tag{6-21}$$

In the above, s_j is the survival probability that a photon emitted from source element j would be detected anywhere; and a_{ij} is transition probability of the measured event A_i' given that it was emitted from the x_j source element, which equals the probability density

function of measurement $A_i^{'}$ given a detected photon emitted from x_j combined with the survival probability[141].

In comparison to the bin-mode MLEM Eq. (6-15), each measured event in the list-mode MLEM may be considered as a unique and infinite small bin, thus $y_i \to 1$ for each detected photon and $y_i \to 0$ for the infinite number events not be detected in the current measurement. The value M is the total number of the detected measurements instead of the total number of detector bins. However, since the measurement $\underline{A}$ does not span the space of all possible events, the survival probability $s_j \neq \sum_{i=1}^{M} a_{ij}$, must be summed over the transition probabilities of <u>all possible measurements</u> originating in source element j, including the events for which $y_i \to 0$.

6.1.3 Parallel MLEM algorithms

As mentioned above, the bin-mode MLEM and list-mode MLEM algorithms are potential image reconstruction methods for both a conventional collimated Anger Camera and Compton Camera. However, the MLEM algorithm poses two problems to practical application using a single computer[143]. First, since convergence of the MLEM algorithm is slow and, as mentioned previously, the number of measured events will be on the order of 10^7. The computational burden is extremely high because of the resulting large matrix vector multiplication combined with the large number of iterations required to obtain a satisfactory estimate. The second limitation is that a very large memory space is required to store the matrix of transition probabilities plus the estimated image vector and data list. To solve this problem, historically, several parallel MLEM programming techniques have been applied for PET and SPECT image reconstruction. Unfortunately, most of these methods depend on a specially designed computational platform. For example, the convolution MLEM is calculated on a VLSI based systolic structure[129]; the MLEM parallelization is realized on a mesh-connected single instruction stream and multiple data stream system[130]; implementing parallelized MLEM 3-D PET image reconstruction on interconnection share memory system [131]; and, realizing the

parallelized MLEM algorithms on multiple instruction stream and multiple data stream based supercomputer[144, 145].

Another approach to parallel computation of MLEM solutions has employed a message passing interface (MPI) based network connected computer cluster. This MPI based computation platform is well suited to the intrinsically parallelizable characteristic of MLEM. The most important advantages of an MPI based cluster are[146]: 1) Separate nodes (processors or general computers) are readily connected by a high speed communication network; 2) The paralleled version of the algorithms can be easily ported to different parallel computation platforms of this type; 3) MPI supports the best way to manage the distributed memory and computation burden to obtain optimal performance. Even though MLEM inherently separates the algorithm into two steps, i.e. forward-projection and back-projection, the computation of each step can be distributed to all nodes. The critical disadvantage of applying an MPI based cluster to the MLEM algorithm is that large amounts of data must be distributed among the nodes via the network between the two steps. Since the total running time is the sum of the CPU ET and MPT, and message passing [147] is slower than executing instructions on the CPU, an efficient parallelized MLEM algorithm depends on the data partition and message passing strategy to trade off execution time and message passing time. The optimization approach[132, 148] is based on the scheme of one master node with multiple slave nodes. This approach limits the ability to balance the execution time and message passing time.

In this section, evaluation of the total performance based on a chess-board data partition is introduced first. To further reduce the total running time and utilize each node more efficiently, a technique of overlapping the execution and message communication is then described[149].

6.1.3.1 Analysis of the Parallel MLEM Algorithm

As illustrated in the previous section, the bin-mode (Eq. 6-15) and List-mode (Eq. 6-21) MLEM formulas are very similar. The bin-mode MLEM formula can be considered as the general format. For the list mode, M is total number of measured events instead of the number of measurement bins, and also Y_i equals 1 for each measured event. Therefore, the general format MLEM may be re-written as

$$\widehat{\lambda}_j^{\,n+1} = \frac{\widehat{\lambda}_j^{\,n}}{s_j} \sum_{i=1}^{M} \frac{y_i a_{ij}}{\sum_{k=1}^{N} a_{ik} \widehat{\lambda}_k^{\,n}} \qquad\qquad (6\text{-}22)$$

where a_{ij} is the transition probability, which is an element of the system matrix **P**, describing the probability of detecting an event in the i-th detector bin given that it was emitted from the j-th source element. $\widehat{\lambda}_j$ is the intensity estimated in the j-th voxel, y_i is the measured event number in the i-th detector bin or equal to 1 for the list-mode case. M is the number of detector bins or number of measured events in the list and N is the number of reconstructed image voxels. Detection sensitivity is s_j.

As described above, the serial MLEM algorithms running on a single CPU require unacceptable execution times and computer memory requirements. Parallel computing of the MLEM algorithm is necessary to enable sufficient iterations in an acceptable running time. Therefore, a parallel computing approach based on using a message passing interface on a network connected computer cluster has been investigated to solve these problems.

For the MLEM reconstruction (Eq. 6-22), each iteration can be divided into four steps as an inherent sequence. The first two steps, the "forward projection", map the image onto the detector. The following two steps perform the "back projection". Because the four steps are "input after output dependent", they must be executed serially, which limits execution of any two steps at the same time in parallel computing. Fortunately, calculation and data in each step, especially the first and third step, can be divided into sub-pieces and distributed to different computing nodes. The challenge of the parallel computation depends on the strategies of the data and task partition as well as the communication schemes to distribute the results among processor nodes. Parallel computation with the busiest CPU load and the minimum network communication time is regarded as the most successful and efficient procedure. This requires a tradeoff between the program execution time and the message passing time on the network. Therefore, a chessboard partition of both processor nodes and system matrix P or $\{a_{ij}\}$ has been evaluated to improve the whole performance of parallel ML-EM computation in the following section.

Step 1, $\quad t(i) = \sum_{k=1}^{N} a_{ik} \hat{\lambda}_k^n$

Step 2, $\quad f(i) = y_i / t(i)$
$\qquad\qquad f(i) = 1 / t(i)$ $\qquad\qquad\qquad\qquad\qquad$ (6-23)

Step 3, $\quad r(j) = \sum_{i=1}^{M} a_{ij} f(i)$

Step 4, $\quad \hat{\lambda}_j^{n+1} = \hat{\lambda}_k^n r(j) / s_j$

6.1.3.2 Parallel MLEM Algorithm Based on Chessboard Data Partition

1. Master-slave based parallel MLEM algorithms

Before presenting the chessboard data partition, execution of the parallel MLEM algorithm on a master-slave based platform is briefly introduced. The disadvantage of this method is it does not optimize the time for passing messages among the process nodes.

The virtual topological master-slave architecture is shown in Figure 6.1. The processor consists of one master node to control the program flow, and a set of slave nodes to handle the tasks assigned by the master node. In the forward projection, the master node will partition and distribute the system matrix P or $\{a_{ij}\}$ and the previously estimated image vector $\hat{\underline{\lambda}}^n$ to each slave-node. When this step is completed, the partial results on all slave nodes are transferred back to the master node which sums the partial results and computes $f(i)$ according to step2 in eq. 6-23. The $\underline{f}$ vector is then partitioned and each subset is assigned to slave nodes. Step3 of the back projection is then completed in each slave node. Step 4 is next executed in the master node after acquiring the partial results from the slave nodes to obtain a new estimation $\hat{\underline{\lambda}}^{n+1}$.

During each iteration, this simple master-slave method needs to transfer the forward-projection results $\underline{f}$ and back-projection image results $\hat{\underline{\lambda}}^n$ between the master-node and slave-nodes twice. Thus, the high cost of message passing will greatly influence the overall performance. The master node and slave nodes can not work simultaneously since they each must wait for the results before processing. Also, entries of the P matrix must be stored in each slave node for calculation of both forward and back projections.
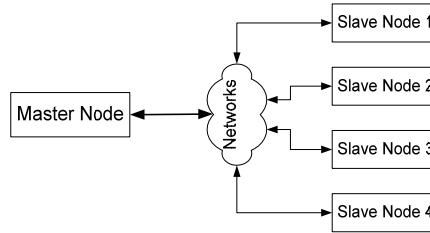
Figure 6.1. The description of master-slave architecture for executing the parallel MLEM algorithm. The single master node and four slave nodes are interconnected by networks.

2. Chessboard data partition based parallel MLEM algorithm

Clearly, the master-slave based parallel MLEM algorithm is not efficient. The key issue to realize a successful parallel MLEM algorithm depends on two critical factors: one is how to divide the system matrix P or transition probability data set $\{a_{ij}\}$ into each node with comparatively smaller memory capacity; another is how to reduce the communication time for message passing in order to decrease total running time. A parallel computing approach based on the chessboard data partition has been investigated here to optimize partition strategy.

All computers are partitioned like a virtual chessboard with Nr rows and Mc columns. As shown in Figure 6.2, nodes in every row and every column are composed of the row group and the column group respectively to achieve efficient communication between the nodes in the group. The partial results are only transferred among nodes in the same group. The image space vector (L), measurement space vector (Y), and system probability matrix (P) containing all of a_{ij} are decomposed on the chessboard. For matrix P, the sub-matrices of P in nodes do not overlap each other, that , the assigned sub-matrix in one node is not changed during the whole calculation. Clearly, this kind of data partition is the most efficacious way to minimize local memory with minimal overlap. The partial results can be calculated from the assigned partial data in each node according to the ML-EM algorithm. By modifying the geometric shape of the chessboard, i.e. the number of rows and columns, according to the dimension of vector L and vector Y, optimal performance is obtained through the appropriate tradeoff between program running time and message passing time.

The parallel MLEM algorithm flowchart is shown in Figure 6.3. For each iteration, the MLEM algorithm is split into two stages and four steps, which can be

decomposed into a partial job that can be completed in each node independently, and the partial results accumulated by master nodes in each row or column group. The first stage is the forward projection, in which the calculated vector [*f(i)*] is obtained from the previously estimated vector L and matrix P; the other is the back projection in which the image L is estimated from the measured data and calculated vector [*f(i)*].
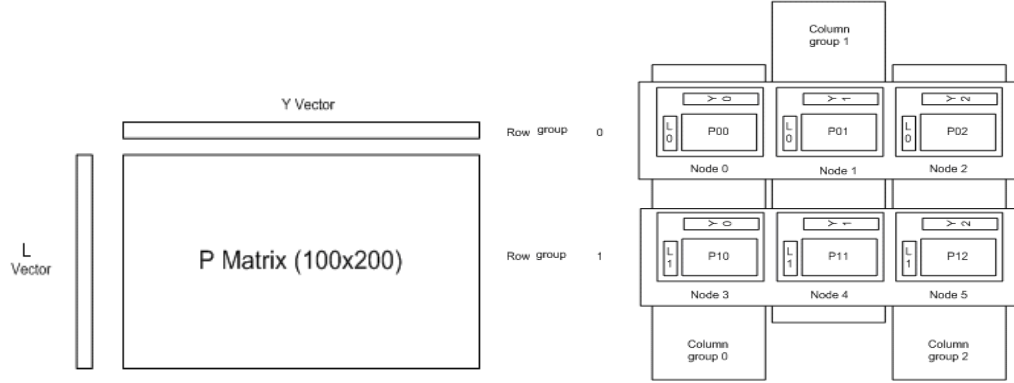
Figure 6.2 Illustration of Chessboard data partition for parallel MLEM algorithm. P matrix is the system matrix or data set of transition probabilities. The Y vector denotes the measured data set and the L vector is the estimated image. There are 6 processing nodes divided into 2 row groups and 3 column groups.

At the middle of the forward-projection, in each column group, every node transmits the partial result to a master node; and then the final result is summed in this node and broadcast to all other nodes in the same group. Finally, the estimated image in this iteration is obtained by summing up the partial results from nodes of the same row group in the back projection. For example, in step 1, the nodes in the same column group only calculate *t'(i)*, i.e. partial result of *t(i)* according to $t'(i) = \sum_{k=1}^{N'} a_{ik} \hat{\lambda}'^{n}_{k}$; total $t(i) = \sum t'(i)$ is the sum of all t'(i) of the nodes in the same column communication group ; and this final *t(i)* is transmitted from the master node to all other nodes in same group. Therefore, due to the structure of the EM algorithm, for the forward projection, the nodes only exchange results with others in the same column-group at the end of step1 and communication of back projection is constrained to the row group, which occurs at end of step3.

To evaluate results of the proposed parallel MLEM algorithm, the parallel program was executed on the parallel system located in the center for advanced computing at the University of Michigan with different data partitioning. The system consists of 128 32-bit AMD processors, and each processor has 2GB RAM. For a chessboard with Nr rows and Mc columns, the data for calculation are distributed into all computers. In each node, data with the size of L/Nr+Y/Mc+P/ (Nr+Mc) is allocated in the local memory space.
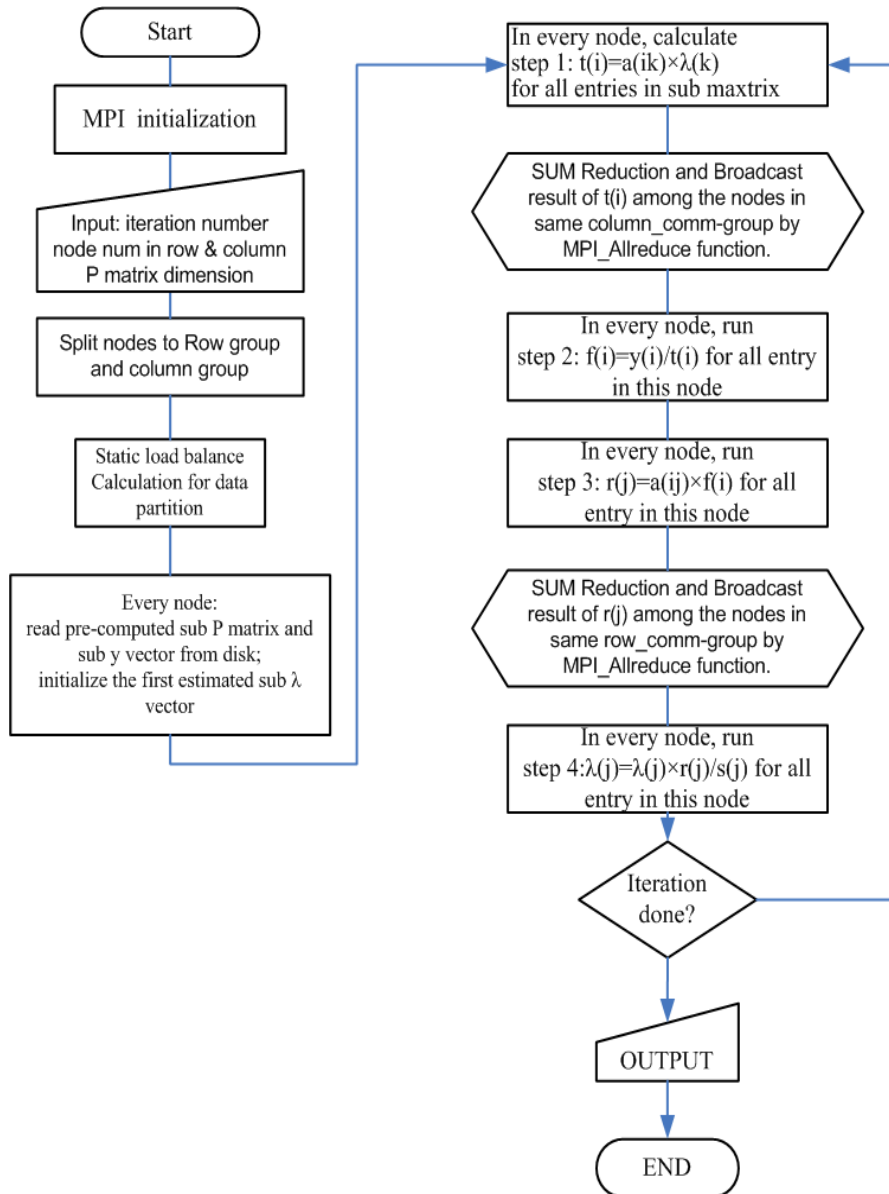
Figure 6.3. Flowchart of the parallel MLEM algorithm based on the chessboard data partition using a message passing interface on a network connected computer cluster.

3. Performance evaluation for a square chessboard with different number of nodes.

Performance of parallel MLEM algorithms for 10 iterations and a 1000×1000000 P matrix with 1000 elements in the L vector and 1000000 measured events, is evaluated on the parallel platform with different numbers of processor nodes.

The speedup rate formula is given in Eq. (6-24)

$$S_N = \frac{T_s}{T_{pN}}, \qquad\qquad (6\text{-}24)$$

N is the number of processor nodes for parallel computation, S_N is the speed up, T_s is the total running time for serial algorithms, T_{pN} is total running time for parallel algorithm on a platform with N nodes. Another helpful criterion is speed up efficiency, which is

$$e_N = \frac{S_N}{N}. \qquad\qquad (6\text{-}25)$$

1000 (L) x 1000000 (Y)
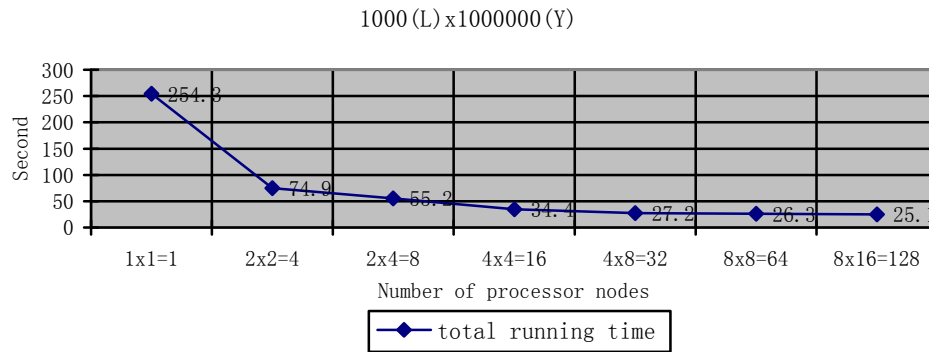
Figure 6.4 Comparison of total running time for parallel MLEM algorithms on the square chessboard as a function of number of computer nodes from 1 to 128. The computation task is 10 iterations with a 1000×1000000 P matrix.

The performance comparisons according to the total running time, speed up S_N and efficiency *e* are illustrated in the Figures 6.4, 6.5 and 6.6, respectively. The parallel MLEM algorithm executing on the square chessboard data partition reduce the total running time as the total number of processor nodes increases. The speedup of parallel MLEM on 128 nodes is approximately 10 times compared to the serial MLEM running on a single processor. In theory, the efficiency should be proportional to the number of processor nodes. However, the efficiency gain is far less, especially for the as the number of processor node exceeds 16. This is because the communication time

increases with the number the number of processor nodes, and, when the node number is more than 32, further speedup is negligible.

1000(L)x1000000(Y)
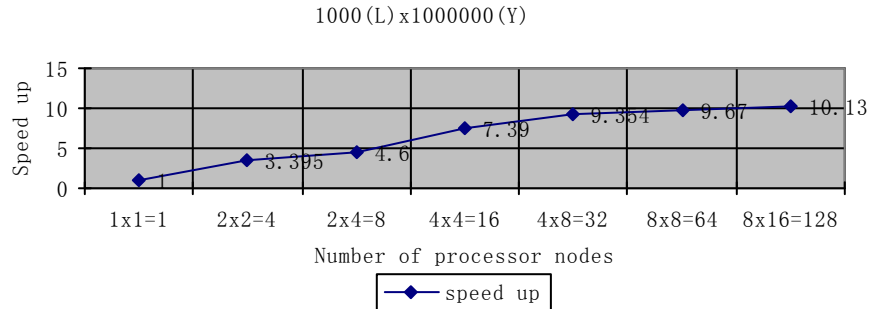
Figure 6.5 Comparison of speedup time for parallel MLEM algorithms on a square chessboard as the number of computer nodes varies from 1 to 128. The computation task is 10 iterations for a 1000×1000000 P matrix.

1000(L)x1000000(Y)
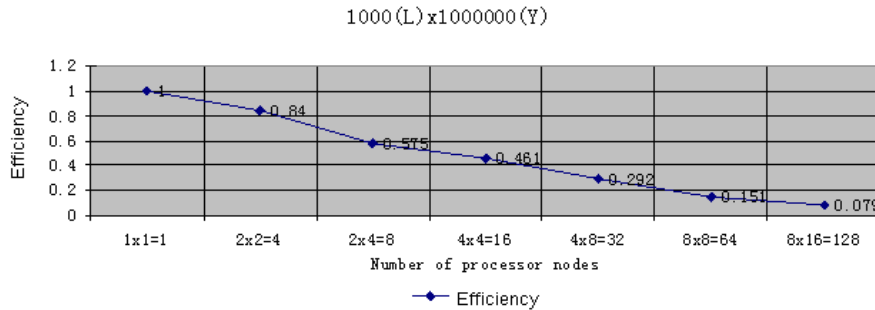
Figure 6.6 Comparison of efficiency for parallel MLEM algorithms on the square chessboard as the number of computer nodes increases from 1 to 128. The computation task is 10 iterations and 1000×1000000 P matrix.

4. Performance evaluation for the different chessboard with same number of nodes.

For chessboards with different shapes but an identical number of computer nodes, illustrated in Figure 6.7, the strip-shaped chessboard with one row achieves the minimum running time of 12s, compared to the chessboard with one column which requires 86s to finish execution. This is because that in the forward projection, 1000000 elements need to be transferred among nodes, whereas just 1000 elements need to be broadcast in the back projection. Therefore, the optimal data partition is 1×64, one row chessboard, for which the message passing time for the forward projection is trivial.

Parallel computing for the ML-EM algorithm not only reduces the run time, but also decreases the local memory requirement for each computer node. In each node, data

160

with the size of L/Nr+Y/Mc+P/ (Nr+Mc) is allocated in the local memory space. If the dimension of the measurement vector is much larger than the dimension of the image vector, the chessboard with one row will obtain the best performance with the least communication time.
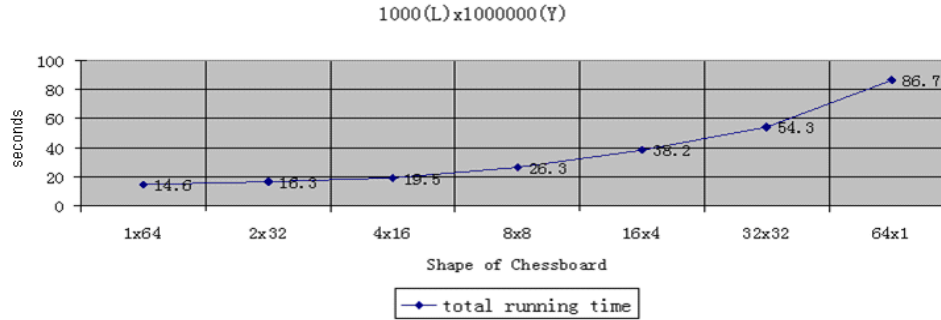
Figure 6.7 Performance comparison of parallel MLEM algorithms for 10 iterations and 1000×1000000 P matrix for different shape chessboards ranging from one column to one row. As the number of measured events become much greater than the number of estimated elements, a strip-shaped chessboard with one row achieves the minimum running time.

6.1.3.3 Overlapping the Computation and Communication

As described in the last section, when the number of measured events M is considerable more than the size of the estimated vector N, such as for Compton camera image reconstruction, the one row data partition achieves the minimum running time by eliminating the communication required between step 1 and step 2 in the forward projection. Thus, reducing the message passing time in the back projection between step 3 and step 4 becomes the major issue to further decrease the total running time.

The technique of overlapping computation and communication [150] has the potential to solve this problem since computation in processor nodes and communication among nodes can take place simultaneously because the processor for computation and hardware for communication are independent of each other.

To realize the overlapping of computation and communication, in each node, step 3 and step 4 in the original parallel MLEM algorithm, the associated data are split evenly into two small parts, that is:

$$\textit{Step 3a,} \quad r1(j) = \sum_{i=1}^{M/2} a_{ij} f(i)$$

161

$$\text{Step 3b,} \quad r2(j) = \sum_{i=M/2+1}^{M} a_{ij} f(i). \tag{6-26}$$

$$\text{Step 4a,} \quad \widehat{\lambda}_{temp} = \widehat{\lambda}_k{}^n r1(j) / s_j$$

$$\text{Step 4b,} \quad \widehat{\lambda}_j{}^{n+1} = \widehat{\lambda}_k{}^n r2(j) / s_j + \widehat{\lambda}_{temp}$$

Therefore, as illustrated in Figure 6.8, the communication of step 3a can overlap the computation of step 3b, and computation of step 4a can overlap with the communication of step 3b. The original total running time for the method without overlapping of computation and communication will be,

$$t_{step1} + t_{comm1} + t_{step2} + t_{step3=step3a+step3b} + t_{comm3=comm3a+comm3b} + t_{step4=step4a+step4b}.$$

And the total running time for the parallel MLEM with overlapping will decrease to

$$t_{step\ 1} + t_{comm\ 1} + t_{step\ 2} + t_{step\ 3a} + \max(t_{step\ 3b} + t_{comm\ 3a}) + \max(t_{comm\ 3b} + t_{step\ 4a}) + t_{step\ 4b}$$

Because a single row chessboard used here eliminates the communication for transporting the results of step 1, the t_{comm1} equals zero.
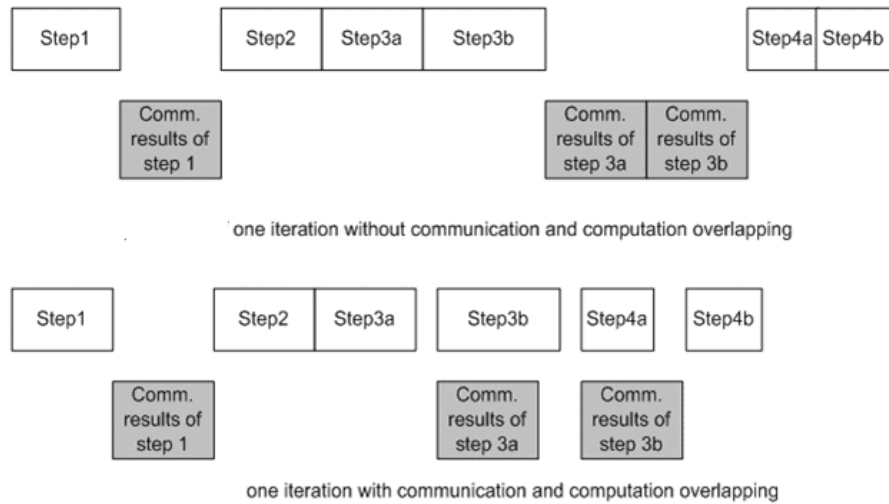
Figure 6.8 Illustration and comparison of parallel MLEM without communication and computation overlapping and with communication and computation overlapping.

The comparison of total running time and speed up of parallel MLEM algorithm with/ without overlapping of computation and communication is shown in the Figure 6.9 and Figure 6.10, respectively. The program with 1000×1000000 P matrixes was executed for 10 iterations on the one row chessboard with different processor nodes. As

mentioned, for the one row chessboard, transporting 1000000 elements between the step 1 and step2 does not occur. Therefore, the communication task is just transporting 500×2 elements during the step3b and step 4a. Even though the load is not very heavy, the program with overlapping communication and computation further saves about 5%~10% of total running time compared to the process without overlapping.
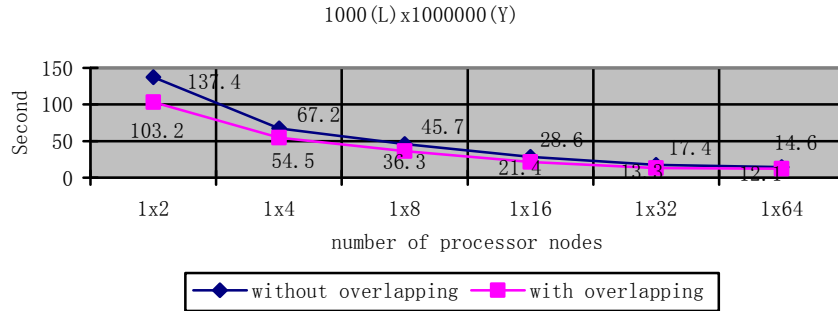
Figure 6.9 Comparison of total running time of parallel MLEM algorithm with/ without overlapping of computation and communication. The task is 10 iterations and 1000×1000000 P matrix on the one row chess board with different numbers of computer nodes.
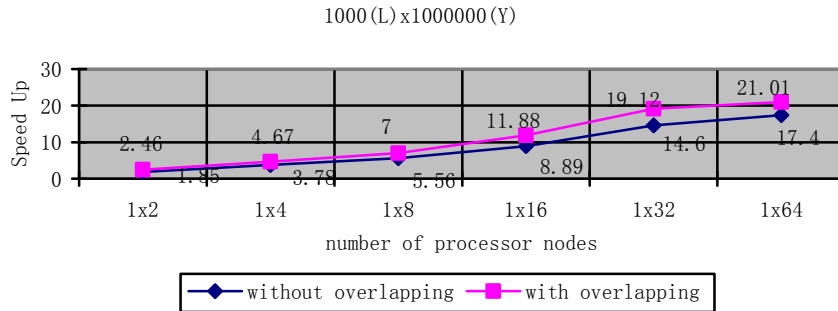
Figure 6.10 Comparison of speed up for parallel MLEM algorithm with/ without overlapping of computation and communication. The task is 10 iterations and 1000×1000000 P matrix on the one row chess board with different numbers of computer nodes.

6.2 A Full Digital Design of Real Time Signal Processing and Pattern Matching for Pileup High Count-Rate Pileup Detection

6.2.1 Introduction

As mentioned in Chapter 2, the scintillation detector such as an un-collimated NaI(TI) Anger camera is used as the second detector for the prototype Compton imaging system. When a gamma-ray interacts in NaI a light pulse is emitted with amplitude proportional to the deposited energy. The wavelength of this light is 4200 angstroms, and the conversion efficiency is about 40 photons per keV of deposited energy. In an Anger camera the light pulse is usually viewed by an array of PMT that produce a number of photoelectrons proportional to the light incident upon the photocathode located inside a vacuum envelope [151].As shown in figure 6.11, for NaI, without noise and pile-up, the ideal electronic pulse acquired from a single PMT has a rise time of 5.3 ns and an exponential decay with a 230ns time constant, (τ). The pulse shape is determined by the rise time and decay time of the NaI light output. If the phototube is a linear device, then the current out of the phototube will be proportional to the light output. The electronic pulse shape can be altered by integration or differentiation of the raw phototube output pulse. The integral of this pulse is proportional to the total light output from the scintillation event. To measure deposited energy of the interacting photon, this signal is usually integrated until its amplitude has decayed to a trivial value. The method calculates the maximum information of the deposited energy.

However, for the prototype Compton imaging system which has no mechanical collimator to limit the incoming photon flux, the second detector directly views the radioactive source and the scattered photons from the first detector. Depending on shielding and imaging geometry, The Anger camera may view the source directly with a resulting high count rate. As illustrated in figure 6.12, the resulting high count-rate makes it highly probable that the signal from two or more gamma-rays will overlap in time. If the pulse waveform is integrated for a fixed time period, which can be as long as 3τ, this conventional approach results in spectral distortions because the deposited energy of the piled up pulses is overestimated by considering several photons as a single one. Because

the position information of deposited photon on the detector need its correct deposit energy value, and determination of random Compton coincidence need accuracy start time of each pulse. Therefore, to accurately measure the photon energy and time deposited in the second detector at high count rates, signal pileup prevention techniques are required.
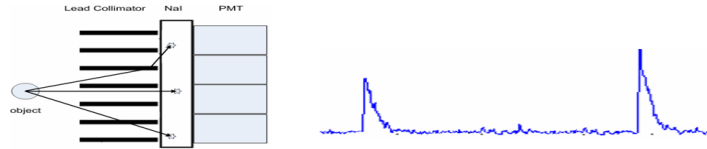
Figure 6.11 Low count rate scintillation signals without pileup for conventional collimated NaI Anger camera. The scintillation time constant (τ) is 230ns.
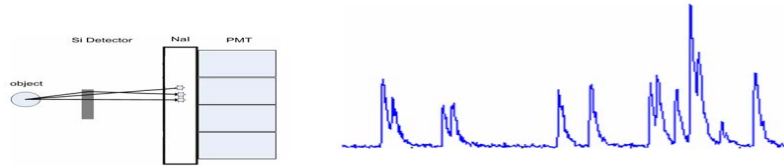
Figure 6.12 High count rate scintillation signals illustrating pulse pileup for the NaI absorption detector in the Compton imaging system.

Table 6.1 Probabilities of No Pile-up and Multiple Event Pile-up for High Count Rate

Integration time	Count rate(cps)	No event pileup	2-events pileup	3-events pileup	4-events pileup	5-events pileup	6 or more events pileup
80ns	0.5M	0.9608	0.0377	0.0012	0.0001	0	0
	1M	0.9231	0.0710	0.0055	0.0004	0.0001	0
	2M	0.8521	0.1260	0.0186	0.0028	0.0004	0.0001
	4M	0.7261	0.1989	0.0545	0.0149	0.0041	0.0011
230ns	0.5M	0.8914	0.1025	0.0039	0.0002	0	0
	1M	0.7945	0.1827	0.0140	0.0016	0.0002	0.0069
	2M	0.6313	0.2904	0.0445	0.0102	0.0028	0.0207
	4M	0.3985	0.3666	0.1124	0.0517	0.0285	0.0421
690ns	0.5M	0.7082	0.2443	0.0281	0.0048	0.001	0.0135
	1M	0.5016	0.3461	0.0796	0.0275	0.0114	0.0339
	2M	0.2516	0.3472	0.1597	0.1102	0.0912	0.0401
	4M	0.0633	0.1747	0.1607	0.2218	0.3673	0.0123

To avoid or reduce the pulse height spectral distortions due to pulse pile-up, active pile-up rejection circuits can be combined in the linear amplifiers to preserve non

pile-up events and to detect and discard pulses that are estimated to be affected by pile-up. Pile-up rejection is commonly used to eliminate piled-up pulses from low count rate signals. However, this technique is not suitable for the high count rate situation since the percentage of piled-up events may greatly exceed non piled-up events. Table 6.1 illustrates the probabilities of no event pile-up and multiple event pile-up for 0.5 Mcps(million counts per seconds), 1 Mcps, 2 Mcps and 4Mcps within a 80ns, 230ns(1τ) and 690ns(3τ) for the gamma-ray emission is random with a Poisson distribution. For example, for a 3τ integration time and 1Mcps count rate, only 50 percent of all events are non pile-up events. All other events will distort the pulse height spectrum if no pile-up rejection is used.

Historically, for the high count rate situation, to reduce the influence of signal pileup and accurately measure the photon energy deposited in scintillation detectors, several signal pileup prevention techniques have been developed[26, 152-154]: (a) The delay-line pulse-clipping (DLC) technique avoids calculating the energy of the next overlapped pulse by cutting its tail and integrating the signal for a fixed short time; (b) The dynamic integration method terminates the integral of pulse signal as soon as the following event arrives, then the energy of the two overlapped pulses is compensated and adjusted by the estimated values; (c) The digital-analog hybrid active pileup prevention energy (PPE) method, is proposed to obtain an estimate of the actual photon energy, which can be carried out in three steps. First, the present event is integrated dynamically until the arrival of the following event is detected. Second, a weighted-value is calculated to estimate the total energy in the scintillation detector which includes the energy from present event and the remnant energy from all the previous events. Third, the energy of the event is obtained by estimating the residual energy using a decay-weighted sum of the previous total energy and subtracting it from the present total energy.

The DLC technique is effective for events with relatively high count rates, as shown in table 6.1. When the integration time changing from 3τ to 1τ, the probability of no pile-up events at 1Mcps true event rate increases from 0.5 to 0.8. However, the energy resolution will be degraded and underestimated for the low count-rate situation and for non-overlapping pulses at high count rates. The dynamic integration is suitable for the

166

simple two event pileup case but becomes complicated for multiple-event pileup. The maximum count rate using this method is limited to under 400kcps for NaI gamma cameras[155]. In comparison, the active PPE method provides more accurate energy calculation results under all conditions since it "cancels the remnant signals from previous events and excludes the pile up of signals from following events". However, performance of this HYPER method is significantly deteriorated due to its inflexibility and sensitivity to noise in the digital – analog hybrid circuit design.

To overcome those restrictions, the analog circuit is replaced by an all digital architecture by using a high sample rate A/D converter to recover photon energy deposited in a NaI scintillation detector. At high count-rates, compared with digital-analog hybrid implementation, this all digital solution offers more flexibility in accommodating different scintillator and higher noise immunity. The digital pileup prevention energy (D-PPE) algorithm is described here for a NaI scintillation detector with decay constant of 230ns and an A/D converter with sampling frequency of 100Mcps, that is, with sampling period of 10ns. The D-PPE Algorithm can be implemented by a high performance Field-programmable gate array (FPGA) or Application-Specific Integrated Circuit (ASIC) Design. To verify this algorithm a Very Large Scale Integration (VLSI) PPE processor is designed and simulated according to ASIC Design rules and up-to-date TSMC 0.18um technologies using a VLSI Cadence CAD platform.

6.2.2 Methods and Algorithms

The all digital implementation for estimating photon energy, when high count rates result in pulse pileup in a scintillation detector, is introduced here. This involves three steps:1) dynamically integrating a present event until the next event is detected; 2) estimating a weighted-value to indicate the total energy deposited in the scintillation detector which includes the energy from present event and the remnant energy from all the previous events;3) deriving the energy of the present event by subtracting the residual energy, i.e. a decay-weighted estimate of the previous total energy from the present total energy.

To obtain the deposited photon energy in the NaI scintillation detector with all digital circuits and speed up the binary calculations on the data acquired from the 100Msps A/D converter, the entire PPE algorithm is discretized. To avoid time consuming steps including floating point multiplication and exponential calculation, some intermediate procedures are accomplished using fast digital calculation logic, such as a simple adder, shifter, inverter and look up table (LUT).

The scintillation value of the jth photon event with energy E obtained by an A/D converter with sampling period Ts at sample n is

$$e[n] = (E/\tau)\exp[-(n-n_j)T_s/\tau]$$ (6-29)

Under high count-rate conditions, however, the following pulse is more likely to occur before the previous pulse has decayed to a trivial value. Within a sequence composed of three overlapped gamma rays as shown in figure 6.13, the jth gamma ray is detected by a scintillator at sample n_j, which overlaps the tail of its preceding (j-1)[th] gamma ray. The following (j+1)[th] gamma ray is also a pileup event which overlaps on the tails of the preceding two events. The scintillation signals from those three events, which start at sample n_{j-1}, n_j, and n_{j+1}, respectively, are obtained from an external 100Msps A/D converter with the sampling period (T_s) of 10ns.
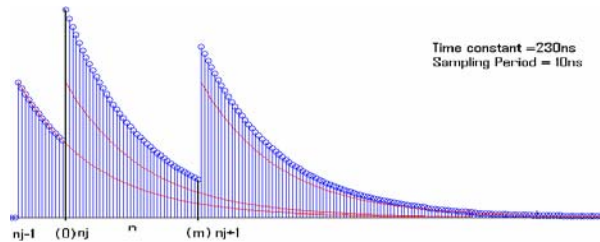
Figure 6.13 Acquisition of NaI scintillation signals without noise from three simulated pileup events, The time constant τ is 230 ns and the sampling period is 10ns. Every vertical line expresses the sampled value by A/D converter.

The acquired instantaneous value, q_n, at sample n that falls in the interval between two dark vertical lines, i.e. $n_j \leq n < n_{j+1}$, contains the energy from the jth and (j-1)[th] gamma rays is calculated according to Equation (6-29), where E_j denotes the energy of the jth gamma ray, T_s denotes the sampling period and equals 10ns, and τ denotes the time constant of the scintillator and equals 230ns for NaI.

$$q[n] = (E_j/\tau)\exp[-(n-n_j)T_s/\tau] + (E_{j-1}/\tau)\exp[-(n-n_{j-1})T_s/\tau].$$ (6-30)

Under the assumption that there are (m+1) samples within the interval from the dark line (0) to another dark line (m), the sample n_j is re-set as the zero index to derive more concise equations. The discrete weighted sum S_j for the jth gamma ray is defined by Equation (6-31), where q[m] is the acquired signal at sample m (the point just before the arrival of the next event).

$$
\begin{aligned}
S_j &= \tau q[m] + T_s \sum_{n=0}^{m} q[n] \\
&= (\tau + T_s)q[m] + T_s \sum_{n=0}^{m-1} q[n] \\
&= E_j + E_{j-1} \exp[-(n_j - n_{j-1})T_s/\tau]
\end{aligned}
\tag{6-31}
$$

Similarly, the discrete weighted sum S_{j-1} is expressed by Eq. (6-32).

$$
S_{j-1} = E_{j-1}
\tag{6-32}
$$

To achieve fast binary calculation of the discrete weighted sum with a digital circuit and avoid the time - consuming multiplication when $T_s = 10$ and $\tau = 230$, another intermediate variable SE_j, one-tenth of S_j, is introduced in Equation (6-33). The multiplication of q[m] with $[(T_s + \tau)/10]$, hence, is implemented by two binary left shifts of q[m], represented as the symbol $<<$.

$$
\begin{aligned}
SE_j &= S_j/10 \quad (\text{for } \tau = 230, T_s = 10) \\
&= (\tau + Ts)q[m]/10 + T_s \sum_{n=0}^{m-1} q[n]/10 \\
&= 24 \cdot q[m] + \sum_{n=0}^{m-1} q[n] \\
&= 2^4 \times q[m] + 2^3 \times q[m] + \sum_{n=0}^{m-1} q[n] \\
&= (q[m] << 4) + (q[m] << 3) + \sum_{i=0}^{m-1} q[i]
\end{aligned}
\tag{6-33}
$$

Following the above deductions, the total energy for the jth pileup gamma ray E_j could be obtained from Equation (6-34) by using the weighted sum of the current event and the decay-weighted sum of the previous event, in which the binary subtraction operation is transformed into 1 plus the result of its inverse operation, i.e. inv( ).

$$
\begin{aligned}
E_j &= S_j - S_{j-1} \exp[-(n_j - n_{j-1})T_s/\tau] \\
&= 10\{SE_j - SE_{j-1} \exp[-(n_j - n_{j-1})T_s/\tau]\} \\
&= (2^3 + 2^1)SE_j \\
&\quad + \{inv(10 SE_{j-1} \exp[-(n_j - n_{j-1})T_s/\tau]) + 1\}
\end{aligned}
\tag{6-34}
$$

To achieve high calculation precision and avoid floating point exponential multiplication, a look-up table for the exponential multiplication is used, in which all the values of the amplified exponential terms are stored. Therefore, the final deposited

169

energy can be obtained from Equation (6-35), where the value of $(80 \cdot \exp[-(n_j - n_{j-1})/23])$ and multiplication with SE_{j-1} can be obtained from the table. The symbols << and >> denotes the operation of shifting the binary left and right, respectively, to realize multiplication and division.

$$E_j = (SE_j << 3) + (SE_j << 1) \\ + inv(\{SE_{j-1}\underline{80\ exp[-(n_j - n_{j-1})/23]}\} >> 3) + 1 \tag{6-35}$$

6.2.3 D-PPE Chip Architecture

To realize and verify the D-PPE algorithm, the digital processor and several corresponding function units have been designed, synthesized, simulated and verified on a VLSI CAD platform that uses TSMC 0.18μm standard CMOS technology and follows the Application-Specific Integrated Circuit (ASIC) procedure. The designed all digital PPE chip, inputs the 10 bit data from the 100Msps A/D converter and outputs the extracted event energy and the time stamp of event start point. The main features and layout of function modules in the PPE-chip are displayed in figure 6.14 and 6.15, which includes (a) ROM Look-up table; (b) Pipelined Energy Extractor; (c) Event Start Arbitrator; (e) 3 byte Median Filter; (f) Controller; (g) High resolution Timer/counter; (h) FIFO output buffer; and (i) input/output pads.
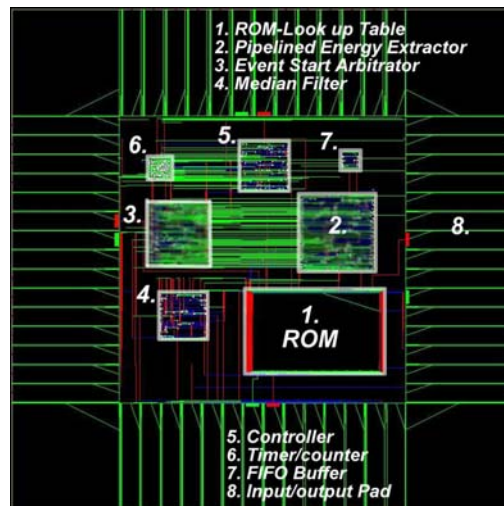
Figure 6.14 Main features and function modules of a D-PPE-chip
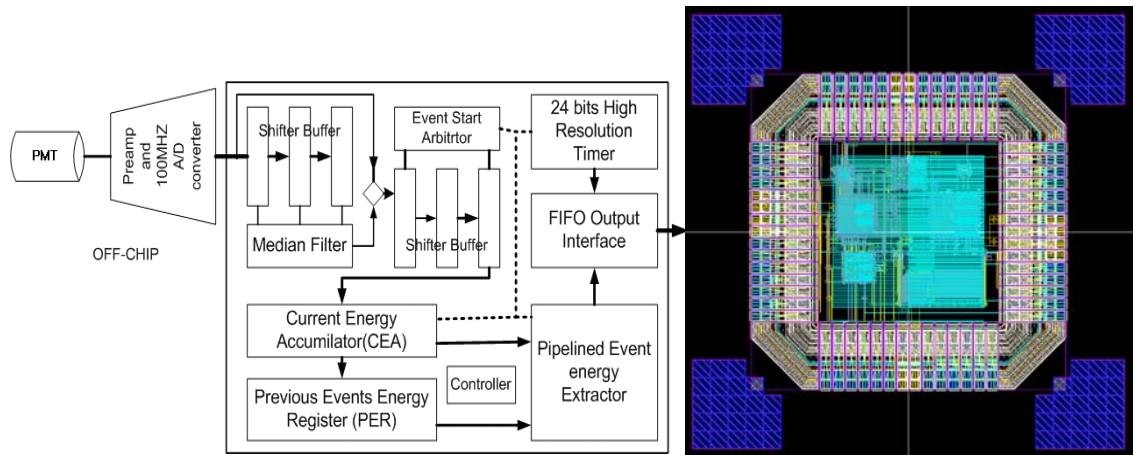
Figure 6.15 Left: internal architecture of the PPE-chip and its implementation details of data flow. Right: layout of a D-PPE-chip

A.   Input Interface

The 10 bit input port is directly connected to the external A/D converter with sampling period of 10 ns, through which the analog events of the NaI scintillation detector are sampled and digitalized.

B.   Median Filter

The obtained digital data from the A/D converter are pushed into shifter buffer which stores the latest three values in the shift registers. A three-value median filter is used here to remove noise spikes from the raw signal without significantly changing the pulse edge[156]. The filter compares the three values in the shifting registers and selects the median as the present value for the next function unit.

C.   Event Start Arbitrator

Instead of using a fixed upper-threshold and lower-threshold to estimate the start point of the coming event, a dynamic threshold is introduced in the PPE-chip to identify start points of overlapped events because fixed thresholds will not work when severely overlapped pulses occur.   In this module, the median values are pushed into another shift buffer, which stores the latest median values in the sequence.   Whenever the difference between the newest median value and the oldest one in the buffer exceeds the predetermined threshold value, the Arbitrator generates a trigger to indicate the occurrence of a new event and starts the energy extractor at the same time to calculate the energy of the last photon event.

171

D. 24-bit High Resolution Timer/Counter

Because the PPE-chip operates at 400MHz, the timer resolution can be as high as 2.5ns. The start index of each event and the interval between two neighboring events are stored for use as indices in the look-up table.

E. ROM Look- up Table

The result of $(80 \cdot \exp[-(n_j - n_{j-1})/23])$ are stored in the 1024×12 bits ROM in advance, which are indexed in a sequence by the combination of the lengths of all possible time-intervals between two neighboring events and the 4-bit partial weighted sum.
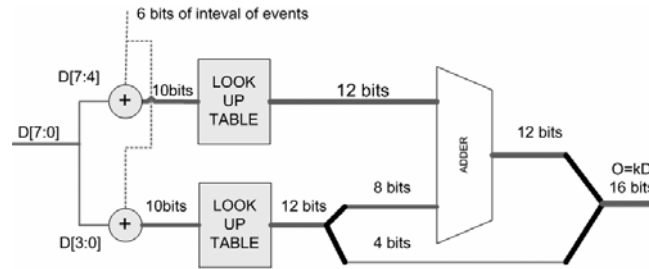
Figure 6.16 An example of the exponential multiplication of 8-bit partial-weighted sum using two 4-bit segments by using a look-up table which is indexed according to the 10-bit input, that is, using (nj-nj-1) and 4-bit partial-weighted sum as a multiplier

As explained in figure 6.16, therefore, the complex 16-bit exponential multiplication is transformed into four times 4-bits operations by dividing the weighted sum into four segments, and the result of 4-bit exponential multiplication is stored in the ROM and could be obtained by the "LOOK-UP TABLE".

F. Pipeline Event Energy Extractor

When the Event Start-Point Arbitrator generates a trigger just before the arrival of the next event, as shown in figure 6.17, the four-stage pipelined Event Energy Extractor calculates the recovered photon energy from the weighted sum of the current and its previous events, and the length of the time interval between these two events. By using the pipelined architecture, four look-up-tables for 16 bits exponential multiplication are replaced by one table, therefore, the size of PPE-chip is decreased greatly and the time of calculation in each stage could be reduced to 2.5ns.
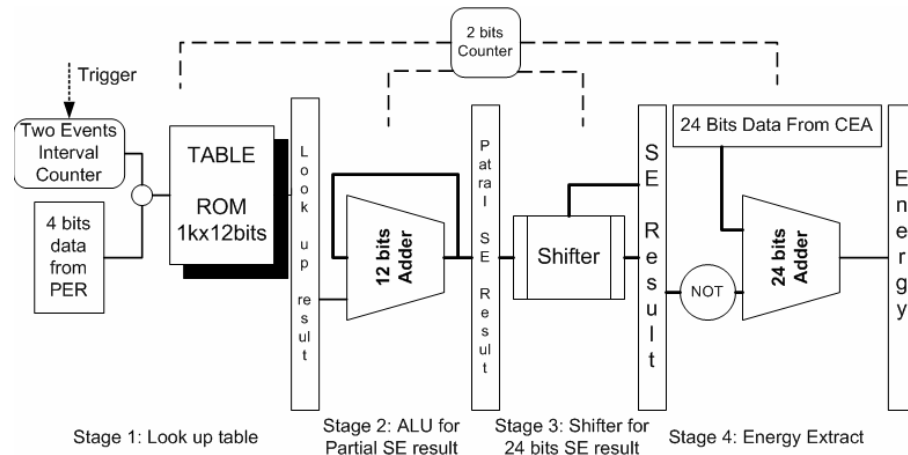
Figure 6.17 Architecture of the four-stage pipelined Event Energy Extractor (CEA is Current Energy Accumulator and PER is previous Events Energy Register)

G. FIFO Output Interface

FIFO output buffer stores 25-bit values of the extracted current event energy together with its corresponding trigger time obtained from the 24-bit High Resolution Timer. The stored data can be read out by the off-chip system.

6.2.4 Results and Data Analysis

In this section, the digital PPE algorithm is compared with the original PPE algorithm. Performance of the digital PPE algorithm is evaluated by digitizing a photomultiplier signal from a NaI scintillator viewing 140keV gamma-rays from ^{99m}Tc using a 100 MHz A/D converter, and the digital data are input to the simulated PPE chip on the CAD platform.

A. Evaluation of the Median filter

The median filter is primarily employed in the image process to reduce the "salt and pepper noise". The acquired NaI scintillation signal, ideal pulses and median filtered NaI signals using filters with windows size of 3 and 7 are compared in figure 6.18.The median filter not only decreases noise but also preserves the fast rise time of the signal for each pulse. The MSE of noise for original signal, median filtered signal with 3 samples and 7 samples wide median filter is 399.7, 157.9 and 107.7, respectively. To

reduce the complexity of real time chip design, the median filter with windows size of 3 is used in the D-PPE chips, which is realized by comparison units in chips.
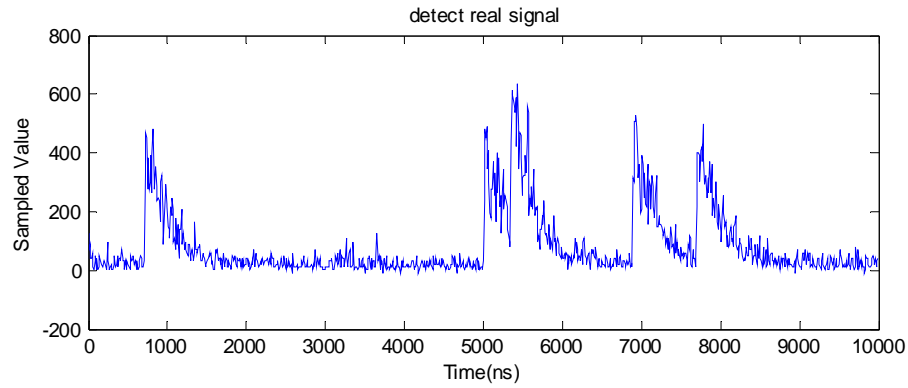
(A)
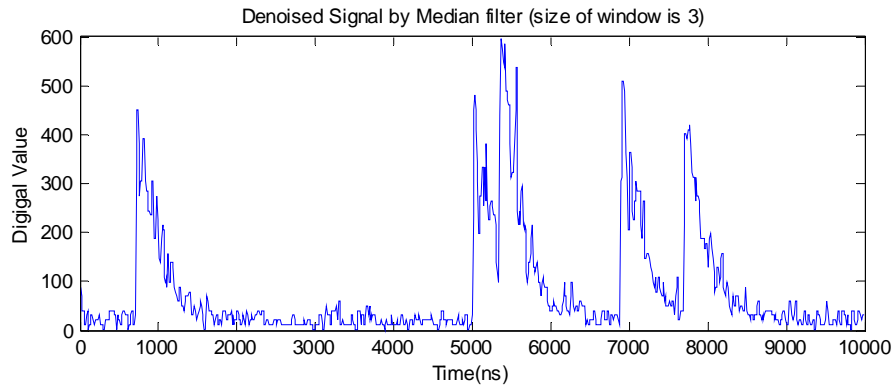
(B)
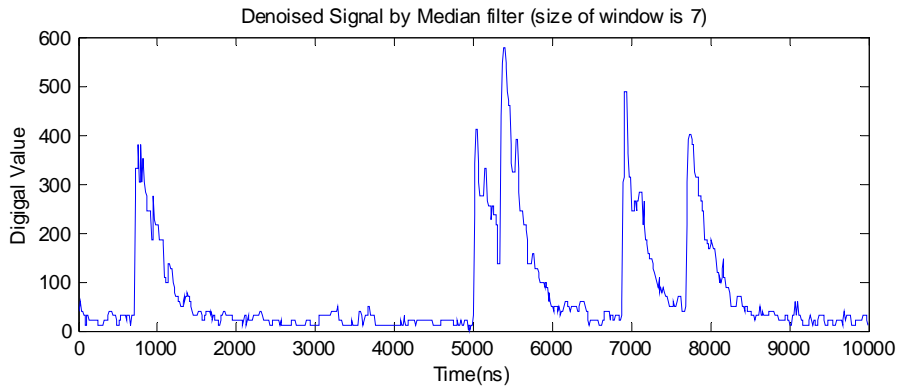
(C)

Figure 6.18 Comparison of the acquired original signal and median filtered signals using median filter with size of windows of 3 and 7, respectively. (A) Original detected signal; (B) De-noised signal with 3 value median filter; (C) De-noised signal with 7 value of median filter.

B. Evaluation of the Performance of Dynamic Threshold Technique

The dynamic threshold technique is used in the circuit to determine the start point of each pile-up event. Unlike conventional methods, which compare the current value with a fixed threshold, the dynamic technique compares the median value of the current three points with the median value of the previous three points. As shown in figure 6.19, the conventional fixed threshold method, implemented with analog circuits, cannot identify the start point of the piled up events within the circled regions. By contrast, the dynamic threshold technique, a digital algorithm, not only estimates the leading edge of every overlapped event, but also estimates the start point of isolated events. The designed circuits can identify two events when the interval between them is longer than 80ns. Thus, according to Table 6.1, for a count rate of 4 million events per send, almost 70% events can be identified correctly..
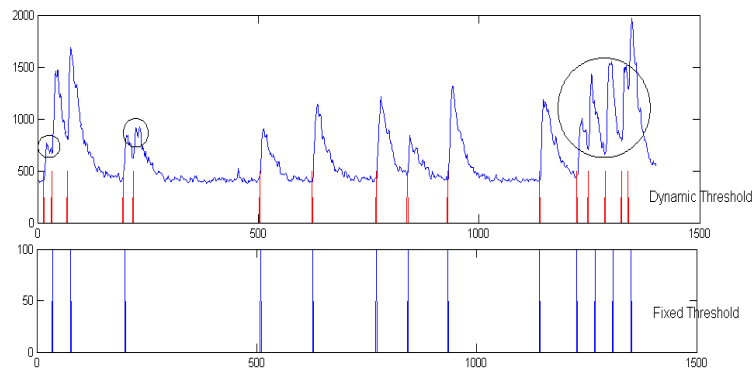
Figure 6.19 Comparison between dynamic threshold technique and fixed threshold method used to determined the start points of pile-up events. For the original signal shown at the top of the figure, the trigger signals determined by dynamic threshold and fixed threshold techniques are displayed in the middle and the bottom, respectively. The dynamic threshold method detects more piled up events than the fixed threshold method.

C. Analysis of Exponential Multiplication using a Look-up Table

To avoid the time-consuming exponential multiplication in calculating a decay-weighted sum, a look-up table is constructed.   As a result, calculation errors will occur when transforming floating point numbers to integers, which have been stored in ROM in advance.   To reduce this error, the original decay terms are amplified by a factor of 80 which results in $INT(80 \cdot \exp[-(n_j - n_{j-1})/23])$. The final multiplicative results are recovered by a left shift operation. Integral results of the amplified decay terms are compared with

the floating point decay terms indexed by (n_j-n_{j-1}) in figure 6.20, which shows that the mean square error (MSE) and the max percentage error associated with the proposed look-up table method are 5.288x10-5 and 1.17%, respectively.   The decay terms may be amplified with an even larger number which will result in more accurate exponential multiplication results, but this will also increase the complexity of the chip.
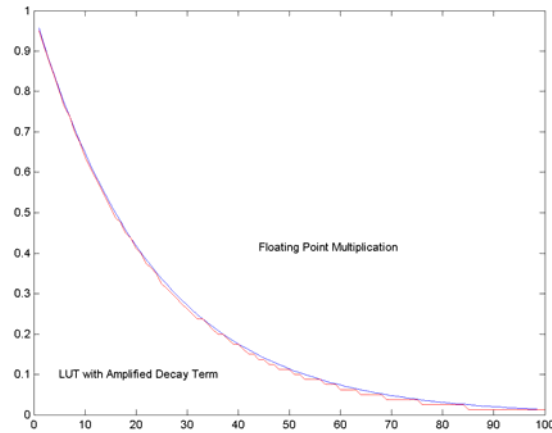
Figure 6.20 Comparison between the floating point exponential multiplications with the Look-up table method with amplified decay term. The upper blue curve is the exponential calculation by floating point multiplication and the bottom red curve is calculated by LUT method.

D. Comparison of the results of original PPE method and all digital PPE method

Compared to the theoretical PPE algorithm, the principal error of the digital PPE method comes from using the shifter and look up table to calculate floating point multiplication and exponential calculation using digital technology. The energy spectrum of ^{99m}Tc detected by NaI scintillator and calculated PPE and D-PPE algorithm are shown in the figure 6.21. The counting rate of γ-ray source is about 900 kcps. According to the calculation for that count rate the spectrum should contains about 50% piled-up pulses for standard 3τ integration. The FWHM of energy around 140keV for original PPE and digital PPE is 24.2keV (17.28% of 140keV) and 26.0keV (18.57% of 140keV), respectively. Therefore, the all digital PPE algorithm slightly increases the width of the energy spectrum around 140keV due to the approximations in the floating point multiplication.

176
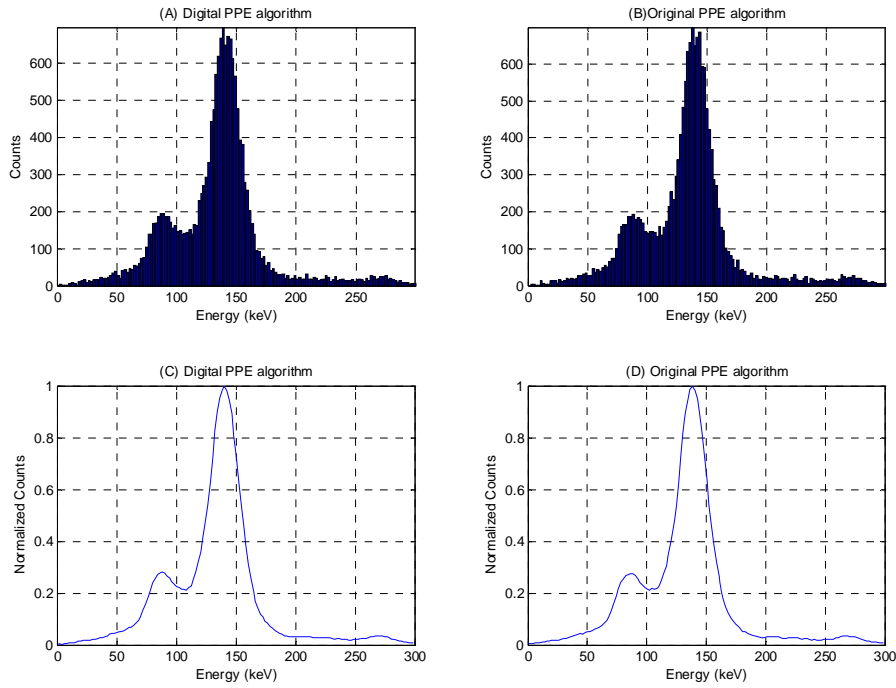
Figure 6.21 Energy spectra (top) and normalized spectra slopes in which maximum value equals 1 (bottom) of ^{99m}TC with 900kcps calculated by original PPE algorithm (24.2keV) and all digital PPE algorithms (26.0keV).

E. Evaluation of Energy Spectra for D-PPE algorithm, DLC technique, and 3τ integration

The energy spectra for ^{99m}Tc by a single PMT with NaI(TI) scintillator obtained at count rates of 1000kcps, 600kcps and 150kcps, are shown in the figure 6.22. The left column of the figure illustrates the spectra simulated by the all digital PPE algorithms; the right column shows the spectra obtained by using the 1τ delay-line pulse-clipping (DLC) technique, which avoids calculating the energy of overlapped pulses by cutting its tail and integrating the signal for a 230 ns. Final value is recovered by being divided by 0.637, which is the estimated percentage of the 230ns integrated pulse over integration of whole pulse. The spectra of the middle column are the results calculated with the conventional integral method i.e. 3τ integration.

The shapes of energy spectra at the three different count rates yielded by the D-PPE algorithm are identical and all of these spectra are similar to the one obtained using conventional integral method at a low count rate which serves as a reference spectrum for comparison. This reference spectrum not only includes the peak around 140keV for

^{99m}Tc, but also contains lead X-rays peak around 84keV. The total number of counts is at different count rates is 16391,10490,8034 for 1Mcps, 0.6Mcps and 0.15Mcps, respectively. If we calculated the energy by 3τ integration, the percentages of piled-up pulses for the case of 1Mcps, 0.6Mcps and 0.15Mcps are 50.1%, 39.9% and 14.2%, respectively. The total counts per second changes for the different methods. The conventional integral method achieves a reasonable spectrum at low count rates. However, it results in a distorted spectrum that overestimates the number of high energy events at high count rates. The DLC technique does not produce as precise a spectrum as the PPE algorithm although the results are better than those obtained from the conventional integral method at higher count rates. The DLC technique needs extra correction to obtain reasonable spectra. Otherwise, spectra at three different count rates are shifted to lower energies than the other two methods since it only integrates for a short time and underestimates the energy in each event. Therefore, the two fixed integration time methods not only distort the spectra, but also lose good events that can be saved by the proposed D-PPE algorithm.
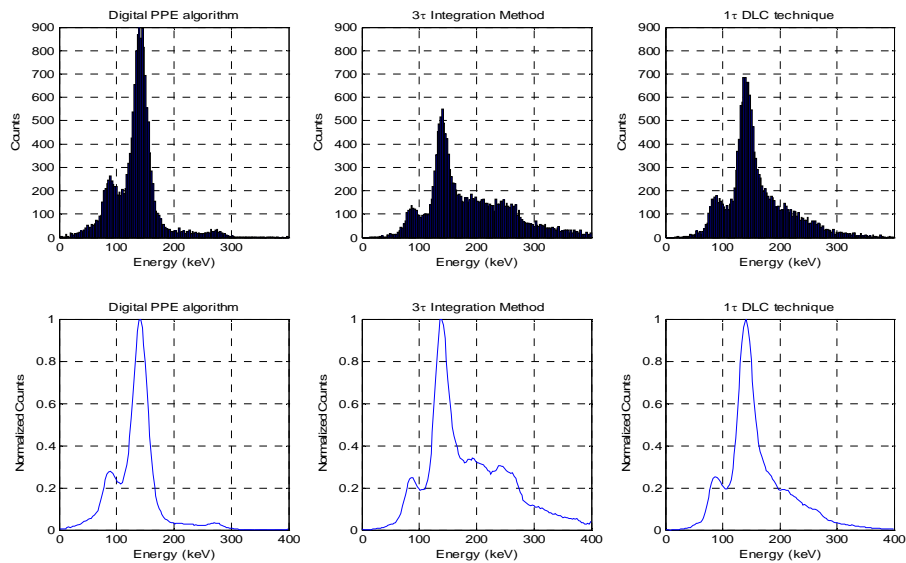
(A) 1000kcps
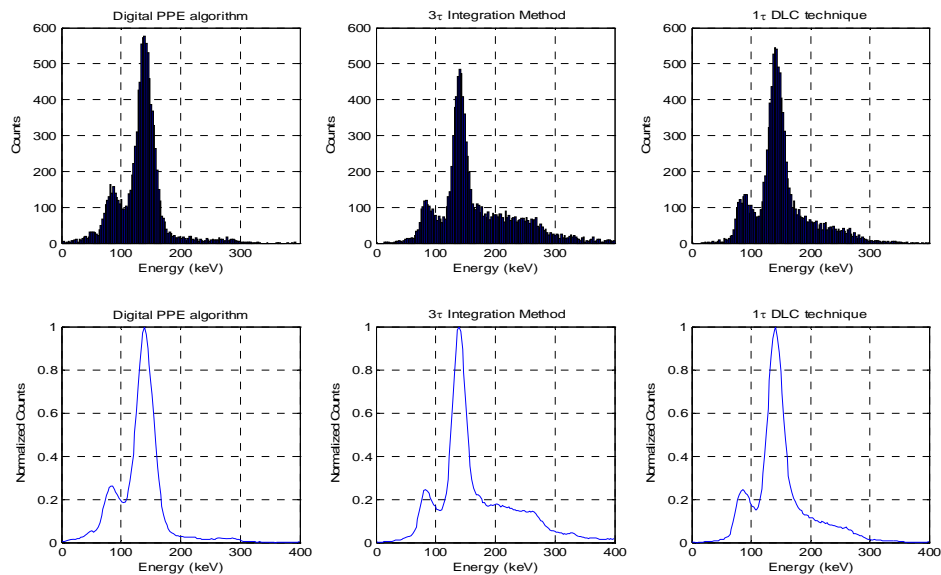
(B) 600 kcps
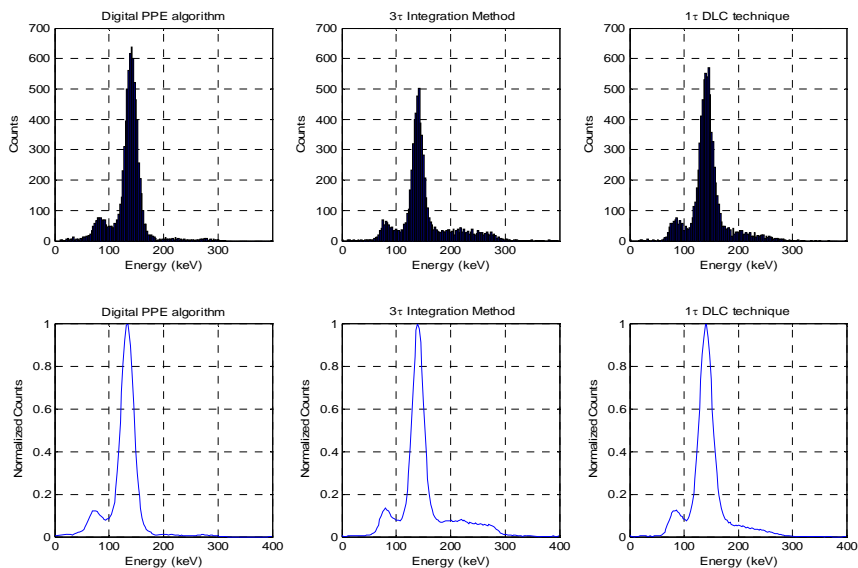
(C) 150kcps

Figure 6.22 Comparisons of energy spectra (top) and normalized spectra slopes with same amplitude (bottom) for the three energy extraction methods at three different count rates. (A) 1M cps; (B) 0.6M cps; and, (C) 0.15M cps. In each group, the left column is for the full digital PPE chip, the middle column is for the conventional 3τ integral method and the right column is for the DLC technique (clipping at τ).

CHAPTER 7

Conclusions and Future Work

In this chapter, we summarize the algorithms and analytical results presented in the previous chapters and suggest future work required to further speed image reconstruction and improve data acquisition.

7.1 Conclusions

This research was focused on a Compton imaging system for medical applications involving the imaging of emitting photon energies of 364.4 keV and higher. This work presented performance analysis of a Compton medical imaging system compared with a conventional collimated Anger camera, practical image reconstruction algorithms for list-mode data, and development of a digital pattern matching algorithm and device for post-signal processing to reduce the effects of pulse pile-up at high count rates in a scintillation camera.

In Chapter 1, we described the medical applications of higher energy single photons emitters, ^{131}I. Tracers labeled with iodine and other elements that emit even higher energies are important and irreplaceable for detecting and treating specific cancers and tracking essential bio-elements in studies of physiology and metabolism. However, the currently available imaging systems based on Anger cameras with a HEGP collimator cannot achieve the desired performance due to limitations imposed by the tradeoff between sensitivity and resolution for high energy photons because of the penetration through the collimator septa. After briefly reviewing and describing the general principles of Compton imaging systems, the supposition was presented that this system has the

potential for better performance for high energy photons than a collimated Anger Camera.

In Chapter 2, we introduced two practical imaging systems for the 364.4 keV photons emitted from ^{131}I: A NaI Anger Camera with HEGP lead collimator and a Compton imaging system with Si-NaI based dual planar detectors. The advantages and disadvantages of these imaging systems were analyzed qualitatively by Monte Carlo simulation and theoretical calculation. The problem with the parallel hole collimator is that spatial resolution is substantially decreased by septal penetration of the high energy gamma-rays, and this can only be reduced by increasing septal thickness which reduces sensitivity for directly transmitted photons as the square of the increase. The Compton imaging system avoids this tradeoff by using electronic collimation technique. However, the conical ambiguity, effect of Doppler broadening and energy resolution are issues that must be considered in any performance comparison since these factors affect the information per detected photon in the two systems.

In Chapter 3, these issues were addressed by using the M-UCRB based on the Fisher Information of the imaging system. This bound compares performance of different imaging system by calculating image variance at each target point response function. To solve the issue of computation complexity, we developed practical algorithms to calculate Fisher information matrix by Monte Carlo method and estimate M-UCRB by FFT based on the assumption of shift invariance.

The algorithm of calculating Fisher information matrix requires the value of transition probabilities that reflects the relation between each detection event and each emission. The system models and corresponding modeling methods to calculate transition probabilities were presented in Chapter 4. For the Anger Camera with HEGP collimator, a serial of point source response at different source to collimator distances were fitted to obtain a system model using a Gaussian plus an exponential function. The system model of Compton imaging system is more complex and requires knowledge of the statistical probabilities of all physical processes in the detection sequence. Meanwhile, the interpolation JPDF matrix is employed to accelerate calculation.

In Chapter 5, the system performance and comparison were analyzed using the M-UCRB algorithms we developed and verified along with the Monte Carlo simulation

platform and effective system modeling. From the illustrated bound curves that compare the effect of Si detector energy resolution and system spatial resolution, the effect of Doppler broadening is the limiting factor for Compton camera performance for imaging 360 keV photons. Performance of two systems was compared and analyzed by simulating a 2D disk with uniform activities. For the situation with the same number of detected events, the proposed Compton imaging system has better imaging performance than the Anger camera with HEGP, especially, as FWHM of desired point source response is less than 1.2 cm. This advantage was also proved by imaging and reconstructing a 2D hot spots phantom.

Two useful advances in both imaging reconstruction and post-signal processing for future application of Compton imaging system were developed and presented in Chapter 6. The paralleled MLEM algorithms based on a chess board date partition strategy can effectively speed up reconstruction for list-mode detection data obtained from Compton system by factor of 10 in our evaluation. The proposed specific data partition balances the time used in computation and communication to achieve an optimal performance. The digital post signal processing algorithms and proposed hardware implementation for reducing pulse pile-up substantially reduces distortion of the energy spectrum from the NaI(TI) second detector at the count rates as high as 10^6/sec.

7.2 Future work

As we described, the practical methods to calculate Fisher Information matrix and M-UCRB, system model, parallel MLEM, and digital algorithms for extracting energy from piled-up signals are useful in practical applications. Meanwhile, there are also some issues that need to be studied in the future.

The Monte Carlo simulation developed in our studies was speed up using force detection and variance reduction algorithm to enforce ingoing Compton process for every simulated photon. Therefore, Compared with Geant4(LECS) Monte Carlo system, the developed CSRNS only uses 5% computation time for the same simulation task. However, the resent CSRNS was developed focusing on the Compton imaging system

with the parallelized dual planer detectors. For other system geometries, the CSRNS need to be revised.

The Anger camera, in our research, was modeled with a Gaussian plus an Exponential function. Even though the model considered the effects of scattering and penetration photon in septa, this approximation of fitting the static point response function cannot evaluate the influence induced from hole pattern. Therefore, directly using a projection of a point source to avoid mathematic model is of worth to study and to compare the imaging performance of Anger Camera.

The list-mode MLEM is a promising algorithm for Compton image reconstruction. However, without parallel computing, the algorithm cannot be employed in actual clinical applications. For example, a list-mode MLEM program was executed on a dual core CPU with 2.8G Hz frequency, and an image with 65x65 pixels was reconstructed from 3 million photons. One iteration reconstruction required about 8 hours. Whereas the bin-mode MLEM for Anger camera reconstruction just takes 20 minutes for one iteration. Therefore, the parallel MLEM algorithm with chess board data partition provides a good method to speed up the reconstruction. In our studies, as the number of CPUs increased to 64, the efficiency of reconstruction increased 20 times. The primary obstacle to increasing speed is data communication latency due to insufficient network bandwidth. This issue can be solved using parallel shared memory systems. It is clearly necessary to optimize and revise our present algorithms on this platform for practical applications.
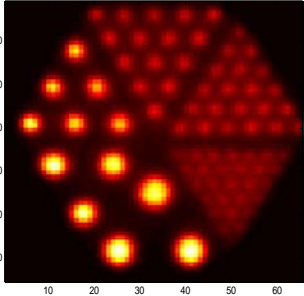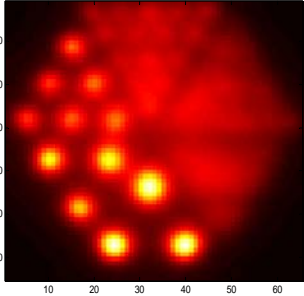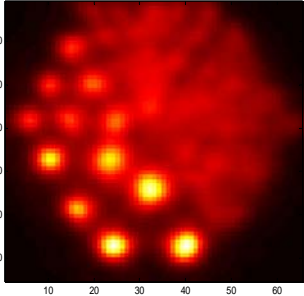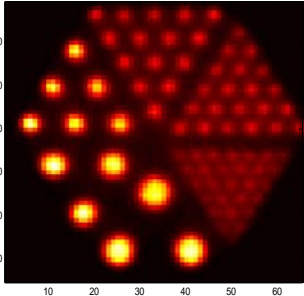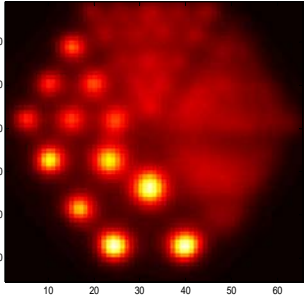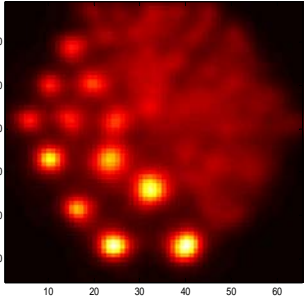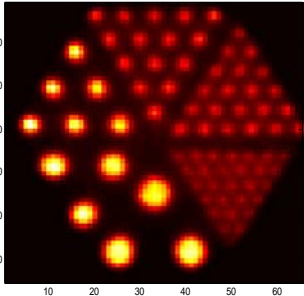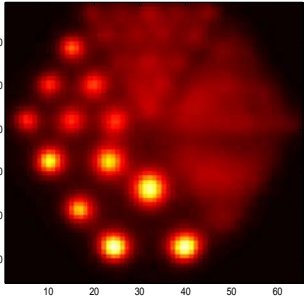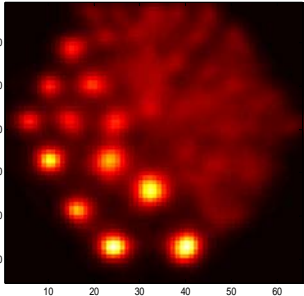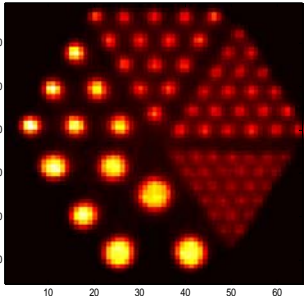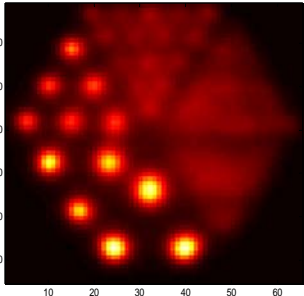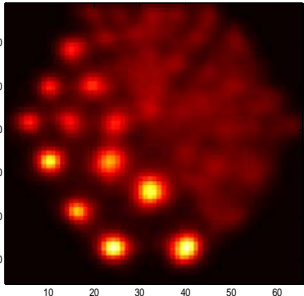
The digital post signal processing and pattern matching algorithm and designed circuit were useful and effective to extract energy information deposited in the pile-upped scintillation signal. Both correct energy information and starting-time of each event are of benefit to retrieve correct position information and coincidence pair for Compton imaging systems. In the future, the analog and digital combined chip is desired including the analogy signal acquisition circuit, high speed A/D converter and our designed digital processing unit.

APPENDIX

APPENDIX

In section 5.4, the images demonstrated were restored by 100 iteration using MLEM for both the Compton imaging system and the Anger camera with HEGP. Since the convergence rates are different for different imaging systems and number of acquired events, reconstructed images as a function of iteration are compared in this section.
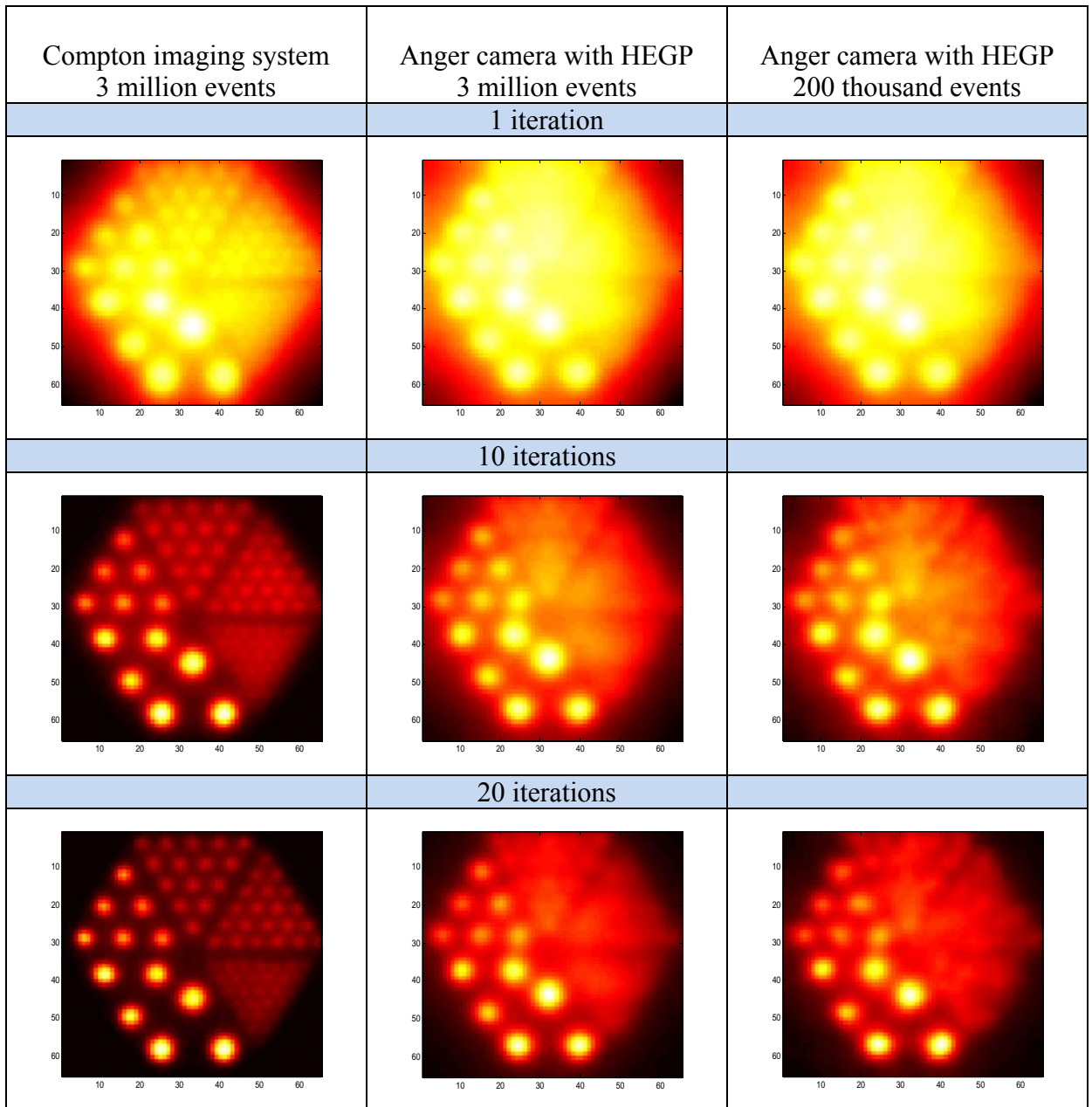
Compton imaging system 3 million events	Anger camera with HEGP 3 million events	Anger camera with HEGP 200 thousand events
1 iteration		
10 iterations		
20 iterations		

Compton imaging system 3 million events	Anger camera with HEGP 3 million events	Anger camera with HEGP 200 thousand events
30 iterations		
40 iterations		
50 iterations		
60 iterations		

186

Compton imaging system 3 million events	Anger camera with HEGP 3 million events	Anger camera with HEGP 200 thousand events
70 iterations		
80 iterations		
90 iterations		
100 iterations		

187
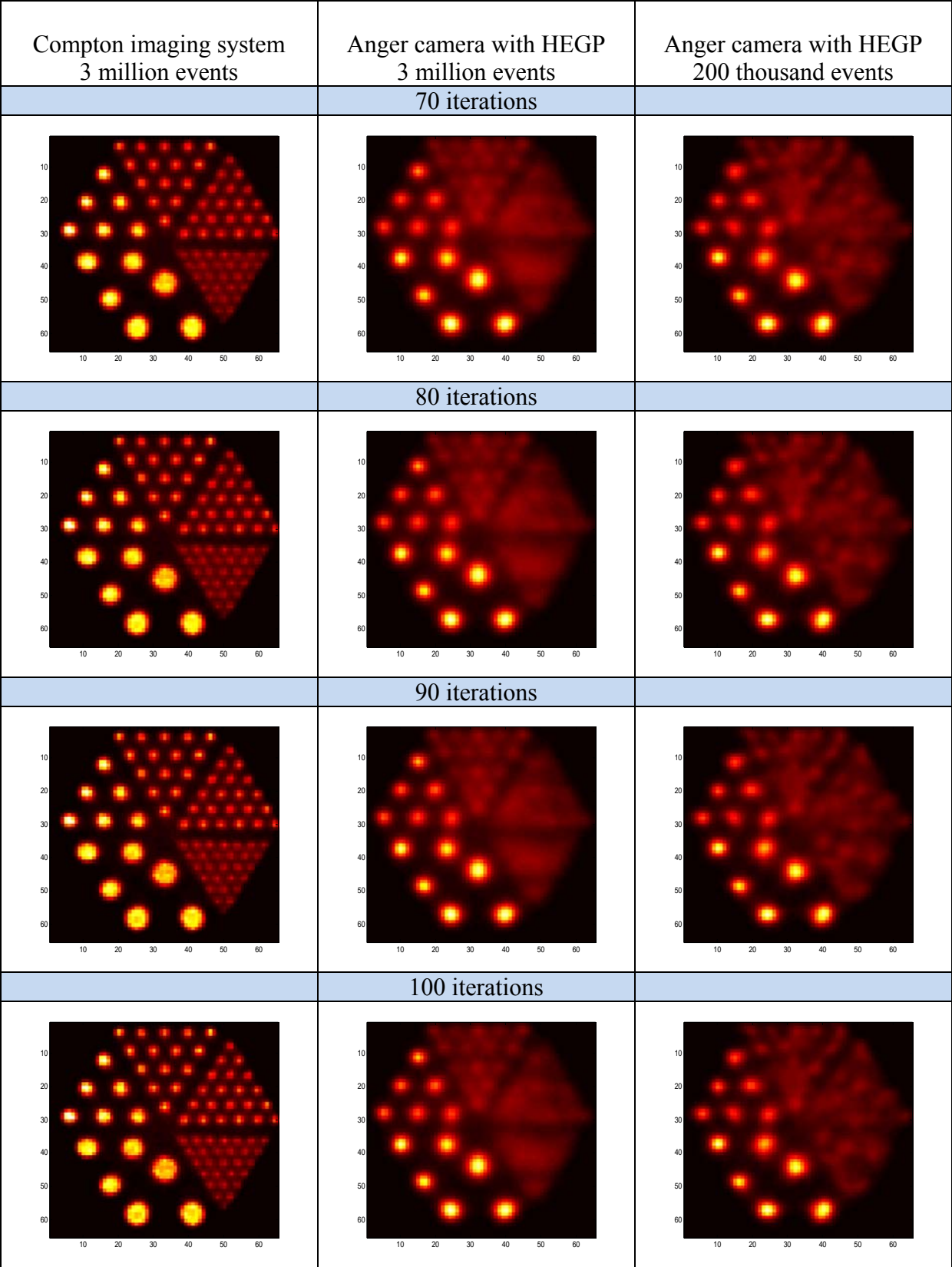
BIBLIOGRAPHY

BIBLIOGRAPHY

[1]   L. J. Meng and N. H. Clinthorne, "A Modified Uniform Cramer-Rao Bound for Multiple Pinhole Aperture Design," *IEEE Transactions on Medical Imaging*, vol. 23, pp. 896-902, 2004.

[2]   M. N. Wernick and J. N. Aarsvold, "Introduction to Emission Tomography," in *Emission tomography-The Fundamentals of PET and SPECT*, M. N. Wernick and J. N. Aarsvold, Eds.: Elsevier Academic.

[3]   P. F. Sharp, H. G. Gemmell, and A. D. Murray, *Parctical Nuclear Medicine*, Third ed: Springer, 2005.

[4]   M. Vorne, S. Sakki, K. Jarvi, and S. Vahatalo, "Tc-99m glucoheptonate in detection of lung tumors," *J. Nucl Med.*, vol. 23, pp. 250-254, 1982.

[5]   B. A. Khaw, H. W. Strauss, M. R., F. J.T., Y. T., G. H.K., and H. E., "Myocardial damage delineated by indium-111 antimyosin Fab and technetium-99m pyrophosphate," *J. Nucl Med.*, vol. 28, pp. 76-82, 1987.

[6]   P. J. ELL and S. S. GAMBHIR, *Nuclear Medicine in Clinical Diagnosis and Treatment*, vol. I: Churchill Livingstone, 2004.

[7]   K. F. Koral, Y. Dewaraja, L. A. Clarke, L. J., Z. K.R., R. S.G., F. I.R., K. M.S., and W. R.L., "Tumor-absorbed-dose estimates versus response in tositumomab therapy of previously untreated patients with follicular non-Hodgkin's lymphoma: preliminary report," *Cancer Biother Radiopharm*, vol. 15, pp. 347-355, 2000.

[8]   J. F. Chatal and C. A. Hoefnagel, *Radionuclide therapy*: Lancet, 1999.

[9]   J. P. Howard, J. M. Maris, L. S. Kersun, and J. P. Huberty, "Tumor Response and Toxicity With Multiple Infusions of High Dose 131I-MIBG for Refractory Neuroblastoma," *Pediatr Blood Cancer*, vol. 44, pp. 232-239, 2005.

[10]   G. L. DeNardo, S. J. DeNardo, and S. Shen, "Factors affecting 131I-Lym-1 pharmacokinetics and radiation dosimetry in patients with non-Hodgkin's lymphoma and chronic lymphocytic leukemia," *J. Nucl Med.*, vol. 40, pp. 1317-1326, 1999.

[11]   A. M. Peters, *Nuclear Medicine in Radiological Diagnosis*: Martin Dunitz, 2003.

[12]   F. Jamar, P. T. Chapman, D. H. Manicourt, D. M. Glass, D. O. Haskard, and A. M. Peters, "A comparison between 111In-anti-E-selectin mAb and 99Tcm-labelled human non-specific immunoglobulin in radionuclide imaging of rheumatoid arthritis," *The British Journal of Radiology*, vol. 70, pp. 473-481, 1997.

[13]   V. W. Wing, E. vanSonnenberg, S. Kipper, and M. P. Bieberstein, "Indium-111-labeled leukocyte localization in hematomas: a pitfall in abscess detection," *Radiology*, vol. 152, pp. 173-176, 1984.

[14]   G. V. Raj, A. W. Partin, and T. J. Polascik, "Clinical utility of Indium 111-capromab pendetide immunoscintigraphy in the detection of early, recurrent prostate carcinoma after radical prostatectomy," *Cancer* vol. 94, pp. 987-996, 2002.

[15]   R. J. Hawker, L. M. Hawker, and A. R. Wilkinson, "Indium (111In)-labelled human platelets: optimal method," *Clinical Science*, vol. 58, pp. 243-248, 1980.

[16]   A. G. Jones, M. A. Davis, and M. K. Dewarjee, "In113m-labeled bone scanning agents," *Radiology*, vol. 117, pp. 727-730, 1975.

[17]   G. Subramanian and J. G. McAfe, "A radioisotope generator of indium-113m," *International Journal of Applied Radiation and Isotopes*, vol. 18, pp. 215-221, 1967.

[18]   H. S. Stern, D. A. Goodwin, U. Scheffel, and H. N. Wagner, "In113m for blood-pool and brain scanning," *Nucleonics*, vol. 25, pp. 62, 1967.

[19]   R. E. O'Mara, G.Subramanian, J.G.McAfee, and C. L. Burger, "Comparison of 113mIn and other short-lived agents for cerebral scanning," *J. Nucl Med.*, vol. 10, pp. 18-27, 1969.

[20]   W. L. Rogers, "Personal communication," 2004.

[21]   W. L. Rogers, N. H. Clinthorne, and A. Bolozdynia, "Compton Cameras for Nuclear Medical Imaging," in *EMISSION TOMOGRAPHY: The Fundamentals of PET and SPECT*, M. N. Wernick and J. Aarsvold, Eds.: Academic Press, 2004.

[22]   J. C. Harbert, *Nuclear Medicine Therapy*: Thieme, 1987.

[23]   C. M. Washington and D. Leaver, *Principles and Practice of Radiation Therapy*, 2nd ed: Mosby, 2004.

[24]   S. Mattsson, L. Jacobsson, and L. Johansson, "Internal Radionuclide Dosimetry:Diagnostic and Therapeutic Nuclear Medicine,Occupational and Environmental Exposures.Differences and Similarities," *Cancer Biotherapy & Radiopharmaceuticals*, vol. 18, 2003.

[25]   H. O. Anger, "Scintillation camera," *Rev. Sci. Inst.*, vol. 29, 1958.

[26]   G. F. Knoll, *Radiation Detection and Measurement*, 3rd ed. New York: Wiley, 2000.

[27]   H. H. Barrett and W. Swindell, *Radiological Imaging: the Theory of Image Formation, Detection, and Processing*. New York: Academic, 1981.

[28]   W. W. Moses, "Overview of Nuclear Medical Imaging Instrumentation and Techniques," presented at Proc . SCFIF97 Conference on Scintillating and Fiber Detectors, 1988.

[29]   A. R. Formiconi, "Collimators," *The Quarterly Journal of Nuclear Medicine*, vol. 46, 2002.

[30]   A. R. Formiconi, "Geometrical response of multihole collimators," *Physics in Medicine and Biology*, vol. 43, pp. 3359-3379, 1998.

[31]   G. J. Hine and J. J. Erickson, "Advances in scintigraphic instruments," in *Instrumentation in nuclear medicine*, vol. 1, G. J. Hine and J. A. Sorenson, Eds. New York: Academic Press, 1974.

[32]   Y. K. Dewaraja, M. Ljungberg, and K. F. Koral, "Characterization of scatter and penetration using Monte Carlo Simulation in 131I imaging," *Journal of Nuclear Medicine*, vol. 41, pp. 123-130, 2000.

[33]   Y. K. Dewaraja, M. Ljungberg, and K. F. Koral, "Accuracy of 131I Tumor Quantification in Radioimmunotherapy Using SPECT Imaging with an Ultra-High-Energy Collimator: Monte Carlo Study," *J. Nucl Med.*, vol. 41, pp. 1760-1767, 2000.

[34]   D. L. Gunter, "Collimator characteristics and design," in *Nuclear Medicine*, R. E. Henkin and M. A. Boles, Eds. St Louis: Mosby, 1996, pp. 96-124.

[35]   R. D. Evans, *The atomic nucleus*. New York: Krieger, 1982.

[36]   S. chonfelder, A. Hirner, and K. Schneider, "A Telescope for Soft Gamma Ray Astronomy," *Nucl. Inst. And Meth. in Phys. Res.*, vol. 107, pp. 385-394, 1973.

[37] R. W. Todd, J. M. Nightingale, and D. B. Everett, "A proposed gamma camera," *Nature*, vol. 251, pp. 132-134, 1974.

[38] M. Singh, "An electronically collimated gamma camera for single photon emission computed tomography:Part I. theoretical considerations and design criteria," *Med. Phys.*, vol. 10, pp. 421-427, 1983.

[39] M. Singh and D. Doria, "An electronically collimated gamma camera for single photon emission computedtomography: Part II. image reconstruction and preliminary experimental measurements," *Med. Phys.*, vol. 10, pp. 428-435, 1983.

[40] M. Singh and R. Brechner, "Experimental test-object study of electronically collimated SPECT," *J. Nucl Med.*, vol. 31, pp. 178-186, 1990.

[41] M. Atac, R. Chaney, and D. Chrisman, "Development of a high-resolution scintillating fiber gamma-ray telescope," *IEEE Transactions on Nuclear Science*, vol. 38, pp. 568-573, 1991.

[42] I. Fujida and V. Perez-Mendez, "Theoretical considerations of a new electronically collimated gamma camera utilizing gas scintillation," *SPIE Proceedings Medical Imaging*, vol. 67, pp. 84-89, 1987.

[43] A. Bologzdynya, V. Egorov, and A. Koutchenkov, "High pressure Xenon electronically collimated camera for low energy gamma ray imaging," presented at Proc. IEEE Nucl. Sci. Symp. Med. Imaging Conf., 1996.

[44] H. J. P. Kuyken and S. A. Audet, "Gamma Ray Imaging with Silicon Detectors – A Compton Camera for Radionulide Imaging in Medicine," *Nuclear Instruments and Methods in Physics Research, Section A: Accelerators, Spectrometers, Detectors and Associated Equipment*, vol. 273, pp. 570-576, 1988.

[45] T. Kamae, N. Hanada, and R. Enomoto, "Prototype design of multiple Compton gamma-ray camera," *IEEE Transactions on Nuclear Science*, vol. 35, pp. 352-355, 1996.

[46] P. Weilhammer, E. Nygard, and W. Dulinski, "Si pad detectors," *Nuclear Instruments and Methods in Physics Research, Section A: Accelerators, Spectrometers, Detectors and Associated Equipment*, vol. 383, pp. 89-97, 1996.

[47] C. Lehner, Z. He, and F. Zhang, "4-pi Compton imaging using a 3-D position-sensitive CdZnTe detector via weighted list-mode maximum likelihood," *IEEE Transactions on Nuclear Science*, vol. 2004, pp. 4, 2004.

[48] M. Singh., F. Doty, S. Friesenhahn, and J. Butler, "Feasibility of using cadmium-zinc-telluride detectors in electronically collimated SPECT," *IEEE Transactions on Nuclear Science*, vol. 42, pp. 1139-1146, 1995.

[49] Y. F. Du, Z. He, G. F. Knoll, D. K. Wehe, and W. Li, "Evaluation of a Compton scattering camera using 3-D position sensitive CdZnTe detector," *Nuclear Instruments and Methods in Physics Research, Section A: Accelerators, Spectrometers, Detectors and Associated Equipment*, vol. 457, pp. 203-211, 2001.

[50] J. B. Martin, G. F. KNOLL, D. K. WEHE, N. DOGAN, V. JORDANOV, N. PETRICK, and M. SINGH, "A Ring Compton Scatter Camera For Imaging Medium Energy Gamma Rays," *IEEE Transactions on Nuclear Science*, vol. 40, pp. 972-978, 1993.

[51] J. W. LeBlanc, N. H. Clinthorne, C.-H. Hua, E. Nygard, W. L. Rogers, D. K. Wehe, P. Weilhammer, and S. J. Wilderman, " C-SPRINT: a prototype Compton

camera system for low energy gammaray imaging," *IEEE Transactions on Nuclear Science*, vol. 45, pp. 943-949, 1998.

[52]   F. Zhang, Z. He, D. Xu, G. Knoll, D. Wehe, and J. Berry, "Improved Resolution for 3-D Position Sensitive CdZnTe Spectrometers," *IEEE Transactions on Nuclear Science*, vol. 51, pp. 2427-2431, 2004.

[53]   A. Laboratories, "ARGUS System specifications."

[54]   S. Jan, G. Santin, and D. Strul, "GATE: a simulation toolkit for PET and SPECT," *Physics in Medicine and Biology*, vol. 49, pp. 4543-4561, 2004.

[55]   P. Weilhammer, E. Nygard, W. Dulinski, A. Czermak, F. Djama, S. Gadomski, S. Roe, A. Rudge, F. Schopper, and J. Strobel, " Si Pad detectors," *Nuclear Instruments and Methods in Physics Research. A.*, vol. 383, pp. 89-97, 1996.

[56]   D. Meier, A. Czermak, P. Jalocha, B. Sowicki, M. Kowal, W. Dulinski, G. Maehlum, E. Nygard, K. Yoshioka, J. Fuster, C. Lacasta, M. Mikuz, S. Roe, J. Weilhammer, C. H. Hua, S. J. Park, S. J. Wilderman, L. Zhang, N. H. Clinthorne, and W. L. Rogers, "Silicon detector for a Compton camera in nuclear medical imaging," *IEEE Trans. Nuclear Science*, vol. 49, pp. 812-816, 2002.

[57]   "www.sintef.no."

[58]   "www.ideas.no."

[59]   S.-J. Park, "A Very High Resolution Small Animal PET Based on The Compton PET Concept," vol. Ph.D. Ann Arbor: The University of Michigan, 2005.

[60]   J. A. Sorenson and M. e. Phelps, *Physics in Nuclear Medicine*, Second Edition ed: W.B. Saunders Company, 1987.

[61]   B. M. W. Tsui, D. L. Gunter, R. Beck, and P. J., "Physics of collimator design," in *Diagnostic nuclear medicine*, M. P. Sandler, J. A. Patton, R. E. Coleman, A. Gottschalk, F. J. T. H. Wackers, and P. B. Hoffer, Eds. Baltimore: Williams and Wilkins, 1988, pp. 67-79.

[62]   D. J. deVries, S. C. Moore, R. E. Zimmerman, S. P. Mueller, B. Friedland, and R. C. Lanza, "Development and validation of a Monte Carlo simullation of photon transport in an anger camera," *IEEE Transactions on Medical Imaging*, vol. 1990, pp. 430-438, 1990.

[63]   C. E. Floyd, R. J. Jaszczak, C. C. Harris, and R. E. Coleman, "Energy and spatial distribution of multiple order compton scatter in SPECT: a Monte Carlo investigation," *Physics in Medicine and Biology*, vol. 29, pp. 1217-1230, 1984.

[64]   D. P. Lewis, B. M. W. Tsui, C. Tocharoenchai, and E. C. Frey, "Characterization of medium and high energy collimators using ray-tracing and Monte Carlo methods.," presented at Conference record of 2000 IEEE Nuclear Science Sympsium and Medical Imaging Conference, 2000.

[65]   I. Buvat and I. Castiglioni, "Monte Carlo simulations in SPECT and PET," *Q. J. Nucl. Med.*, vol. 46, 2002.

[66]   S. Staelens, D. Strul, and G. Santin, "Monte Carlo simulations of a scintillation camera using GATE: Validation and application modeling," *Physics in Medicine and Biology*, vol. 2003, pp. 3021, 2003.

[67]   G. Santin, D. Strul, and d. Lazaro, "GATE, a Geant4 based simulation platform for PET integrating movement and time management," *IEEE Transactions on Nuclear Science*, vol. 50, pp. 1516, 2003.

[68] A. V. Oppenheim and A. S. Wilsky, *Signals and Systems*. Englewood Cliffs: Prentice-Hall, 1983.

[69] J. H. Hubbell, "Photon Mass Attenuation and Energy Absorption Coefficients from 1 keV to 20 MeV," *Int. J. Appl. RadiatIsotopes*, vol. 33, pp. 1269-1290, 1982.

[70] M. J. Berger, J. H. Hubbell, S. M. Seltzer, J. Chang, J. S. Coursey, R. Sukumar, and D. S. Zucker, "XCOM: Photon Cross Sections Database," National Institute of Standards and Technology, 1998.

[71] O. Klein and Y. Nishina, "Uber die Streuung von Strahlung durch freie Elektronen nach der neuen Quantendynamik von Dirac," *Z. Phys.*, vol. 52, pp. 853-868, 1929.

[72] G. A. Carlsson, C. A. Carlsson, K. F. Berggren, and R. Ribberfors, "Calculation of scattering cross sections for increased accuracy in diagnostic radiology. I. Energy broadening of Compton-scattered photons," *Medical Physics*, vol. 9, pp. 868-879, 1982.

[73] R. Ribberfors, "Relationship of the relativistic Compton cross section to the momentum distribution of bound electron states. II. Effects of anisotropy and polarization " *Physics Review B*, vol. 12, pp. 3136-3141, 1975.

[74] R. Ribberfors and K. F. Berggren, "Incoherent-S-ray-scattering functions and cross sections by means of a pocket calculator," *Physics Review A*, vol. 26, pp. 3325-3333, 1982.

[75] F. Biggs, L. B. Mendelsohn, and J. B. Mann, "Hartree-Fock Compton Profiles for the Elements," *Atomic Data and Nuclear Data Tables*, vol. 16, pp. 201-309, 1975.

[76] W. Reed and P. Eisenberger, "Gamma-ray Compton profiles of diamond,silicon and germanium," *Physics Review B*, vol. 6, pp. 4598-4604, 1972.

[77] C. E. Ordonez, W. Chang, and A. Bolozdynyz, "Angular Uncertainties due to Geometry and Spatial Resolution in Compton Cameras," *IEEE Transactions on Nuclear Science*, vol. 46, pp. 1142-1147, 1999.

[78] S. Furuie, G. Herman, T. Narayan, P. Kinahan, J. Karp, R. Lewitt, and S. Matej, "A methodology for testing for statistically significant differences between fully 3D PET reconstruction algorithms," *Physics in Medicine and Biology*, vol. 39, pp. 341-354, 1994.

[79] A. E. Burgess, "Image quality, the ideal observer, and human performance of radiologic decision tasks," *Academic Radiology*, vol. 2, pp. 522-526, 1995.

[80] H. V. Trees, *Detection, estimation, and modulation theory, Part I.* New York: Wiley and Sons, 1968.

[81] H. V. Poor, *An Introduction to Signal Detection and Estimation*. New York: Springer-Verlag, 1994.

[82] A. O. Hero, J. A. Fessler, and M. Usman, "Exploring estimator bias-variance tradeoffs using the uniform CR bound," *IEEE Trans. Signal Processing*, vol. 44, pp. 2026-2041, 1996.

[83] T. Kragh and A. Hero, "Bias-resolution-variance tradeoffs for single pixel estimation tasks using the uniform cramer rao bound UCRB," presented at In Proc. of IEEE Nuclear Science Symposium and Medical Imaging Conf, FRANCE, 2000.

[84] A. O. Hero, M. Usman, A. C. Sauve, and J. A. Fessler, "Recursive algorithms for computing the Cramer-Rao bound," *IEEE Trans. on Signal Processing*, vol. 45, pp. 803-807, 1997.

[85] H. Cramer, *Mathematical Methods of Statistics*. Princeton: Princeton University Press, 1946.

[86] A. O. Hero, "A Cramer-Rao Type Lower Bound for Essentially Unbiased parameter Estimation," Lincoln Laboratory, MIT 1992.

[87] T. J. Kraph, "Tradeoffs and Limitations in Statistically Based Image Reconstrustruction Problems," in *Electrical Engineering: Systems*, vol. Ph.D. Ann Arbor: The University of Michigan, 2002.

[88] J. A. Fessler and W. L. Rogers, "Spatial resolution properties of penalized likelihood image reconstruction methods: Space-invariant tomographs," *IEEE Transactions on Image Processing*, vol. 5, pp. 1346-1358, 1996.

[89] J. LeBlanc, "A Compton Camera for Low Energy Gamma Ray Imaging In Nuclear Medicine Applications," vol. Ph.D: University of Michigan, 1999.

[90] J. Berger, *Statistical Decision Theory and Bayesian Analysis*. New York: Springer-Verlag, 1985.

[91] W. H. Press, S. A. Teukolsky, W. T. Vetterling, and Brian P. Flannery, *Numerical Recipes in C: the art of scientific computing*: Cambridge University Press, 2002.

[92] P. J. Davis, *Circulant Matrices*. NY: Wiley-Interscience, 1979.

[93] G. H. Golub and C. F. Van, *Matrix computations*: Johns Hopkins University Press, 1996.

[94] J. M. Hammersley and D. C. Handscomb, *Monte Carlo Methods*. London: Methuen, 1964.

[95] M. Ljungberg, S.-E. Strand, and M. A. King, *Monte Carlo Calculations in Nuclear Medicine*. Bristol and Philadelphia: Institute of Physics Publishing, 1998.

[96] F. James, "A review of pseudorandom number generators," *Comput. Phys. Commun.*, vol. 60, pp. 329-344, 1990.

[97] D. E. Knuth, *Seminumerical Algorithms*, vol. 2, 2nd ed: Addison-Wesley, 1981.

[98] D. R. Haynor, R. L. Harrison, and T. K. Lewellen, "The use of importance sampling techniques to improve the efficiency of photon tracking in emission tomography simulations," *Medical Physics*, vol. 18, pp. 990-1001, 1991.

[99] R. M. Kippen, "The Geant low energy Compton scattering (GLECS) package for use in simulating advanced Compton telescopes," *New Astronomy Review*, vol. 48, pp. 221-225, 2004.

[100] A. F. Bielajew and D. W. O. Rogers, *Variance reduction techniques Monte Carlo Transport of Electrons and Photons*. New York: Plenum, 1988.

[101] H. Kahn, "Application of Monte Carlo," Rand Corp., Santa Monica, CA 1956.

[102] T. Hebert, R. Leahy, and M. Singh, "Maximum likelihood reconstruction for a prototype electronically collimated single photon emission system," *SPIE Proceedings Medical Imaging*, vol. 767, pp. 428-435, 1987.

[103] S. J. Wilderman, W. L. Rogers, G. F. Knoll, and J. C. Engdahl, "Fast Algorithm for List Mode Back-Projection of Compton Scatter Camera Data," *IEEE Transactions on Nuclear Science*, vol. 45, pp. 957-961, 1998.

[104]   S. J. Wilderman, W. L. Rogers, G. F. Knoll, and J. C. Engdahl, "Monte Carlo Calculation of point spread functions of Compton scatter cameras," *IEEE Transactions on Nuclear Science*, vol. 44, pp. 250-254, 1997.

[105]   S. J. Wilderman, J. A. Fessler, N. H. Clinthorne, and W. L. Rogers, "Improved Modeling of System Response in List Mode EM Reconstruction of Compton Scatter Camera Images," presented at Proc. IEEE Nuc. Sci. Symp. Med. Im. Conf., 2000.

[106]   A. C. Sauve, A. O. Hero, W. L. Rogers, S. J. Wilderman, and N. H. Clinthorne, "3D image reconstruction for a Compton SPECT camera model," *IEEE Transactions on Nuclear Science*, vol. 46, 1999.

[107]   A. Laboratories, "ARGUS   SYSTEM SPECIFICATIONS."

[108]   L. Parra and H. H. Barrett, "List-Mode Likelihood: EM Algorithm and Image Quality Estimation Demonstrated on 2-D PET," *IEEE Transactions on Medical Imaging*, vol. 17, pp. 228-235, 1998.

[109]   A. Macovski, *Medical Imaging Systems*. New Jersey: Prentice-Hall, 1983.

[110]   D. Brusa, G. Stutz, J. A. Riveros, J. M. Fernandez-Varea, and F. Salvat, "Fast sampling algorithm for the simulation of photon Compton scattering," *Nuclear Instruments and Methods in Physics Research. A.*, vol. 379, pp. 167-175, 1996.

[111]   S. J. Wilderman, N. H. clinthorne, J. A. Fessler, and W. L. Rogers, "List-mode Maximum Likelihood Reconstruction of Compton Scatter Camera Images in Nuclear Medicine," presented at IEEE Nuclear Science Symposium and Medical Imaging Conference, Toronto, 1998.

[112]   D. L. McLeigh, *Monte Carlo simulation and finance*. Hoboken, NJ: Wiley, 2005.

[113]   P. Glasserman, *Monte Carlo Methods in Financial Engineering*: Springer, 2000.

[114]   C. H. Hua, N. H. Clinthorne, S. J. Wilderman, J. W. LeBlanc, and W. L. Rogers, "Quantitive evaluation of information loss for Compton cameras," *IEEE Trans. on Nuclear Science*, vol. 46, pp. 587-593, 1999.

[115]   R. Todd, J. Nightingale, and D. Everett, "A proposed gamma camera," *Nature*, vol. 251, pp. 132-134, 1974.

[116]   R. C. Rohe, M. M. Sharfi, K. A. Kecevar, J. D. Valentine, and C. Bonnerave, "The spatially-variant back-projection proint kernel function fo an energy-subtraction Compton scatter camera for medical imaging," presented at IEEE Nuclear Science Symposium and Medical Imaging Conference, Anaheim, CA, 1996.

[117]   M. J. Cree and P. J. Bones, "Towards direct reconstruction from a gamma camera based on compton scattering," *IEEE Transactions on Medical Imaging*, vol. 13, pp. 298-407, 1994.

[118]   R. Basko, G. L. Zeng, and G. T. Gullberg, "Application of spherical harmonics to image reconstruction for the compton camera," *Physics in Medicine and Biology*, vol. 43, pp. 887-894, 1998.

[119]   L. Parra and H. Barrett, "Reconstruction of cone-beam projections from Compton scattered data," *IEEE Transactions on Nuclear Science*, vol. 47, pp. 1543-50, 1998.

[120]   D. L. Gunter, "Filtered backprojection algorithms for compton cameras in nuclear medicine," 2006.

[121] T. Tomitani and M. Hirasawa, "Image reconstruction from limited angle Compton camera data," *Physics in Medicine and Biology*, vol. 47, pp. 2129-2145, 2002.

[122] N. H. Clinthorne and W. L. Rogers, "Fast maximum likelihood reconstruction of Compton-scatter camera images," *J. Nucl Med. Supp.*, vol. 38, pp. 58p, 1997.

[123] M. Singh and R. R. Brechner, "Experimental Test-Object Study of Electronically Collimated SPECT," *J. Nucl Med.*, vol. 31, pp. 178-186, 1990.

[124] R. R. Brechner and M. Cingh, "Iterative Reconstruction of Electronically Collimated SPECT," *IEEE Transactions on Nuclear Science*, vol. NS-37, pp. 1328-1332, 1990.

[125] L.A.Shepp and Y. Vardi, "Maximum Likelihood Reconstruction for Emission Tomography," *IEEE Transactions on Medical Imaging*, vol. MI-1, pp. 113, 1982.

[126] T. Hebert, R. Leahy, and M. Singh, "Three-dimensional maximum-likelihood reconstruction for an electronically collimated single-photon-emission imaging system," *J. Opt. Soc. Am. A*, vol. 7, pp. 1305-1313, 1990.

[127] L. Zhang, "Compton Gamma-Ray Imaging Probes for Prostate and Breast," in *Biomedical Engineering*, vol. Ph.D. Ann Arbor: University of Michigan, 2004.

[128] J. A. Fessler and A. O. Hero, "Space-alternating generalized expectation maximization algorithm," *IEEE Trans. Signal Processing*, vol. 42, pp. 2664-2677, 1994.

[129] W. F. Jones, L. G. Byars, and M. E. Casey, "Positron emission tomographic images and expectation maximization: a VLSI architecture for multiple iterations per second," *IEEE Transactions on Nuclear Science*, vol. 35, pp. 620-624, 1988.

[130] A. W. McCarth and M. I. Miller, "Maximum Likelihood SPECT in Clinical Computation Times Using Mesh-Connected Parallel Computers," *IEEE Transactions on Medical Imaging*, vol. 10, pp. September, 1991, 1991.

[131] C. M. Chen, S. Y. Lee, and Z. H. Cho, "Parallelization of the EM Algorithm for 3-D PET image reconstruction," *IEEE Transactions on Medical Imaging*, vol. 10, pp. 513-522, 1991.

[132] D. W. Shattuck, J. Rapela, A. Chatzioannou, J. Qi, and R. M. Leahy, "Internet2-based 3D PET image reconstruction using a PC cluster," *Physics in Medicine and Biology*, vol. 47, pp. 2785-2795, 2002.

[133] D. S. Lalush and M. N.Wernick, "Iterative Image Reconstruction," in *Emission tomography. The Fundamentals of PET and SPECT*, M. N. Wernick and J. N. Aarsvold, Eds., 1st ed. San Diego: Elsevier Academic Press, 2004.

[134] L. A. Shepp and Y. Vardi, "Maximum Likelihood Reconstruction for Emission Tomography," *IEEE Transactions on Medical Imaging*, vol. MI-1, pp. 113, 1982.

[135] K. Lange and R. Carson, "EM reconstrucion algorithms for emission and transmission tomography," *Journal of Computer Assisted Tomography*, vol. 8, pp. 306-326, 1984.

[136] A. P. Dempster, N. M. Laird, and D. B. Clark-Pearson, "Maximum likelihood from incomplete data via the EM algorithm," *Journal of Royal Statistics Society Ser. B*, vol. 39, pp. 1-38, 1977.

[137] H. V. Trees, *Detection, Estimation, and Modulation Theory, Part I.* New York: John Wiley & Sons, 1968.

[138] E. Veklerov and J. Llacer, "Stopping rule for the MLE algorithm based on statistical hypothesis testing," *IEEE Transactions on Medical Imaging*, vol. 6, pp. 313-319, 1987.

[139] J. A. Fessler and A. O. Hero, "Penalized maximum-likelihood image reconstruction using space-alternating generalized EM algorithms," *IEEE Transactions on Image Processing*, vol. 4, pp. 1417-1429, 1995.

[140] D. L. Snyder, M. I. Miller, L. J. Thomas, and D. G. Politte, "Noise and edge artifacts in maximum-likelihood reconstructions for emission tomography," *IEEE Transactions on Medical Imaging*, vol. 6, pp. 228-238, 1987.

[141] H. H. Barrett, T. White, and L. C. Parra, "List-Mode Likelihood," *J. Opt. Soc. Am. A*, vol. 14, pp. 2914-2923, 1997.

[142] R. H. Huesman, G. J. Klein, W. W. Moses, J. Qi, B. W. Reutter, and P. R. G. Virador, "List-Mode Maximum-Likelihood Reconstruction Applied to Positron Emission Mammography (PEM) with Irregular Sampling," *IEEE Transactions on Medical Imaging*, vol. 19, pp. 532-537, 2000.

[143] C.-M. Chen and S.-Y. Lee, "On Parallelizing the EM Algorithm for PET Image Reconstruction," *IEEE Trans. Parallel and Distributed System*, vol. 5, pp. 860-873, 1994.

[144] L. Kaufman, "Implementing and accelerating the EM algorithm for positron emission tomography," *IEEE Transactions on Medical Imaging*, vol. 6, pp. 37-50, 1987.

[145] S. P. Olesen, "Parallel computation for positron emission tomography with reduced processor communications," vol. Ph.D. Knoxville: The University of Tennessee, 1996, pp. 78.

[146] W. Gropp, E. Lusk, and A. Skjellum, *Using MPI -portable parallel programming with the Message Passing Interface*. Cambridge, Massachusetts: The MIT Press.

[147] B. Parhami, *Introduction to Parallel Processing-Algorithms and Architectrues*: Kluwer Academic Publishers, 2002.

[148] C. A. Swann, "Maximum Likelihood Estimation Using Paralle Computing: An Introduction to MPI," *Computational Economics*, vol. 19, pp. 145-178, 2002.

[149] W. George, "Dynamic Load-Balancing for Data-Parallel MPI programs," presented at Message Passing Interface developers and users conference, 1999.

[150] A. Suarez and C. N. Ojeda-Gueera, "Overlapping computations and communications in Torus networks," presented at 4th Euromicro Workshop on Parallel and Distributed Processing, 1996.

[151] R. W. Engstrom, "Photomultiplier Handbook," RCA Corporation, 1980.

[152] J. S. Karp, G. Muehllehner, D. Beerbohm, and D. Mankoff, "Event localization in a continuous scintillation detector using digital processing," *IEEE Transactions on Nuclear Science*, vol. 33, pp. 550-555, 1986.

[153] J. Kolodziejczuyk, "Method and apparatus for measuring the time integrals of exponentially decaying pulses," vol. 5,430,406, U. Patent, Ed., 1995.

[154] W. H. Wong and H. Li, "A scintillation detector signal processing technique with active pile up prevention for extending scintillation count rates," *IEEE Trans. Nucl. Sci.*, vol. 45, pp. 838-842, 1998.

[155] T. K. Lewellen, A. N. Bice, K. R. Pollard, and J. B. Zhu, "Evaluation of a clinical scintillation camera with pulse tail extrapolation electronics," *J. Nucl Med.*, vol. 30, pp. 1554-1558, 1989.

[156] D. R. K. Brownrigg, "The weighted median filter," *Comm. ACM.*, vol. 27, pp. 807-818, 1984.